Optical and infrared studies of distant galaxies

Alfonso Aragón Salamanca

OPTICAL AND INFRARED STUDIES OF DISTANT GALAXIES

by

Alfonso Aragón-Salamanca

August 1991

An account of work done at the Department of Physics, submitted to the University of Durham in accordance with the regulations for admission to the degree of Doctor of Philosophy.

ABSTRACT

This thesis investigates the evolution of galaxies as a function of look-back time, concentrating on early-type cluster galaxies. We demonstrate that selecting galaxies in the near-infrared produces samples that are representative of the galaxy population at intermediate and high redshift, and that such samples are likely to contain approximately the same proportion of all galaxy classes independently of z, avoiding the biases introduced by optical selection criteria.

We have developed observing and data processing techniques using infrared arrays that yield high precision near-infrared photometry to very faint limits. Combining such data with optical photometry for the galaxy samples, we have been able to quantify the amount of colour evolution in early-type cluster galaxies up to redshifts $z \sim 0.9$.

At $z = 0.37$ the *mean* colour-luminosity (c-L) relation for early-type cluster galaxies is compatible in slope and zero point with that of present-day ellipticals, indicating that the bulk of the stellar population at that epoch does not show any significant colour evolution. However, the scatter around the main c-L line is significantly larger than the observational errors, and distinctively non-Gaussian. We interpret this as evidence that a large fraction ($\sim 60\%$) of the early-type members have suffered a burst of star formation (involving $\sim 10\%$ of the galaxy mass) ~ 1 Gyr prior to the epoch of observation.

In the redshift range $0.5 < z < 0.9$, we detect systematic colour evolution with redshift in the *red* cluster galaxies. In particular, at $z \sim 0.9$ there are *no* galaxies as red as present day ellipticals at all wavelengths. The detected evolution is compatible with the passive ageing of stellar populations formed before $z \approx 2$. Superimposed on that, there is evidence for subsequent bursts of star formation happening on a substantial fraction of the cluster galaxies, but affecting only a small fraction of the total galaxy mass. We suggest this may be related to the *Butcher-Oemler effect* observed at lower redshifts. We did not detect significant amounts of galaxy luminosity evolution at 2μm, in contrast with the results for radio galaxies.

We finally propose and test three new approaches to the study of *normal* field and cluster galaxies beyond $z = 1$: a study of gravitationally lensed galaxies, a search for galaxies producing clustered metallic absorption lines in QSOs and an infrared follow-up of ROSAT X-ray detected high redshift clusters.

PREFACE

The work presented in this thesis was carried out between 1988 and 1991 while the author was a research student under the supervision of Prof. R.S. Ellis, in the Physics department at the University of Durham.

Some of the work was carried out in collaboration with the following research staff: Prof. R.S Ellis (Chapters 2 and 6); Prof. R.S. Ellis and Dr. R.M. Sharples (Chapter 3); Dr. W.J. Couch (of the Anglo Australian Observatory) and Prof. R.S. Ellis (Chapter 4); Dr. W.J. Couch, Dr. D. Carter (of the Royal Greenwich Observatory) and Prof. R.S. Ellis (Chapter 5). The major part of the research presented is, however, the author's own work. This work has not been submited for any degree, diploma or other qualification at any other University.

Certain results have appeared in the following papers:

Aragón-Salamanca, A. & Ellis, R.S., 1990. in *Gravitational Lenses*, p. 288, Eds Mellier, Y., Soucail, G., Fort, B., Springer-Verlag, Berlin.

Aragón-Salamanca, A. & Ellis, R.S., 1991. in *Astrophysics with Infrared Arrays*, p. 15, Ed. Elston, R., Astronomical Society of the Pacific Conference Series, vol. 14.

Aragón-Salamanca, A., Ellis, R.S. & Sharples, R.M., 1991. *Mon. Not. R. astr. Soc.*, **248**, 128.

To my family,

to my friends.

A mi familia,

a mis amigos.

Un astro fijo iluminando el tiempo,

Aunque su luz al tiempo desconoce.

A fixed star illuminating time,

although its light of time knows aught.

— LUIS CERNUDA

LIST OF CONTENTS

1 INTRODUCTION

We know today that our Galaxy, the Milky Way, is similar to countless other galaxies, which are thought to be the major structural units of the Universe. Mankind has always looked at the sky and asked itself questions about the Universe we live in: Where?, When?, How?..., and, perhaps, Why? Astronomy and Cosmology are the Sciences that try to answer some of these questions. As scientists we will not try to answer the *why's*, even though we also feel the need to know. We leave that to the Philosophers and Theologians.

If we want to find answers to these questions, we need to understand galaxies, because they play an essential role in the Universe. In particular, we need to understand how they evolve, since this has important consequences for our understanding of when/how galaxies formed, and the history and ultimate fate of the Universe. This Thesis aims to make a modest contribution in that direction using Astronomical observations as the principal tool.

1.1 A Universe of Galaxies

Extragalactic Astronomy, as we understand it today, was born in the 1920's, when galaxies were definitively recognized as isolated systems of stars, comparable to the Milky way, but at very great distances from us (Hubble 1925a). However, as early as 1750 Thomas

Wright speculated that some of the 'nebulae' might be separate huge systems of stars, like our own Milky Way. His ideas were extended by Immanuel Kant in 1755, arguing in favour of 'island universes', large rotating disks of myriads of stars widely scattered across space. Kant even proposed that the Andromeda Nebula is a good example, a vast stellar system virtually identical to our Galaxy. His ideas were largely ignored. After the vast cataloguing effort of William and John Hershel, published in 1864 as *The General Catalogue of Nebulae*, continued by John Dreyer in *The New General Catalogue* (1895) and the *Index Catalogues*, the observational techniques had to develop considerably before the distances to these objects could be reliably estimated, confirming their extragalactic nature in the initial decades of this century.

After the discovery of a new class of objects, the usual first step towards understanding their nature is to classify them, first qualitatively and then quantitatively, from their morphological properties (Hubble 1925b, 1936; de Vaucouleurs 1959; Morgan 1958, 1959, 1972; van den Berg 1960a,b, 1976; Sandage 1961). An excellent review on the subject can be found in Mihalas & Binney (1981). Galaxies exhibit great variety in their appearance, physical properties, and star forming activity and history. For our purposes, galaxies —at least *giant* ones— can be divided into three major classes: *spirals*, characterized by having a thin stellar and gaseous disk which is actively forming stars, and a stellar bulge which decreases in relative size along the Hubble sequence; *S0's*, that possess a stellar disk and a very prominent stellar bulge, with no or very little gas, and are no longer forming new stars; and *ellipticals*, amorphous stellar ellipsoids, with no disks and no young stars. In addition to this, there is a wide variety of *dwarf* galaxies. Since their small luminosities make them very difficult to detect at cosmological distances, we will not attempt to discuss their origin or evolution in this thesis.

With the exception of rare classes of active galaxies (*e.g.*, radio galaxies, Seyfert galaxies and quasars), most of the bolometric luminosity of galaxies is produced by stars,

even if in a subset (IRAS galaxies) a significant proportion is re-radiated by dust clouds. We know that stars are born, evolve and eventually die, and that their properties, and those of the light they emit, change with time. Successive generations of stars have different chemical composition: they are enriched in heavy elements by nuclear processes that take place in the stellar interiors, and whose products are ejected mainly by supernova explosions. All these processes —star formation and evolution, and chemical enrichment— produce changes in the stellar populations of galaxies, and therefore in their light. When trying to understand how galaxies form and evolve, we need to understand how their stellar populations change, and this thesis is mainly concerned with that.

The finite speed of light gives us the opportunity of observing galaxies as they were in the past, and testing how they change as a function of look-back time. The availability of large telescopes and the advances in detector and instrument technology make it possible to study galaxies over large cosmological distances, and therefore, over large temporal baselines. The study of local galaxies provides essential information on the properties of present-day galaxies and therefore important constraints for any evolutionary theory; but it is now realized that there are many evolutionary routes by which the present galaxy population might have resulted. Ultimately, only by gathering data on galaxies over a large range of look-back times, reaching as close as possible to the epoch of galaxy formation, can ambiguities be resolved and theories of galaxy formation and evolution directly tested.

1.2 Cosmological framework

The Hot Big Bang theory is currently the most accepted paradigm in modern Cosmology. Although some difficulties do exist, its success explaining some crucial observations

—expansion of the Universe, Microwave Background Radiation (MBR), primordial abundances of the chemical elements— justifies its acceptance. The inflationary hypothesis (Guth 1981) provides a solution to long-standing difficulties of the original theory, such as the horizon and flatness problems, which otherwise would require fine tuning of the initial conditions. It also naturally explains the primordial density fluctuations, placing their origin in the microscopic quantum domain. This forms the implicit background of the Thesis. Detailed reviews on cosmological models and observational tests can be found in Weinberg (1972), Gunn, Longair & Rees (1978), Efstathiou & Silk (1983), Sandage (1988), White (1989), and Kolb & Turner (1990).

The basic assumption behind this cosmological model is the 'cosmological principle', which states that the Universe at large scales should look homogeneous and isotropic to any observer. The best evidence for isotropy* comes from the smoothness of the microwave background radiation. Apart from the dipole caused by the Earth's motion in the MBR, any anisotropies are $\lesssim 2 \times 10^{-5}$ from scales of 10′–2° to the entire sky (see, *e.g.,* Davies *et al.* 1987, Readhead *et al.* 1989, Smoot *et al.* 1991). The assumptions of homogeneity and isotropy greatly restrict the geometry of space-time, described by the Robertson-Walker metric. At any given cosmic time, the three-dimensional position space has constant curvature. This metric, when combined with Einstein's General Theory of Relativity, is able to describe the kinematics and dynamics of the Universe, after making some assumptions on its matter and energy content. In the absence of a cosmological constant, once two observational parameters —the Hubble constant H_o (rate of expansion at the present time) and the deceleration parameter q_o— have been determined, the overall geometry of the Universe is described. The evolution with cosmic time of global properties, such as mean density and temperature, can be predicted, allowing for detailed

* If the Universe is isotropic for all observers, it must be homogeneous.

calculations of, for instance, the characteristics of the primordial nucleosynthesis. The theory also gives distances, angular diameters, timescales, cosmological effects on the light emitted by distant objects, etc. as a function of redshift. The necessary equations, extensively used throughout this Thesis, are derived in the literature mentioned above, and will not be reproduced here.

Within this framework, several theories of the formation of galaxies and structure of the Universe have been developed. The most accepted view at present is that galaxies and structures at larger scales originated from the growth, due to gravitational instability, of primordial density fluctuations. Basic ingredients in these models are the amount and nature of the Dark Matter, *i.e.*, material that does not emit light, but that reveals its presence by gravitational interaction. Dynamical studies reveal the presence of some dark matter, and standard inflationary models require that its amount should be such as to render the universe 'flat', *i.e.*, its cosmic mass density equals a critical value such that the expansion terminates at infinite time. The actual nature of the dark matter is not known. Its properties would determine the spectrum of primordial density perturbations and the way they grow. Current theories of galaxy formation can be divided into two principal types. The first one, the Hot Dark Matter scenario, assumes that the dark matter is dominated by low rest mass particles that are relativistic. In this model, the first structures to form are very large: protoclusters and superclusters forming large pancakes (*e.g.*, White 1986). Individual galaxies then form by fragmentation in a top-down process. This model has two serious difficulties: it makes the Universe excessively inhomogeneous on 10–100 Mpc scales (White, Frenk & Davis 1983) and predicts galaxies to form at a very late epoch ($z \lesssim 2$), which is difficult to reconcile with the observation of quasars and radio galaxies at $z > 3$ (see also Chapter 5). The second scenario, Cold Dark Matter, assumes that the dominant constituents of the dark matter are particles with larger masses and hence non-relativistic velocities. The standard model (Blumenthal *et al.* 1984, Davis *et al.*

1985) produces objects of roughly galactic mass and reproduces the small-scale clustering and internal dynamics of galaxies, making it the most successful theory of galaxy formation so far. However, there is now some controversial evidence that this model produces too little power on large scales (Maddox *et al.* 1990, Collins, Nichol & Lumsden 1991, Saunders *et al.* 1991). The model can be renormalised to match large-scale power, while non-linear effects could bring down the power on smaller scales (Couchman & Carlberg 1991), so, despite the difficulties, this model could still survive.

These models describe how the mass collapses to form galaxies and larger scale structures, but do not predict directly how galaxies form stars and evolve. Spectral evolution models start from the point at which a certain amount of gas is assembled and stars begin to form (see next section). Since galaxy formation models make predictions about the epoch of galaxy formation, a direct measure of the rate at which the spectral energy distributions of galaxies evolve, in connexion with spectral evolution models, would provide a direct test for both galaxy formation and evolution theories.

1.3 Galaxy evolution models

When studying the stellar populations of distant galaxies, one major problem is that their stars cannot be resolved, and therefore we have to analyze their integrated light. Different approaches have been used to determine the stellar content and evolutionary status of a composite population from its integrated colours or spectra. One of these methods is what we can call *Empirical Population Synthesis*, which uses a library of stellar properties (colours, spectra) to deconvolve the distribution of individual stars from their composite light. The method works by choosing the combination of stars that *best* minimizes the differences between the observed and synthetic systems. However, a large

number of solutions are indistinguishable within the observational uncertainties, and some astrophysical constraints need to be introduced (*e.g.*, positive number of stars, number of main sequence stars should decrease with mass, number of giant stars should be compatible with the number of their progenitors, etc.) to narrow the range of acceptable solutions. However, despite this, the uniqueness difficulties remain and it is also often unclear how a given solution is robust to uncertainties such as the noise of the data (in the stellar library and in the composite system) and the completeness of the stellar library (particularly in its contents of stars of different chemical compositions). Another difficulty is that this technique can only provide the stellar population at a given time, but not the evolutionary path that led to it. Examples of the application of this method can be found in, *e.g.*, Wood 1966, McClure & van den Berg 1968, Faber 1972, O'Connell 1976, 1980; Turnrose 1976, and Pritchet 1977). A somewhat different approach that includes theoretical *isocrones* to constrain the acceptable solutions of the spectral synthesis was introduced by Pickles (1985).

An alternative to this full synthesis technique is to use carefully-chosen spectral lines to diagnose particular properties of the constituent stars, such as the relative contributions of dwarf and giant stars to the integrated light (Rose 1985, Rose *et al.* 1989, Bower 1990, Bower *et al.* 1990). The line ratios used by these authors are a powerful diagnostic of the presence of a significant population of intermediate-age stars, and are insensitive to both metallicity and to the presence of stars in poorly understood phases of stellar evolution. The application of this method requires spectroscopic data of considerable signal-to-noise ratio and spectral resolution, and it is therefore not suitable for the study of faint, distant galaxies.

Another approach, introduced by Tinsley (1972) is based on the application of the knowledge of stellar evolution to the analysis of stellar populations. The models assume that stars are born from a gas cloud, with their masses distributed according to an Initial

Mass Function (IMF) at a rate governed by the Star Formation Rate (SFR). The IMF is usually assumed to be constant (*i.e.*, the physical processes that determine the mass spectrum with which stars are formed do not change as the system evolves). It is usually parameterised as a power law of the stellar mass, with constant or variable slope (Salpeter 1955, Miller & Scalo 1979, Scalo 1986). The SFR is either imposed *a priori*, assuming some functional form (*e.g.*, constant, exponentially decreasing) or parameterised as a function of properties such as the gas density. Given an SFR and an IMF, the models compute the number of stars of each mass that are formed at any given time. The stars are then evolved according to theoretical *evolutionary tracks*, so that it is possible to predict, as a function of time, the distribution of stars on the theoretical Hertzsprung-Russell diagram (Luminosity-Effective temperature). Using empirical or theoretical calibrations of the observed properties of stars as a function of their physical parameters, the theoretical H-R diagram can be converted into a Colour-Magnitude diagram, and by using a library of stellar properties (colours, spectra, line strengths), we can integrate the observed colours or spectra of the composite population as a function of time, and compare it with observations of stellar systems (star clusters or galaxies).

Several problems arise when applying this approach. First, the poor theoretical knowledge of the late stages of stellar evolution after the onset of the helium core burning: Horizontal Branch (HB), Asymptotic Giant Branch (AGB) and Post-AGB (see Renzini & Fusi Pecci 1988). In some cases, these stellar classes are just ignored or introduced in a semi-empirical way, but a fully satisfactory procedure has not been developed so far (see, *e.g.*, Renzini 1989), Therefore, large uncertainties still exist on the spectral evolution in the near infrared, where AGB stars could play an important role, and in the ultraviolet, where the poorly-known Post-AGB stars might make a substantial contribution. Another major problem is the way these models deal with stars of different chemical compositions and the chemical evolution of the system. Composite stellar systems might contain stars with a

wide range of metallicities. In particular, the cores of giant elliptical galaxies are believed to contain stars that are considerably more metal rich than those in the solar neighbourhood, and stellar libraries do not cover the complete range of metal abundances. Moreover, theoretical stellar evolutionary tracks for metal rich stars are difficult to compute precisely because of the uncertainties in the opacities, and are less reliable than solar abundance ones.

Several authors have used this technique with variable degrees of success, making different sets of assumptions when dealing with the problems mentioned above. It is beyond the scope of this Chapter to describe all the models, and we refer the reader to the original papers (see, *e.g.,* Tinsley 1972, 1980; Tinsley & Gunn 1976, Bruzual 1983, Renzini & Buzzoni 1986, Arimoto & Yoshii 1986, 1987; Guiderdoni & Rocca-Volmerange 1987, 1990; Aragón, Gorgas & Rego 1987; Buzzoni 1989; Charlot & Bruzual 1991). In successive chapters, we will describe the particular characteristics of the models that we have used, stressing the points that are more relevant to our work.

A method that side-steps some of these problems has recently been introduced by Bica & Alloin (1986, 1987). They use a library of *star cluster* spectra of empirically-determined properties such as age and metallicity. In this way, they do not need to refer to theoretical isocrones and the IMF is avoided (although they have to assume that the star cluster IMF is universally valid). In addition, all phases of stellar evolution are included, assuming that they are all statistically represented in the star clusters.* A large number of clusters from our Galaxy and the Magellanic Clouds are present in their library, providing a wide coverage of age and metallicity (up to 0.1 dex solar). For higher metallicities, they extrapolate the observed trends in line strengths and spectral shapes, introducing *artificial*

* This might be a problem when considering *rare* stellar classes, where the statistical fluctuations could be important if the total number of cluster stars is relatively small compared with the number of stars present in galaxies.

high-metallicity clusters in their library. Bica (1988) applied this technique to a number of local elliptical galaxies, showing that they present a variety of properties, both in terms of their metallicities and the age of their youngest stellar components, although some concern exists about the uniqueness of the solutions. It is also questionable whether a galaxy can be represented by a sum of star clusters, since they could represent biased regions in the same way as clusters of galaxies present very different galaxy populations from that of the field. Applying this technique requires spectral information difficult to obtain for faint objects. Jablonka, Alloin & Bica (1990) have used it to analyze the averaged spectra of several galaxies in Abell 370 ($z = 0.37$) published by Soucail *et al.* (1988a). They find no evidence for spectral evolution among the red cluster members to this redshift.

The main advantage of the evolutionary synthesis approach is that it provides a complete *evolutionary* picture, and it is able to predict the properties of composite stellar populations as a function of time. For that reason, we consider this kind of model a suitable tool to interpret our observations. When comparing the model predictions with present-day galaxies, there is substantial freedom in the choice of model parameters. By extending the observations over a substantial time baseline, we hope to be able to narrow the range of acceptable hypotheses, and choose which of the possible evolutionary paths has led to the present galaxy population. The questions we would like to answer are simple: are galaxies evolving synchronously? Are they all coeval, *i.e.*, did they all form the bulk of their stars at a common epoch? Is the witnessed evolution compatible with *passive evolution*, in which most of the stars formed in a short time (compared with the galaxy lifetime) and the stellar population simply aged afterwards, without any significant subsequent star formation? We will carry out simple tests, without getting involved in an unmanageable number of parameters. Since significant uncertainties still exist in the models, we will use them mainly as a guide to optimize the observational programme.

Even if some of the conclusions might be model dependent, the data will still be valid, and can be used to test future refinements in the galaxy formation and evolution theory.

1.4 Observation of High Redshift Galaxies

Several approaches have been followed to study galaxies over a wide range of redshifts. Direct studies of field galaxies via number counts in the optical were pioneered with photographic plates (Kron 1978, 1980; Peterson *et al.* 1979, Tyson & Jarvis 1979, Jarvis & Tyson 1980). The main results showed that the number-magnitude relation rises more steeply than expected, above the rate required to avoid Olber's paradox, and the population shows a monotonic trend to bluer colours at fainter limits. With the advent of CCDs in the optical and imaging detectors in the near-infrared, the number count work has substantially increased its depth and wavelength coverage (*cf.* Tyson 1988; Cowie *et al.* 1990, 1991; Lilly, Cowie & Gardner 1991; Glazebrook 1991) confirming a strong excess of blue galaxies in the optical wavelengths (when compared with no-evolution predictions), not present in the near IR. This suggests strong colour and luminosity evolution (see also Yoshii & Takahara 1988). The excess of very blue galaxies detected in the deep number counts were once thought to be produced by primaeval galaxies at $z \simeq 2$–3 (Tyson 1988), but statistically-complete redshift surveys of randomly-chosen areas to the limits of 4-m class telescopes have revealed that most galaxies have surprisingly low redshifts ($z < 0.5$). Many of the bluest 'flat spectrum' sources are local star-forming dwarfs (Broadhurst, Ellis, & Shanks 1988, Colless *et al.* 1990; see Ellis 1990a and Koo 1990 for recent reviews on the subject). This implies that using direct studies of field galaxies is not a very effective way of trying to find high-redshift galaxies, because of the plethora of local, underluminous

objects than can only be eliminated via time-consuming spectroscopy. Clearly, alternative approaches are needed.*

Pioneering work on selected high redshift objects such as quasars and radio galaxies provides a way to investigate the conditions in the early Universe. Sources have been identified and studied with redshifts reaching $z \sim 4$, indicating that certain objects existed at surprisingly early epochs (see, *e.g.*, Lilly & Longair 1984; Lilly 1988, 1989; Chambers & Charlot 1990, and references therein). These are *rare* objects whose special nature is not yet physically understood, for which selection effects undoubtedly operate, and their link with more *normal* galaxies is not well established. There is some controversy at the time of writing concerning the interpretation of the spectral energy distributions of such objects as a means of constraining their ages (*cf.* Lilly 1989, and Chambers & Charlot 1990), and the implications for the epoch of normal galaxy formation remain unclear. It is also unknown to what extent the fact that they are powerful radio sources affects their stellar populations, as suggested by the alignments between the optical/infrared continua and the radio axis claimed by Chambers, Miley & van Breugel (1987), McCarthy *et al.* (1987) and Eisenhardt & Chokshi (1990). Evidently, more normal objects for which present-day counterparts can be identified need to be studied.

Rich clusters stand out against the fabric of galaxies that make up the visible Universe, even though they contain only a small fraction of the galaxies in space. Because of their high surface densities and large number of very luminous galaxies, they have been found up to $z \approx 1$ in optical searches. They provide, in principle, a source of sizeable samples of distant galaxies for evolutionary studies over a wide range of epochs. It was found in very early studies that nearby rich clusters are dominated by early-type galaxies (Hubble & Humason 1931). The discovery was quantified by Dressler (1980) in terms of

* In Chapter 6 we will present a method that circumvents these problems using clusters of galaxies as gravitational telescopes.

a Morphology-Density (M-D) relation. He demonstrated that the fraction of early-type galaxies increases with the projected density. The relation also holds in terms of the 3D density (Salvador-Solé, Sanromà, Rdz. Jordana 1989). Even though it is not clear if the M-D relation is governed by the local density or by global cluster parameters such as the projected distance from the centre (Whitmore & Gilmore 1991), clusters can provide substantial numbers of red early-type galaxies. Early-type galaxies in local clusters show remarkably homogeneous properties, particularly in their optical and infrared colours, suggesting a common formation process and a small dispersion in their epoch of formation (*e.g.*, Bower 1990, Bower, Lucey & Ellis 1991). Since early-type galaxies are believed to be very old stellar systems that experienced their *major* star formation at very early epochs, their stellar populations are simpler and older than those of later types, which have longer-lasting star formation. This means that evolutionary changes will be easier to interpret when studying the *reddest* cluster galaxies, and inferences about the main epoch of *normal* galaxy formation will be easier to make.

Provided that high-redshift clusters can be identified as distant counterparts of nearby examples, the observed properties of their galaxy population can be compared with that of local clusters, quantifying the detected changes in terms of galaxy evolution. Extensive work has been done in this respect in the optical regime covering a wide redshift range. Butcher & Oemler (1978, 1984) showed that the fraction of blue galaxies in clusters increases as a function of redshift up to $z \lesssim 0.5$. Although various biases and contaminations were found to affect the early Butcher-Oemler studies (Dressler & Gunn 1982, Ellis *et al.* 1985, Koo 1988), the reality of the effect has been confirmed by these and other observational studies (*e.g.*, Couch & Newell 1984, Dressler, Gunn & Schneider 1985, Lavery & Henry 1986, Couch & Sharples 1987, MacLaren *et al.* 1988, Mellier *et al.* 1988, Soucail *et al.* 1988a). The spectroscopic work of these authors showed that the *blue* Butcher-Oemler galaxies belong to three general types (*cf.* Gunn 1990, Pickles & van der

Kruit 1991, and references therein): (i) objects with strong [O II], [O III] and Hβ emission lines and filled continuum, indicative of active galactic nuclei; (ii) galaxies with weaker emission lines and noticeable absorption lines (particularly Balmer lines), indicative of current star formation in gassy systems at rates comparable to present-day spirals; and (iii) those with no emission lines but with strong Balmer absorption lines, the 'E+A' or 'post-starburst' spectra, indicative of recently completed ($\sim$ 1 Gyr ago) star formation in systems lacking much residual gas. The frequency of occurrence of the different types of blue galaxies varies from cluster to cluster, and not as a function of redshift, but in most cases the largest fraction appears to be the third type, indicating that most of the blue galaxies are systems that have undergone a burst of star formation not long before the epoch of observation, and lack significant amounts of residual gas (Dressler, Gunn & Schneider 1985, Couch & Sharples 1987, Dressler & Gunn 1990). The 'active fraction', defined as the fraction of galaxies falling into one of the above three bins, rises from a few percent at $z \simeq 0.0$–0.05 to about 30% at $z \simeq 0.4$–0.55 (Gunn 1990). The active galaxies show differences in their kinematics and spatial distribution when compared with other cluster members. They are much less centrally concentrated than the red galaxies, tending to avoid the central regions of the cluster (Butcher & Oemler 1984, Schneider, Dressler & Gunn 1986, Thompson 1986, Pickles & van der Kruit 1991), and their velocity dispersion is almost 70% larger than that of the passive galaxies (Dressler 1986a, Henry & Lavery 1987, Couch & Sharples 1987, Dressler & Gunn 1988, Gunn 1990). There is some evidence (Ellis *et al.* 1985, MacLaren *et al.* 1988, see also Chapter 3) that a significant fraction of the optically *red* galaxies are also involved in some form of star formation activity, but involving probably only a small fraction of their total mass.

Two mechanisms have been proposed to explain the larger fraction of star-forming galaxies in higher redshift clusters. Lavery & Henry (1988) have suggested galaxy collisions

and mergers as a star formation triggering mechanism, from the increased number of near-neighbours observed around blue, as opposed to red, galaxies in clusters out to redshifts of $z \sim 0.2$. Dressler & Gunn (1988, 1990) failed to detect the same effect in higher redshift clusters. Dressler, Gunn & Schneider (1985) and Bothum & Dressler (1986) proposed that the activity is associated with the interaction of galaxies entering the cluster for the first time with the hot intracluster medium. The gas pressure at the centre of the cluster is 10–100 times greater than the pressure in the interstellar medium of today's typical galaxies (*cf.* Dressler & Gunn 1990). These authors have suggested that the sweeping of the fragile intercloud medium by ram pressure (Gunn & Gott 1972) and its replacement by a much higher-density gas may have triggered the molecular clouds, harder to remove, to collapse and produce a burst of star formation. The hydrodynamical models by Evrard (1990) for the evolution of the intracluster medium predict a steeply rising pressure in it that flattens within the cluster core. At $z \sim 0.5$ the transition zone is abrupt, a 'shock' which occurs at ~ 0.5 Mpc radius. The model predicts that as the cluster evolves the shock moves outwards, becoming more gradual and at a pressure comparable or below typical interstellar medium pressures. This could explain why this mechanism is so efficient at producing starburst activity at $z \sim 0.5$, but is nearly absent today. If this is correct, we can expect the phenomenon to happen only once in the lifetime of a galaxy, and after the burst the galaxy would quickly become passive. This is supported by the statistics of active objects (Gunn 1990), and accords with the lack of emission or ongoing star formation in the 'E+A' galaxies. The higher velocity dispersion of the active galaxies and their tendency to avoid the cluster core, and to be distributed in a shell (Pickles & van der Kruit 1991) are also compatible with this idea.

Despite the detected increase in the fraction of blue cluster galaxies with redshift, a large number of cluster members are as red as present-day ellipticals, showing negligible colour and spectral evolution up to $z \sim 0.5$. These objects, presumably the oldest in the

clusters, show no or very little star formation activity at $\sim 60\%$ of the age of the Universe. This would be the case if their stars formed at very early epochs and evolved passively since then, as already suggested by the models of Tinsley & Gunn (1976). Hamilton (1985) found that there are still some galaxies whose spectra are compatible with that of present-day ellipticals up to $z \sim 0.8$, but his sample only included four galaxies with $z > 0.6$. Dressler & Gunn (1990) detected significant spectral evolution in the reddest objects at $z > 0.7$, but their selection of the objects in the optical could have missed some of the reddest objects (see Chapters 2 and 5).

If we want to constrain the epoch of major star formation in the oldest cluster galaxies, and distinguish it from transient episodes of star formation that happened subsequently, we need to be able to build samples that are not biased towards blue, star forming objects. Increasing the redshift range with sizeable samples for which the selection effects are under control is clearly necessary. Ideally, we would like to be able to select galaxies in a way that is independent of the effect we are trying to measure (their evolution), and that gives the same proportion of galaxy types at all redshifts. Most of the work so far has been carried out at optical wavelengths because of the practical constraints of detector technology and atmospheric transmission. As redshift increases, the optical photometric bands sample light that comes from progressively deeper in the ultraviolet part of the spectrum, where the effects of star formation are stronger due to the high temperature and luminosity of young, massive stars. This means that optically-selected samples will be progressively more biased towards star-forming objects as redshift increases, and selection effects would severely distort the measured evolution (Chapters 2 and 5). The advent of efficient imaging detectors that operate in the near-Infrared (IR) opens new opportunities in observational cosmology, and provides a way to circumvent this problem. Since the infrared light comes mainly from older and cooler stars, and the near-IR spectral energy

distribution of galaxies is remarkably independent of galaxy type, near-IR selected samples would be much more representative of the cluster galaxy population than optically selected ones (Chapter 2). The new IR arrays available on 4-m class telescopes provide the means to do that in reasonable amounts of observing time. Since the optical regime for high redshift objects is strongly affected by even small amounts of star formation, optical and optical-IR colours are very sensitive to evolution. In this Thesis we will exploit the ability of near-IR photometry to build fair, representative samples of cluster galaxies in a wide redshift range, and, in combination with optical data, we will try to detect evolutionary changes in the galaxy population. To do that using spectroscopy for large samples would be a formidable task. Photometry will provide a much larger number of objects for a given amount of observing time. Even though we will lack redshift information for most of the objects, we will demonstrate that the field contamination can be dealt with in a statistical way using published number counts (Chapter 5).

1.5 Aims and layout of this Thesis

Understanding the origin and evolution of *normal* galaxies requires studying them as a function of look-back time, reaching as close as possible to the epoch of galaxy formation. Selection effects need to be kept under control to avoid a biased picture of the galaxy populations. The earlier work presented above is centred on the evolutionary status of cluster galaxies to $z \simeq 0.5$. This thesis aims to extend the present knowledge in this field to $z \sim 1$, providing a homogeneous base of data for the cosmologically more important interval $0.5 < z < 1$. We hope to make a significant contribution towards the determination of the epoch of galaxy formation and to constrain the evolutionary path that led to the present galaxy population.

As a first step, we will demonstrate quantitatively the advantages of near-IR selected samples over optically-selected ones when dealing with high redshift galaxies from a general point of view (Chapter 2) and with concrete examples (Chapter 6). We will also show that recent developments in near-IR detector technology provide an efficient way to do that, and that reliable and accurate photometry can be obtained with infrared arrays (Chapter 2). Since we are dealing with new detectors, it will be necessary to develop and test new observational techniques and data reduction procedures, and a detailed analysis on the errors will be carried out (Chapter 2).

Sizeable samples of near-IR selected cluster galaxies will be built, and high quality optical and optical-IR colours will provide the means for detecting and quantifying evolutionary changes in the cluster galaxy populations. To do that we need to develop techniques to compare high-redshift galaxies with nearby samples in a reliable way. We will proceed in various stages, starting from intermediate redshift clusters for which extensive photometric and spectroscopic information exists, to test if the optical-infrared photometry provides the kind of information on evolution obtained by other means. This will also allow us to choose the best strategy to follow when extending our study to higher redshifts. We also develop a way to predict the observational properties of present-day galaxies if they were at any redshift, avoiding the uncertainties introduced by using K-corrections. Optical-IR photometry for a large sample of Abell 370 cluster members will show evidence for recent star formation in a substantial fraction of the galaxies, because the optical-IR colours are able to detect longer-lasting signatures of the star formation than optical data alone (Chapter 3).

Chapter 4 presents a detailed study of two clusters ($z = 0.55$ and $z = 0.66$) that are representative of the high redshift sample ($0.5 < z < 0.9$). Some membership information is available for them, and this allows us to test the conclusions that we obtain statistically without such information, confirming the validity of our strategy. The chapter

also demonstrates that our technique can be extended to higher redshift objects with the required accuracy. We will present evidence for colour evolution in the reddest cluster members and analyze it in the framework of current galaxy evolution models.

In Chapter 5 we present the core of the Thesis. We analyze the observed optical and near-IR magnitudes and colours of a sample of $\sim$ 160 $K(\equiv 2\mu\mathrm{m})$-selected galaxies in 9 clusters with $0.5 < z < 0.9$. After correcting from the field contamination, we use the optical-IR colours to detect and quantify systematic changes on the spectral energy distributions of the cluster galaxies as a function of redshift. We compare the detected evolution with that obtained from previous work carried out with optically-selected samples, showing the advantages of selecting in the near-IR. Current models of galaxy evolution are used to interpret the observed systematic change in colours. The range of models that predict results that are compatible with our data is used to constrain the properties of the star formation history in cluster galaxies, such as the epoch of the major episode of the star formation.

Chapter 6 introduces new ways of efficiently extending the study of the evolution of *normal* galaxies towards higher redshifts ($1 < z < 2$), aiming to extend the look-back time baseline to epochs as close as possible to the major episode of star formation in galaxies. We describe the aims of each approach and the methods that we are applying to achieve them. We present the progress so far, demonstrating that the projects are feasible, and some interesting results.

Chapter 7 summarizes the main conclusions of the Thesis.

2 INFRARED OBSERVATIONS OF HIGH REDSHIFT GALAXIES: AN OVERVIEW

2.1 Introduction

The infrared photometry of high redshift galaxies provides a substantial fraction of the observational basis of this thesis. It constitutes a most significant and original contribution to the understanding of the properties of galaxies at high red-shift. It is a relatively new, rapidly evolving and expanding field due to recent technical advances. Therefore, there are a few new concepts and techniques that need detailed descriptions, and the purpose of this chapter is to provide them. In particular we describe how the near-infrared observations can provide information on high z galaxies that optical observations alone cannot.

In the last few years we have witnessed a rapid development in the use of arrays as detectors in ground-based infrared astronomy. It means a very substantial multiplex gain over the traditional single-pixel detectors, and new arrays with an ever-growing number of pixels are becoming available for the astronomical community in more telescopes. We have been gaining experience on the understanding of the performance of such devices when used for precision photometry of faint objects, and we have reached an stage in which real science can be learnt from the images obtained with them. The 'pretty pictures' era for infrared arrays is over. The observational techniques in optical and near-IR astronomy are different, but the impact of new technology (CCD's in the optical, arrays in the IR) is similar, with the significant difference of the lack of IR photography. The high background

levels will remain an important difference, but techniques have been developed to produce extremely accurate flat-fielding to deal with this problem.

One such array is currently used as detector with the camera IRCAM at the 3.8 m U.K. Infrared Telescope. Section 2.3 describes the instruments —telescope and camera— and section 2.4 the observation and data reduction techniques that we have developed and used to exploit IRCAM data.

2.2 Why do we need the Infrared to study high-redshift galaxies?

2.2.1 High redshift clusters: $0.5 < z < 1$

When trying to understand the evolution of galaxies with look-back time, we need to build samples that are representative of the galaxy population at different redshifts, *i.e.*, we have to select galaxies in a way that does not depend on the evolutionary effects that we are trying to detect. Ideally we would like to have a sample that contains the same proportion of galaxy types at all redshifts.

Figure 2.1 shows the rest-frame Spectral Energy Distribution (SED) of different types of galaxies. The UV-optical region of the spectrum comes from Pence (1976), extended to the near-IR using broad-band colours from Persson, Frogel & Aaronson (1979), and Gavazzi & Trincheri (1989). It can be seen that the position of the optical photometric bands sample the UV for a redshift of ~ 0.7, where the SEDs of the galaxies show very large differences (*i.e.*, they have very different K-corrections). That means that,

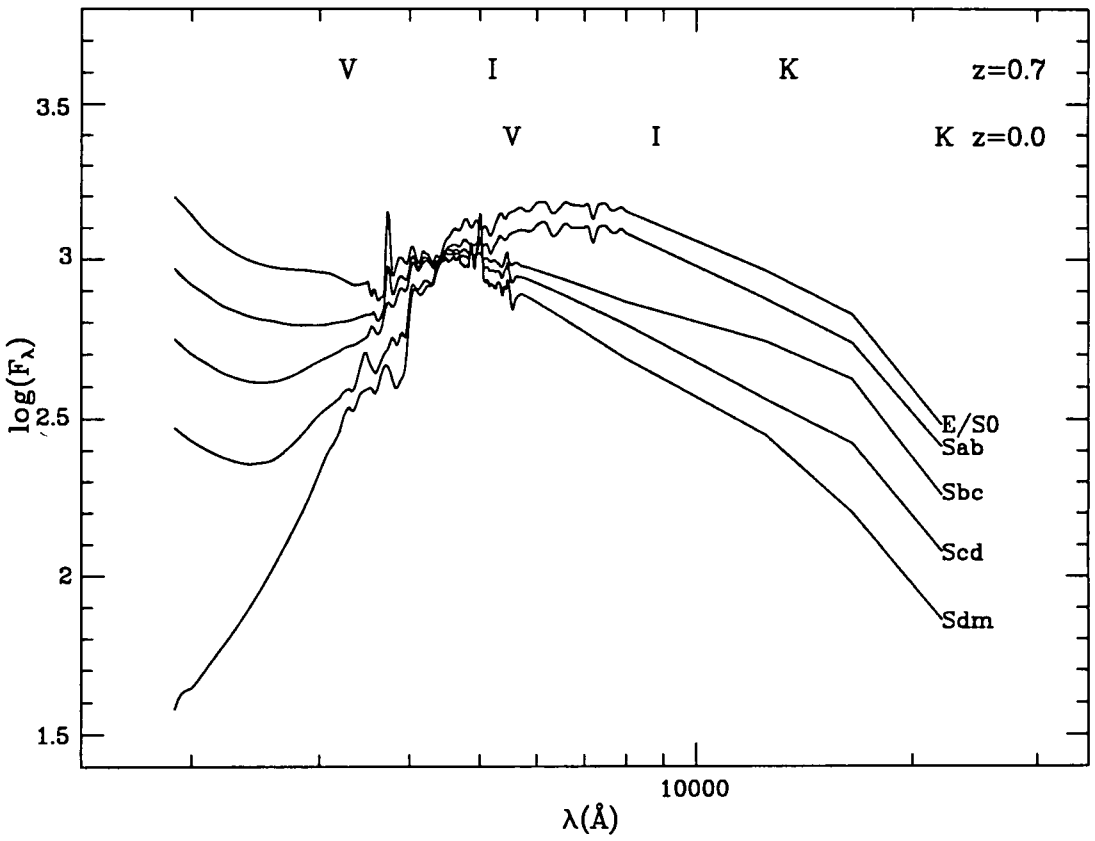

Figure 2.1. Spectral Energy Distribution of different types of galaxies. The letters indicate the position of the rest-frame and the red-shifted ($z = 0.7$) optical VI and IR K photometric bands.

even in the case of no evolution, an optically-selected sample would be severely biased towards UV-bright late-type galaxies at higher redshifts, and would produce a very different mixture of galaxy types at different z's.

If evolution is present, we can expect the UV part of the spectrum to be affected more strongly, because the presence of relatively few hot, young stars would significantly increase the UV flux. Selecting in the optical at high z would favour the objects with recent star formation against quiescent galaxies. We will refer to these problems as *ultraviolet bias*.

Selecting in the near-IR (*e.g.*, at 2μm), the situation is much more favourable. The shape of the SED depends much less on the galaxy type, and therefore the K-corrections are more uniform along the Hubble sequence (see, *e.g.*, Elston 1991). That means that in the case of no evolution, IR-selected samples would contain a more uniform mixture of galaxy types at all redshifts (see also Figure 2.2). If evolution takes place, we can expect the luminous, hot, young stars to affect the near-IR to a much lesser extent than to the UV, and therefore we would select in a region of the spectrum almost independent of what we are trying to measure: the evolution.*

Summarizing, K-selected samples of galaxies at different redshifts would contain practically the same mixture of galaxy types if the luminosity evolution in the near infrared is similar for all galaxy types. In any case, we can expect the luminosity evolution for different galaxies to be much more uniform in the near-IR than in the UV. Therefore, the selection biases at high redshift are much more under control in K than in the optical. The effects of extinction are also considerably reduced.

---

* Important uncertainties still exist about the contribution of Red Supergiants and Asymptotic Giant Branch stars to the IR SEDs of galaxies and their evolution (see, *e.g.*, Renzini & Fusi Pecci 1988, and references therein) but the uniformity of the galaxy SEDs in this region suggests that the influence of recent star formation has a much less dramatic effect in the near-IR than in the UV.

In the present work we study galaxies selected in the near-IR and use optical photometry to determine the amount of colour evolution as a function of redshift, which provides important information regarding the star formation history of *normal* cluster galaxies.

2.2.2 Towards higher redshifts: $z > 1$

At even higher redshifts ($z > 1$), we have to consider two more advantages of the near-IR photometry. First, the optical bands sample the very poorly-known far UV spectrum, while the near IR bands (JHK) sample the familiar rest-frame optical region, making the understanding of the observations much more straightforward.

The second advantage is that, for very high red-shift objects, we need to observe in the near-IR to get reasonable exposure times that keep in approximately the same proportion for all galaxy types independently of z. This is shown in Figure 2.2. It presents the exposure time required to detect a L^* galaxy ($M_V^* = -21\overset{m}{.}8$ for $H_o = 50\,\mathrm{km\,s^{-1}\,Mpc^{-1}}$, Tamman, Yahil & Sandage 1979) of different spectral types using a 4-meter telescope as a function of z in the optical R and IR K bands. It is obvious that to detect an elliptical galaxy at $z > 1$ in R would require much longer integrations than to detect a late type galaxy, and this difference increases substantially with z. The situation gets worse when using bluer bands.Therefore, for a given amount of telescope time, optically-selected high-z samples would be practically devoid of early type galaxies, and strongly biased towards blue, star forming galaxies.

The solid lines in Figure 2.2 are practically parallel. This indicates that the exposure time that we need to detect an L^* galaxy in K remains in the *same proportion* for the different types of normal galaxies at all redshifts. Therefore, the mixture of galaxy types

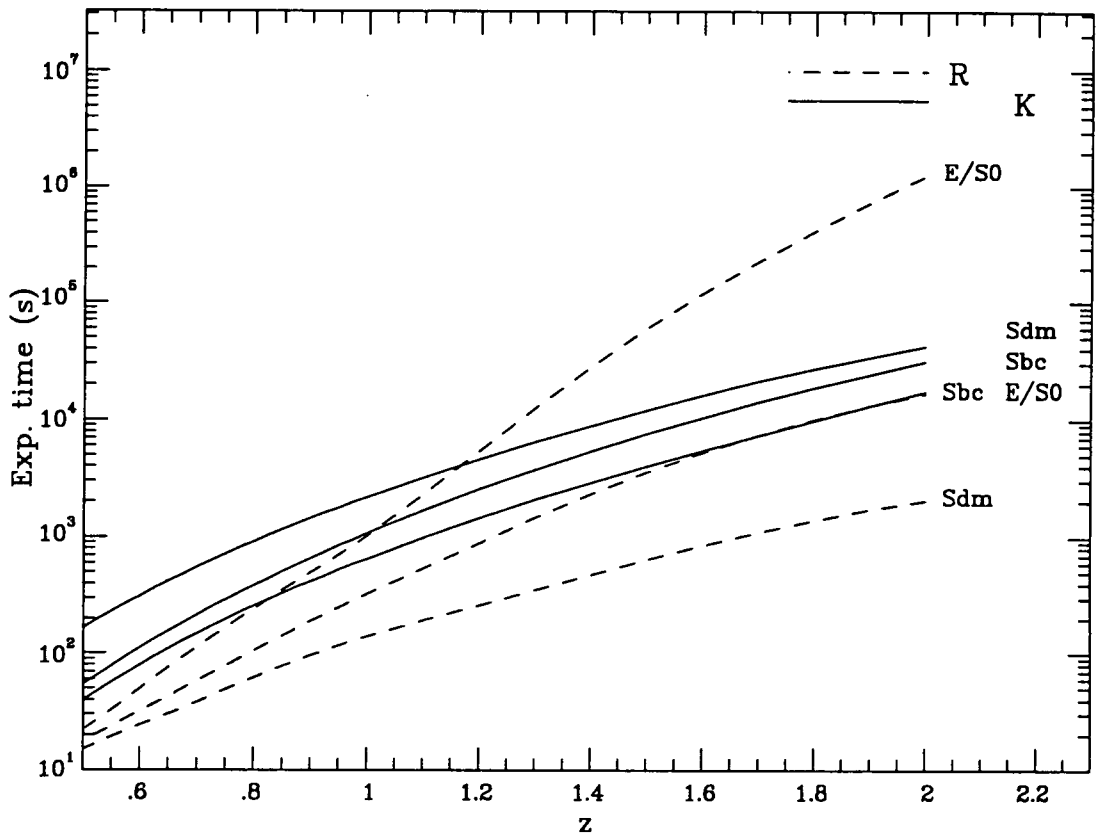

Figure 2.2. Exposure time as a function of z to detect an L^* galaxy with a 4-m telescope in R and K

will be the same at any z in a K selected sample. This is true in the absence of evolution, but the same considerations discussed in §2.2.1 apply here in the case of evolution.

Although part of the conclusions of this section do not apply directly to the cluster work presented in this thesis because we are still in the $z < 1$ regime, they are relevant to the extension of this work, which is already under progress (see Chapter 6).

2.3 The instrument: IRCAM at UKIRT

2.3.1 The U.K. Infrared Telescope

All the K-band (2.2μm) observations presented in this work have been carried out with the 3.8-m United Kingdom Infrared Telescope (UKIRT). This is the largest telescope in the world designed specifically for infrared observations. It is located on the summit of Mauna Kea, Hawaii, at an altitude of 4,200 m. This superb site is particularly well suited for infrared programs, which require low water vapour and low sky thermal emission. The very good seeing conditions (sub-arcsecond seeing is not exceptional) also make this site well-suited for most programmes.

The telescope has a very light and compact design, with the primary mirror made from an unusually thin glass that weighs $\frac{1}{3}$ of that of conventional telescope mirrors. It allows a very light-weight supporting structure, with subsequent reduction of costs. The small secondary acts as an aperture stop to reduce thermal effects, and it is designed for chopping. A small central obscuration, together with its light open telescope tube result in a very weak thermal emissivity. The effective aperture of the telescope is 3.75 m. The mounting arrangement and the small dome size restrict the telescope elevations to

altitudes grater than 23°, and also make it more sensitive to vibration by the wind than most other conventional telescopes. The instruments are mounted at the f/36 Cassegrain focus.

The telescope control is completely computerized, and the targets can be acquired with an accuracy better than two arcseconds by driving the telescope to a bright star in the vicinity (which is chosen automatically by the software), and then offsetting to the required coordinates. Once acquired, the telescope can track on an object with an error of a few arcseconds per hour. Better offsetting and tracking accuracies can be achieved by using the TV autoguider, which is mounted on an XY crosshead below the dichroic mirror.* Thus if a positional reference star brighter than $V \simeq 15$ mag is available within 2 arcminutes of the object to be acquired, offsetting of the telescope to a fraction of a second of arc can be accomplished by moving the crosshead while autoguiding.

Despite its low cost, continuous improvements, particularly in its optical performance and in the software-driven control system have given this telescope capabilities far beyond its original design. More information about the telescope can be found in Mobasher (1987) and the "UKIRT Observer's Manual" (U.K. Infrared Telescope Support Unit, 1989, 1991).

2.3.2 The Infrared Camera IRCAM

IRCAM is one of UKIRT's common user instruments. It has been designed and developed at the Royal Observatory, Edinburgh. A complete technical description of IRCAM is beyond the scope of this chapter. We will briefly describe its mean features and capabilities

* A computer-controlled flat dichroic mirror is used to reflect the IR light coming from the secondary in an angle of 90° and redirect it towards one of the four ports that support instruments. This mirror is transparent to visual light, behind which is the TV camera.

from the user's point of view. It should help an understanding of the observing techniques and the data reduction procedures involved. A detailed description of the instrument has been published by its project team (McLean *et al.* 1986). A comparative study of several IR cameras in different observatories, including IRCAM at UKIRT, has been carried out by Vauglin (1988). Most of the information presented in this section can be found in Lee, McLean and Wade (1989) and the "IRCAM User's Guide", written by M. Casali, C. Aspin and I. McLean.

IRCAM is a near-IR (1–5 μm) imaging system based on a 62 x 58 Indium Antimonide (InSb) array manufactured by Santa Barbara Research Centre (SBRC). It consists of an array of reverse-biased InSb photodiodes bonded to an array of silicon MOSFET devices to form a direct readout (DRO). Odd and even numbered pixels are read out separately. Light detection translates into progressive de-biasing of the photodiodes. Saturation of the device corresponds to a fully de-biased detector; the detector is still light sensitive, and it does not 'bleed' (or 'bloom'), but integration ceases. The whole camera is cooled to cryogenic temperatures and the detector operates at 35 K, to minimize dark current. Table 2.1 shows typical characteristics of the two SBRC InSb arrays currently used with IRCAM.

The camera is basically a side-looking cryostat mounted on a general purpose Instrument Mounting Platform attached to the UKIRT Instrument Support Unit at the Cassegrain focus. Light emerging from the telescope (reflected on the dichroic mirror) is collimated and redirected into the entrance window of IRCAM by gold-coated off-axis mirrors and refocussed by cold optics onto the detector array. A Fabry-Perot etalon can be placed in the collimated beam and a polarimeter module can be lowered into the beam (remotely). Two filter wheels carry a set of standard broad band filters ($JHKL'M$), a set of high-throughput narrow band filters (bandwidth $\approx$ 1% of wavelength) for selected spectral features, several narrow band continuum filters and a set of polarizers. A cold

Table 2.1. Characteristics of the present SBRC InSb arrays used with IRCAM.

Operating Temperature	35 K
Quantum efficiency	80% at 3 μm
Readout noise	450 e^-
Dark current	100 $e^- s^{-1}$
Pixel dimension	76 μm $\times$ 76 μm
Bad pixels	$< 1\%$
80% Full well capacity	780,000 e^-
Photoelectrons per Data Number (DN) conversion	30 e^-/DN

Note: Values as in July 1990.

lens images the pupil situated behind the filter onto the array. Different magnifications (0.″6, 1.″2 and 2.″4 pixel^{-1}) are possible by using different lenses. As this lens is located inside the cryostat, the pixel scale can only be changed by warming up the camera and exposing the detector to air, which can deteriorate the performance of the array. There are currently two of such arrays installed in two separated cryostats, called IRCAM 1 and IRCAM 2. Both cryostats are nearly identical in design, but usually carry different pixel scales, thus minimizing the number of changes of the re-imaging lens inside.

IRCAM is operated remotely from a terminal situated at the UKIRT control room and software has been provided for the acquisition, quick-look and preliminary reduction of the data. Automation of the camera operation is particularly beneficial when operating on the summit of Mauna Kea (4,200 m). On-line preliminary data reduction has proved to be necessary when imaging faint sources to have an idea of the quality of the acquired data, as many single frames need to be combined to get the final image. This significantly increases the observing efficiency because we can estimate the signal to noise (S/N) of the data, and decide on optimum exposure times, which are difficult to estimate with unknown-brightness sources and changing observing conditions.

At present IRCAM has three data-collection modes which are called STARE, CHOP and SNAPSHOT. The STARE mode consists of timed integrations of arbitrary length at a fixed position on the sky. In CHOP mode, data-taking is synchronized with the chopping secondary mirror to subtract the sky background, as used with single channel detectors. It is used when the sky background is high, but in the near IR it has been found to offer no benefits over STARE mode, while adding significant overheads to the observing. The third option, SNAPSHOT, consists of continuous short exposures of a fixed position at a maximum rate of 3 frames per second.

2.4 Overview of observational techniques and data reduction procedures

2.4.1 Standard observation and reduction technique

We have used IRCAM in the STARE mode (like an optical CCD), with on-chip exposures long enough to give background-limited operation. An arbitrary number of coadded exposures (coadds) can be accumulated in the memory of the Array Data Preprocessor to achieve much longer integrations. Individual coadds are not stored, only the sum, which is called a frame or image. The on-chip exposure time has to be chosen such as to give background limited performance (BLIP) without exceeding the well capacity of the chip. Since the readout noise is approximately constant for each coadd, BLIP is achieved when $\sqrt{number\ of\ photons\ counted} > readout\ noise$ ($450e^-$), that is $number\ of\ photoelectrons > 200{,}000$. For faint objects (as in our case) the dominant source of photons is sky + telescope + camera ($K \sim 12^m.6$ arcsec^{-2}) and the exposure times required to reach BLIP are independent of the object brightness, but they change with observing conditions and have to be determined every night. They are chosen so that the detector wells are $\frac{2}{3}$ filled with photoelectrons (5–600,000 photoelectrons $\simeq$ 20,000 DN above bias). This leaves more than enough dynamic range for faint-object photometry without getting close to saturation, where strong array non-linearity occurs (see ahead). Typical on-chip exposures in the K-band are 8–15 secs using the $1''.2$ pixel^{-1} configuration.

The signal in a raw IRCAM frame is in counts or Data Numbers (DN —typical gain gives 30 e$^-$/DN). It consists of contributions from each of the following:

- BIAS — A constant offset introduced during readout. Before April 1990, its value was 36,000 DN. After this date, a new readout scheme that significantly improves the signal to noise has been in operation. This new scheme eliminates this bias.

- DARK current — It is due to the thermal production and recombination of free charge carriers, and the diffusion of carriers though the junction. The first effect dominates below 80 K, and it decreases very fast with temperature until 40 K, but this decrease slows down below this temperature. That is the reason for the camera operating at 35 K. It produces, on average, $100\,e^{-}\,s^{-1}\,pixel^{-1}$. It varies spatially across the array and from pixel to pixel. It can vary during the night with timescales of a few hours, and it tends to be higher at the start of the night. A few 'hot' pixels exist, which have a very high dark current, and saturate on even short exposures.

- PHOTOELECTRONS — They are produced by the background + object. Every detected photon produces a reduction in the electric biasing of the detector. Quantum efficiency (average $\sim$ 80% at 3 μm) varies by a few percent from pixel to pixel on small spatial scales, but can vary by 5–10% on larger scales on the array, so flatfielding correction is required.

Taking all these contributions into account, we describe now the observation and data reduction procedures that we have developed to obtain the final images with the required quality for faint object photometry.

First, the response of the array deviates slightly from linearity in the high count regime in the sense that the observed count above the BIAS level is progressively less than it should be. This effect is not severe when working far from saturation and does not show any variation with time. It has been calibrated by M. Casali (private communication) and a correction factor is applied to the counts in each pixel of the raw images. This correction is applied by UKIRT staff after each observing run, and it is generally small (a few percent) in the count regime of our frames.

The DARK current has to be subtracted using DARK frames taken every few hours during each night, and the closest in time is generally used. They are simply images taken with the same on-chip exposure time (and usually the same number of coadds) as the object frames, with cold BLANKS in the filter wheels. Note that the DARK frames also contain the BIAS signal (in the cases in which it was not zero), so it is also subtracted using these frames.*

Flatfielding is needed to correct from the response variations across the detector. It is especially critical in the IR because of the high background photon flux. High accuracies are obtained by using SKYFLAT images taken in blank areas of the sky near the target, generally with the same on-chip exposure and number of coadds as the object frames. Significant variations have been found in the SKYFLAT images on timescales as short as 10–15 minutes, and when pointing towards directions separated more than a few degrees on the sky. The cause is not clear. The most likely explanation is that the colours of the sky (probably OH emission) is varying on that sort of time or spatial scales, and affecting the flatfield through the wavelength sensitivity of the array quantum efficiency. Whatever the cause, to ensure the maximum signal-to-noise it is necessary to spend as much time on SKYFLATS as on target OBJECTS, nodding the telescope between targets and sky with exposures shorter than $\sim$ 10 minutes. Since our required integrations are almost always longer than that, the procedure is repeated until the required total exposure time is obtained. Every SKYFLAT frame is taken on a different position (separated about half an arcminute), to eliminate faint star images by median filtering. The OBJECT frames are also taken at slightly different positions (separated a few arcseconds) to minimize residual pixel-to-pixel variations in sensitivity and the effect of the bad pixels and cosmic rays. Since defective frames are obtained sometimes, (i.e. with 'glitches', etc.), a good way

* BIAS frames are also taken. They are just like DARK frames but with very short (145 ms) on-chip exposures. They are usually used to DARK-subtract the standard-star frames, which are taken with this on-chip exposure.

of minimizing the losses is breaking every OBJECT and SKYFLAT exposures in several (2–4) sub-integrations, without moving the telescope in between. If no problem occurs, they are coadded together during the data reduction, but if any of the frames is defective, only a fraction of the total exposure is lost. The extra overhead is negligible compared with the advantages.

Once all the relevant frames have been obtained, the reduction procedure can be summarized in the following steps:

1. DARK frame subtraction from every OBJECT and SKYFLAT images.

2. Normalization of the SKYFLAT by dividing by its median value.

3. Division of every OBJECT frame by the normalized SKYFLAT. Due to the rapid changes in the flatfield, the most convenient procedure is to use the SKYFLAT taken immediately before or after the OBJECT. Since sometimes sudden changes on the SKYFLATS occur, the result can be better using one or the other, and the one that gives the best results (*i.e.* flatter images) is chosen in every case. In general, building a 'superflat' by median-filtering several SKYFLATS does not work very well due to the short timescale for the changes in the flatfield. It is better to use single SKYFLATS taken as close in time as possible and then medianning the flatfielded OBJECT frames (see ahead).

5. Removal of artifacts (e.g. bad pixels) by interpolation between adjacent pixels. As there are several ($\sim$ 20) known 'hot' pixels, their removal can be done automatically.

6. Registration of the flatfielded OBJECT frames using sufficiently bright point-like sources when possible (in most cases) or the crosshead positions if not (autoguiding was always in use). Sub-pixel shifts are used.

7. The final image is obtained as the median of all the registered OBJECT frames for one night. They are normalized additively to a common sky value. This eliminates the effect of any residual faint-star image on the SKYFLAT frames (seen as 'holes' on the flatfielded OBJECT frame), and any remaining bad pixel or cosmic ray.

Since the field of view of the camera is quite small, sometimes it is necessary to image the targets at different positions to obtain a mosaic. Then, the last stage of the data reduction consist of the mosaicing of the frames by offsetting them and averaging the overlapping areas.

Very flat images (flatter than 7 parts in 10^5 in exposure times of the order of 5000 sec) have been obtained using the method described above. This corresponds to 1σ surface brightness detection limits of $\sim 22\overset{m}{.}8$ arcsec^{-2}. Figure 2.3 (a) shows a histogram of the normalized sky values for an image taken on July 1990, with a total exposure time of 4800 secs.

2.4.2 Alternative method: 'in-field' chopping

An alternative technique, similar to the 'in-field' chopping used with very deep optical CCD images (see Tyson & Seitzer 1988 and references therein), can be used in certain cases, but it must be taken into account the timescale of SKYFLAT variation in the IR (see Cowie *et al.* 1990 for a detailed description of the method). If the target objects are small, and there is plenty of sky between sources, then the OBJECT frames can be taken at different positions, and a flatfield free of sources can be obtained by median-filtering the resulting stack of frames. The positional shift between frames should be more than the size of the objects in the field, and not smaller than ~ 5 arcseconds. Empiric measurements show that the optimum integration time for an image is ~ 80 secs to get maximum signal-to-noise. Exposure times as short as that are required to adequately

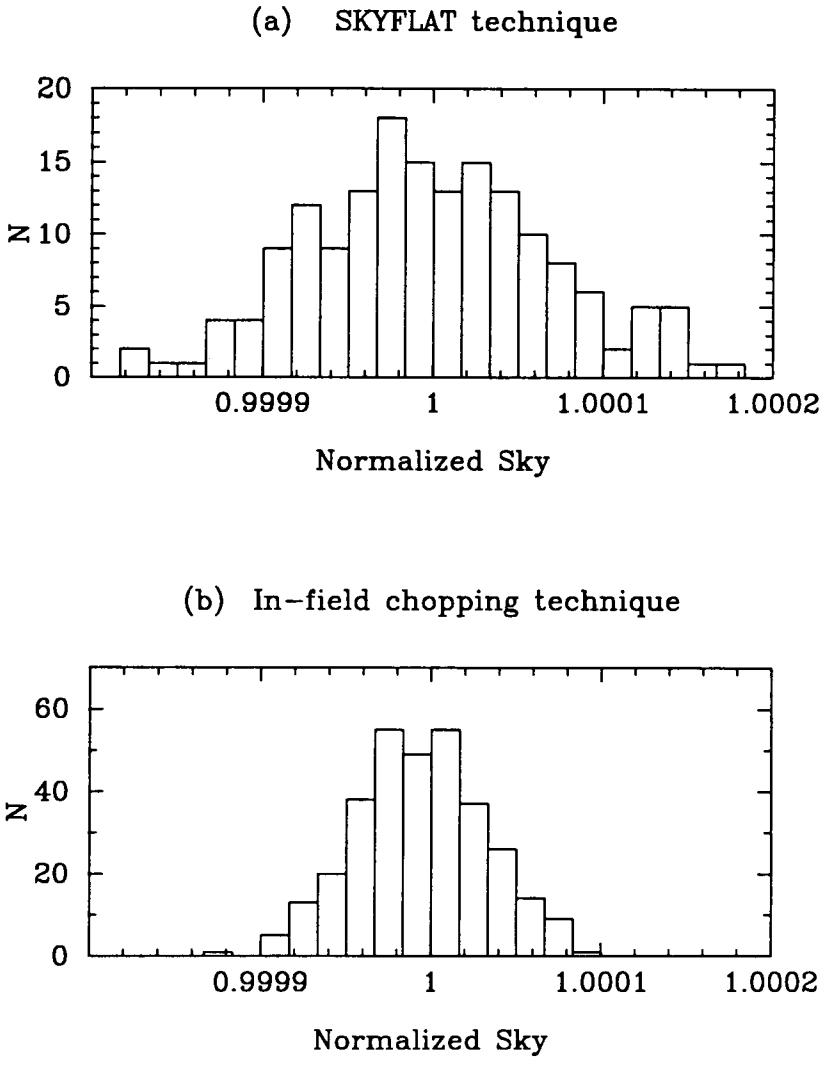

Figure 2.3. **(a)** Histogram of the normalized sky values for an image taken on July 1990 using the SKYFLAT technique, with a total exposure time of 4800 secs. The sky is flat to 7 parts in 10^5, corresponding to a 1σ detection limit of $22\overset{m}{.}8\,\mathrm{arcsec}^{-2}$. **(b)** Same as (a) for an image taken using the 'in-field' chopping technique, with a total exposure time of 6972 secs. The sky is flat to 3.8 parts in 10^5, corresponding to a 1σ detection limit of $23\overset{m}{.}6\,\mathrm{arcsec}^{-2}$

sample the sky variations. Shorter exposures increase the overheads, without producing any sizeable improvement of the performance. If the total integration is longer than the timescale for flatfield variation, not all the frames should be included in the median to obtain the flatfield that is used with each frame. Usually we use a running median that includes approximately five frames on each side of the frame to be flatfielded. This procedure avoids the need of separate SKYFLATS taken on adjacent 'sky' areas.

We have not used this technique with the galaxy clusters because the field is usually too crowded, and the galaxies are too faint to be seen in exposures as short as the optimum ones, making the registration of the images very difficult. However, an ideal case is the imaging QSO fields (see Chapter 6), in which there is plenty of sky on the frames and the QSO itself is easily visible on individual frames. This method has provided images flatter than 4 parts in 10^5 in exposure times of the order of 7000 secs. This corresponds to 1σ surface brightness detection limits of $\sim 23^m.6$ arcsec^{-2}. Figure 2.3 (b) shows a histogram of the normalized sky values for an image taken on July 1990 using this technique, with a total exposure time of 6972 secs.

2.4.3 Comparison with theoretical performance

Calculation of the S/N can be done taking into account that there are essentially four noise sources:

- photon noise form the source
- photon noise from the background (OH plus thermal emission)
- dark current from the detector
- readout noise from the detector

For any given pixel in the dark-subtracted and flat-fielded image

$$(S/N)_{pixel} = \frac{S\sqrt{T}}{\sqrt{(S+B+R^2/t)+\epsilon_D(D+R^2/t)+(1+f)^2\epsilon_B(B+D+R^2/t)+(1+f)^2\epsilon_D(D+R^2/t)}} \qquad (2.1)$$

where S, B and D are the source, background and dark signals respectively in $e^-s^{-1}pixel^{-1}$; R is the readout noise, t and T the on-chip exposure time and total integration time respectively, *i.e.*, $T = N_S t$ where N_S is the number of coadds, N_S/ϵ_B the number of coadds on SKYFLAT, N_S/ϵ_D the number of coadds on DARK and f is S/B. For a point source extended over n pixels then S must be summed over those pixels and the terms involving B, D and R must each be entered n times.

Figure 2.4 shows the predicted and measured K surface brightness 1σ detection limits of IRCAM in the 1.″24 pixel mode as a function of total integration time. The solid line shows the theoretical prediction from equation 2.1 using the parameters contained in Table 2.1 and a K background of $\sim 12^m.6$ arcsec^{-2} ($3.2 \times 10^4 e^-s^{-1}$arcsec^{-2}). An equal integration on source and on sky has been considered. On the same figure we plot the measured detection limits for images taken in different observing runs under photometric conditions (see caption). A substantial improvement with time is apparent, due to our better knowledge of the camera, and the observation and reduction procedures, together with several technical improvements on IRCAM and the telescope. In fact, the results for July 1990 seem to be *better* than the theoretical ones. The reason is that just before our observing run, changes in the wiring on the telescope dome produced a substantial reduction of the readout noise, and the calculations have been made with parameters that correspond to earlier times. A low K background during those nights also helped.

This figure, together with Figure 2.3 show the superior performance of the 'in-field' chopping technique over the use of separate SKYFLATS. For a given total exposure time on source, the images are approximately $0^m.5$ deeper. Since this technique practically halves the observing time for a given total exposure and produces much better results, it

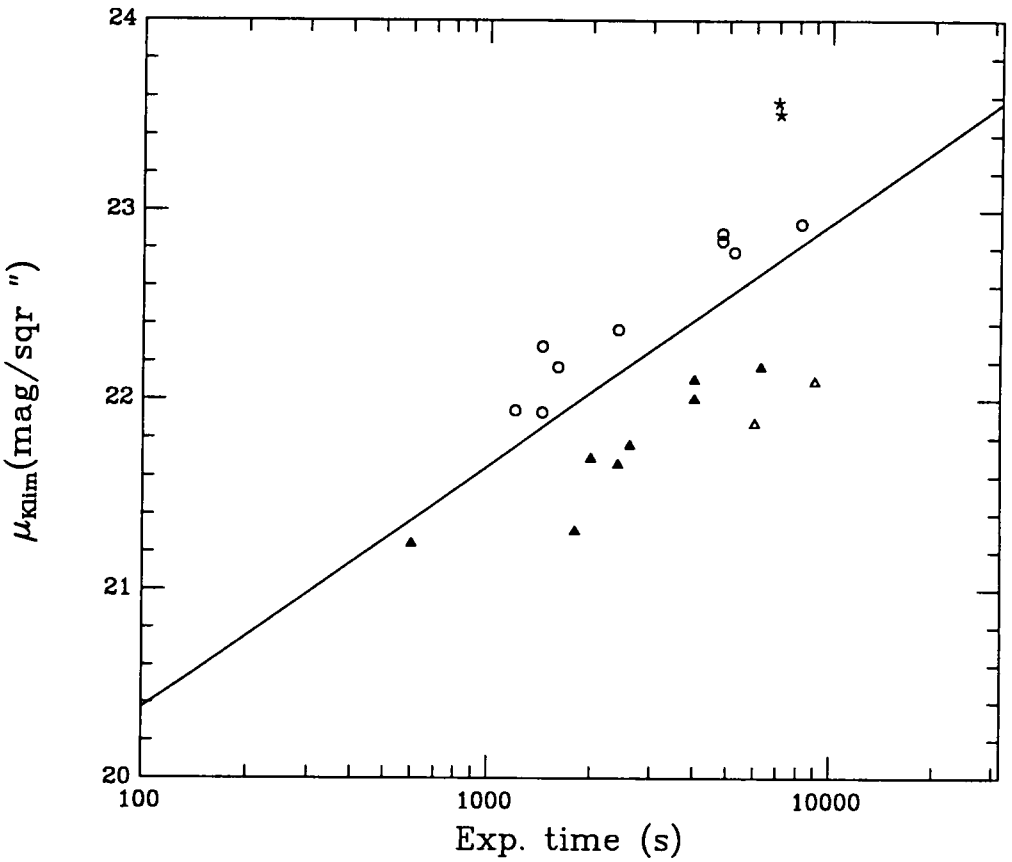

Figure 2.4. IRCAM K surface brightness 1σ detection limits as a function of total exposure time. Solid line: theoretical prediction (see text). Symbols: empirical determination from different observing runs. Open triangles: April 89; filled triangles: October 89; open circles: July 90. All these use the SKYFLAT method for flatfielding. Stars: July 90 using the 'in-field' chopping technique.

should be used when possible. Regrettably, it is not well suited for cluster work due to the problems mentioned above. It also reduces considerably the final usable field of the images, which is a major problem with small detectors. With the advent of larger chips, this problem will be less important, and only the crowding factor should be considered.

2.4.4 Absolute photometric calibration

Absolute photometric calibration is performed by taking images of standard stars several times during the night with different air-masses. To avoid saturation and non-linearity problems, standards as faint as possible should be used. We have used several UKIRT standards with $K \sim 7\overset{m}{.}0$. Ideally, stars with brightness comparable to that of the target objects should be used, but they are not available at the moment. UKIRT staff are carrying out a program to define a set of faint standards.

The current shortest on-chip exposure (145 milliseconds) is used, and the telescope is de-focussed when observing the standards in the $1\overset{''}{.}2$ configuration with broad-band (JHK) filters. The standard-star frames are reduced in a similar way as the OBJECT frames, but using BIAS exposures for dark subtraction. The flatfielding is not so crucial (the signal is much higher), and only one or two images and SKYFLATS are taken for the each standard at each air-mass.

2.4.5 Aperture photometry and errors

Photometry was obtained on the images using circular apertures centered on each object, and a local sky was estimated from the mode inside similar apertures in carefully chosen blank areas close to each object.

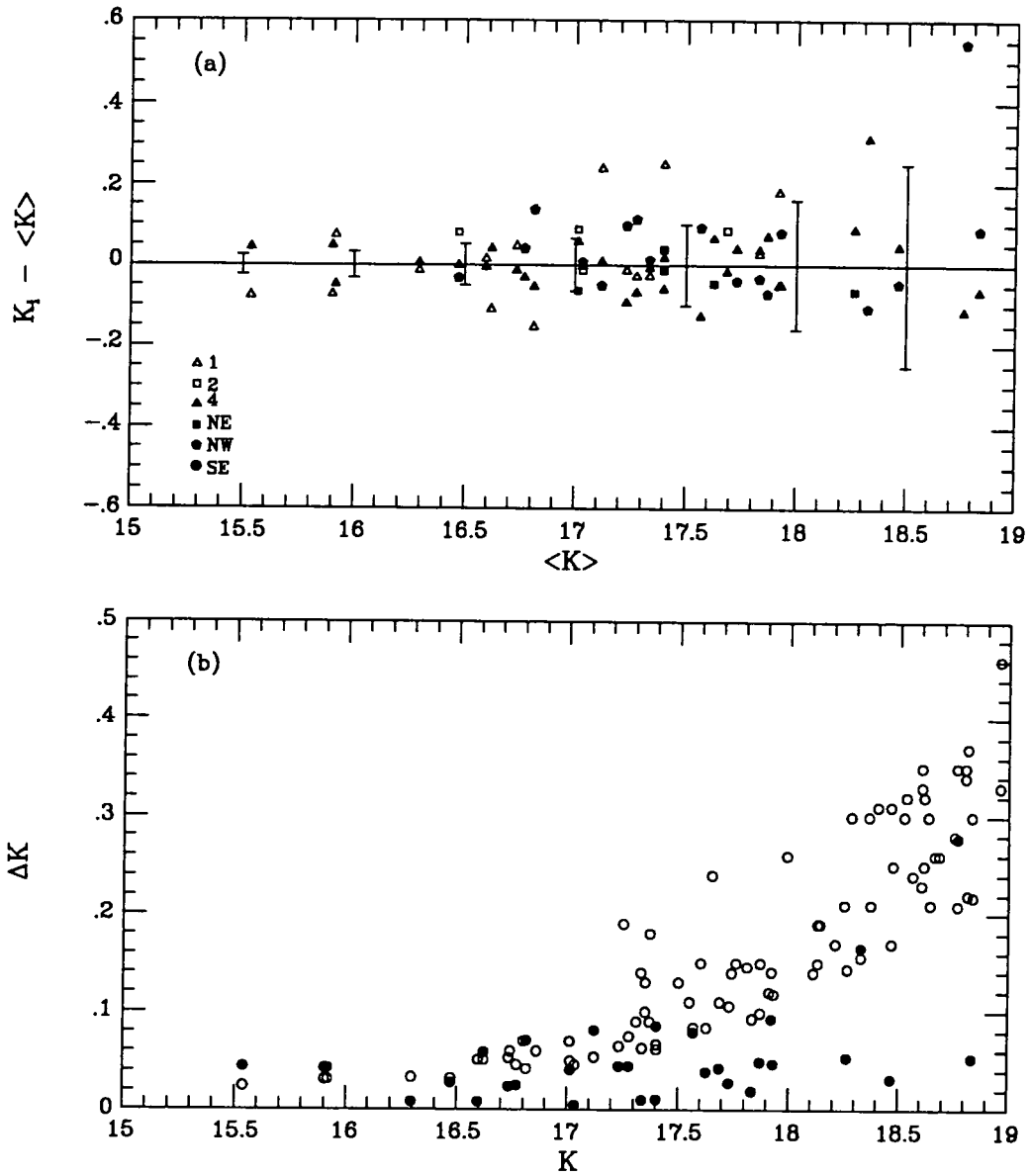

Figure 2.5. **(a)** Differences between the K magnitudes measured in different images and the adopted mean magnitude for the objects in the 0016+16 field as a function of K. The error bars show typical 1σ errors estimated from the variance of the sky at representative K magnitudes. Symbols refer to data obtained from the different images: open symbols for data taken in October 88, and filled ones for data taken in subsequent runs (see Chapter 4). **(b)** Final adopted errors (open circles) together with the errors estimated from the repeats when available (filled circles).

We estimated the random errors of the photometry first using the sky variance, and second by direct comparison between the values measured on overlapping areas and repeats (estimating the errors as $\sigma/\sqrt{n}$, where n is the number of measurements).* Both estimates give compatible answers, even when we compared photometry obtained in different observing runs (Figure 2.5). This gives confidence to the reproducibility of our photometry.

For most of the objects we have more than one independent measurement, and the final K value is computed as the average of all of them weighted with the inverse of the variance (calculated as the square of the errors estimated above), combining the individual errors to get the error on the mean in the standard way (see, *e.g.*, Bevington 1969). Figure 2.5 (b) shows an example (for 0016+16, see Chapter 4) of the final adopted errors together with the errors estimated from the repeats for comparison (when available). We decided to keep the values from the sky variance because the small number statistics make the estimation of the σ unstable.

The data reduction has been performed using standard STARLINK software, including a package specially designed to reduce IRCAM images. We have developed procedures to automate the whole process. We are specially indebted to M. Casali for providing a flatfielding routine, and I. Smail for his program PELE** that automates the registration and normalization of the frames.

---

* The standard deviations were estimated following the prescription of Keeping (1962) for small number statistics, which gives more stable results than the standard method when the samples are small.

** 'Pele' is the name of the Hawaiian goddess of the volcanoes. It is specially appropriate, since the program was written on the summit of Mauna Kea, a dormant volcano, during one of our observing runs.

2.5 Summary and Conclusions

In this chapter we have studied several scientific and technical aspects of infrared observations of high redshift galaxies. Our main conclusions are:

1. We demonstrate the advantages of using near-IR imaging to build representative samples of *normal* galaxies at high redshift. IR-selected samples of distant galaxies do not suffer from the ultraviolet bias, and are less affected by the evolutionary effects that distort optically-selected samples. K-selected samples would contain approximately the same proportion of all galaxy types independently of redshift.

2. At very high redshifts ($z > 1$), near-IR imaging can be used to detect galaxies of all types in reasonable amounts of observing time, while optical imaging would almost exclusively detect blue, star forming galaxies.

3. Optical-IR colours of IR-selected samples of galaxies at different z's can be used to study the effects of star formation and evolution on *normal* galaxies as a function of look-back time.

4. We have shown that Infrared Arrays can be used to obtain high precision photometry to very faint limits. Techniques have been developed to flatfield the images to a few parts in 10^5, giving 1σ surface brightness detection limits fainter than $23\overset{m}{.}6$ arcsec^{-2}.

3 STAR FORMATION IN MODERATE REDSHIFT CLUSTERS: ABELL 370 AT z = 0.37

3.1 Introduction

Our understanding of the nature of galaxies in distant clusters ($0.2 < z < 0.5$) has improved considerably in recent years due to systematic studies at optical wavelengths. Carefully-compiled photometric catalogues (Butcher & Oemler 1978, Butcher *et al.* 1983) have revealed a systematic excess of blue galaxies associated with rich clusters at modest redshifts, $z \simeq 0.4$, when compared to the number seen in taxonomically similar clusters of the present epoch. Multiple object spectroscopy of representative clusters at $0.3 < z < 0.5$ (Dressler & Gunn 1983, Couch & Sharples 1987) demonstrated not only that these blue galaxies are indeed cluster members but also that their star formation was likely to have been recently enhanced.

Physical explanations for this enhanced star formation usually point to an environmental process which may be connected with the removal of gas from disk systems destined to become S0 galaxies (*cf.* Gunn 1989). An important development in this context, is the claim by MacLaren, Ellis and Couch (1988, hereafter MEC) and Lilly (1987) that recent star formation may have also occurred in some *red* members of the cluster. MEC found that a significant proportion of optically-red galaxies in Abell 370 ($z = 0.37$) displayed an excess of ultraviolet ($\lambda_{rest} \simeq 270\,\mathrm{nm}$) light consistent with small amounts of ongoing star formation. A similar effect was seen in the more distant cluster 0016+16

(Ellis *et al.* 1985). Available UV data suggest few nearby ellipticals have a significant excess at this wavelength. MEC postulated that such enhanced activity must have been a common feature in a larger fraction of cluster galaxies at $z \sim 0.4$ than the original studies implied, particularly when account is taken of the difficulty of observing such transient effects in the overall population.

By extending the photometry to infrared wavelengths in a number of distant clusters, Lilly (1987) found a discrepancy in the rest-frame $(V - H)$ colours of otherwise well-behaved early type galaxies when compared to corresponding values in the nearby Coma cluster. This was attributed to a contribution from massive intermediate-age giant branch stars, such as might be present if there had been significant star formation events in the recent history of the distant clusters. Although Lilly sampled over 50 galaxies, the typical number per cluster was small ($\simeq 10$) and so it is not clear what *proportion* of red galaxies at $z > 0.3$ display this infrared excess. Additionally, the effect claimed ($\simeq 0\overset{m}{.}1$ averaged over all objects) is only marginally larger than the observational scatter within each cluster.

Our approach is somewhat different, although our goal is similar, namely to study the red cluster members. Using a significant sample of galaxies, and adopting a simple model for the effects of a short-term enhancement in star formation activity, we hope to use the proportion of galaxies displaying anomalies of the various kinds (UV excess, IR excess, blue optical colours) to estimate the extent of this activity in a given environment. This is an important precursor to any successful physical explanation of the *Butcher-Oemler* effect.

Abell 370 ($z = 0.37$) was chosen for this study, because of the wealth of accurate optical photometry including the near ultraviolet from the CCD data of MEC. This cluster is one of the richest examples displaying an excess of blue galaxies and has extensive

spectroscopic coverage from the surveys of Henry & Lavery (1987), Newberry, Kirshner & Boroson (1988) and Soucail *et al.* (1988a).

3.2 Observations and data reduction

New infrared observations were obtained with the 3.8m United Kingdom Infrared Telescope (UKIRT) on Mauna Kea during the nights of 1988 October 13 to 16. K-band (2.2μm) images were secured with IRCAM 1 in the $1\farcs2$ pixel configuration. Due to the small field of view, three different positions within the cluster were imaged in order to obtain photometry for a significant number of objects. Table 3.1 gives a log of the observing run. Chapter 2 gives a detailed description of the observational technique and data reduction procedures.

We reached a 1σ detection limit of $\mu_K = 21\fm5\,\mathrm{arcsec}^{-1}$. The images of the three different regions were mosaiced by offsetting them and averaging the overlapping areas. A contour plot of the resulting image can be seen in Figure 3.1. The FWHM image quality is $2\farcs0$. Note that the giant arc (see e.g. Soucail *et al.* 1988b) is clearly visible; photometry for that object will be presented and analyzed in Chapter 6. (see also Aragón-Salamanca and Ellis 1989). A contour plot of an optical CCD image of the area (see MEC) is shown in Figure 3.2 at the same spatial resolution for comparison.

Standard stars from Elias *et al.* (1982) were observed frequently to secure an absolute photometric calibration, and were reduced in a similar way. The zero-points have an internal uncertainty of $0\fm02$. Photometry of the galaxies in Abell 370 was obtained using a $4\farcs8$ diameter circular aperture centered on each object, and a local sky was estimated from the mode inside similar apertures in carefully chosen blank areas close to each

Table 3.1. Log of Abell 370 K-band observations.

Object	R.A. (1950)	Dec. (1950)	Date	Exposure (s)
Abell 370 (Field 1)	$02^h37^m20\overset{s}{.}0$	$-01°47'34\overset{''}{.}9$	1988 October 13/14	6825
			1988 October 15/16	1500
Abell 370 (Field 2)	$02^h37^m20\overset{s}{.}0$	$-01°46'36\overset{''}{.}5$	1988 October 14/15	4575
			1988 October 15/16	6000
Abell 370 (Field 3)	$02^h37^m23\overset{s}{.}1$	$-01°47'34\overset{''}{.}5$	1988 October 16/17	6750

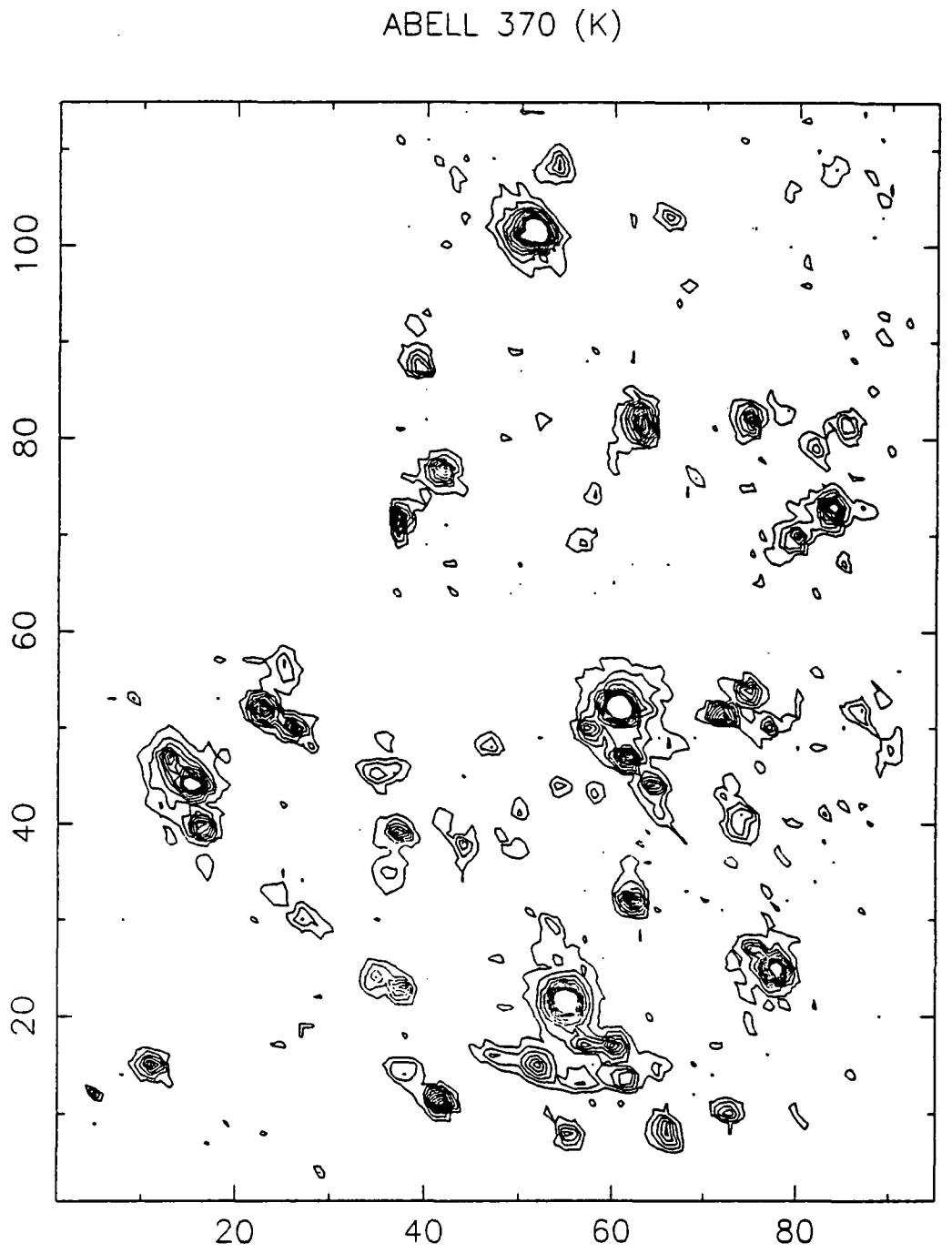

Figure 3.1. Contour plot of the Abell 370 K-band (2.2μm) mosaic. The scale is $1\farcs24$ pixel^{-1}. The numbers on the axes are pixels. North is up and East is left. The contours follow a linear intensity scale, the lowest corresponding to $\mu_K = 20\fm7\,\mathrm{arcsec}^{-2}$ (2σ above average sky level) and the highest to $\mu_K = 18\fm2\,\mathrm{arcsec}^{-2}$. Note that part of the North-East quadrant and a strip near y=60 were not imaged.

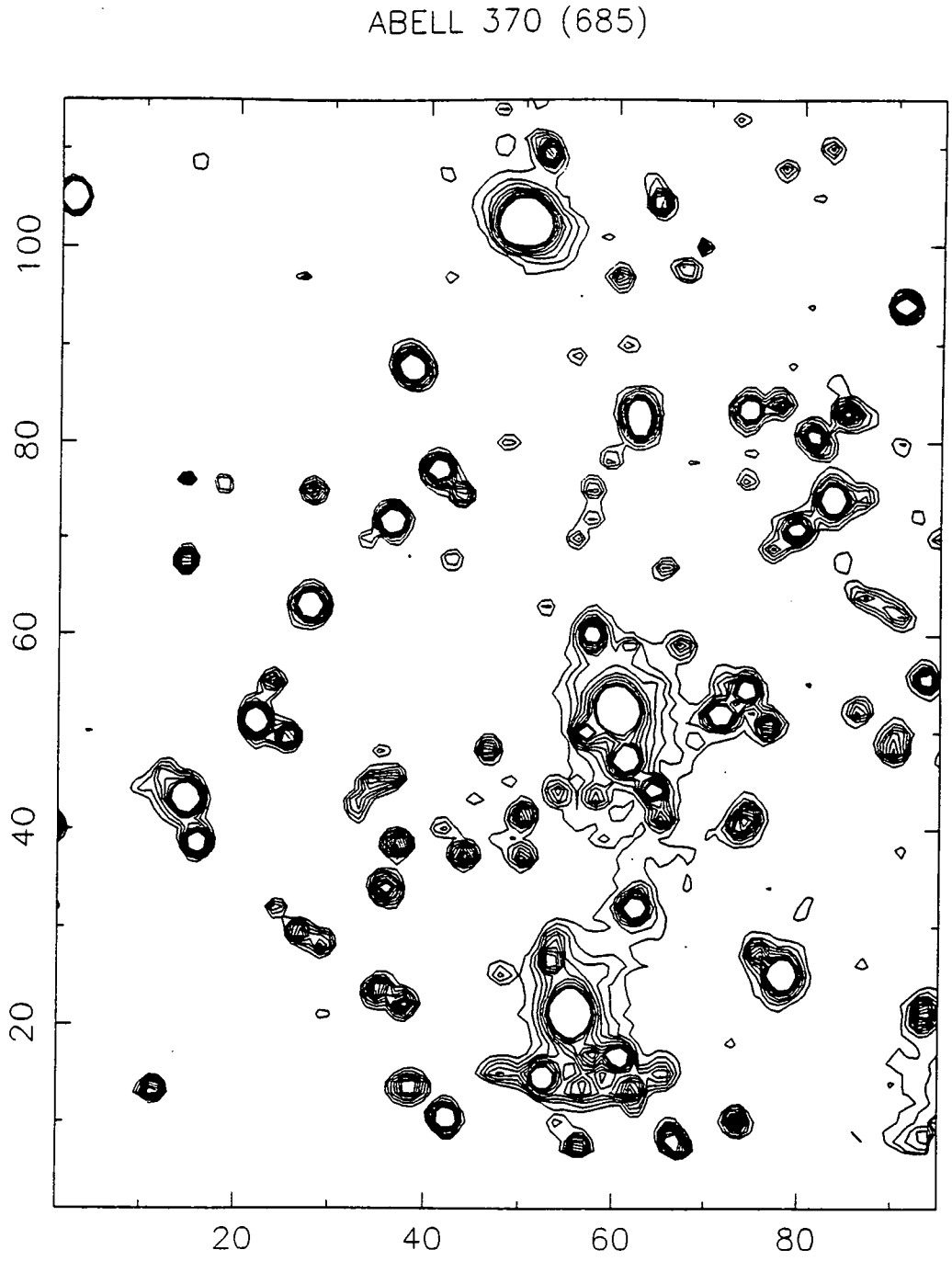

Figure 3.2. Contour plot of Abell 370 685-band CCD image (see MEC) rebinned to the same pixel scale and covering the same area and equivalent contour levels (from 2σ to 20σ above sky) as in Figure 3.1. Scale and orientation as in Figure 3.1.

object. Internal errors were estimated firstly from the sky variance and then by comparing photometry from images obtained on different nights and in overlapping areas. Both methods give comparable answers, providing a reassuring check on the reproducibility of our photometry (see Chapter 2). An independent cross-check was provided by comparing with photometry obtained from a very deep image of the giant arc secured with IRCAM 2 during UKIRT service time on October 29, 1989 (see Chapter 6). The measurements for the objects in common agree well within the estimated errors ($\sigma = 0^m.05$), and the zero points differ by only $0^m.006$. Since the K photometry reaches $K = 17^m.5$ with a precision better than $0^m.2$, which is a 5σ detection inside the aperture, we consider our sample 100% complete to this limit.

An external check to our photometry is provided by the subsequent work of Pickles & van der Kruit (1991, hereafter PK). Their K-band photometric data for Abell 370 was also obtained with IRCAM on UKIRT, but using a $7''.0$ diameter aperture. Their sample does not reach as deep as ours, but it allows a direct comparison for objects with $K \lesssim 17^m.0$, which is presented in Figure 3.3 for the objects in common. There is a good agreement, with a 1σ dispersion of $0^m.29$, which is broadly compatible with the quoted errors of both data sets.

PK magnitudes are systematically $0^m.20$ brighter than ours (independently of the magnitude), which corresponds to the different size of the aperture used. A $4''.8$ aperture was chosen as a compromise between including the maximum light from each galaxy and minimizing the errors due to sky contamination and the effects of crowding. As we have seen, the magnitudes measured using that aperture underestimate the total magnitudes, but in this study we are mainly interested in colours, and the aperture effects will be properly taken into account in the analysis. As we will see, the optical-infrared colour-magnitude relation for early-type cluster members is very flat, so using aperture

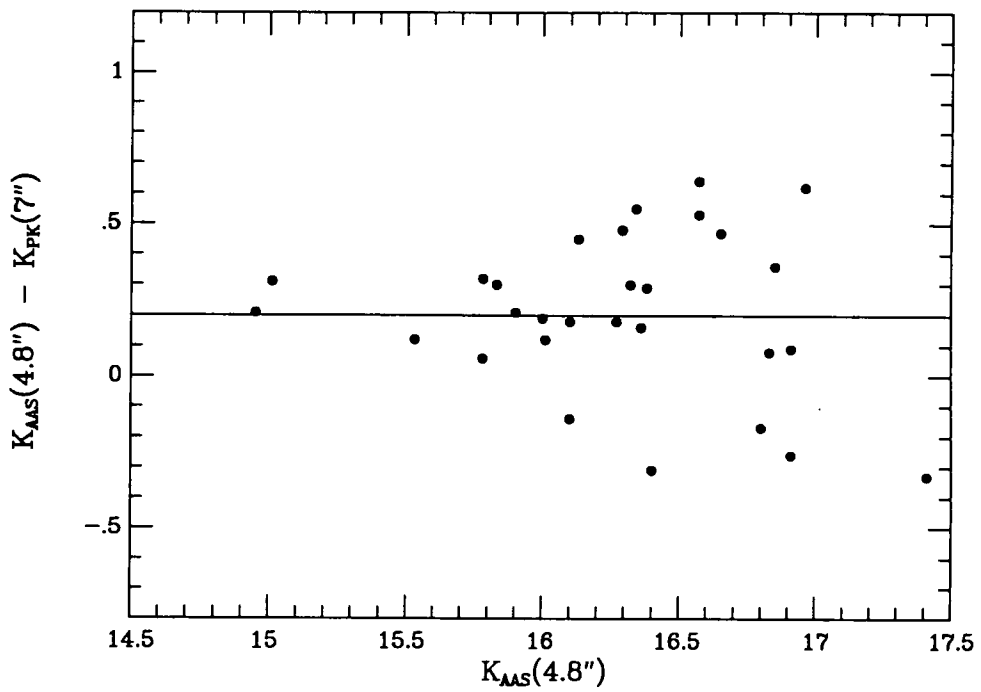

Figure 3.3. Comparison between our K magnitudes (4.″8 aperture) and those from Pickles & van der Kruit (1991) (7.″0 aperture). The average offset ($0^m.20$), indicated by the solid line, is probably an aperture effect, and the dispersion of $0^m.29$ is compatible with the quoted errors of the two data sets.

magnitudes instead of total ones has no effect in our conclusions, but it reduces considerably the errors in the colours.

MEC obtained broadband U and several intermediate band magnitudes (effective wavelengths 418, 502, 685 and 862 nm) for the galaxies in Abell 370. We have combined our K photometry with their optical data (measured with the same 4.″8 diameter aperture, number 3 in their nomenclature) to obtain long baseline optical-infrared spectral energy distributions (SEDs). In order to compare these with data for nearby galaxies (Persson, Frogel and Aaronson 1979, hereafter PFA) we have transformed the MEC 685 magnitudes onto an R (Landolt 1983) scale using two 400-sec CCD images obtained with the 1-m Jacobus Kapteyn Telescope at La Palma during a photometric night on July 8, 1989. These images were reduced using standard procedures and calibrated using Landolt photometric standards. Figure 3.4 shows the comparison of the R and 685 magnitudes for the brightest objects. It can be seen that a linear transformation with unit slope gives the required accuracy due to the fact that both passbands are quite close. The colour term is proportional to $-0.11(B-V)$ but the colour range in $(B-V)$ of the PFA data is smaller than $0^m.2$, and we thus ignore it. From the La Palma data we conclude that:

$$R(4.''8) = 685(4.''8) + 4.468 \pm 0.008 \qquad (3.1)$$

Table 3.2 contains the final photometric catalogue. Column 1 gives the galaxy number (the numbering scheme follows MEC). Columns 2 and 3 give the K magnitudes (within a 4.″8 diameter aperture) and the estimated errors. Columns 4 and 5 give the $(U-K)$ and $(685-K)$ colours within the same aperture.

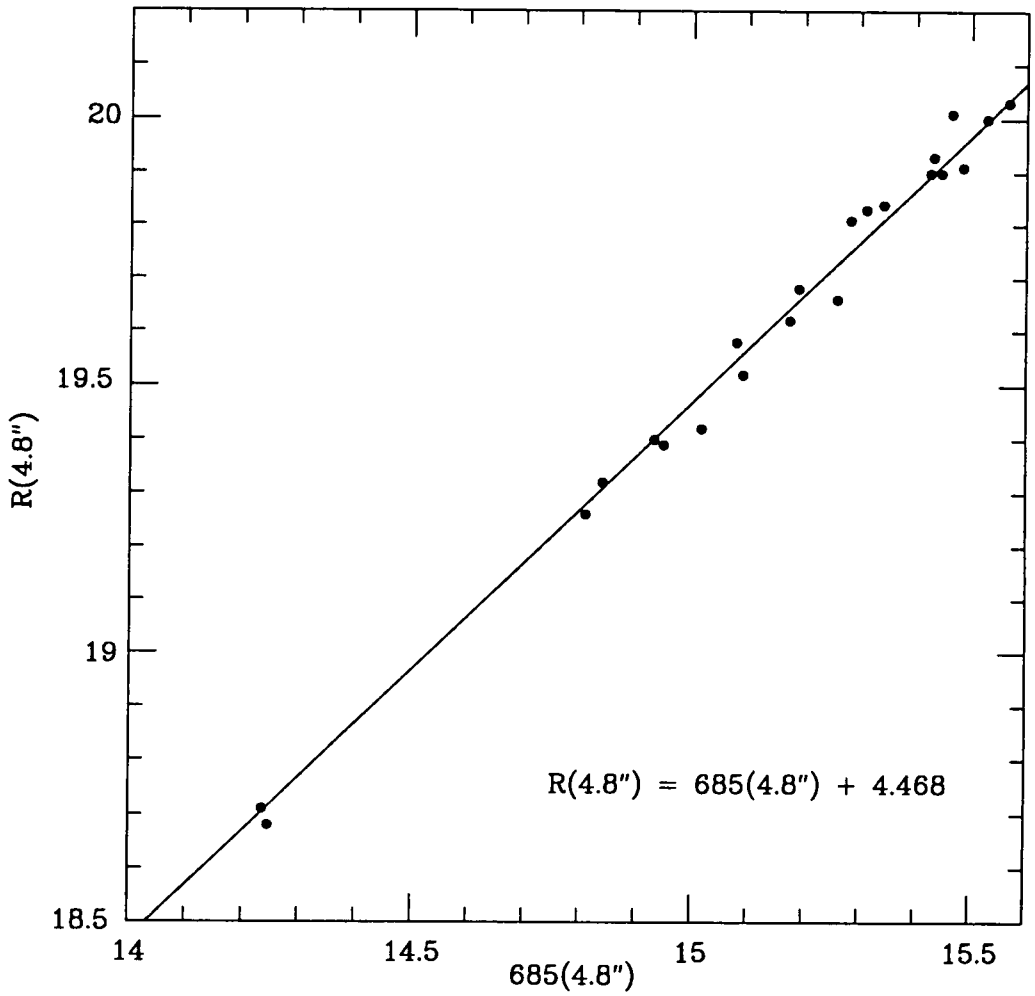

Figure 3.4. Calibration of MEC 685 magnitudes with R magnitudes for the objects brighter than $R = 20^m.2$. We used a 4.″8 diameter aperture. The line shows the relation given by equation (3.1).

Table 3.2. Photometric Catalogue.

CCD#	K	σ_K	$(U-685)$	$(685-K)$	Class	References
1	14.95	0.03	4.29	−0.71	E/S0	(1)(2)(4)
107	15.01	0.03	4.22	−0.76	E/S0	(1)(2)(4)
81	15.35	0.04	3.58	−0.63	E/S0+uvx	(1)(2)
20	15.53	0.05	3.55	−0.72	E/S0+uvx	(1)(2)(3)
3	15.78	0.09	4.94	−0.59	E/S0	(1)(2)(4)
29	15.78	0.05	4.14	−0.70	E/S0	(1)(2)(3)
47	15.83	0.06	6.81	−0.90	E/S0	(1)(2)
42	15.90	0.06	4.24	−1.06	E/S0	(1)(2)(4)
32	16.00	0.06	4.18	−0.91	E/S0	(1)(2)
94	16.01	0.06	4.61	−0.68	E/S0	(1)(2)
80	16.01	0.06	4.24	−0.67	E/S0	(1)(2)(3)
22	16.10	0.08	4.14	−0.67	E/S0	(1)(2)
102	16.10	0.07	2.83	−0.93	E/S0+uvx	(1)(2)
105	16.13	0.08	4.26	−0.68	E/S0	(1)(2)
28	16.27	0.08	4.12	−0.51	E/S0	(1)
106	16.29	0.09	4.78	−0.72	E/S0	(1)
36	16.32	0.08	4.15	−1.01	E/S0	(1)(2)
2	16.33	0.08	4.59	−0.64	E/S0	(1)
15	16.34	0.09	4.92	−1.06	E/S0	(1)(2)
68	16.36	0.08	4.01	−0.93	E/S0	(1)(2)
86	16.38	0.08	2.59	−0.63	E/S0+uvx	(1)(2)
4	16.38	0.10	4.91	−0.61	E/S0	(1)(2)
91	16.40	0.09	4.27	−0.39	E/S0	(1)
6	16.49	0.10	4.09	−0.71	E/S0	(1)
14	16.57	0.12	3.61	−1.04	E/S0 (f)	(1)
46	16.57	0.10	2.94	−0.95	E/S0+uvx	(1)(2)
66	16.62	0.10	1.50	−1.60	S	(1)(2)(3)
110	16.65	0.11	4.30	−0.72	E/S0	(1)(4)
90	16.69	0.11	2.24	−0.70	S	(1)(2)(3)
21	16.69	0.12	4.01	−0.60	E/S0	(1)
103	16.74	0.12	2.85	−0.75	E/S0+uvx	(1)
30	16.76	0.12	4.07	−0.36	E/S0	(1)
100	16.80	0.14	2.15	−0.20	S	(1)
26	16.83	0.13	—	−0.83	E/S0	(1)(2)
93	16.85	0.13	2.26	−1.06	S (f)	(1)(3)

Table 3.2. *continued.*

CCD#	K	σ_K	$(U-685)$	$(685-K)$	Class	References
27	16.90	0.14	3.60	−1.14	E/S0+uvx	(1)(2)(4)
69	16.91	0.16	2.69	−0.90	E/S0+uvx	(1)(2)
109	16.91	0.14	4.58	−0.72	E/S0	(1)(2)
101	16.93	0.14	1.69	−0.41	S (b)*	(1)(2)
16	16.96	0.15	3.85	−0.81	E/S0	(1)
108	16.99	0.14	1.98	−1.28	S (f)	(1)(3)
88	17.00	0.14	3.49	−0.93	E/S0	(1)
25	17.00	0.15	1.50	−0.59	S	(1)
17	17.17	0.18	3.59	−0.33	E/S0	(1)
258	17.17	0.17	4.83	−0.01	E/S0 (b)	(1)
292	17.26	0.19	2.03	−1.18	S (b)	(1)
19	17.36	0.19	1.66	−1.21	S (f)	(1)(3)
71	17.40	0.22	4.21	−0.87	E/S0	(1)
23	17.41	0.20	3.80	−1.11	E/S0	(1)
70	17.44	0.20	1.97	−1.67	S	(1)(2)(3)(4)(5)
5	17.50	0.24	4.69	−0.85	E/S0	(1)
24	17.51	0.20	2.36	−1.18	S	(1)
45	17.52	0.20	2.41	−0.79	S	(1)(2)(3)(5)

Notes:

All objects are members unless indicated: (b) background, (f) foreground.
E/S0: Normal elliptical.
E/S0 + uvx: Elliptical with ultraviolet excess.
S: Spiral.
(1) MEC (photometry)
(2) Soucail *et al.* (1988a) (spectroscopy)
(3) Henry & Lavery (1987) (spectroscopy)
(4) Newberry, Kirshner & Boroson (1988) (spectroscopy)
(5) Thompson (1988) (imaging)
* East part of the giant arc.

3.3 The colour-magnitude diagram

Figure 3.5 shows the observed $(685 - K)$ versus K colour-magnitude (C-M) relation for Abell 370 cluster members with $K < 17^m.5$. Spectral classification and cluster membership were determined from the spectroscopic data published by Henry and Lavery (1987), Mellier *et al.* (1988), Newberry, Kirshner and Boroson (1988) and Soucail *et al.* (1988a), when available, and from photometric spectral energy distribution (SED) classifications from MEC for the remaining galaxies. Some morphological information from high-resolution imaging (Thompson 1988) was also used. Column 6 of Table 3.2 gives the spectral classification and cluster membership information for the galaxies in the sample, and column 7 the references. From a total sample of 53 galaxies with $K < 17^m.5$, 34 (64%) have spectroscopic information. Where comparisons can be made we found an excellent agreement between the spectroscopic and photometric classifications/redshifts for the galaxies in common. 82% of the objects (28 out of 34) agree, and the ones that disagree are mainly late type galaxies, whose flat spectrum makes the photometric redshift very uncertain. As we are mainly interested in early-type galaxies, classification errors from the MEC photometry should have almost no effect on our conclusions. It should be noted that several cross-identification errors are present in MEC's Table 3; CCD# 3, 80, 36, 27 and 93 correspond to BO# 58, 62, 55, 105 and 129 respectively, and CCD# 46, 4 and 35 do not have a BO# counterpart. Note also that CCD# 109 was misclassified as an ultraviolet excess object; its $(U - 685)$ colour is normal. The red members (objects classified as E and S0 galaxies from spectroscopy and/or narrow band photometry) show a tight C-M relation, with a scatter of $0^m.3$ around the predicted line (see below).

To compare our observed C-M relation with that obtained for nearby galaxies, we have used photometry from PFA, who published $UBVR$ and JHK magnitudes for nearby E and S0 galaxies using several different aperture sizes. We use their photometry

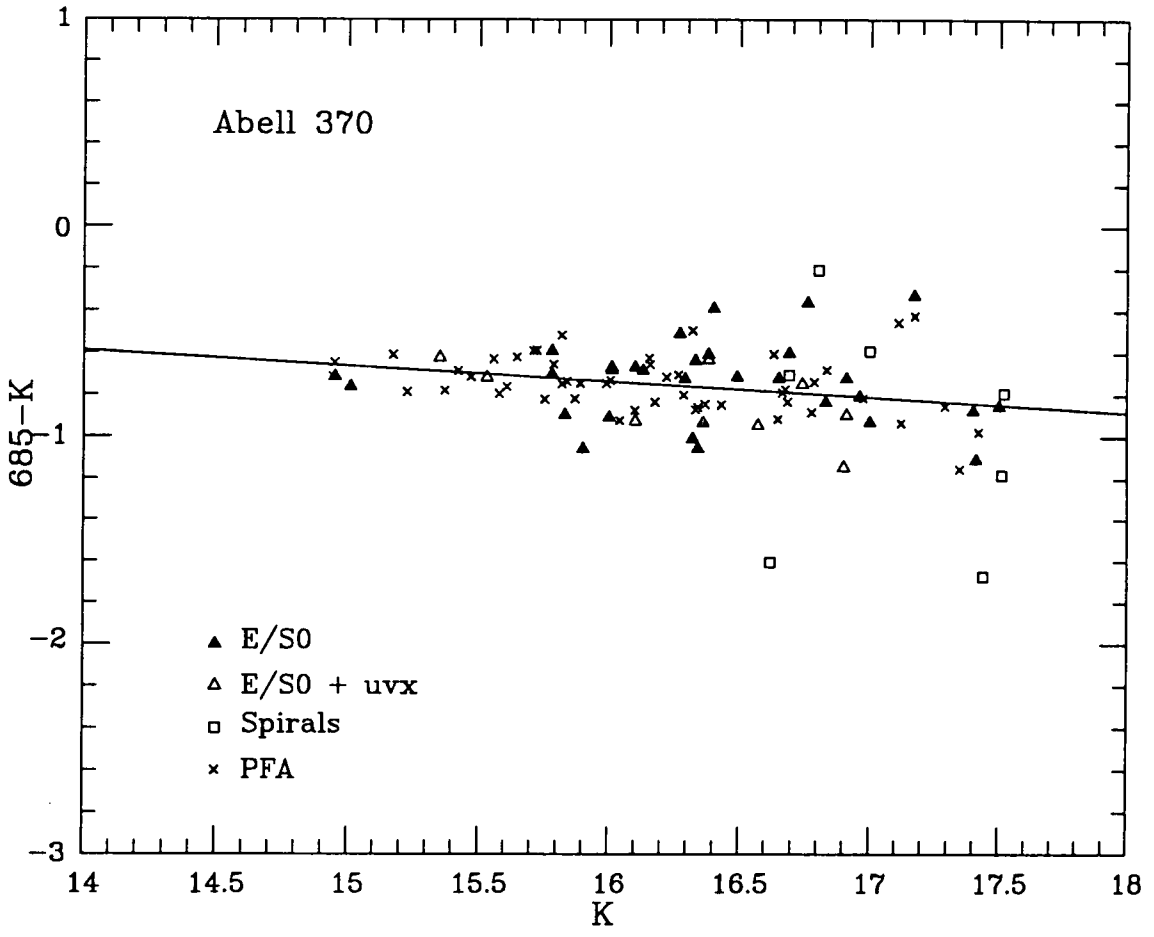

Figure 3.5. Observed $(685 - K)$ versus K C-M diagram for Abell 370 cluster members with $K < 17^{m}.5$. Filled triangles indicate *normal* E/S0s, open triangles E/S0 with ultraviolet excess and open squares spiral galaxies (see text for membership information and classification). The crosses represent the photometric data for nearby galaxies studied by Persson, Frogel and Aaronson (1979) transformed to the same projected linear aperture and redshift as the cluster (see text for the details of the transformation). The line shows a least-squares fit to the crosses, with a slope of 0.07.

to build a local C-M relation for early-type galaxies, and transform it into our observed $(685 - K)$ versus K diagram at $z = 0.37$. The transformation involves redshifting the rest-frame colours, allowing for differences in the responses of the photometric bands, and reducing the photometry to an equivalent aperture to that used in the observations. We transformed the photometry into a 30-kpc metric aperture (4.″8 diameter at $z = 0.37$ with $H_o = 50\,\mathrm{km\,s^{-1}\,Mpc^{-1}}$ and $q_o = 0.5$*). The Sandage and Visvanathan (1978) growth curve in V and a mean colour gradient of $\Delta(V - K)/\Delta\log(A/D(0)) = -0.1$ (PFA) were used. Their infrared photometry was transformed from the CIT system to the UKIRT (AAO) system using colour terms published by Bessell and Brett (1988). This correction is very small but was included for consistency.

The K-correction in the infrared is very uncertain due to the lack of observed SEDs for early-type galaxies in this wavelength range. Instead of predicting the rest-frame K magnitudes from the observed ones we have made use of the fact that the K passband for a galaxy at $z = 0.37$ ($K_{z=0.37}$) corresponds very closely to the H passband at $z = 0$ ($H_{z=0}$) (see Figure 3.6). This allows us to determine a very accurate transformation of $H_{z=0}$ into $K_{z=0.37}$ *almost independently* of the object SED (we ignore any small colour gradient in $H - K$). The transformation was computed by numerical convolution of the filter response curves (UKIRT Observer's Manual, UK Infrared Telescope Support Unit, 1989, 1991) with several SEDs at the appropriate redshift. The SEDs were determined using broad band photometry (PFA, Gavazzi and Trincheri 1989) to obtain very low resolution SEDs of present-day ellipticals and S0s, Bruzual (1983) c-models with different ages (from 3 to 16 Gyrs), a giant elliptical model provided by N. Arimoto (a revised galactic wind model based on Arimoto and Yoshii 1987) and finally, the airborne spectrophotometry for the

* The choice of q_o has negligible effect in the following discussion due to the fact that the C-M relation is very flat.

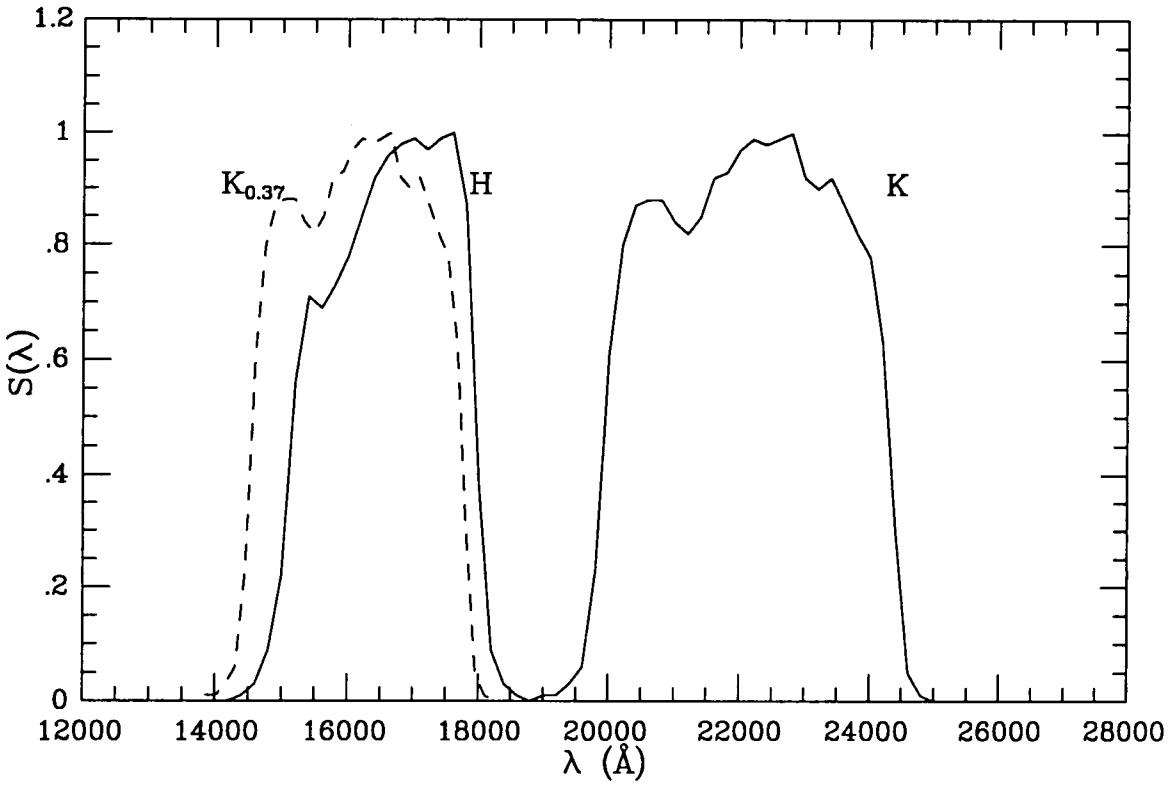

Figure 3.6. Bandpasses of observed H and K (solid line) and rest-frame K at a redshift of 0.37 (dashed line).

K5 giant α-*Tau* (Strecker, Erickson and Whitteborn 1979, see also Lilly and Gunn 1985). We find:

$$H_{z=0} - K_{z=0.37} = 0.83 \pm 0.02 \tag{3.2}$$

where the scatter indicates the variation in the 4 different approaches, which we accept as a suitable transformation for all the ellipticals and S0s.

The prediction of the observed 685 magnitudes (via R) is not as straightforward because the $R_{z=0.37}$ magnitudes have $\lambda_{eff} \sim 507\,\mathrm{nm}$, which lies between the B and V bands. However, detailed early-type galaxy SEDs are available in this region of the spectrum so we can convolve the filter responses with them at the relevant redshifts to get a calibration between $R_{z=0.37}$ and $V_{z=0}$ as a function of $(B-V)_{z=0}$. We used the Pence (1976) SEDs for present day galaxies of different morphological types and also a sequence of spectra used by Couch (1981) to derive a synthetic C-M relation for ellipticals. A linear fit to the resulting transformation gives:

$$R_{z=0.37} = V_{z=0} - 0.464 + 0.398(B-V)_{z=0} \tag{3.3}$$

with an rms scatter of $0^m.005$. This transformation, together with equations 3.1 and 3.2, allows us to predict the observed $(685 - K)$ versus K C-M diagram for galaxies at $z = 0.37$ from the PFA data for nearby galaxies. We estimate that the total uncertainty in the colour transformation is $\lesssim 0^m.05$. The crosses in Figure 3.5 show the transformed PFA data. The straight line is a least squares fit to these points and has a slope of 0.07 and an rms scatter of $0^m.16$. It agrees very well with the main locus of the observed colours of the E/S0s in Abell 370. The latter are, on average, $0^m.02$ redder than the local prediction. This suggests that the extinction towards Abell 370 must be small *assuming that the local C-M relation is valid for Abell 370.* Using the Savage and Mathis (1979) reddening law (see also Mathis 1990) and the estimated errors on the transformation, we get a nominal value of $E(B-V) = 0.01 \pm 0.03$, i.e. consistent with zero.

Several independent estimates of the foreground extinction towards Abell 370 are available in the literature. MEC used two different approaches. First they followed the procedure developed by Couch *et al.* (1983) and Ellis *et al.* (1985), which estimates the reddening from the observed SEDs using colours redward of ~ 685 nm. This method gave a very small extinction (they obtained a formal value of $E(B-V) = -0.014 \pm 0.020$). The second method, described by Couch (1981), uses a study of the colour distribution of field galaxies in the vicinity of Abell 370, and gives $E(B-V) = 0.12 \pm 0.05$. MEC rejected the first estimate (although the method gave results that are reasonably consistent, both from object to object and with infrared colours within a given object) and accepted the higher value on the basis of the good agreement between their observed and predicted optical ($502-685$, $418-685$ and $U-685$ versus R_f) C-M relations when this extinction was applied. On the other hand, the Burstein and Heiles (1982) reddening maps give $E(B-V) \lesssim 0.03$ for this region, and work by Jablonka, Alloin and Bica (1990), using a library of stellar cluster properties to analyze the spectra of several red galaxies in Abell 370 observed by Soucail *et al.* (1988a), suggests a total reddening of $E(B-V) \simeq 0.05$.* Bica (1988), using the same technique, estimates an average *internal* reddening for nearby ellipticals of $E(B-V) \simeq 0.04$, which again implies a very small foreground extinction in this direction ($E(B-V) \simeq 0.01$). We conclude, therefore, that there is strong evidence in favour of a small reddening towards Abell 370. If the Couch (1981) estimate is correct, either our predicted C-M relation is wrong by $\sim 0\overset{m}{.}2$ (and we have underestimated the uncertainties of the transformation because there are some poorly-understood systematics in the optical-infrared colours), or most of the early-type galaxies in the cluster are too blue in the observed $(685-K)$ colour by the same amount, which is difficult to understand in the framework of our current knowledge of galaxy evolution (Tinsley 1980, Bruzual 1983,

* It is referred to as 'intrinsic reddening', but, since no foreground extinction correction was applied, it actually includes the total amount of reddening present (Jablonka, private communication).

Arimoto & Yoshii 1987). In the rest of the Chapter we will assume that the reddening is small (i.e. consistent with zero), as most of the evidence suggests.

The observed rms scatter of the early-type galaxy colours around the predicted line is $0^m.3$, while the mean observational error is only $0^m.12$. Monte-Carlo simulations of samples with the observed error distribution show that this difference is highly significant (to more than a 99% confidence level), so most of the scatter would appear to be intrinsic. A close examination of the distribution of these colours around the predicted C-M relation suggests a bimodal behaviour, especially when looking at objects brighter than $K = 17^m.0$, where the errors are smaller than $0^m.15$. Figure 3.7 shows a histogram of the residuals of the observed colours around the predicted line for two different limiting K magnitudes ($K < 17^m.0$ and $K < 16^m.5$). Two peaks, one $0^m.2$ bluer and the other $0^m.1$ redder than the prediction are evident. Whilst this is a small effect, it is potentially very interesting because it might point to some evolutionary differences within the red population. First we estimate the statistical significance of the effect, and then we examine, using evolutionary models, what its cause might be.

Several statistical tests are available to assess the significance of departures from normal distributions, and in particular to study bimodality. First we have followed the method outlined by Lucey, Currie and Dickens (1986) (see references therein) which calculates several test statistics for the data points and examines whether these are significantly different to those expected from a normal distribution by constructing (using Monte-Carlo simulations) a large number of control samples (100,000 in our case) with the same population, mean and σ as the data. Not all the normality tests are equally suitable for searching for bimodality in the data. These authors conclude that the Kurtosis test (see D'Agostino 1982) is particularly suitable because it is sensitive to the flattening of the distribution. From this test we find that the observed distribution for $K < 17^m.0$ would arise from a single Gaussian with a probability of only 0.02 (this probability reduces to 0.01 for $K < 16^m.5$,

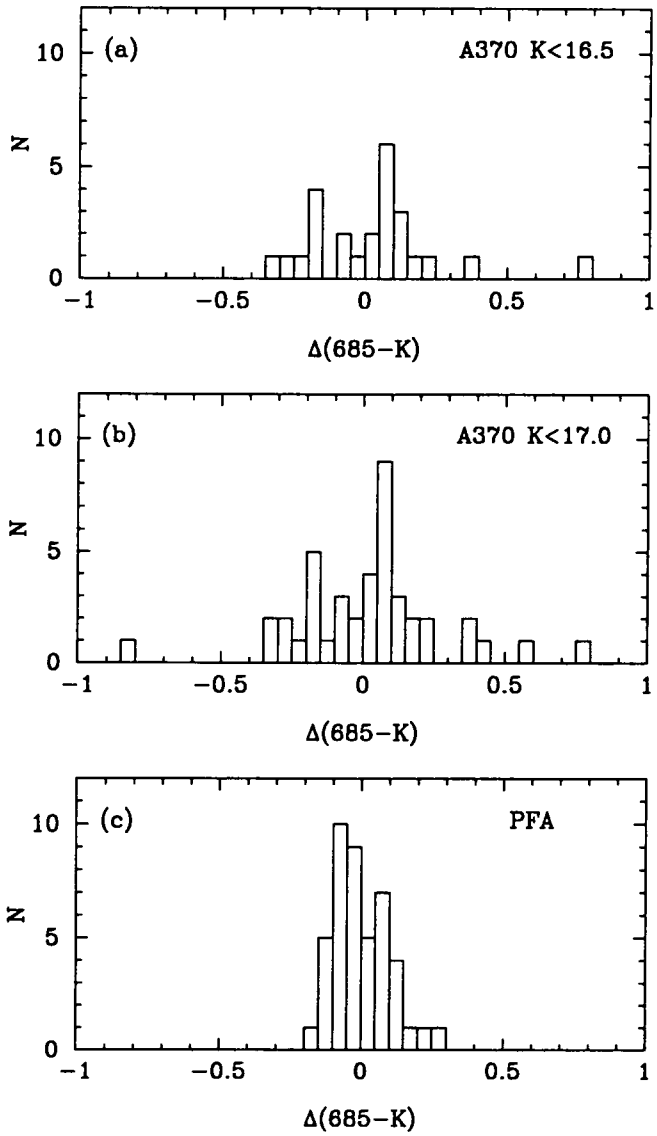

Figure 3.7. Distribution of the residuals of the observed $(685 - K)$ colours around the predicted C-M relation (see text) for the Abell 370 early-type galaxies brighter than $K = 16\overset{m}{.}5$ (a), brighter than $K = 17\overset{m}{.}0$ (b), and for the PFA nearby galaxy sample (c).

Table 3.3. Statistical study of bimodality.

		Probability	
Sample	Colour	Kurtosis test	Lee test
Abell 370 ($K < 16\overset{m}{.}5$)	$(685 - K)$	0.009	0.004
Abell 370 ($K < 17\overset{m}{.}0$)	$(685 - K)$	0.018	0.002
PFA	$(685 - K)$	0.758	0.745
Coma	$(V - K)$	0.861	0.642

Note:

Probabilities are for the colour distributions arising from a single Gaussian.

for which the photometric errors are below $0^m.1$). A second test, specifically sensitive to bimodality, is provided by a one-dimensional version of the Lee statistic (Lee 1979; see Fitchett 1988 for a complete description of the method). In both cases ($K < 17^m.0$ and $K < 16^m.5$) the probability of the distribution arising from a single Gaussian (as opposed to being bimodal) is only 0.002 and 0.004 respectively. The same tests applied to the PFA data show no significant departure from normality: at the same equivalent magnitude limit, the probability of the colour distribution around the main C-M line arising from a single Gaussian is 0.76 from the Kurtosis test and 0.75 from the Lee statistic. Since the PFA sample is dominated by field galaxies it is also desirable to compare our result with objects in a similarly dense nearby environment. Bower (1990) and Bower, Lucey & Ellis (1991) present very accurate U, V and K photometry for a sample of E/S0 galaxies in the Coma cluster. Since they have not measured B magnitudes, we cannot perform an identical analysis to the one carried out using the PFA data. However, we have analyzed the $(V-K)$ versus K C-M relation for the galaxies in their sample and again find no evidence for bimodality (the Kurtosis and the Lee tests give probabilities of 0.86 and 0.64 respectively for the $(V-K)$ colour distribution arising from a single Gaussian). Table 3.3 summarizes the results of the statistical tests for the different samples.

3.4 The colour-colour diagram

All but one (CCD# 26) of the cluster members included in our $K < 17^m.5$ sample have $(U-685)$ colours from MEC, so we can study the $(U-685)$ versus $(685-K)$ colour-colour diagram for an essentially K-magnitude limited sample (Figure 3.8). This diagram can be compared with incomplete versions published by Lilly and Gunn (1985) and Lilly (1987) for Cl0024+1654 ($z = 0.39$). Lilly's diagram shows rest-frame $(U-V)_0$ versus

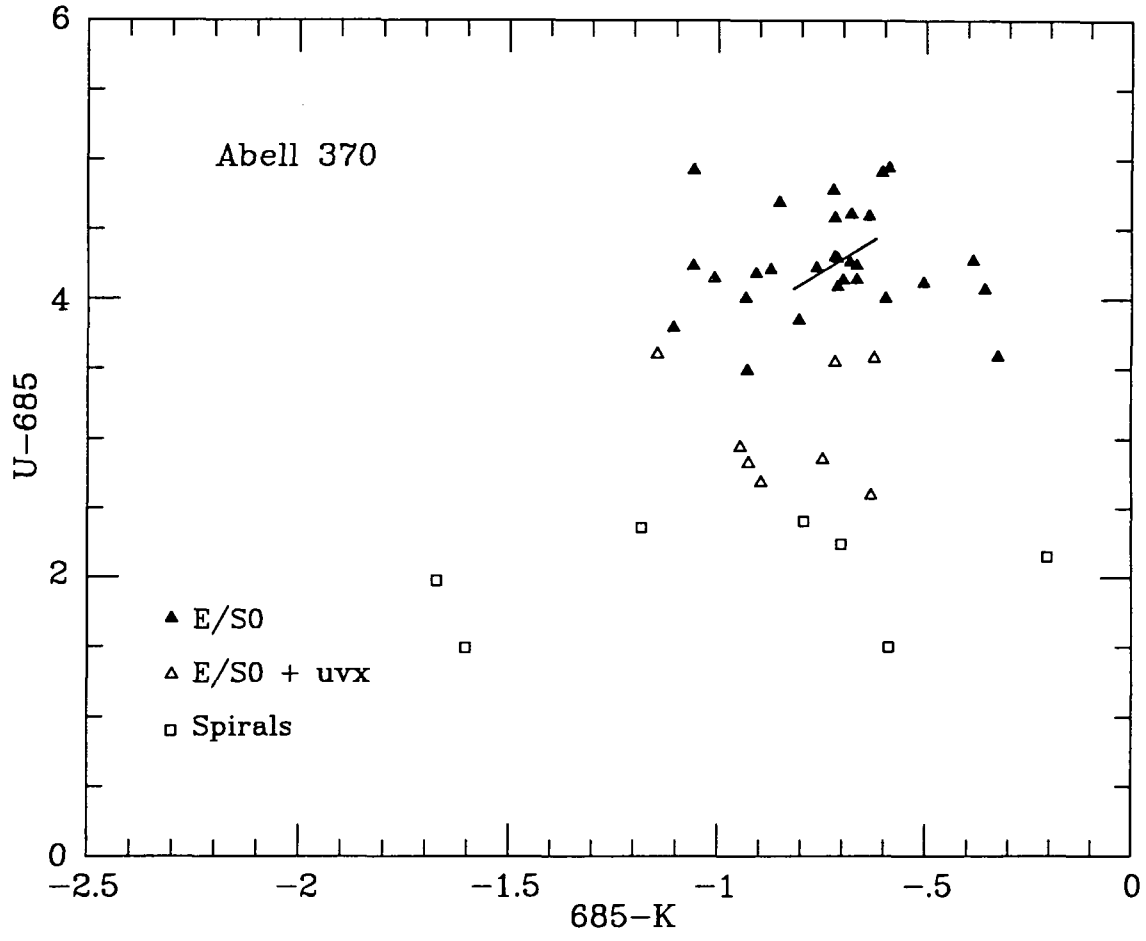

Figure 3.8. Observed $(U - 685)$ and $(685 - K)$ colours for Abell 370 members with $K < 17^m.5$. The symbols are the same as in Figure 3.5. The line shows the C-M effect in $(685 - K)$ (Figure 3.5) and $(U - 685)$ (MEC).

$(V-H)_0$ instead of observed magnitudes, but as we have shown above, the $(685-K)_{z=0.37}$ magnitudes should contain very similar information to the rest-frame $(V-H)_0$. We have made no attempt to K-correct the observed U magnitudes to avoid degrading the data with the uncertainties due to the shapes of the ultraviolet SEDs for different objects, but it should be kept in mind that the U-band is sampling light at ~270 nm. in the rest-frame.

The morphology of both diagrams is remarkably similar, bearing in mind that the present work contains a factor three more objects for a single cluster. Three groups of objects populate clearly distinct regions of the diagram. Those classified as *normal* elliptical galaxies form a relatively tight group, especially if we take into account that the C-M relation in both colours will be responsible for some of the scatter because we are sampling a range of $2^m.5$ in K, which corresponds to $0^m.2$ colour change in $(685-K)$ (with the C-M slope derived above), and $0^m.3$ in $(U-685)$ (MEC). This, together with the observational uncertainties in the photometry, accounts for much of the apparent dispersion in colours of these objects in the UV-optical range and some of that observed in the optical-infrared. However, the bimodality of the optical-infrared colours is also responsible for part of the scatter in this axis.

The objects that MEC classified as ultraviolet excess E/S0s form a distinct group on this diagram with $(U-685)$ colours in between those of what MEC called *normal* ellipticals and the spirals. The colours of these objects were interpreted by MEC as a manifestation of an elliptical galaxy that has experienced a burst of star formation and is decaying via the post-starburst and UV excess phase to a normal E/S0. Interestingly, we find that these galaxies show $(685-K)$ colours that belong to both 'red' and 'blue' peaks in the colour-magnitude relation (see Section 3.5).

Finally, the galaxies classified as *spirals* form a group which has the bluest $(U-685)$ colours, as expected from the SEDs of nearby spirals, but their $(685-K)$ colours span

a very wide range, from the reddest E/S0s to $\sim 0^{m}.5$ bluer than the bluest ones. This is compatible with the wide range of optical-infrared colours shown by nearby spirals (Aaronson 1977, 1978; Gavazzi and Trincheri 1989, see also Lilly and Gunn 1985 Figure 3).

3.5 Analysis

The physical nature of the bimodality in the optical-infrared C-M diagram of Abell 370 can be understood by close examination of the objects that are in the two peaks. In the following discussion 'red' and 'blue' objects are those members with $(685 - K)$ colours redder and bluer than the predicted C-M line respectively. In the $K < 17^{m}.0$ sample there are 25 (60%) red and 17 (40%) blue objects according to this definition (10 and 15 in the $K < 16^{m}.5$ sample). Ten of the 'red' objects (CCD# 3, 4, 20, 22, 29, 80, 81, 86, 94 and 105) and nine of the 'blue' ones (CCD# 1, 15, 32, 36, 42, 47, 68, 102, and 107) in the $K < 16^{m}.5$ sample have published spectra (Henry and Lavery 1987; Newberry, Kirshner and Boroson 1988; Soucail *et al.* 1988a). Table 3.4 summarizes the available spectral information. In the 'red' group, 5 objects show clear evidence of recent star formation in the form of intense Balmer lines and/or UV excess (MEC), and for the rest the data are too poor to reach any conclusion. In the 'blue' group, *none* of the objects with spectroscopy available shows any evidence of departures from a normal early-type galaxy spectrum, except for the case of CCD# 102. This galaxy lies superimposed on the giant arc, and may be contaminated by the light from the arc, which is believed to be the gravitationally-lensed image of an intermediate-type spiral galaxy at $z = 0.72$ (Soucail *et al.* 1988b, Aragón-Salamanca and Ellis 1990. See also Chapter 6). The spatial distribution of the galaxies does not seem to be correlated with *red/blue* category, although the area imaged in K only reaches a maximum of 1'.8 ($\sim$0.7 Mpc) away from the cluster center in the North direction, and

Table 3.4. Spectroscopic details for early-type cluster members.

Red objects

CCD#	z (1)	Class.(1)	z (2)	Class.(2)	Comments
3	~0.37	E/S0	0.466	E	z=0.379; E type?; Mg, H + K? (4)
4	~0.37	E/S0	0.373	E	Poor spectrum (2).
20	~0.37	E/S0+uvx	0.372	Sa	z=0.370; Red galaxy, Hδ in absorpt. (3)
22	~0.37	E/S0	0.389	E	—
29	~0.37	E/S0	0.376	E	z=0.375; Red galaxy, Hδ in absorpt. (3)
80	~0.37	E/S0	0.368	Sa	z=0.378 (3).Balmer lines in absorpt.? (2)
81	~0.37	E/S0+uvx	0.370	E	Balmer lines in absorption? (2)
86	~0.37	E/S0+uvx	0.372	Sa	Balmer lines in absorption? (2)
94	~0.37	E/S0	0.382	E	—
105	~0.37	E/S0	0.370	Sb?	Very poor spectrum (2).

Blue objects

CCD#	z (1)	Class.(1)	z (2)	Class.(2)	Comments
1	~0.37	E/S0	0.379	E	z=0.378; E Type, CN_1 (4)
15	~0.37	E/S0	0.383	E	—
32	~0.37	E/S0	0.383	Sa?	Very poor spectrum (2).
36	~0.37	E/S0	0.363	E	—
42	~0.37	E/S0	0.377	Sa/E	z=0.3807; E Type, CN_1, CN_2 (4).
47	~0.37	E/S0	0.378	E	—
68	~0.37	E/S0	0.370	Sa?	Poor spectrum (2).
102	~0.37	E/S0+uvx	0.370	Sb?	Two galaxies superimposed? (2).
107	~0.37	E/S0	0.374	E	z=0.373; E Type, CN_1 (4)
			/0.368		Arc contamination?

Notes:

References as in Table 3.2. See text for definition of 'red' and 'blue' objects.

considerably less in any other direction. The outer parts of the cluster are therefore not well-sampled. However, optical-infrared colour segregation was found in PK photometric sample, which covers a larger area but with smaller depth.

The evidence above suggests that some star-formation activity occurred in the recent past in objects that show *red* optical-infrared colours. Although counter-intuitive at first sight, one explanation of the *red* colours is that they are due to the appearance of red Asymptotic Giant Branch (AGB) stars approximately 10^8 years after a burst of star formation has occurred (Bica, Alloin and Santos 1990, and references therein). The other red phase found by these authors (due to red supergiants) seems to be too short-lived, lasting only from 7 to 10 Myrs, to have a significant statistical effect.

Lilly (1987) argued that galaxies in rich clusters at $z \sim 0.45$ are systematically $0^m.1$ redder in rest-frame $(V-H)$ (which is very close to our observed $685-K$ colour) than local cluster galaxies (Coma). He also interpreted this as an AGB effect, but the conclusions of his work are sensitive to the luminosity evolution correction that he applied, which was based on the evidence found by Lilly and Longair (1984). Our present work is not very sensitive to such evolution because the C-M relation is very flat. In contrast with Lilly, we do not find any evidence for the *average* $(685-K)$ colours of the early-type galaxies in Abell 370 being any different from the colours of present day E/S0s, as the very good agreement between the predicted and observed C-M diagrams shows. However, the bimodality of the observed C-M diagram strongly suggests that a significant fraction of the early type galaxies in Abell 370 are undergoing some colour evolution. A quantitative study of the implications of the AGB evolution on the star formation history of these galaxies is difficult because most evolutionary models for elliptical galaxies usually neglect these late stages of stellar evolution or introduce them without the desired accuracy (Tinsley 1980, Bruzual 1983, Arimoto & Yoshii 1987). However, Wyse (1985) and Chokshi & Wright (1987) have used the theoretical work by Renzini (1981) and Renzini & Buzzoni (1983, 1986) to study

the effect of the late stages of stellar evolution (especially the AGB) on existing galaxy evolution models. Although Frogel, Mould and Blanco (1990) find a deficiency of luminous AGB stars in Magellanic Cloud clusters compared with the theoretical predictions (perhaps due to the effects of mass loss and/or convective overshooting in the late stages of the stellar evolution), the net effect of this result would only be to retard the appearance of the AGB phase (see Figure 15 in Frogel, Mould and Blanco 1990) whilst conserving the order of magnitude of its relative contribution to the integrated bolometric luminosity of the stellar system.

We have used the results of Chokshi & Wright (1987) to model the effect of a burst of star formation on the colours of a normal giant elliptical. We take a galaxy with $M_V^* = -21.77$ ($H_o = 50\,\mathrm{km\,s^{-1}\,Mpc^{-1}}$), $(B-V)_0 = 0.975$ and $(V-H)_0 = 3.10$ (Tamman, Yahil & Sandage 1979, PFA) and superimpose a burst of star formation that transforms 5%, 10% and 20% of the galactic mass into stars. There is no *a priori* information about the timescale and location of the star formation. It could consist of a global burst that affects a substantial fraction of the galaxy or one or several smaller bursts. As the time dependence of the Star Formation Rate (SFR) is unknown, our model is just one of several possibilities. The SFR is assumed to be exponentially decaying with time, with a parameter $\mu = 0.7$ (Bruzual 1983), that corresponds to an e-folding time $\tau = 0.83$ Gyrs. A Miller & Scalo (1979) Initial Mass Function (IMF) was assumed. The rest frame colours of the composite galaxy + burst system are computed as a function of time and then transformed into the observed $(685 - K)$ colour using the same procedure applied in Section 3.3. Figure 3.9(b) shows the expected change in observed colours produced by such a burst (including the AGB contribution) as a function of the time elapsed after the beginning of the burst. For comparison we have computed a similar model that neglects the late stages of stellar evolution (i.e. a standard Bruzual model) and its predictions are shown in Figure 3.9(a).

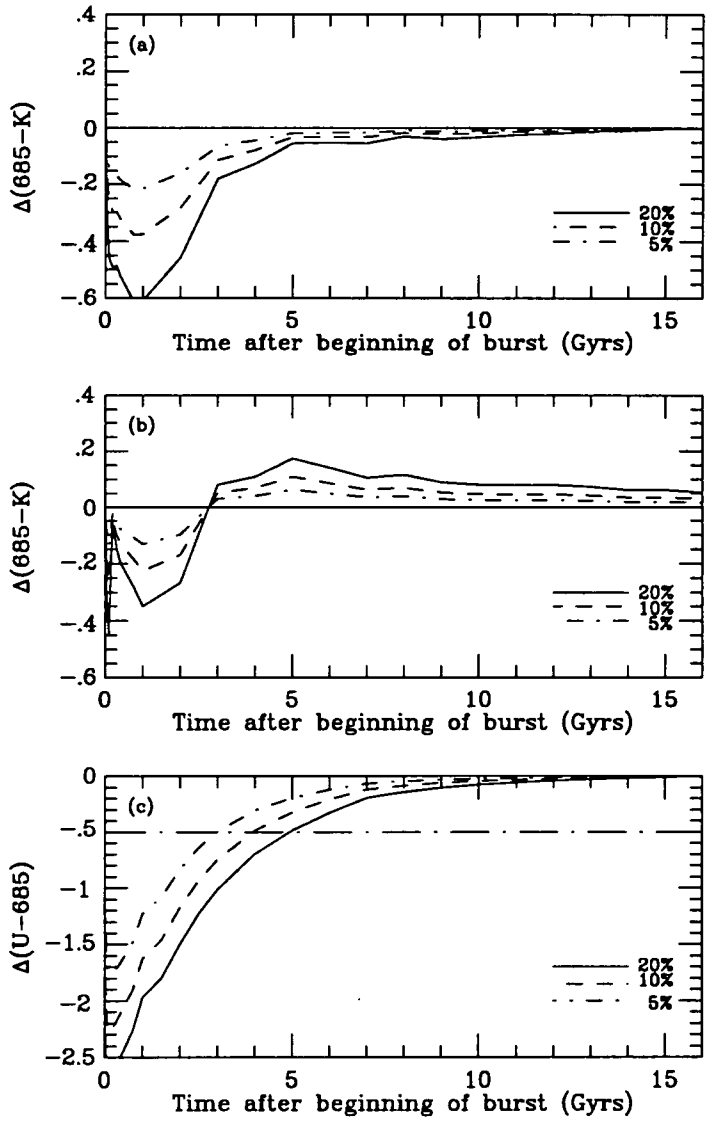

Figure 3.9. Model predictions of the change in the observed $(685 - K)$ colours of a normal giant elliptical at $z = 0.37$ undergoing a burst of star formation that transforms 5, 10 and 20% of its mass into new stars: **(a)** neglecting the late stages of the stellar evolution (i.e. Bruzual 1983 model), and **(b)** taking them into account account (including AGB). **(c)** Same as (a) but for $(U - 685)$. The horizontal dash-dotted line separates the UV excess objects from the normal E/S0s according to the MEC definition.

If we neglect the AGB contribution, the recent star formation produces a blueing of the colours that lasts approximately two e-folding times, decaying into normal galaxy colours afterwards. However, if the AGB is included, the blue phase is shorter and less pronounced, and is followed by a much longer (several e-folding times) period in which the infrared colours are redder than a passively evolving elliptical before the galaxy reverts to its pre-burst colours. The change in the colours is $\sim 0\overset{m}{.}1$ when $\sim$10% of the mass is transformed into stars, i.e. similar to the observed effect. The expected number of galaxies in the *red* category depends on the SFR timescale and on the fraction of the galactic mass that is transformed into new stars, but this result seems to fit into the MEC scheme in which a substantial fraction of the early-type galaxies in clusters at intermediate redshifts undergo bursts of star formation decaying via the post-starburst and UV excess phase to normal E/S0s. The red optical-infrared colours in some of these objects are then a manifestation of the burst population passing through an AGB phase. The very high fraction of members that belong to this category (60%) agrees with the relatively long duration of this phase and implies that a large fraction of the galaxies in the cluster must go through it at some point in their evolution. The fact that the objects that MEC classified as E/S0s with ultraviolet excess belong to both *red* and *blue* groups suggests that, if our interpretation of the red optical-infrared colours is correct, the AGB and the ultraviolet phases overlap partly in time. This is possible if the burst of star formation is not instantaneous but has a timescale comparable to the duration of these phases. As can be seen from Figure 3.9(c), which shows the evolution with time of the observed $(U-685)$ colours of the galaxy + burst model, we predict that $\sim$50% of the galaxies with UV excess should have *red* $(685-K)$ colours, in agreement with the distribution in Figure 3.8. More detailed optical spectra of larger samples of galaxies in Abell 370 will be required to fully explore the extent to which this model can explain the wide variety of activity seen in this cluster.

3.6 Summary and conclusions

This chapter contains a detailed optical-infrared study of the rich cluster of galaxies Abell 370 at $z = 0.37$. The main results and conclusions are:

1. We have constructed a new catalogue of galaxy photometry for 53 galaxies in the rich cluster Abell 370 ($z = 0.37$). The catalogue is limited at $K = 17^{m}.5$ and optical-infrared aperture colours have been determined with the optical CCD photometry of MacLaren *et al.* (1988). Cluster membership has been determined from earlier spectroscopic and spectrophometric work. For the red galaxies of interest in this Chapter, these membership criteria are demonstrated to be very reliable.

2. The optical-infrared colour-luminosity (c-L) relation for galaxies expected to be members of Abell 370 from both spectroscopy and optical colours is closely similar in slope and zero point to that expected on the basis of present-day observations when red-shift corrections are applied. The flatness of the relation and reddening uncertainties makes it hard to place strong limits on luminosity evolution over this interval.

3. Whilst the mean c-L relation suggests no evolution, on closer examination the scatter is found to be larger than the observational errors and appears to be distinctly non-Gaussian. Interestingly, the spectra of those galaxies with colours redder than the mean line (60% of the early-type members) generally show post-starburst type features, whereas those bluer are largely normal early-type galaxies. This suggests some portion of the scatter in the c-L relation *may* represent the effects of recent star formation.

4. We demonstrate, using a simple evolutionary model, that a self-consistent star formation cycle can be constructed whereby an early-type galaxy undergoes a

short-term burst of star formation whose post-burst phase may drive it to the red section of the c-L relation via the contribution of asymptotic giant branch (AGB) stars. The size and duration of the AGB effect is broadly compatible with earlier explanations for the blue bursting population and the ultraviolet-excess ellipticals. However, the predominance of this effect does suggest the bulk of the galaxy population in Abell 370 must have suffered this activity at some time and that it is not restricted to recently-arrived galaxies destined to form the less-substantial S0 population.

4 A DETAILED STUDY OF TWO DISTANT CLUSTERS: 0016+16 AT z = 0.55 AND F1767.10TC AT z = 0.66

4.1 Motivation

In this chapter we will continue detailed studies of galaxy clusters begun in Chapter 3, extending the analysis to higher redshifts. The motivation for this is threefold:

First, we aim to show that obtaining accurate optical-IR photometry of sizeable K-selected samples of galaxies at high redshift is technically feasible using 4-m class telescopes in reasonable amounts of observing time, and that this information is very useful in monitoring evolutionary changes in the red population of galaxies. By selecting galaxies at 2μm we form a sample that is representative of the galaxy population at high redshift, avoiding biases that could arise from optically-selected samples, as demonstrated in Chapter 2.

Second, we plan to use this photometry to constrain the evolution present in the galaxy populations at the relevant redshifts. We choose two clusters (0016+16, and F1767.10TC) for detailed study because information concerning cluster membership and object classification is available from optical studies. External checks of the photometry will also be possible.

Finally, we will use the conclusions of this study to determine a strategy for extending such work to even higher redshifts (Chapter 5) where membership information

is more scarce. We will use the results obtained here to test if the methods applied in Chapter 5 to deal with the field contamination, give answers that are compatible with what we find when membership and object classification information are available.

4.2 The cluster 0016+16 at z = 0.546

This rich cluster was originally discovered by Richard Kron on a Kitt Peak 4.0-m telescope prime focus III-aF plate. It was assigned a redshift of $z = 0.546$ by Spinrad (1980) on the basis of the spectrum of one of the close pair of galaxies with similar magnitudes and colour at the centre of the cluster, but spectroscopy of a somewhat brighter galaxy ~ 40 arcsec SW of this pair gave $z = 0.3$. The cluster was subsequently studied photometrically by Koo (1981) who analyzed six 4-m plates in four passbands, $UJFN$ (see original paper for a definition of the photometric system), and found the cluster to be of BM type II-III, with no dominant central member, and to be about twice as rich as Coma. He described it as having a structure elongated NE-SW with an axial ratio of ~ 0.6, and a core radius of 0.38 Mpc ($H_o = 50\,\mathrm{km\,s^{-1}\,Mpc^{-1}}$, $q_o = 0$). He found that the colour distribution of the reddest galaxies was compatible with $z = 0.546$ and not with $z = 0.30$. He also concluded that there is no significant excess of blue galaxies within a 1.5 Mpc diameter circle, and that most of the cluster galaxies are intrinsically red. Within the limits of Bruzual's (1981) models he estimated that star formation must have ceased in the S0s at least 9 Gyr ago. Spectroscopy from Dressler & Gunn (1991) give an average redshift of $\langle z \rangle = 0.5455$ and a velocity dispersion of $\sigma = 1324\,\mathrm{km\,s^{-1}}$.

The lack of excess blue galaxies in this cluster was confirmed by Butcher & Oemler (1984), showing that it significantly deviates from the trend shown by other clusters at

smaller redshift in which the blue fraction increases systematically with z, suggesting that the Butcher-Oemler effect is not an universal phenomenon.

The cluster was detected in X-rays by White, Silk and Henry (1981). They determined an intrinsic 0.5–4.5 keV luminosity $L_X \approx 3.0 \times 10^{45}\,\mathrm{ergs\,s^{-1}}$ ($H_o = 50\,\mathrm{km\,s^{-1}\,Mpc^{-1}}$, $q_o = 0$). They found its gas to be hot and considerably more luminous than upper limits set for other clusters at these redshifts (Henry *et al.* 1982). Its X-ray structure resembles that seen in the brightest nearby cluster sources. Evidence for a detectable microwave continuum dip has been claimed by Birkinshaw, Gull & Moffet (1981), Birkinshaw & Gull (1984) and Birkinshaw, Gull & Hardebeck (1984). They claim this is produced by inverse Compton scattering of the Microwave Background Radiation by hot gas (Sunyaev-Zel'dovich effect: Sunyaev & Zel'dovich 1972). It has also been studied at radio wavelengths (1440, 4860 and 14940 MHz) by Moffet & Birkinshaw (1989), looking for sources that might contaminate observations of the Sunyaev-Zel'dovich effect. It was found that the cluster appears to possess a faint, central, steep-spectrum, extended source.

Koo (1981) pointed out the existence of a blue star-like object ($B \sim 18$), 3'.25 (4.5 core radii) north of the cluster centre, suspected to be a QSO from its ultraviolet excess. It was detected as an X-ray point source by White, Silk & Henry (1981) using the *Einstein* High Resolution Imager (HRI). Its spectroscopical confirmation as a QSO at $z = 0.553$ by Margon, Downes & Spinrad (1983) suggests that it is probably a cluster or supercluster member. These authors discussed the implications of the presence of a QSO in a rich cluster of galaxies regarding the nature of QSOs and their large scale distribution. The HRI data, combined with the measured redshift, imply a 0.4–4.5 keV luminosity $L_X \approx 8 \times 10^{44}\,\mathrm{ergs\,s^{-1}}$ (Margon, Downes & Chanan 1985).

A detailed study of the cluster has been carried out by Ellis *et al.* (1985) (see also MacLaren 1987), using multiband CCD photometry. They present photometry through

six intermediate-band ($\Delta\lambda/\lambda < 0.1$) filters ranging in wavelength from 418 to 862 nm (Figure 4.6), and used their measurements to reconstruct low-resolution spectral energy distributions (SEDs) for individual objects in the 0016+16 field. Based on these SEDs they classify the galaxies by type and approximate redshift, thereby identifying the members of the cluster. They conclude that the field-subtracted colour distributions are not compatible with a single uniformly red population of early-type members at $z = 0.546$, and they detect a significant intermediate colour component that they consider may be associated with the spectroscopic object at $z = 0.30$. This further reduces the possibility that the $z = 0.546$ cluster exhibits an excess of blue members, adding weight to previous conclusions in this respect. On the basis of their membership determination, they found that the cluster richness is comparable to that of the Coma cluster, arguing that Koo's (1981) richness measurements were overestimated due to contamination from the $z \sim 0.30$ group. A sizeable scatter in the far-ultraviolet colours of optically-red E/S0 members is also noted and attributed either to variable evolutionary corrections for the E/S0s or to enhanced star formation in the discs of what may be spiral precursors of present day S0 galaxies.

After the Ellis *et al.* (1985) study was carried out, some spectroscopy for this cluster become available from Dressler and Gunn (1985, private communication), and a direct comparison between 17 of their photometric redshifts and classifications and the spectroscopic ones was possible (MacLaren 1987). Good agreement was generally found for the objects classified as red members, but some discrepancies occurred for the objects believed to be at $z \sim 0.30$ (what Ellis *et al.* call the 'intermediate population'). Spectroscopy suggests that this component does not come from a single group at $z \sim 0.30$, but from various smaller groups with redshifts $z \sim 0.21$, 0.31, and 0.38. As the number of objects studied spectroscopically is small and does not form a complete sample, those objects could simply represent normal field contamination. Nevertheless, as the spectroscopy reveals a very

high success rate for the photometric classifications and redshifts for cluster members, it justifies the photometric membership for the red objects lacking spectroscopy.

The photometric studies of this cluster were extended to the near-infrared by Lilly (1987), who presented V and I CCD photometry and single-channel photometer K magnitudes for 15 objects believed to be members on the basis of the Ellis *et al.* (1985) work. This, together with similar data for other 4 clusters, allowed him to produce rest-frame $(U-V)$ and $(V-H)$ colours for a sample of cluster galaxies at $\langle z \rangle \sim 0.45$. He found these galaxies systematically 0.12 mag bluer in rest frame $(U-V)$ when compared to present-day E/S0s, as expected from evolutionary models. However, the colours are about 0.1 mag too red in the rest frame $(V-H)$. This systematic reddening was interpreted as the effect of the AGB stars on the colour evolution of the galaxies. Our previous work (see Chapter 3) shows evidence for such effect on the optical-infrared colours of some E/S0s in Abell 370 ($z = 0.37$).

4.2.1 Infrared Photometry

In this work we will extend this photometric study to a considerably larger sample of galaxies by obtaining very deep optical V and I and near-infrared K images. This high precision photometry will enable us to check the previous conclusions on the galaxy population of 0016 + 16 and to test the reliability of our method before extending it to higher redshifts.

The near-infrared K photometry was obtained in three different runs (October 88: R. Ellis & R. Sharples; October 89 and July 90: R. Ellis and the author) using IRCAM I and IRCAM II at the 3.8-m UKIRT, in the 1.″24 pixel configuration. Due to the small field of view of the camera we imaged 5 different positions in the cluster (with some overlap), to increase the number of objects. Table 4.1(a) gives a log of the

Table 4.1(a). Log of 0016+16 K-band observations.

Object	R.A. (1950)	Dec. (1950)	Date	Exposure (s)
0016+16 (Field 1)	$00^h15^m57^s.0$	$+16°09'05''.6$	1988 October 13/14	6000
			1988 October 16/17	3000*
0016+16 (Field 2)	$00^h15^m57^s.0$	$+16°10'14''.2$	1988 October 13/14	3000
			1988 October 15/16	3000*
0016+16 (Field 4)	$00^h15^m57^s.0$	$+16°09'37''.0$	1989 October 3/4	4000
0016+16 (Field NE)	$00^h16^m01^s.4$	$+16°10'14''.0$	1990 July 20/21	1600
0016+16 (Field NW)	$00^h15^m54^s.2$	$+16°09'38''.5$	1990 July 21/22	1440
0016+16 (Field SE)	$00^h16^m03^s.0$	$+16°09'10''.0$	1990 July 22/23	1440

* non-photometric.

Table 4.1(b). Log of 0016+16 optical observations.

Band	Date	Seeing	Exposure (s)
V	21/22 July 1990	$\sim 0''.9$	11 × 1000
I	23/24 July 1990	$\sim 1''.1$	10 × 1000

Telescope:	4.2-m WHT (La Palma)
Instrument:	Taurus-II (f/4)
Detector:	GEC-EEV (770 × 1152 pixels)
Pixel size:	$0''.27\,\mathrm{pixel}^{-1}$

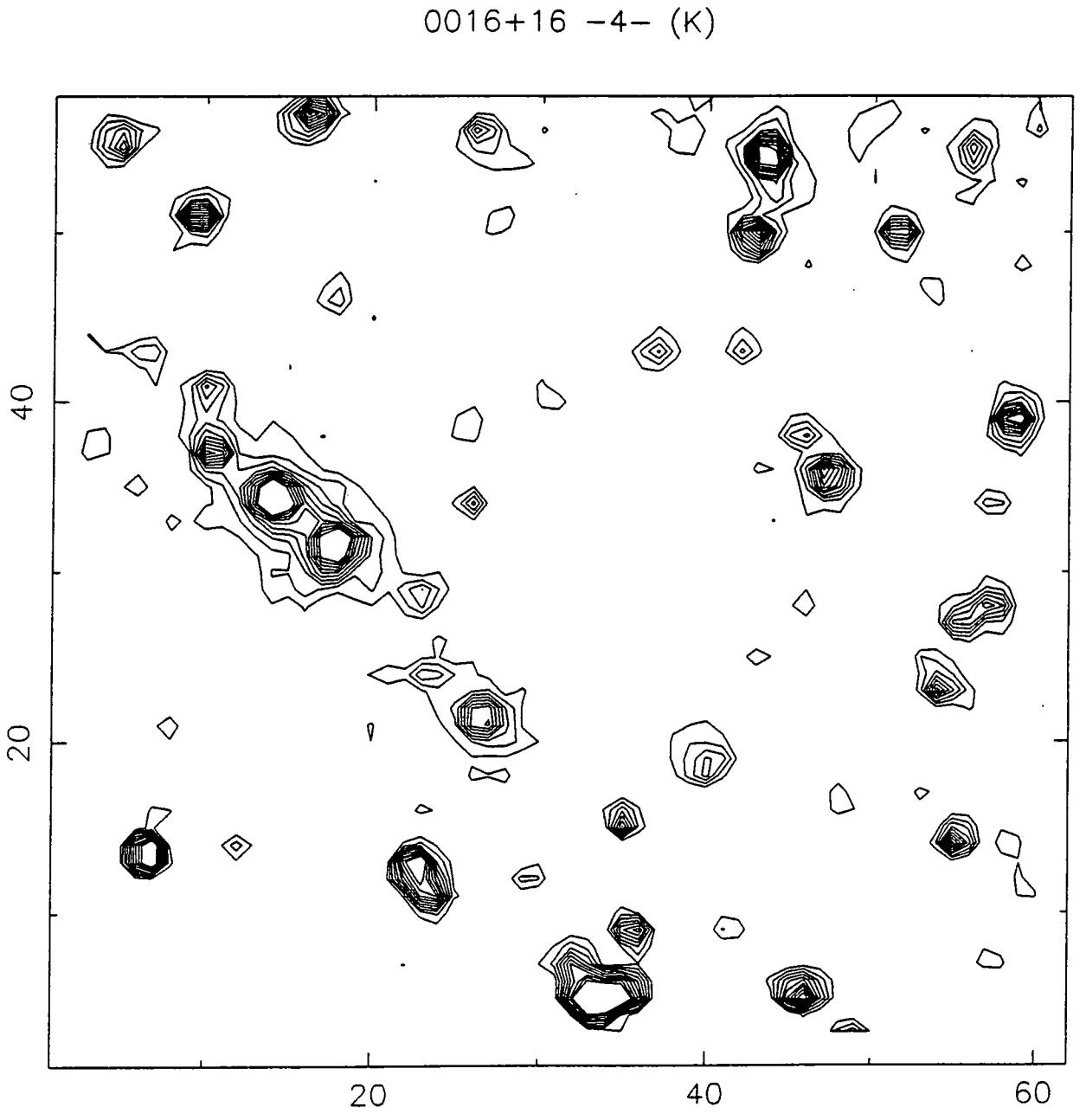

Figure 4.1. Contour plot of the 0016+16 K band image (Field 4). The scale is $1\farcs24$ pixel^{-1}. The numbers on the axes are pixels. North is up and East is left. The contours follow a linear intensity scale, the lowest corresponding to $\mu_K = 21\fm35$ arcsec^{-2} (2σ above average sky level) and the highest to $\mu_K = 18\fm85$ arcsec^{-2} (20σ).

observations. We followed the observational techniques and data reduction procedures described in Chapter 2. Figure 4.1 shows a contour plot of the K band image of the centre of the cluster.

Zero-points were measured from frequent observations of standard stars from the list of Elias *et al.* (1982), reduced as described in Chapter 2. The r.m.s. for the residuals of the magnitudes of the standards was in the range of $0^m.02$–$0^m.03$. Some of the data was collected in non-photometric conditions, but we used the observations in photometric nights to obtain absolute photometric calibrations for all the images. Zero-points for different nights and runs could be compared using objects in common, yielding agreement to better than $\sim 0^m.02$.

The images of the four areas taken on and after October 89 are of higher quality than the ones taken before for various reasons. First, UKIRT staff carried out significant improvements in the optical performance of the telescope and the cameras, which has substantially increased the image quality, producing a much better signal-to-noise; and second, our understanding of the camera, especially the flat-fielding problems, also improved with time, and we were able to optimize exposure times for the images and the frequency of observation of the sky. Some reduction of the read-out noise also happened just before the July 90 run. An indication of the quality of the frames is the degree of flatness achieved for the sky and the image quality (measured as the FWHM of the images of unresolved objects). The images labeled 'Field 4', 'SE', 'NE' and 'NW' are flat to $\frac{\sigma_{sky}}{sky} \sim 10^{-4}$ (1σ detection limit of $\mu_K \simeq 22^m.1\,\mathrm{arcsec}^{-2}$), and their image FWHM is $\sim 1''.6$–$1''.7$. We estimate that they have comparable quality, as we will see on the errors of the photometry, although 'Field 4' is a bit deeper. Fields 1 and 2 are of somewhat poorer quality, but their effect on the photometry will be small since only four objects in the sample were not imaged afterwards.

Photometry was derived using a 4.″8 diameter aperture. This size was chosen as a compromise to get reliable colours for the galaxies with minimum contamination from the neighbours in crowded areas and the minimum acceptable diameter given the pixel size and the image quality. The sky was estimated locally from the mode inside similar apertures in carefully-chosen blank areas close to each object.

Random errors for the photometry were calculated as described in Chapter 2 (see Figure 2.5). For most of the objects we have more than one independent measurement, and the final K value is computed as the average weighted according to the inverse of the variance, combining the individual errors to get the error on the mean in the usual way (see, *e.g.*, Bevington 1969).

We will restrict our sample to those objects with photometric uncertainties smaller than $0^m.2$ (5σ detections), *i.e.*, $K < 18^m.2$ except for the few cases in which photometry comes only from Fields '1' and '2'.

Near infrared photometry for some of the objects in the 0016+16 field has been published by Ellis & Allen (1983) and Lilly (1987), and this provides a valuable external check of our photometry. Ellis & Allen (1983) measured K magnitudes for two objects (#2 and #62) using a 7.″0-diameter aperture using the 3.9-m AAT, and Lilly (1987) used UKIRT to obtain K magnitudes for 15 objects inside 7.″6-diameter aperture of which 12 were imaged by us. To make a direct comparison, we re-measured the relevant objects using apertures of the same size as these authors. We agree (within the quoted errors) with one of the objects (#62) measured by Ellis & Allen (1983), but we find object #2 $0^m.14$ brighter. However, our measurement for this object agrees with Lilly's.

The comparison with the objects in common with Lilly (1987) is shown in Figure 4.3. The r.m.s. scatter is $0^m.21$ including all the objects, and the difference in zero point ($0^m.07 \pm 0^m.06$) is not significant. The average error of our measurements is $0^m.09$, and

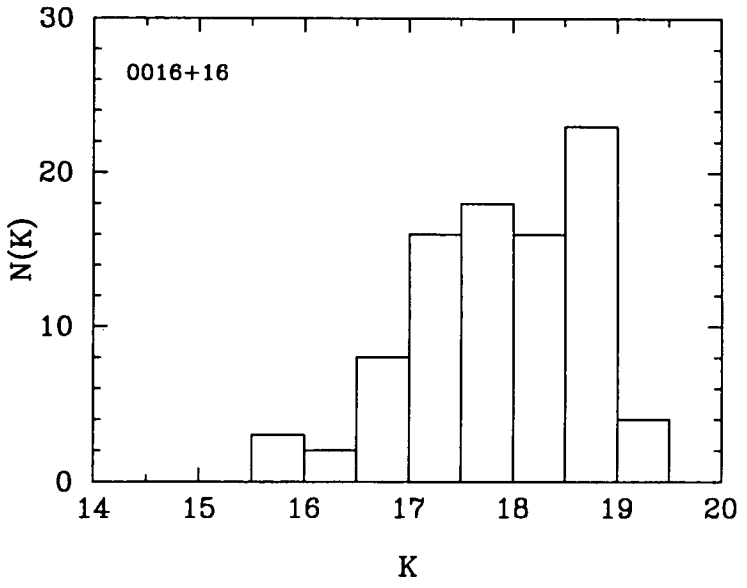

Figure 4.2. Histogram of the measured K magnitudes in the 0016+16 field.

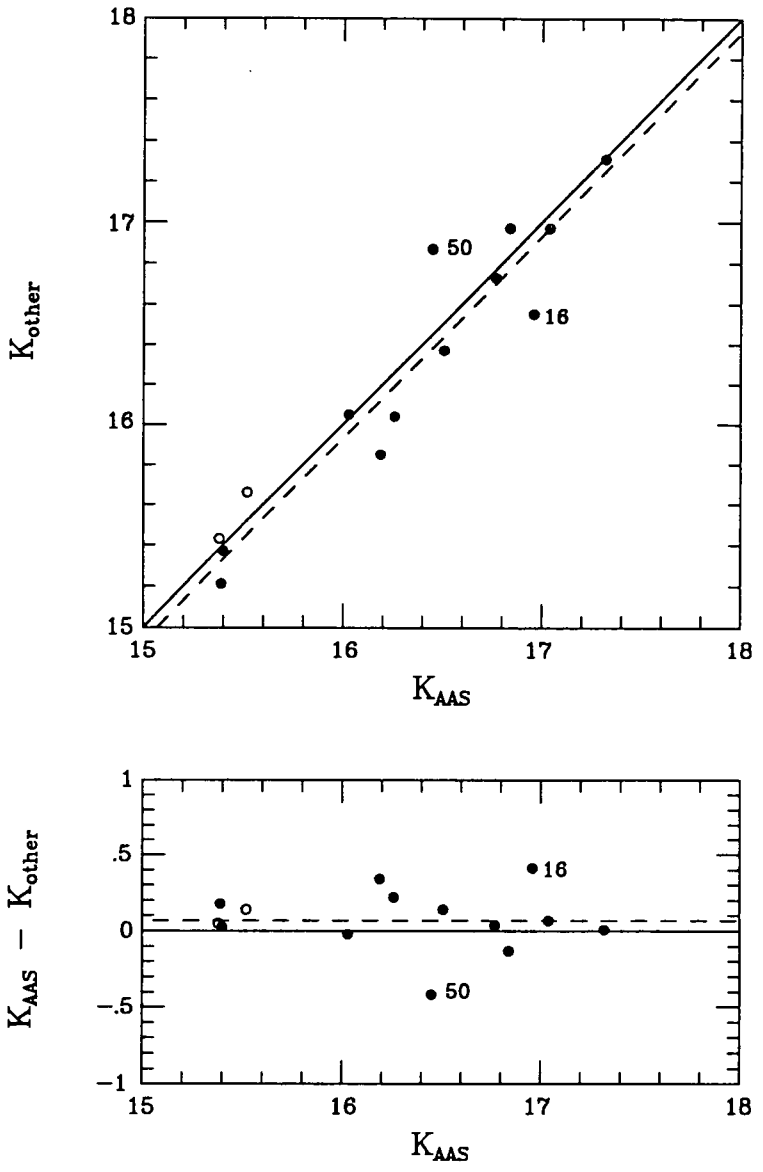

Figure 4.3. Comparison of Ellis & Allen (1983) —open circles— and Lilly (1987) —filled circles— K magnitudes with the ones measured in our images in a 7.″6-diameter aperture for the 0016+16 objects in common. The solid line represents the 1 to 1 relationship, and the dashed line shows the formal zero-point offset $\langle K_{AAS} - K_{Lilly} \rangle = 0^m.07$. The two most discrepant objects (#50 and #16) have been labeled.

Lilly claims that his uncertainty is only $0^m.07$, so the scatter is larger than expected. Two objects show significant discrepancies: #50 and #16. We will see that object #50 largely disagrees also in the optical, so we are confident that it is a misidentification. Ignoring these objects, the r.m.s. scatter reduces to $0^m.13$, closer to what we can expect. Given the nature of Lilly's photometry (obtained with a single channel photometer in a crowded field and using a fairly large aperture) pointing errors can be crucial, and contamination from close objects in the object aperture or in the reference beam can be very important (consider, for instance, objects #1, 6, 66 and 3 for which the discrepancy is larger than the quoted errors, but which have objects nearby).

It is difficult to believe that the errors in our photometry are larger than Lilly's, because the problems mentioned above are lessened when working with an imaging detector and the tests on the repeatability of our results seem conclusive. We believe that our random errors are well understood. In any case it is clear that such a large aperture as $7''.6$ diameter will introduce contamination from close objects in a field as crowded as that, and the colours inside our aperture are more reliable. Regardless, we find an excellent agreement between both sets of photometry, considering that they have been obtained using very different instruments and techniques.

4.2.2 Optical photometry

The optical data were gathered at the 4.2-m WHT (La Palma) by I. Smail, M. Fitchett and D. Carter in July 1990 as part of a very deep imaging survey of intermediate and high redshift clusters to look for faint gravitationally distorted images of background galaxies (Smail *et al.* 1991, *in preparation*). The details of the optical observations are presented in Table 4.1(b). The *in-field* chopping technique (Tyson & Seitzer 1988, and references

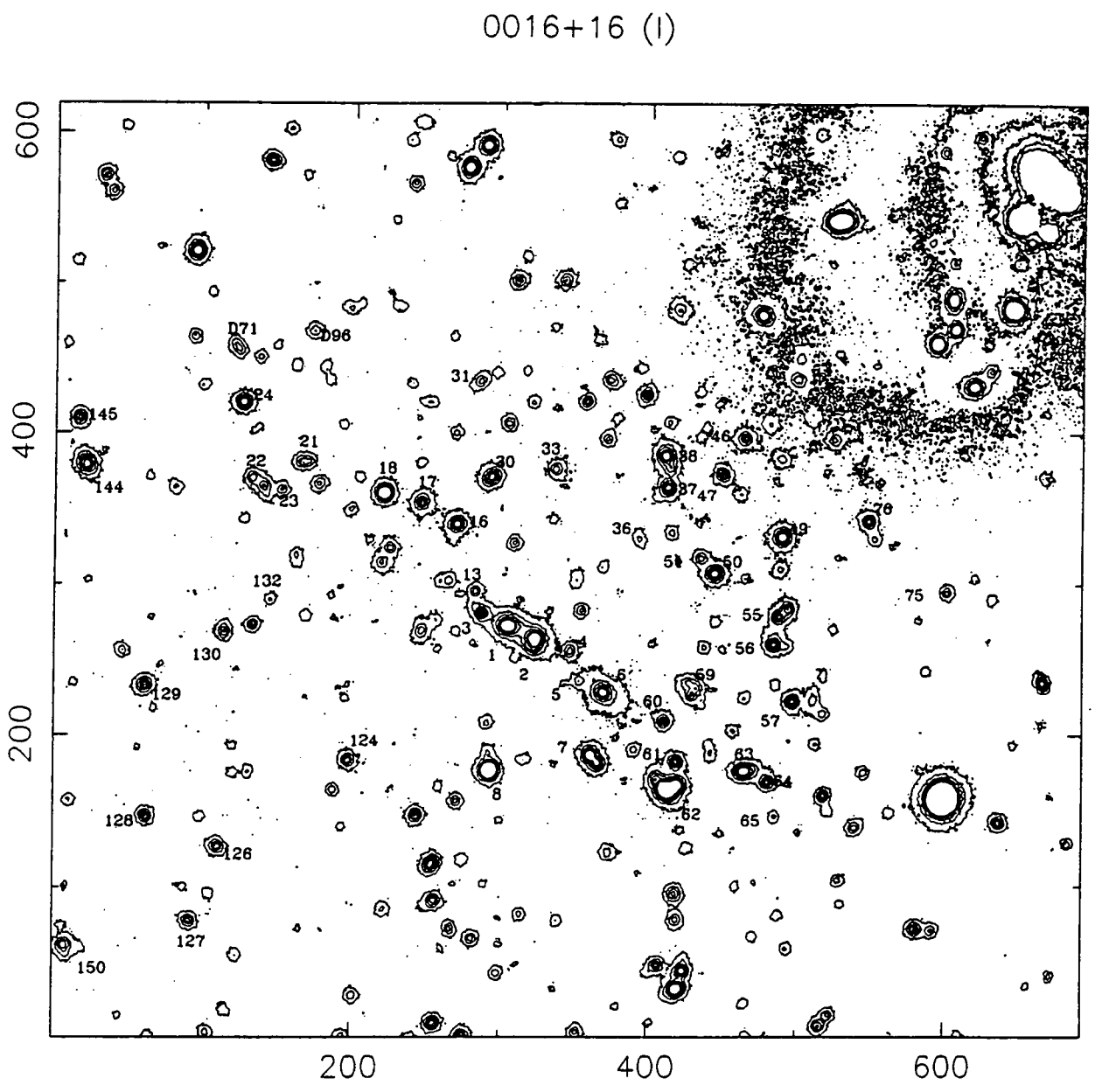

Figure 4.4. Contour plot of the central area of the 0016+16 I band image. The scale is $0\farcs27$ pixel^{-1}. The numbers on the axes are pixels. North is up and East is left (approximately). The contours follow a linear intensity scale, the lowest corresponding to $\mu_I = 24\fm84$ arcsec^{-2} (3σ above average sky level) and the highest to $\mu_I = 20\fm03$ arcsec^{-2}. See text for numbering scheme.

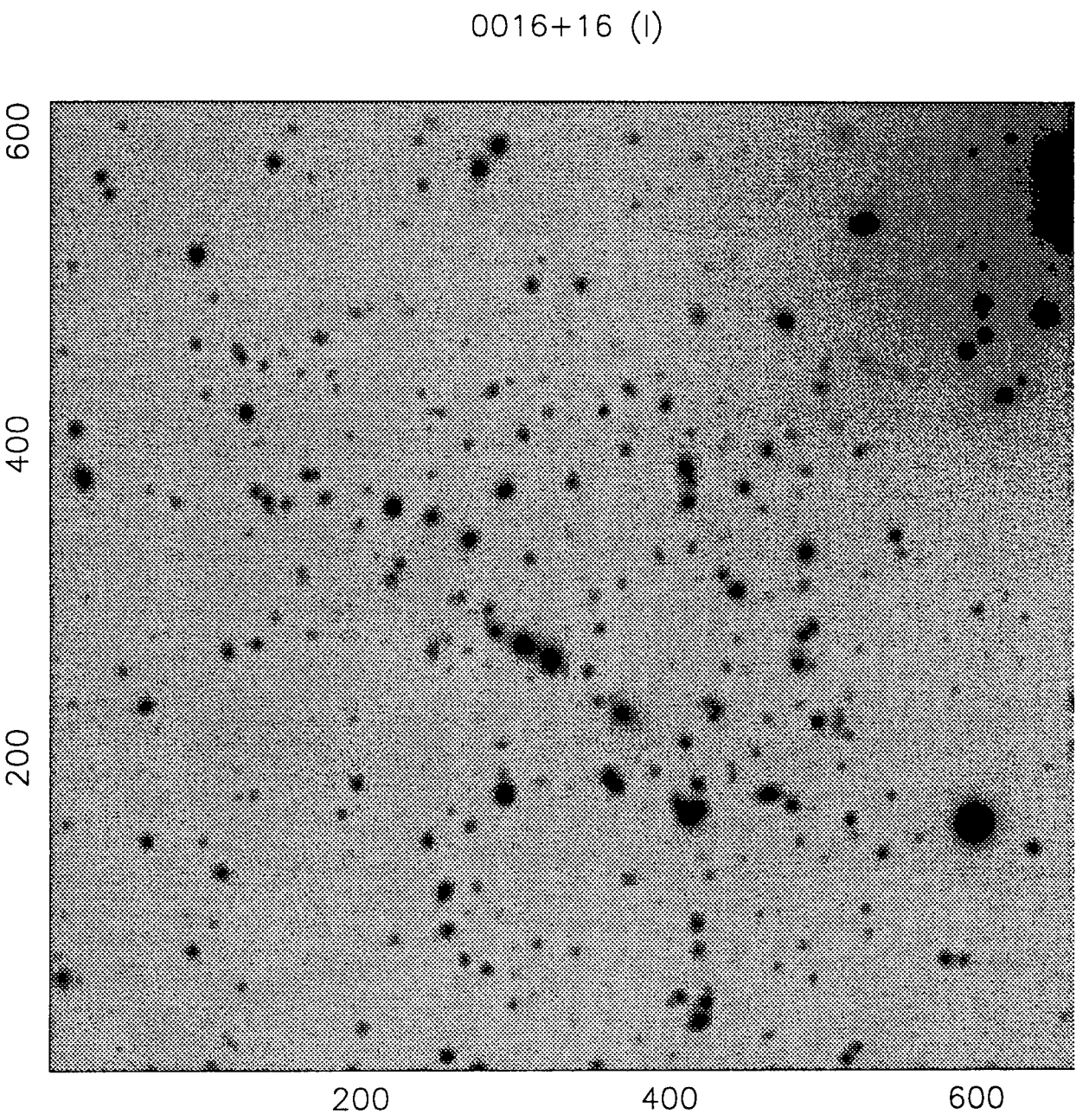

Figure 4.5. Grey-scale picture of the same image shown in Figure 4.4.

therein) was used, and the de-registered individual images were combined by median-filtering (after bias-subtraction and normalization) to obtain a *super-flat* that was used to flat-field each image. The flat-fielded images were registered and put to a common sky level additively, and a final image obtained by median filtering of them. This procedure naturally eliminates all cosmic-ray events and bad pixels, and yields images whose sky fluctuations are smaller than 0.3% in V and 0.2% in I, corresponding to surface brightness detection limits of $\mu_V = 27\overset{m}{.}3\,\mathrm{arcsec}^{-2}$ and $\mu_I = 26\overset{m}{.}1\,\mathrm{arcsec}^{-2}(1\sigma)$. The optical images were kindly processed by I. Smail.

Landolt (1983) standards were also observed during the nights at different air masses and used for zero-pointing purposes. They were defocused to avoid saturation. The frames were individually calibrated, and 11 bright but unsaturated objects were used to obtain a zero-point for the combined final frames. An accuracy of $\lesssim 0\overset{m}{.}02$ is estimated for the final zero-points from the residuals of the measured magnitudes for the standards and the variations from frame to frame. Independent checks of the zero-points were provided by a 600 s V exposure taken at the WHT in service time during the night of 11/12 September 1990, and a 1500 s I integration taken at the 1-m JKT during the night of 12/13 June 1991 by J. Lucey and D. Carter, confirming the zero-points within the errors.

The filters used were the ones available with Taurus II at WHT (Kitt Peak filters, see Unger *et al.* 1988). The V filter + CCD response is close to the standard system of Landolt (1983), and has very small colour terms. For the average colour of our target galaxies, the colour-term correction to the V magnitudes is $\sim 0\overset{m}{.}02$, and almost constant given the narrow range in colours. The I filter has a response similar to I_{KC} (Cousins 1976), but it has a significant colour term. The correction to put our I photometry in the I_{KC} system is $\approx 0\overset{m}{.}15$. This should be taken into account when comparing our magnitudes and colours with the ones obtained elsewhere. In the following analysis we will use the

filter + CCD responses directly, automatically taking such details into account (Benn & Nicholson 1988).

Photometry was obtained on the final V and I images using a 4.″8 diameter circular aperture centered on each object, and a local sky estimated as before. The internal random errors of the photometry can be estimated from the standard deviation of the values obtained for different images. We used several frames in V and I and measured the magnitude for objects of different brightness, and estimated σ for each object following the prescription of Keeping (1962) for small number statistics. The adopted errors are then $\sigma/\sqrt{n}$ ($n = 11$ for V and $n = 10$ for I). We note that this procedure overestimates the random errors for two reasons. Firstly, the residual flat-fielding errors are reduced significantly by the median, because the image of a galaxy will be sampled by different pixels in each frame. Secondly, cosmic-ray events affecting some objects in individual frames are eliminated. The random errors estimated above are therefore conservative, giving $1\sigma \lesssim 0^{m}.10$ for $V < 24^{m}.0$ and $I < 22^{m}.5$. Therefore, the errors in the optical-IR colours are dominated by the errors in K.

As before, we can use Lilly's (1987) V and I photometry as an external check of our data. He used a much larger aperture (7.″6 diameter) to match his infrared observations, and we proceeded to measure the magnitudes in our images using his aperture and the same way of estimating the sky (from the mode inside an annulus of internal radius 3.″8 and external radius 13.″0 around the objects) as he did. Object #50 is very discrepant (by almost 1 mag) as in the K case, confirming that it is probably a misidentification. For the rest of the sample in common (14 objects), we obtain an r.m.s. scatter of $0^{m}.22$ in V and $0^{m}.21$ in I. This is very large, since our average error in this magnitude range is $0^{m}.05$, and Lilly claims that his uncertainty is $\sim 0^{m}.07$. This indicates that either Lilly or we (or both) have seriously underestimated the errors. We expect our photometry to be much better because of the longer exposure times (11,000 sec in V and 10,000 sec in I versus

$\sim$2,400 and $\sim$1,800 respectively), and larger aperture (4.2-m versus a 2.2-m). Further justification is provided by our tight internal errors.

A direct comparison with Ellis *et al.* (1985) CCD photometry is not possible because they used an intermediate-band system and none of the filters matches V nor I (see Figure 4.6). But V lies comfortably between their 507 and 578 nm bands, and I is between 748 and 862. We plotted V vs. $\frac{502+578}{2}$ for objects with $V < 23^m.0$ and the correlation appeared to be excellent, with an r.m.s. scatter of only $0^m.14$, and the residuals show no trend with magnitude or (578 – 502) colour (Figure 4.7 (a, b, c)). The scatter now is significantly smaller than when comparing with Lilly's photometry for the same range of object brightnesses, and more compatible with our average errors and those of Ellis and his colleagues ($\sim$10%).

Proceeding the same way with I we plotted it against $\frac{748+862}{2}$ for $I < 20.6$, and the scatter is now $0^m.15$, and again no trend with magnitude or (862 – 748) colour is apparent (Figure 4.7 (d, e, f)). This compares very favourably with results obtained using Lilly's data, and close to what we can expect from the estimated errors. As the correlations of V vs. $\frac{502+578}{2}$, and I vs. $\frac{748+862}{2}$ can not be perfect, they must be responsible for some of the scatter, adding more confidence to our estimated random errors.

To be completely sure that everything has been taken into account, we repeated the measurements using two different software packages: PHOTOM (part of the STARLINK standard software) and IRAF. An excellent agreement (to a few millimags) was found. All these tests reveal that our optical photometry has a very high degree of reliability, and confirm our estimate of the internal errors.

All the objects detected with $K < 18^m.2$ have been detected in V and I, (except #151, that was outside the I frame) so we have essentially a K-selected complete sample. The high quality of the optical data means that the errors in the colours will be dominated

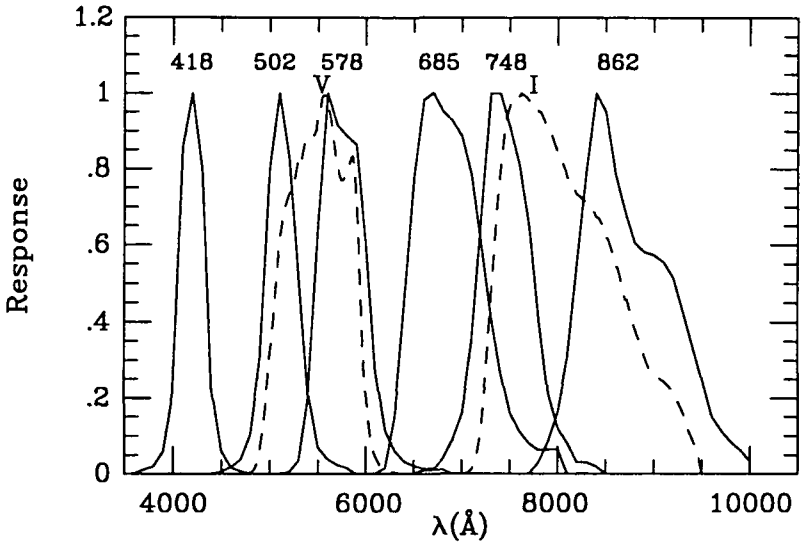

Figure 4.6. Bandpases for the intermediate-band filters used by Ellis *et al.* (1985) (solid lines) compared with our V and I (dashed lines).

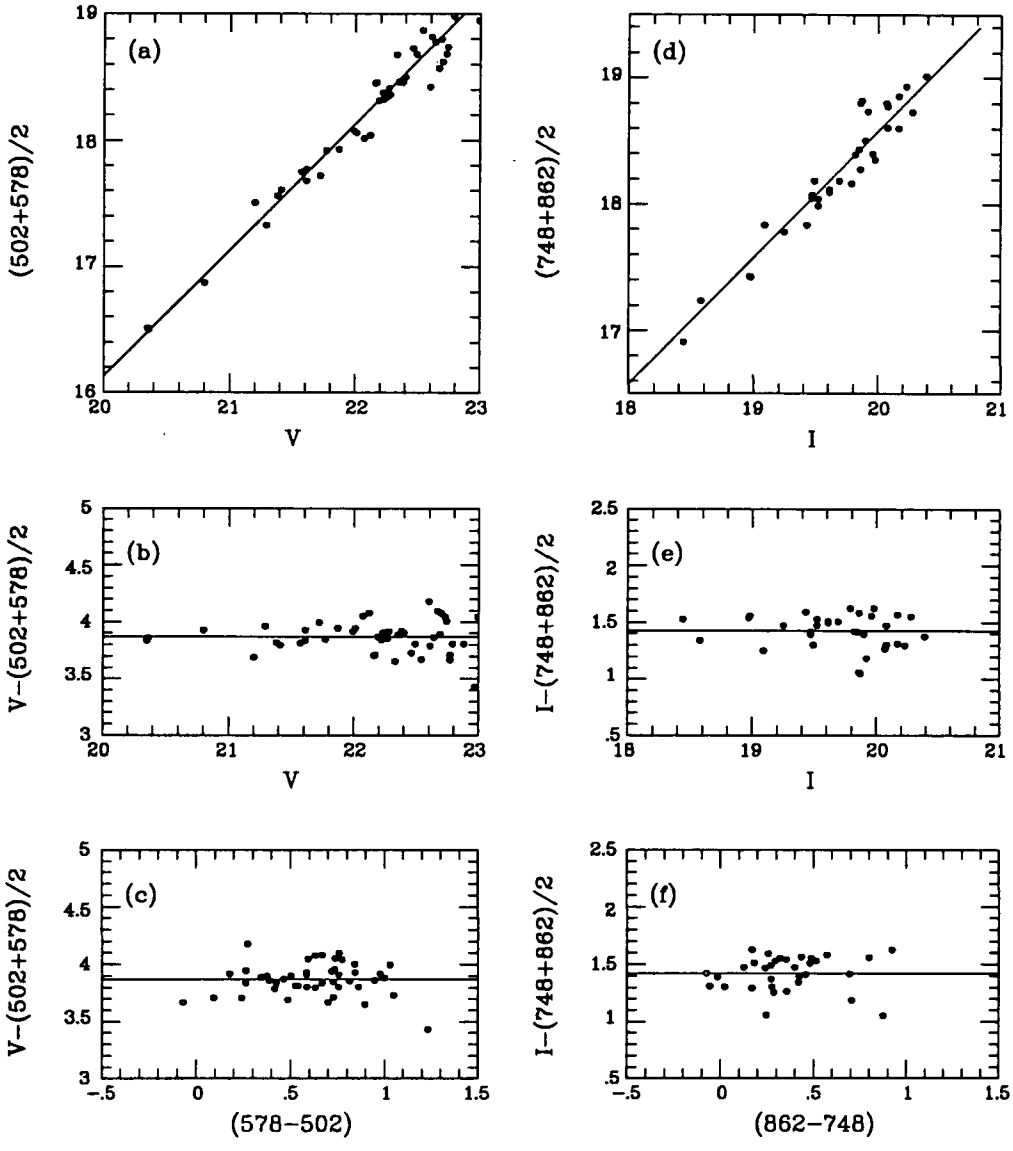

Figure 4.7. **(a)** Comparison of our V magnitudes with $\frac{502+578}{2}$ from Ellis *et al.* (1985) in a 4.″8-diameter aperture for the 0016+16 objects in common. The solid line has unit slope. The r.m.s. scatter around this line is $0^m.14$. **(b)** Same data as in (a) but plotting the differences between both sets of data as a function of V. **(c)** As before but as a function of the (578 − 502) colour. The solid lines in (b) and (c) represent the average offset $\langle V - \frac{502+578}{2} \rangle = 3^m.870$. **(d)** Same as (a) but for I vs. $\frac{748+862}{2}$. The r.m.s. scatter is now $0^m.15$. **(e)** Same as (b) for I. **(f)** As before but as a function of the (862 − 748) colour. The solid lines in (e) and (f) represent the average offset $\langle I - \frac{748+862}{2} \rangle = 1^m.424$.

Table 4.2. 0016+16 Photometric Catalogue.

#	K	σ_K	$(V-I)$	$(V-K)$	$(I-K)$	$\sim z^{\dagger}$	Class†	Spectroscopy‡
62	15.54	0.02	1.91	4.81	2.90	0.3	E/S0	0.301
2	15.90	0.03	2.44	5.51	3.07	0.55	E/S0	0.543 Early
1	15.92	0.03	2.40	5.46	3.06	0.55	E/S0	0.532 Early
7	16.29	0.03	2.76	5.72	2.96	0.55	E/S0	0.540
38	16.47	0.03	2.28	5.30	3.02	0.3–0.4	Sab	0.654
8	16.59	0.05	1.93	3.72	1.79	—	—	0.000 K star
6	16.62	0.05	2.56	5.37	2.81	0.6–0.7	E/S0	0.539 Poor s/n
63	16.73	0.05	1.82	4.56	2.74	0.4–0.6	Scd	0.546 [OII]
144	16.74	0.06	2.09	4.87	2.78	0.3	Sab	0.560 PSG
49	16.77	0.05	2.51	5.35	2.84	0.3	E/S0	—
3	16.80	0.07	2.37	5.53	3.16	0.55	Sab	0.541 Early
50	16.81	0.04	2.54	5.42	2.88	0.55	E/S0	0.547 Early
18	16.86	0.06	2.98	5.21	2.23	0.6	E/S0	0.000 M star
16	17.01	0.05	2.58	5.39	2.81	0.55	E/S0	—
24	17.01	0.07	2.69	5.53	2.84	0.55	E/S0	—
37	17.03	0.05	2.40	5.24	2.84	0.45–0.6	E/S0	0.537 Poor s/n
55	17.12	0.05	2.59	5.37	2.78	0.55	E/S0	—
56	17.23	0.06	1.71	4.34	2.63	0.1–0.2	Sab	0.398 Early
30	17.25	0.19	2.43	4.97	2.54	0.55	E/S0	—
61	17.28	0.08	2.39	5.18	2.79	0.45–0.55	E/S0	—
22	17.31	0.09	2.38	5.46	3.08	0.45–0.55	E/S0	—
129	17.33	0.14	2.52	5.36	2.84	0.6	E/S0	—
59	17.34	0.06	1.95	4.53	2.58	0.2–0.3	Sab	0.209
151	17.35	0.13	—	5.79	—	—	—	—
126	17.35	0.10	2.16	5.35	3.19	0.3	E/S0	—
31	17.37	0.18	2.39	5.90	3.51	—	—	—
145	17.37	0.09	2.51	5.42	2.91	—	—	—
57	17.40	0.07	2.65	5.33	2.68	0.55	Sab	—
17	17.40	0.06	2.57	5.34	2.77	0.3/0.6	Sab/Scd	—
124	17.50	0.13	2.37	5.49	3.12	—	—	—
21	17.55	0.11	2.12	5.06	2.94	0.5–0.55	Sbc	—
47	17.57	0.08	2.58	5.48	2.90	—	—	—
150	17.60	0.15	1.53	4.01	2.48	0.2–0.3	Scd	—
13	17.63	0.08	2.50	5.64	3.14	—	—	—
64	17.65	0.24	1.94	4.52	2.58	0.3	E/S0	0.556 PSG
33	17.69	0.11	2.49	5.57	3.08	—	—	—

Table 4.2. *continued.*

#	K	σ_K	$(V-I)$	$(V-K)$	$(I-K)$	$\sim z^{\dagger}$	Class†	Spectroscopy‡
46	17.73	0.11	2.54	5.39	2.85	—	—	0.548 Early
128	17.74	0.14	2.31	5.14	2.83	—	—	—
D71	17.76	0.15	2.30	5.15	2.85	—	—	—
4	17.81	0.15	1.63	4.54	2.91	>0.45	Sdm	0.658 [OII]
60	17.83	0.09	2.59	5.34	2.75	—	—	—
132	17.87	0.15	2.53	6.80	4.27	—	—	—
36	17.87	0.10	1.60	5.25	3.65	—	—	—
127	17.91	0.12	2.43	5.21	2.78	—	—	—
5	17.92	0.14	2.17	5.17	3.00	—	—	—
51	17.93	0.12	2.43	5.24	2.81	—	—	—
65	17.99	0.26	2.38	6.29	3.91	—	—	—
D96	18.11	0.14	1.83	4.76	2.93	—	—	—
23	18.13	0.19	2.47	5.37	2.90	—	—	—
76*	18.13	0.15	3.05	5.21	2.16	—	—	—
75	18.14	0.19	2.29	5.22	2.93	—	—	—
130	18.21	0.17	1.89	4.39	2.50	0.3	E/S0	—

Notes:

† From Ellis *et al.* (1985): SED 'redshift'.

‡ From Dressler & Gunn (1985, private communication): spectroscopic redshift.

E/S0: Normal elliptical.

Sab, Sbc, Scd, Sdm: Spirals.

PSG: Post-starburst galaxy (*i.e.* early-type SED with strong Balmer lines)

* Classified as a star from its colours and optical images.

by the errors in K. Table 4.2 contains the final adopted values for the photometry with the estimated uncertainties given as 1σ errors. The numbering scheme (see Figure 4.4) follows mainly that of Ellis *et al.* (1985), except for a few objects that were not detected in their original data. For those we will use the identifications of Dressler and Gunn (1985, private communication), labeling them with a 'D' to distinguish them. The Table also gives the photometric redshifts and classification from Ellis *et al.* (1985) (columns 7 and 8) and the available spectroscopic information from Dressler & Gunn (column 9).

4.2.3 The Colour-Magnitude diagrams

In Table 4.2 we present data for 52 objects in the imaged 0016+16 field to a limit of $K < 18\overset{m}{.}2$. This is $0\overset{m}{.}7$ deeper than the sample for Abell 370 (Chapter 3), with similar photometric errors. The difference in distance modulus for those two clusters should be $\sim 0\overset{m}{.}7$–$0\overset{m}{.}9$ (depending on q_o), so the samples for both clusters are clearly comparable.

Membership and spectral classification is available for 32 objects (62%). Since the agreement between the spectroscopic and the photometric redshifts and classification is good for the red members (see Ellis *et al.* 1985, and MacLaren 1987 for a detailed comparison), our membership information should be reliable. In the few cases in which there is discrepancy, the spectroscopic redshift is adopted. We find 19 members, 9 foreground galaxies,* 2 background galaxies, and 2 stars. For the remaining 20 objects, there is no membership information available, since our K-selected sample reaches deeper than Ellis *et al.* (1985) photometric sample and Dressler & Gunn spectroscopic sample. One of the objects without membership information (#76) has a comparatively blue $(I - K)$, and this colour is a good discriminator for stars. Its VIK colours are compatible with those of

* The classification for object #17 is ambiguous because of the lack of data in one of the Ellis *et al.* bands. We have counted it as foreground. It could also be a background object (see Table 4.2) but is excluded as a member.

M-giants (*e.g.*, #17; see Chapter 5 for a detailed discussion on this topic), but not with the ones expected from normal galaxies at any z. This, together with its star-like appearance in the optical images (taken under good seeing) gives enough evidence to classify it as a star, and we ignore it in the rest of the discussion. We will keep the remaining 19 objects in the sample, expecting some contamination from non cluster members.

Using the available photometry, we can produce colour-magnitude (C-M) diagrams for our K selected sample, and compare them to what we can expect from nearby objects. We will present the data as observed, to avoid degrading them with uncertain corrections. We have tried to predict the *observed* photometry, *i.e.*, the position of nearby early-type galaxies on these observed C-M diagrams once the redshift and aperture corrections have been taken into account, mimicking the observing conditions as accurately as possible. We will refer to that as the *no-evolution prediction,* which we describe first.

We have used two sets of local photometry: the data published by Person, Frogel & Aaronson 1979 (hereafter PFA) for field and Coma ellipticals, and the photometry presented by Bower (1990) and Bower, Lucey & Ellis (1991, BLE hereafter), together with unpublished H magnitudes for Coma (we are indebted these authors for providing the data before publication, and for the filter response of their U system). The Coma data from PFA lacks U magnitudes, so we will not use it to predict the observed V.

We have followed the same procedure used for Abell 370. The observed V and I bands correspond closely to rest-frame U and V respectively at this redshift, and computed the additive constants by convolving the appropriate response curves with different galaxy type SEDs (see Chapter 3). The variation in the transformations from one SED to another is very small ($\lesssim 0\overset{m}{.}02$) so using the same one for all the objects is sufficient for our purposes.

In the infrared, the observed K band shifts to a rest-frame $\lambda_{eff} \sim 1430$ nm, that lies between the rest-frame J and H ones. We can compute a linear transformation between

the observed K at $z = 0.55$ and the rest-frame J as a function of rest-frame $(J-H)$, using again the appropriate filter responses and different infrared SEDs. We used the same SEDs described in Chapter 2, with the addition of ones presented in Yoshii & Takahara (1988), kindly provided by Dr. Yoshii in a machine-readable form. As in Chapter 2, we transformed PFA photometry (CIT system) into the UKIRT (AAO) system.

Table 4.3 presents the transformation equations, together with the estimated internal uncertainties. The predictions of $K_{0.55}$ is less straightforward, but the fact that very different SEDs produce consistent answers (with a very small formal error), gives weight to its reliability. Note that different equations are used for PFA and BLE data, because the photometric systems are not the same.

These equations are used to predict redshifted magnitudes and colours of the galaxies in both samples with aperture effects taken into account using the V growth curve of Sandage & Visvanathan (1978) and a mean $(U-V)$ gradient of $\Delta(U-V)/\Delta\log[A/D(0)] = -0.15$ (Sandage & Visvanathan 1978, Peletier *et al.* 1990). The local data are converted to an aperture equivalent to the observed 4″.8-diameter. This corresponds to a projected linear size of 35 kpc ($H_o = 50\,\mathrm{km\,s^{-1}\,Mpc^{-1}}$, $q_o = 0.5$). The choice of q_o has negligible effect on the prediction of the colours to the required accuracy.

Systematic errors on the transformation are more difficult to estimate, and can arise from inaccuracies in the filter response functions and inappropriate SEDs. The first problem (poor knowledge of the filter response) should be less severe for BLE data, because we know exactly the system used and good response curves are available (Benn & Nicholson 1988; "UKIRT Observer's Manual", U.K. Infrared Telescope Support Unit 1989, 1991). The use of inappropriate SEDs could however be more important when computing K-corrections, but not so much in our case because we do not predict an observed magnitude M_z from a rest-frame M_0, but from a rest-frame M_0' whose effective wavelength lies very

Table 4.3 No-evolution prediction for $z = 0.55$

— Transformations for PFA photometry (after converting to UKIRT system):

$$U_0 - V_{0.55} = -0.47 \pm 0.02 \tag{4.1}$$

$$V_0 - I_{0.55} = 0.78 \pm 0.02 \tag{4.2}$$

$$J_0 - K_{0.55} = 1.265 + 0.491(J - H)_0 \quad (r.m.s = 0.02) \tag{4.3}$$

— Transformations for Bower (1990), and BLE photometry:

$$U_0 - V_{0.55} = -0.42 \pm 0.02 \tag{4.4}$$

$$V_0 - I_{0.55} = 0.78 \pm 0.02 \tag{4.5}$$

$$J_0 - K_{0.55} = 1.265 + 0.491(J - H)_0 \quad (r.m.s = 0.02) \tag{4.6}$$

— — —

— Adopted no-evolution C-M relations for $z = 0.55$.

($H_o = 50\,\mathrm{km\,s^{-1}Mpc^{-1}}$, $q_o = 0.5$, 4″.8-diameter aperture, no reddening included):

For field galaxies from PFA:

$$(V - I) = -0.012I + 2.87 \tag{4.7}$$

$$(V - K) = -0.084K + 7.13 \tag{4.8}$$

$$(I - K) = -0.063K + 4.14 \tag{4.9}$$

For Coma galaxies from PFA:

$$(I - K) = -0.107K + 4.81 \tag{4.10}$$

For Coma galaxies from Bower (1990) and BLE:

$$(V - I) = -0.096I + 4.52 \tag{4.11}$$

$$(V - K) = -0.173K + 8.62 \tag{4.12}$$

$$(I - K) = -0.084K + 4.52 \tag{4.13}$$

close to that of M_z, and so the transformation is very independent on the actual shape of the SED. We estimate that systematic uncertainties are $\lesssim 0^m.05$ from the variations from one SED to another and differences in photometric systems.

The $z = 0.55$ predictions are compared in Figure 4.8, together with a least-squares linear fit to each set of data. The equations of those fits are given in table 4.3. The overall agreement is convincing. The two predictions based on Coma (from PFA and BLE data) are virtually identical, and very close to the prediction based on PFA's field galaxies, but the latter has a slightly larger scatter. This small difference in dispersion is probably due to uncertainties in the distances for PFA *field* sample and the fact that some of those galaxies do not belong to a homogenous set (some belong to groups). Since Coma probably represents the local environment closest to that in 0016+16, BLE's data is the most appropriate to use. It is also of superior quality and forms a homogenous set, and we will refer to it when we talk about the non-evolutionary prediction in the rest of the section. The very good agreement of both sets of data suggests that we have not underestimated the systematic errors of the prediction.

Prior to any understanding of the colour difference we must consider the possibility of Galactic reddening. The galactic latitude of 0016+16 ($b^{II} = -45°$) suggests little Galactic extinction in its direction. Burstein & Heiles (1982) maps give $E(B-V) \approx 0.03$, which lies within the errors of Ellis *et al.* determination. Lilly (1987) adopts this value, and we will do so also. Using Savage & Mathis (1979) reddening law (see also Mathis 1990), this translates to $A_V = 0.093$, $A_I = 0.045$ and $A_K = 0.011$. Figures 4.9, 4.10 and 4.11 show the observed colour-magnitude (C-M) diagrams for the cluster members and unclassified objects, and the no-evolution prediction lines with the above reddening (solid lines).

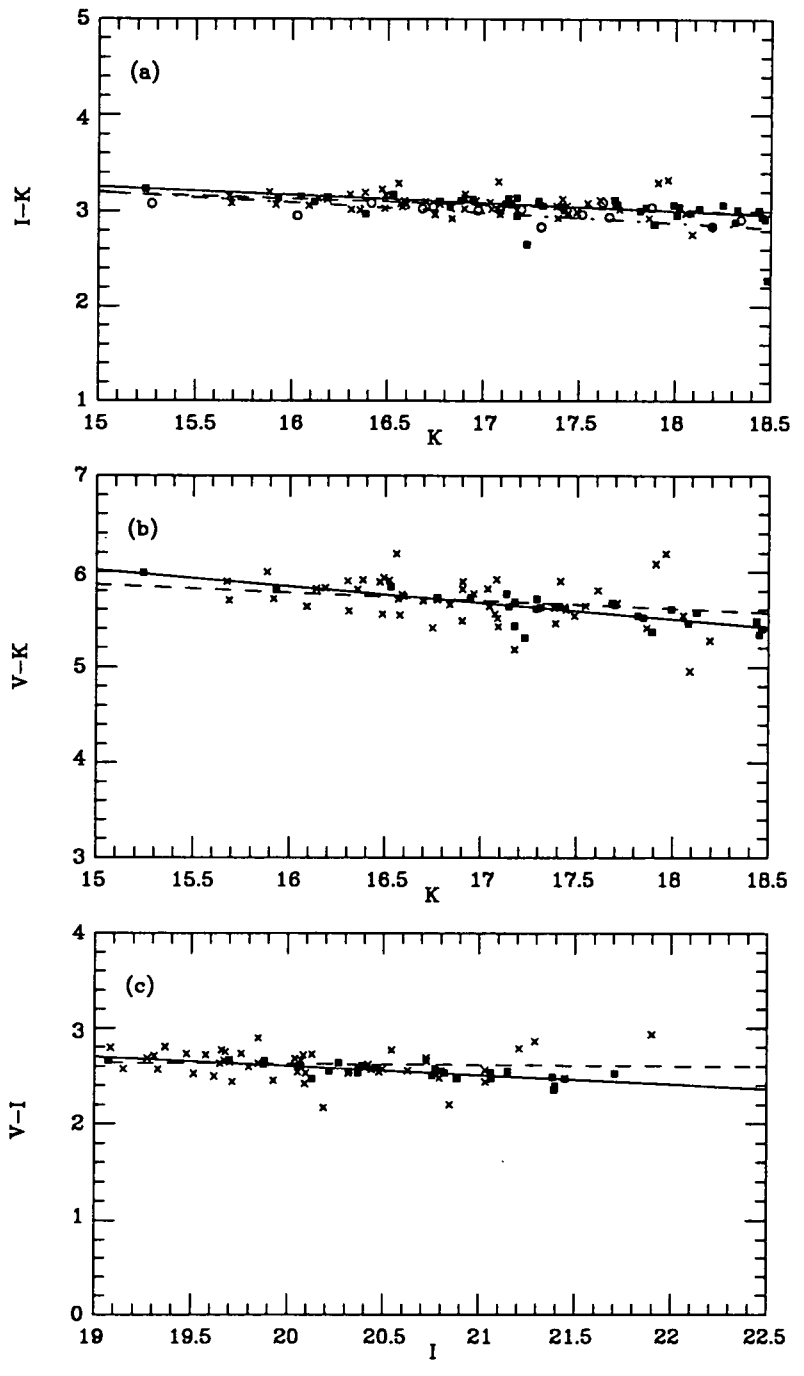

Figure 4.8. Comparison of the no-evolution predictions in the observed bands for $z = 0.55$ from PFA and BLE data. (see text). Filled squares and solid line: Coma galaxies from BLE. Crosses and dashed line: field galaxies from PFA. Circles and dot-dashed line: Coma data from PFA. The ranges of the plots are the same as for our data.

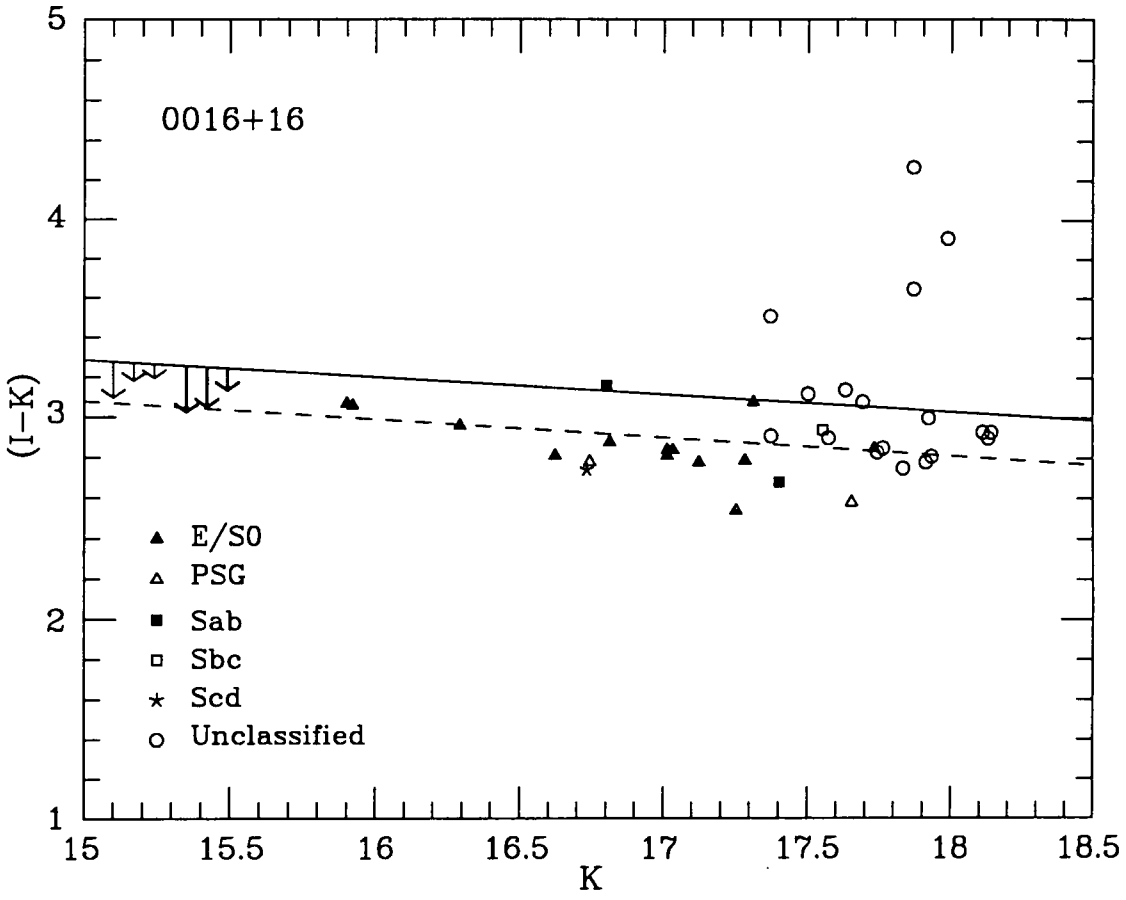

Figure 4.9. Observed $(I - K)$ vs. K colour-magnitude diagram for 0016+16 members and unclassified objects with $K < 18^{m}.2$. Different symbols denote different types of objects (see legend). The solid line shows the no-evolution prediction obtained as explained in text. The dashed line shows a fit to the *red* members (see text) with the same slope as the no-evolution line. The arrows show the colour change at $z = 0.55$ predicted by a Bruzual (1983) c-model for $q_o = 0.0$ (thin arrows) and $q_o = 0.5$ (thick arrows) with $z_{for} = 2$, 5 and 10 (in decreasing order of arrow length). See §4.2.5 for details.

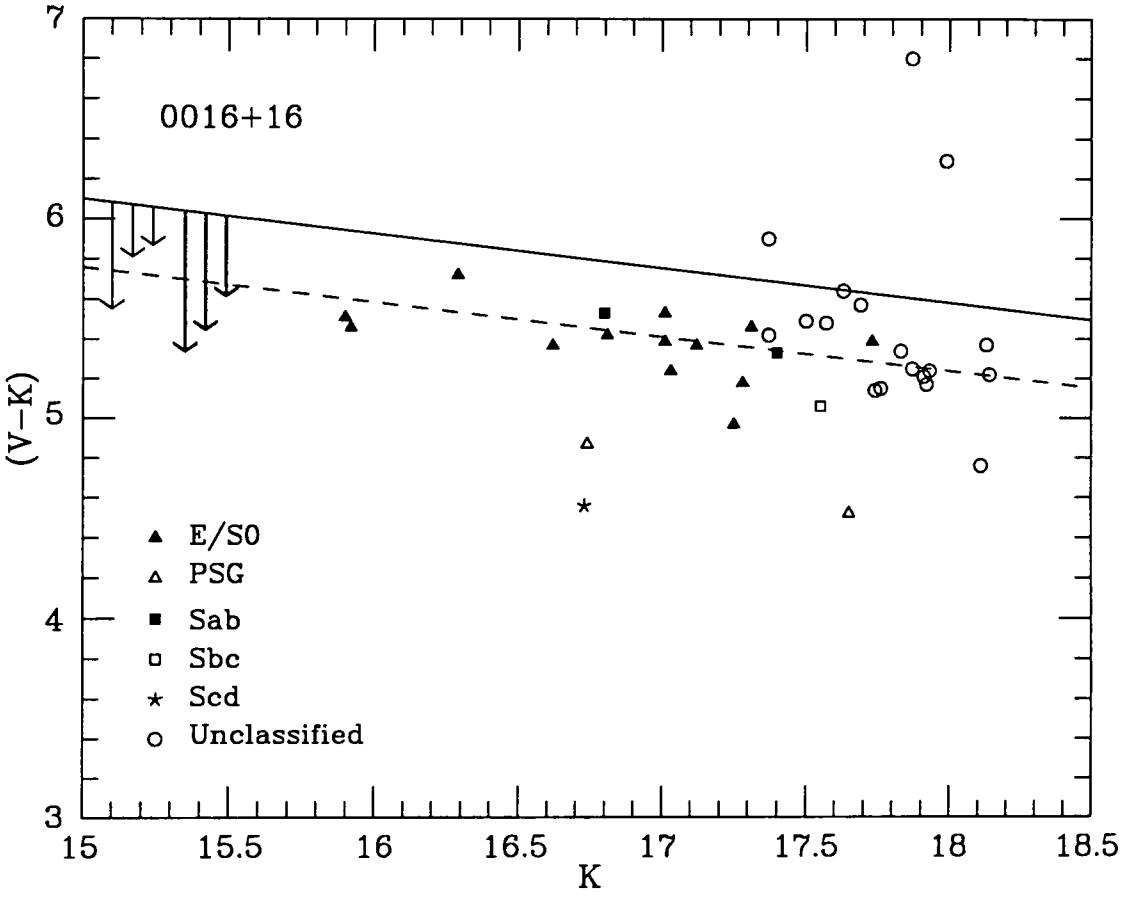

Figure 4.10. Same as 4.9 but for $(V-K)$ vs. K.

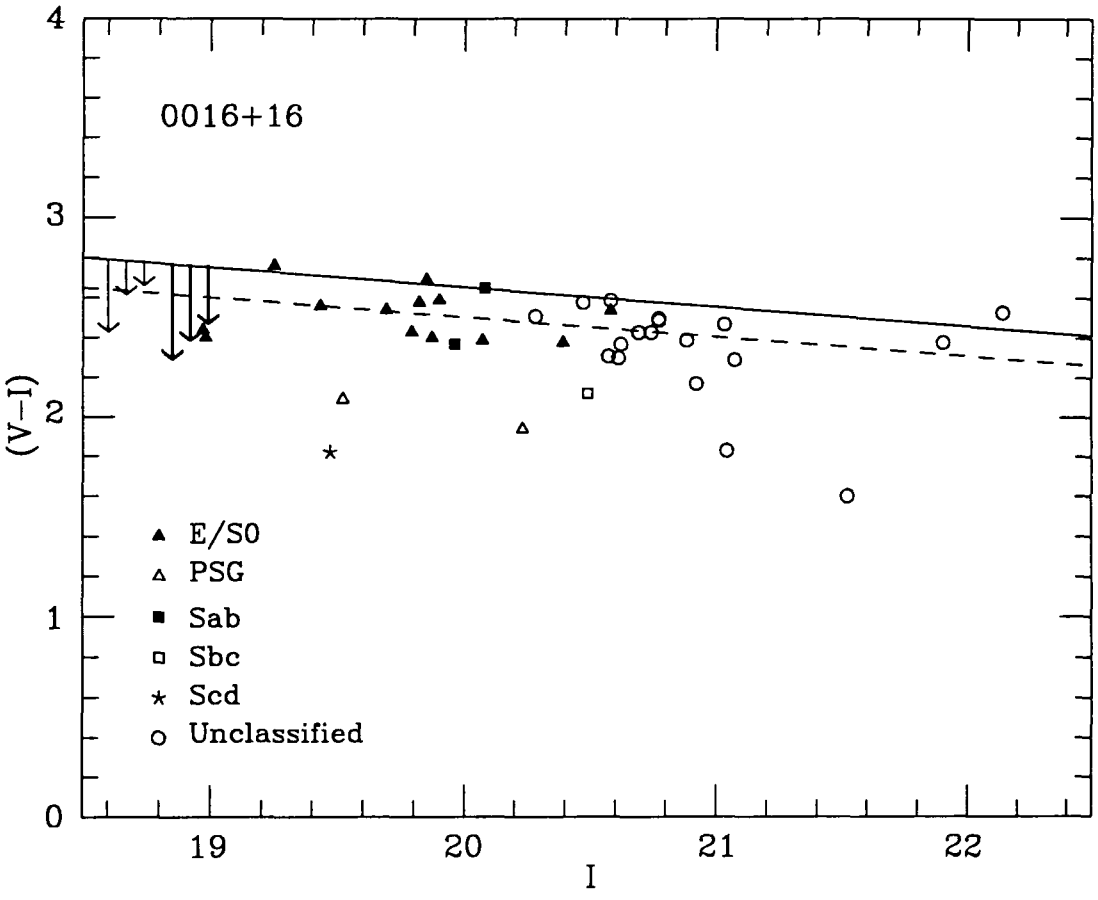

Figure 4.11. Same as 4.9 but for $(V - I)$ vs. I.

The $(I-K)$ vs. K diagram (Figure 4.9) shows (with the exception of four very red objects: #31, 132, 36 and 65, none of which has membership information) a tight C-M relation, and no objects scatter to the blue. It is remarkable that the position of the objects on the diagram is largely *independent* of their spectral classification. To make a direct comparison with the prediction, we have fitted a straight line to the points (excluding the four red objects mentioned above) and obtained a slope of -0.04 ± 0.05 that is compatible with the one of the non-evolving line (Table 4.3), and an r.m.s. scatter of $0\overset{m}{.}15$. We repeated the fit using the predicted slope, which yields and offset of $0\overset{m}{.}20\pm0\overset{m}{.}03$ * bluer than the no-evolution prediction, and the r.m.s. is similar. Given the size of the uncertainties in the reddening correction and in the non-evolving prediction, this discrepancy is very significant (more than 3σ), and the data show strong evidence for colour evolution in the observed $(I-K)$ colour (restframe $\sim(V-J)$ or $\sim(V-H)$).

However, Lilly (1987), using the same reddening, found that the rest-frame $(V-H)$ colours for 0016+16 were, on average, $0\overset{m}{.}21$ *redder* than those of Coma.** A small part of the difference could arise from a different prediction (Lilly used PFA's Coma photometry). The offset found in K zero-points (§4.2.1) could also explain part of the difference (no direct comparison is possible between I zero-points, as we do not use the same system), but a sizeable residual discrepancy remains. Lilly's correction for luminosity evolution could also play some role. We do not understand this discrepancy, but Chapter 5 shows that the result for 0016+16 is consistent with the results found for higher redshift clusters.

The observed scatter ($0\overset{m}{.}15$) around our adopted C-M relation seems too large for our estimated errors. Monte-Carlo simulations of samples with the observed magnitude

---

* The quoted uncertainty only includes random errors, but systematic errors of the order of $\sim 0\overset{m}{.}05$ in the prediction should be added to that.

** Lilly found 0016+16 to be the reddest cluster of his sample in rest-frame $(V-H)$, but the bluest in rest-frame $(U-V)$.

and error distributions show that we should expect an r.m.s. of $0^m.11$ if no internal scatter were present. This difference is significant at the 97% confidence level, particularly since the scatter does not seem to increase with K, as would be expected from random errors. Simulations indicate that the internal dispersion in the colours is $\approx 0^m.10$. The effect is present just for the objects classed as early-types, but no significant bimodality is seen.

The four objects with very red $(I-K)$ colours: #31, 132, 36 and 65., for which no membership information is available, do not fit in our current understanding of galaxy evolution if they are cluster members. We will find more examples in our high z cluster sample, and we will discuss them there, ignoring them in the rest of this chapter.

We can proceed the same way with the $(V-K)$ vs. K C-M diagram (Figure 4.10). There are two main differences with the previous diagram: some objects clearly lie to the blue (#144, 64, 63 and D96). The first two have been classified as Post Star-burst Galaxies (PSG), the third is a late-type spiral with [O II] emission, and the last is unclassified. Earlier-type spirals remain on the main C-M line. As before, a least-squares fit to the non-deviant points gives a slope of -0.13 ± 0.05, compatible with the prediction, and we then fit the points using a line with the predicted slope. This line is $0^m.34$ bluer than the non-evolving one, and the r.m.s. scatter of the observed points is $0^m.15$, similar to the one found before. As the photometric errors are of the same order as for $(I-K)$, some intrinsic scatter has again been detected.

Finally we consider $(V-I)$ vs. I (Figure 4.11). This colour is not independent from the other two, but the diagram contains extra information since we represent it vs. I instead of K. Some objects scatter to the *blue*. We find again #144 and 64 (PSGs), and #63 (Scd). A newcomer to the blue class is #21 (Sbc). The objects classified as Sab (#3 and 57) remain near the line (but remember than Ellis *et al.* classification is claimed to be accurate to ± 1 spectral class, so they could be E/S0s, and the spectroscopy for #3

classifies it as 'early'). The unclassified object #D96 is consistent with being either a PSG or a late-type spiral.

The line fitted to the remaining points (with the same slope as the prediction because no change is detected) is shown as the dashed line. It is $0^m.15$ magnitudes bluer than the non-evolving prediction, and the points (excluding the ones that clearly deviate into the blue) show an r.m.s. of $0^m.12$ around this line. Lilly also detected a similar blueing ($0^m.16$) of the average rest-frame $(U-V)$ colours of 0016+16 red galaxies when compared with Coma ellipticals.

The reduction in the scatter is explained by the smaller photometric errors. Monte Carlo simulations with the observational errors and the same magnitude distributions predict an r.m.s. of only $0^m.06$, and the difference is very significant (to better than 99.9% level). Therefore, the intrinsic scatter should be of the same order as the ones found in the other C-M diagrams (the simulations predict again an internal dispersion in the colours of $0^m.10$). This indicates that the small intrinsic differences in the galaxies show at the same level in the optical-infrared colours as in the pure optical (rest-frame $(U-V)$) colours. It would be interesting to have purely infrared colours (*e.g.* $(H-K)$) to see if any intrinsic scatter remains there.

This diagram can be compared with the one presented in Figure 7 of Ellis *et al.* (1985), that shows (502 – 685). Although the bands do not coincide exactly, we can expect both to contain comparable information. They look remarkably similar, showing the same kind of behaviour and evolution, even though our samples are different (we select in the near IR while they do in the optical F-band, $\lambda_{eff} \simeq 610\,\mathrm{nm}$, see Koo 1981). It is interesting to note that the dramatic differences present in their (418 – 685) colour of normal E/S0s (restframe (270 – 440)) disappear at longer wavelengths, showing the wide

range of far UV SEDs among Ellipticals of homogeneous optical and infrared colours (see, *e.g.*, Burstein *et al.* 1988).

Summarizing, the bulk of the early-type galaxies show a tight C-M relation that is significantly bluer than the present-day one in all colours. An internal scatter of $\sim 0\overset{m}{.}1$ magnitudes has been detected. A few objects (4–5), classified as spirals and PSGs are significantly bluer in $(V-K)$ and $(V-I)$ than the mean C-M line for ellipticals.

4.2.4 The Colour-Colour diagram

Figure 4.12 shows the observed $(V-I)$ vs. $(I-K)$ colour-colour (C-C) diagram for 0016+16 members and unclassified objects with $K < 18\overset{m}{.}2$. If we exclude the four objects with unusually red $(I-K)$ colours that we mentioned in the previous section, the diagram shows a very tight group that includes all the E/S0's and the objects classified as Sab's. Part of the scatter of that group is explained by the observed C-M effect, shown as the dashed line. The solid line shows the predicted one. The latter-type spirals and PSG's scatter into bluer $(V-I)$ colours, but present very little deviation in $(I-K)$. When compared with Figure 1(b) of Lilly (1987), which shows rest-frame colours that closely correspond to our observed ones, the morphology of both diagrams is very similar, showing that the discrepancies with his work do not come from differences in the relative colours, but perhaps from differences in zero-points or in his treatment of the luminosity evolution.

It is worth commenting here that all the objects that have *blue* $(V-I)$ colours tend to avoid the central areas of the cluster. A similar effect been detected in clusters at comparable redshift by Dressler & Gunn (1990, 1991) and at lower redshifts by Pickles & van der Kruit (1991). These authors consider this effect as evidence for the idea that interaction with the Intra Cluster Medium induces star formation.

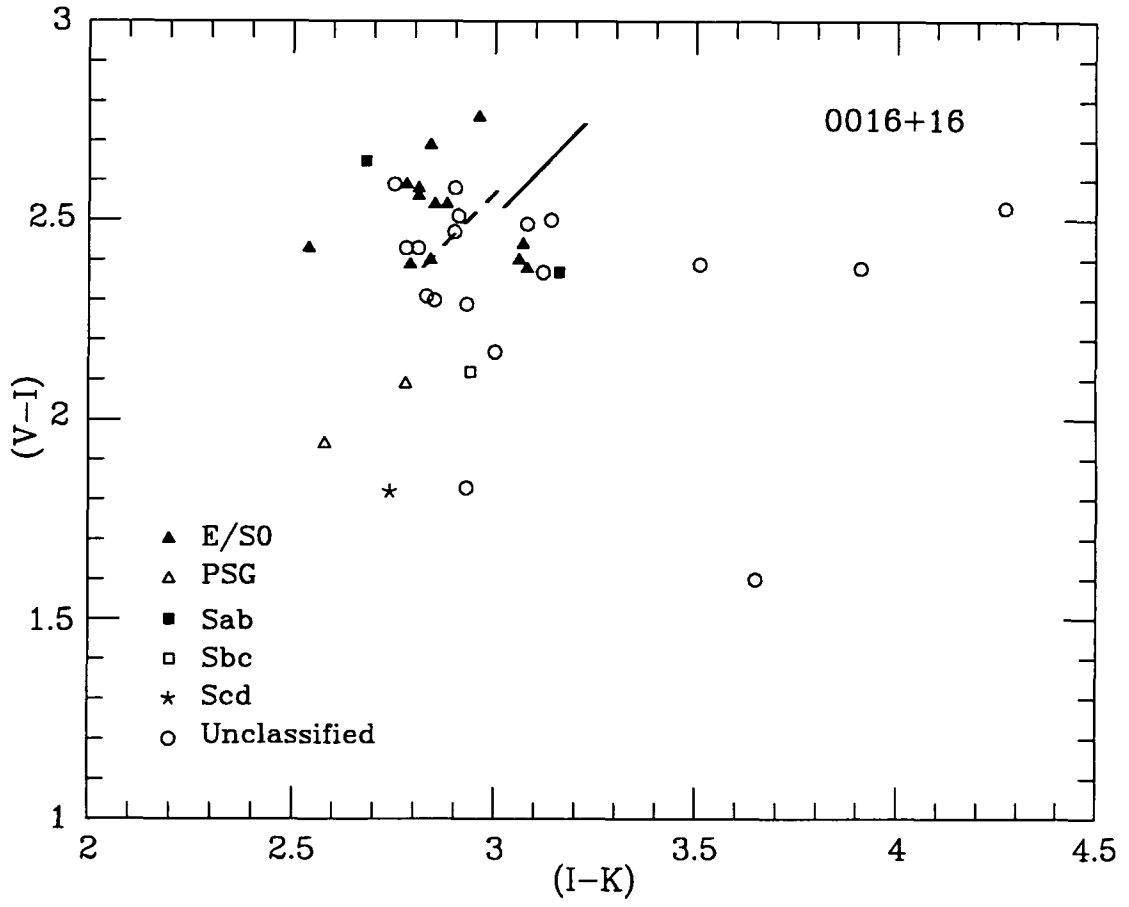

Figure 4.12. Observed $(V - I)$ vs. $(I - K)$ colour-colour diagram for 0016+16 members and unclassified objects with $K < 18^m.2$. The symbols are the same as in Figure 4.9. The solid line shows the no-evolution prediction for the C-M effect, and the dashed line the observed one.

4.2.5 Comparison with galaxy evolution models

In previous sections we have seen that the bulk of the red population in 0016+16 shows the same amount of photometric evolution for all the objects in each colour, *i.e.*, the whole C-M line is shifted. This suggests that most are experiencing similar evolutionary processes, with much smaller differences shown by the intrinsic scatter.

Let us first consider the form such evolution might take. The simplest to consider is *passive evolution*, in which the changes in colour between $z = 0.55$ and the present epoch are produced by the ageing of an old population in which negligible star formation has occurred after the initial birth of the galaxy.

Several models are available, and they differ mainly in the input stellar tracks, the treatment of the chemical evolution and the way in which they include late stages of stellar evolution (*i.e.* Horizontal Branch —HB—, Asymptotic Giant Branch —AGB—, ...). Differences in other details like the input stellar parameters (colours or spectra), the treatment of the Star Formation Rate (SFR), the form of the Initial Mass Function (IMF) and the assumptions built in the codes also exist and might be important. Extensive discussion about the merits and demerits of each particular set of models exists in the literature (see, *e.g.*, Tinsley & Gunn 1976, Tinsley 1980, Bruzual 1983, Renzini & Buzzoni 1986, Guiderdoni & Rocca-Volmerange 1987, 1990, Arimoto & Yoshii 1987, Buzzoni 1989, Charlot & Bruzual 1991; see also Chapter 1).

The predictions of the models depend also on cosmological parameters like H_o and q_o through their role in the timescales involved. Stellar evolution theory and therefore the galaxy evolution timescales are in conflict with high values of H_o, so we will restrict our considerations to $H_o = 50\,\mathrm{km\,s^{-1}\,Mpc^{-1}}$. q_o enters by determining not only the age of the universe at the present epoch, but also the age difference between $z = 0$ and $z = 0.55$. For that reason, q_o values of 0.0 and 0.5 will be considered.

And, of course, we do not know the epoch of galaxy formation (or z_{for}), by which we mean the epoch in which the bulk of the star formation took place. It might well change from galaxy to galaxy or from cluster to cluster, but the uniformity in the colours of the red galaxies in 0016+16 suggests that we can start by considering to be the same for most of the early-type galaxies in this cluster.

For the different models, our aim is to try and find the set of parameters that produce results that are compatible with our observed colour evolution for an old evolving stellar population. We are trying to explain colour changes to the blue of the order of $0^m.15$ in rest-frame $(U-V)$, and $0^m.2$ in rest-frame $(V-J)$ or $(V-H)$ as one moves from $z = 0.0$ to $z = 0.55$.

We begin with Bruzual (1983) models, adopting a local Miller & Scalo (1979) IMF. They assume solar metallicities (for the stellar properties and evolutionary tracks), and no chemical evolution is considered. We use a c-model in which all the star formation happens at a constant rate in the first 1 Gyr, and a $\mu = 0.5$ model, in which the SFR is exponentially-decreasing so that half of the mass is converted into stars in the first Gyr (e-folding time of 1.4 Gyr). The c-model gives reasonable fit to the optical and near-IR SED of a present-day elliptical for ages $\gtrsim 11$ Gyr, although it is deficient in UV light. This could be due to the lack of Post-AGB or young stars in the models. The μ-model behaves similarly in the optical and near-IR for the same range of ages, but it contains more light in the UV because of the presence of a small amount of young stars. Even if the models do not produce a perfect fit to the SED of a present-day elliptical, they are still valid for our purposes, since we are interested in *relative* changes in the colours, and not *absolute* values, and any uncertainty on the latter should affect the former only to second order.

The amount of evolution predicted by the c-model in the different colours at $z = 0.55$ is shown by the vertical arrows in Figures 4.9, 4.10 and 4.11. Thin and thick arrows

correspond to $q_o = 0.0$ and $q_o = 0.5$ respectively, with $z_{for} = 2$, 5 and 10 (in decreasing order of arrow length).

For $q_o = 0.0$ the c-model predicts changes in the colours that are broadly compatible with the observed ones (taking into account the uncertainties) for $z_{for} \approx 5$–10 (age of the galaxy today $T \approx 16$–18 Gyr), The same models with $q_o = 0.5$ require $z_{for} \gtrsim 10$ ($T \gtrsim 12.7$ Gyr).

The $\mu = 0.5$ model predicts too much evolution in a $q_o = 0.5$ Universe. In the $q_o = 0.0$ case, the results are similar to the ones obtained for the c-models, but for older ages, since in a μ-model the star formation continued longer, even though it was in a small amount.

We conclude that the amount of evolution detected at $z = 0.55$ for the early-type galaxies is broadly compatible with the ageing of an old stellar population when the model uncertainties (particularly concerning the lack of late stages of stellar evolution in the models) are taken into account. Therefore, the bulk of the stellar populations in early-type galaxies show colour changes compatible with *passive evolution*. In Chapter 5 we will extend the comparison with evolutionary models to a broader redshift range, obtaining more stringent constrains to the range of acceptable model parameters, and strengthening this conclusion.

To test if our conclusions depend strongly on the kind of models applied, we will consider other approaches to the modeling of galaxy evolution. Arimoto and Yoshii (1987) present galaxy evolution models in which the chemical and photometric evolution are taken into account at the same time. Their elliptical galaxy model includes a wind phase in which the energy input by supernovae exceeds the binding energy of the gas, which is expelled, stopping the star formation. This scenario could explain the metallicity-luminosity relation that elliptical show in the C-M diagrams. Another difference is that in order to make the

predicted colours fit the observations they have to use an IMF that is flatter than the local neighbourhood one (Salpeter 1955 gives a slope $x = 1.35$ and they use $x = 0.95$). This slope also predicts the correct metallicity distribution of K-giant stars in the galactic bulge (Rich 1988, 1990).

The model we have used is an improved version of the one published in Arimoto & Yoshii (1987), kindly provided by Dr. N. Arimoto (private communication). In their *best model* for a bright elliptical of $2 \times 10^{12} M_{\odot}$ the SFR goes to zero (and therefore the chemical enrichment stops) at an age of ~ 0.85 Gyrs because the wind phase occurs. The predictions of this model for the colour evolution at $z = 0.55$ are quite similar to the ones from Bruzual *c*-model, because its star formation history is almost the same (see Figure 4.13), and our conclusions stand unchanged.

Let us show now the results of applying very recent models published by Charlot & Bruzual (1991).* They claim to have made significant improvements on the existing models (in particular Bruzual 1983 ones) by using an updated stellar library and a new, more accurate, method of computing the distribution of stars in the theoretical C-M diagram. They also include AGB stars in a semi-empirical way (see the original paper for details). A solar neighbourhood IMF (Salpeter 1955) and solar metallicity are used, with no chemical evolution. They treat the SFR in the same way as Bruzual (1983). Their models are able to reproduce reasonably well the observed colours of young (0.01–4 Gyr) star clusters in the Large Magellanic Cloud from the UV to the near-IR and of present-day galaxies of various morphological types.

We find that these models generally predict a much larger amount of evolution than observed in the range of ages that we are considering (see also Chapter 5). Charlot

* We are indebted to these authors for providing their model results in machine-readable format, which has made the comparison with our results much easier.

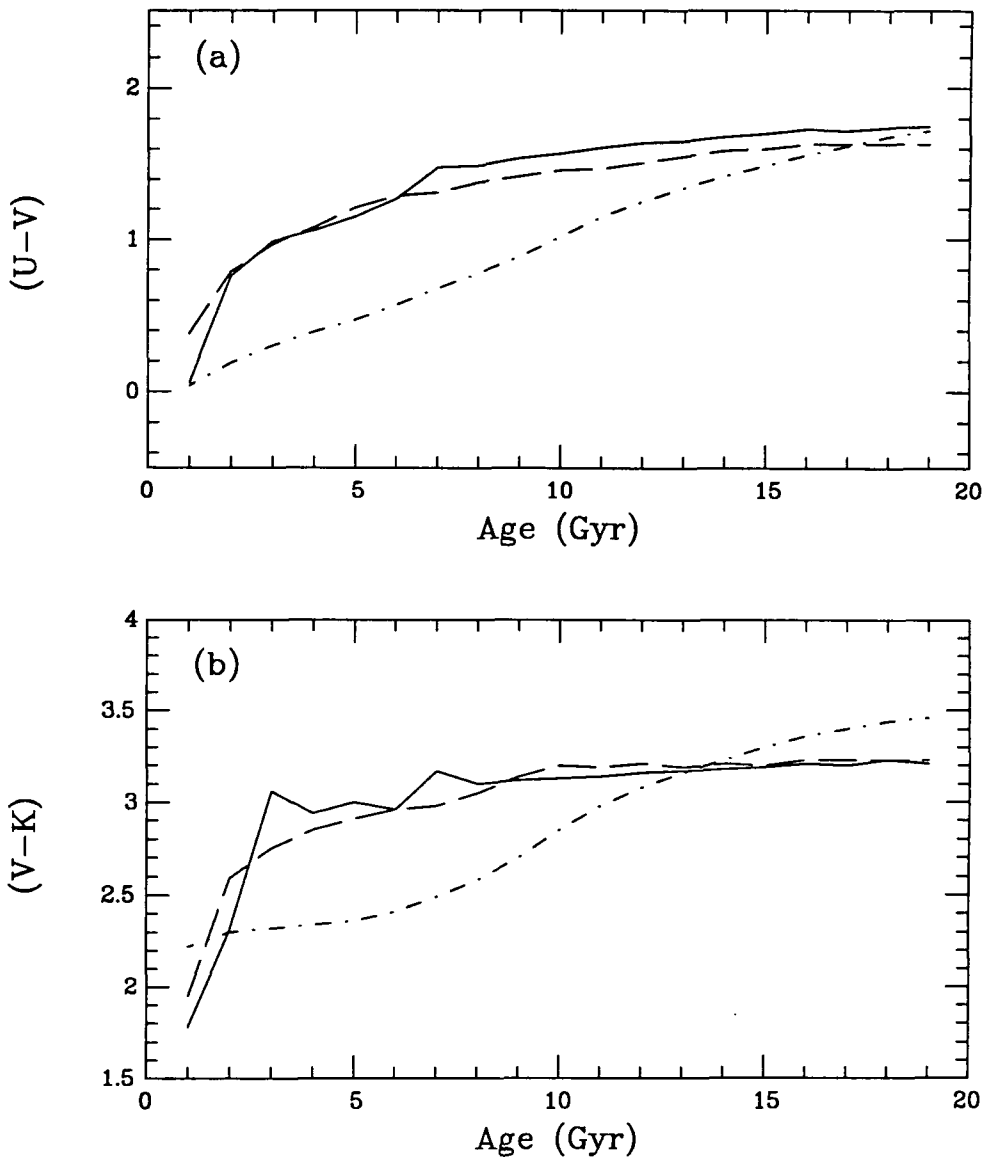

Figure 4.13. **(a)** Time evolution of rest-frame $(U - V)$ for different galaxy evolution models. Solid line: Bruzual (1983) c-model with a constant SFR lasting 1 Gyr; dash-dotted line: Charlot & Bruzual (1991) c-model with the same SFR; long-dashed line: Arimoto & Yoshii (1987) model. **(b)** As (a) but for $(V - K)$. See text for details.

& Bruzual (1991) models have not been tested for ages between 4 and 13 Gyr, that are crucial when comparing with objects at intermediate redshift. In fact, their model suffers an increase in the rate of evolution in this range of ages (see Figure 4.13, and Figure 6 of their paper). Therefore, Charlot & Bruzual models are unable to explain the observed change in the colours of 0016+16 red galaxies.

To illustrate the differences among the models applied, Figure 4.13 shows their colour evolution predictions in rest-frame $(U - V)$ and $(V - K)$. Two of the models considered (those of Bruzual 1983 and Arimoto & Yoshii 1987) give similar conclusions when applied to our data, but Charlot & Bruzual (1991)'s results are incompatible with the measured evolution. This is a good example of the large uncertainties that still exist in galaxy evolution models, and the conclusions reached when applying them should be regarded with caution.

After having considered the global changes in colours of the red population of the cluster, we will now try to explain the observed scatter in the colours of individual galaxies around the C-M line. The intrinsic scatter is of the order of $0^m.1$ in the different colours if our errors are realistic. It could come as the result of including objects of slightly different spectral classes and non-members (Ellis *et al.* 1985 classification is only accurate to $\pm$ one spectral class and ± 0.05 in z, and about 40% of the objects included do not have membership information). In fact, the changes that we can expect from this variations are of this order of magnitude, so probably part of the scatter (perhaps all of it) comes from that.

If we try to explain all the scatter as intrinsic differences in a homogeneous population of red members, a possible explanation could be an intrinsic spread of ages. The actual value of this age variation depends on cosmology and the epoch of galaxy formation. Bower, Lucey & Ellis (1991) related the scatter on the colour-magnitude diagram for

early-type galaxies with the spread in the epoch of galaxy formation (see original paper for a detailed description of the method). If we follow their approach, we find that for $q_o = 0.5$ and the limits on z_{for} discussed above, the maximum spread in age is $\Delta T \lesssim 2$ Gyr. If $q_o = 0.0$, we get $\Delta T \lesssim 3$ Gyr. These are upper limits, since some other sources of scatter could be present.

If we assume that all the galaxies were born at the same time, a small amount of star formation in some of the objects could easily produce the observed variation. Models of the type shown in Chapter 3, in which an old galaxy experiences a burst of star formation that affects a small fraction of its mass show that this is in fact possible. The actual fraction of the galaxy mass involved in the burst depends on the age and time duration of the star formation, but about 5% of its mass being converted into stars could explain the observed effect.

Chemical composition differences could also be responsible through their effect on the colours. As the chemical enrichment is supposed to happen at very early stages of the galaxy evolution (Tinsley 1980, Arimoto & Yoshii 1987), age differences of the order of the ones considered above cannot be responsible for that. In the framework of Arimoto & Yoshii models, the mass of the galaxy controls its chemical composition by affecting the epoch in which the wind phase occurs. Therefore, changes in the M/L ratio, via different amounts of dark matter (which does not contribute to the chemical enrichment but affects the binding energy of the gas in the galaxy) could be the cause. However, changes of a factor ~ 10 in M/L are needed. Photometric data alone cannot rule out this possibility, but some dynamical information like velocity dispersions could determine if such changes in M/L are present.

4.2.6 Summary and discussion

In this section we present very accurate optical and near-IR K-band photometry for 0016+16 at $z = 0.546$. We have obtained a K-selected ($K < 18^m.2$) sample comparable to the Abell 370 one ($z = 0.37$). This proves the feasibility of extending this kind of studies to higher redshifts with the same kind of accuracy.

After studying in detail the colour evolution of the red galaxies in 0016+16 a coherent picture emerges:

- The red members show a very tight C-M diagram, indicating that they form a very homogeneous population. However, a small but significant scatter in the colours around this line has been detected. As we do not observe significant changes in the slope of the C-M line when compared with nearby samples (Coma), the colour evolution must have very little dependency with luminosity.

- The bulk of the red population is significantly bluer in the optical and optical-IR colours than present-day galaxies in rich clusters (Coma). The detected colour changes are consistent with the ageing of an old stellar population.

- Stressing the fact that the similarities are more important than the differences among the red stellar population of 0016+16, the detected scatter suggests that some small dispersion in the properties of the red galaxies could exist. Some possible causes have been considered: presence of objects that belong to a different spectral class or non-members, spread in age, residual star formation or differences in chemical composition, but the photometric data alone can not decide which one is more likely. In fact all of them could play a role in it.

The detected colour evolution of the 0016+16 red galaxies will be addressed in Chapter 5 when studying the evolution of cluster galaxies as a function of redshift. We

have not addressed the problem of the luminosity evolution in this section because for one single cluster it is not possible to disentangle it from q_o. We will consider it for the whole sample of clusters in Chapter 5.

4.3 The cluster F1767.10TC at z = 0.664

This cluster was discovered by visual inspection of a high contrast film derivative of a prime focus AAT photographic plate taken in the F passband. This was done as part of a systematic search for faint, high redshift ($z \gtrsim 0.2$) southern galaxy clusters carried out by Couch *et al.* (1991) It shows a 7σ density enhancement above the fluctuations in the local field counts inside a circular area of ~ 3.1 arcmin diameter. In the spectroscopic follow up of a subsample of the cluster candidates, these authors obtained redshifts for 8 objects in the cluster field, of which 2 are stars, 2 foreground galaxies and 4 have similar redshifts, with $\langle z \rangle = 0.664$. The cluster has the second highest redshift in their catalogue.

Multicolour intermediate-band photometry of the type described in Couch *et al.* (1983), Ellis *et al.* (1985), and MacLaren, Ellis & Couch (1988) is available for a complete sample of galaxies with $I \leq 22.5$ in this cluster, and a detailed analysis will be presented elsewhere (Aragón-Salamaca *et al., in preparation*). These multi-band observations should allow us to classify galaxies to ± 0.05 in redshift and ± 1 in Hubble type. The data confirm the reality of the cluster. In the field of study ($3' \times 4'$) there are 96 galaxies detected to $I = 22.5$, with 60% of them being classified at redshift $z \sim 0.66$. This cluster component is dominated by objects with SEDs typical of normal present-day E/S0's, and contribution from later type objects is less than 10%.

The redshift distribution of the galaxies classified as non-members (40%) has a broad component that one would expect from the general distribution of field galaxies along the line of sight to the cluster, but has superimposed upon it a narrow and quite strong peak centered at $z \sim 0.425$. Thus it appears that F1767.10TC suffers from contamination by a foreground cluster or group of galaxies, which probably explains the very high number density contrast of this cluster.

In this section we will carry out a similar study as the one presented for 0016+16, using VIK photometry to constrain the evolution of the galaxies in F1767.10TC at $z = 0.664$. The smaller number of objects present in the sample will impose restrictions to what we can learn in this case but it will be a very good test about what we will be able to learn for other clusters where no or very little membership information is available.

4.3.1 Infrared photometry

The K-band photometry was obtained with IRCAM I at UKIRT in two observing nights (10/11 and 11/12 April 1989). This was before the improvements carried out in the image and noise performance of the telescope and camera, so longer exposure times were required to get equivalent signal-to-noise ratios as the ones presented in the previous section. We used the $1\farcs24\,\mathrm{pixel}^{-1}$ mode, and imaged an area of $\sim 74'' \times 70''$ centered $\sim 5''$ N of galaxy $d(\#44)$.* Table 4.4(a) shows a log of the observations.

The observations, data reductions and photometric calibration were carried out as described in Chapter 2. The combined final image is shown in Figure 4.14(a). It is flat to $\frac{\sigma_{sky}}{sky} \sim 10^{-4}$, which corresponds to a surface brightness detection limit of $\mu_K = 22\overset{m}{.}3\,\mathrm{arcsec}^{-2}$ (1σ). The image quality is $\sim 2\farcs1$ (FWHM). The zero-point for the coadded image has an uncertainty of $\sim 0\overset{m}{.}03$.

Photometry was obtained inside a $6\farcs4$-diameter aperture in the usual way. The choice of a larger aperture in this case was made for several reasons. First, the poorer image quality in the K-image and the worse seeing in the optical (see ahead), and second because the crowding problems in this field are much less severe than in the 0016+16

* The numbering scheme is indicated on the K band contour-plot. The letters correspond to the spectroscopic targets of Couch *et al.* (1991).

Table 4.4 (a) Log of F1767.10TC K-band observations.

Object	R.A. (1950)	Dec. (1950)	Date	Exposure (s)
F1767.10TC	$08^h44^m53\overset{s}{.}4$	$+18°04'08\overset{''}{.}6$	1989 April 10/11	9000
			1989 April 11/12	6000*

* non-photometric.

Table 4.4 (b). Log of F1767.10TC optical observations.

Band	Date		Seeing	Exposure (s)
V	13/14 December	1985	$\sim 1\overset{''}{.}8$	1000 + 820 + 600*
	12/13 March	1986	$\sim 2\overset{''}{.}0$	500
I	13/14 December	1985	$\sim 1\overset{''}{.}7$	1000 + 500 + 500

* non-photometric.

Telescope:	3.9-m Anglo-Australian Telescope
Instrument:	Prime focus (f/3.3)
Detector:	RCA CCD (320 x 512 pixels)
Pixel size:	$0\overset{''}{.}49\,\text{pixel}^{-1}$

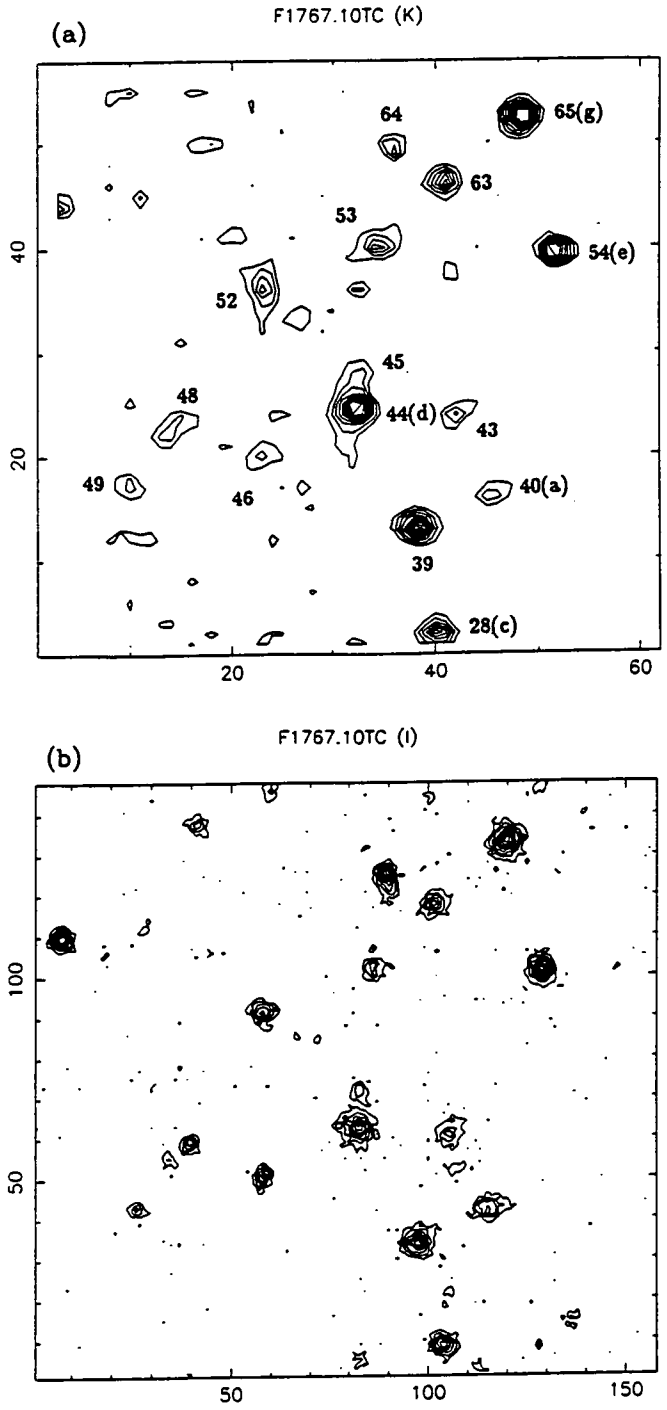

Figure 4.14. **(a)** Contour plot of the F1767.10TC K band image. The scale is $1\farcs24$ pixel^{-1}. The numbers on the axes are pixels. North is up and East is left. The contours follow a linear intensity scale, the lowest corresponding to $\mu_K = 21\fm3$ arcsec^{-2} (2.5σ above average sky level) and the highest to $\mu_K = 19\fm1$ arcsec^{-2} (20σ). **(b)** Contour plot of the F1767.10TC I band image (covering the same area as the K image). The scale is $0\farcs49$ pixel^{-1}. The contours follow a linear intensity scale, the lowest corresponding to $\mu_I = 23\fm6$ arcsec^{-2} (2.5σ above average sky level) and the highest to $\mu_I = 21\fm3$ arcsec^{-2} (20σ).

Table 4.5. F1767.10TC Photometric Catalogue.

#	K	σ_K	$(V-I)$	σ_{VI}	$(V-K)$	σ_{VK}	$(I-K)$	σ_{IK}	$\sim z^{\dagger}$	Class†	$z^{\ddagger}_{spec}$
44(d)	16.24	0.05	2.57	0.09	5.73	0.10	3.16	0.06	0.66	E/S0	0.663
65(g)	16.40	0.05	2.20	0.07	4.98	0.08	2.78	0.06	0.66	E/S0+uvx	0.665
39	16.56	0.06	2.75	0.14	5.64	0.15	2.89	0.07	0.72	E/S0	
54(e)	16.85	0.06	2.42	0.10	5.13	0.11	2.71	0.07	0.66	E/S0	0.673
28(c)	17.02	0.09	2.36	0.12	5.13	0.14	2.77	0.10	0.66	E/S0	0.653
52	17.26	0.10	2.51	0.08	5.34	0.12	2.83	0.12	0.4	E/S0	
63	17.30	0.10	2.75	0.21	5.55	0.22	2.80	0.12	0.66	E/S0	
40(a)	17.45	0.14	1.37	0.06	3.90	0.15	2.53	0.15	0.4–0.5	Sab	0.562
53	17.57	0.11	2.59	0.25	5.50	0.26	2.91	0.13	0.72	E/S0	
43	17.62	0.16	2.34	0.16	4.98	0.22	2.64	0.17	0.66	E/S0	
64	17.69	0.15	3.03	0.08	4.94	0.17	1.91	0.16	0.66	E/S0+uvx	
46	17.99	0.22	2.30	0.20	4.83	0.28	2.53	0.23	0.66	E/S0	
45	18.00	0.20	1.96	0.18	4.58	0.26	2.62	0.22	0.4–0.5	E/S0	
48	18.01	0.21	2.44	0.22	4.90	0.30	2.46	0.22	0.66	E/S0	
42	18.02	0.22	2.25	0.29	5.26	0.35	3.01	0.25	0.44	E/S0	
49	18.02	0.21	1.92	0.21	4.74	0.28	2.82	0.24	0.4–0.45	E/S0	

Notes:

† Photometric redshift and classification.

‡ From Couch *et al.* (1991).

E/S0: Normal elliptical.

E/S0+uvx: Elliptical galaxy with UV excess.

Sab, Sbc, Scd, Sdm: Spirals.

case. We carried out an error study similar to the one described in Chapter 2. The final aperture magnitudes and errors are shown in Table 4.5.

The increase in distance modulus from 0016+16 to F1767.10TC is $\simeq 0.5$. To have a sample of similar depth, we need to reach $K = 18^m.7$ in a 4″.8-diameter aperture, which corresponds approximately to $18^m.5$ in a 6″.4 one. Keeping the same criterion as we did before, *i.e.* restrict the sample to objects with errors $\lesssim 0^m.2$, we only reach $\sim 18^m.1$, so the sample in this case is approximately half a magnitude shallower than the one for 0016+16. This, together with a smaller area coverage yields a much smaller number of objects.

4.3.2 Optical photometry

Optical CCD images in the V and I bands were obtained by W. Couch at the 3.9-m Anglo-Australian Telescope, using the f/3.3 prime focus (doublet corrector) in two observing runs (13/14 December 1985, 12/13 March 1986). The detector was a 320 x 512 RCA CCD, and the pixel size was 0″.49 pixel^{-1}. Table 4.4(b) shows a log of the optical observations. Standard flat-fielding and de-fringing procedures were applied. Figure 4.14(b) shows a contour plot of the coadded I image covering the same area as the K image.

Landolt (1983) standards were used for zero-pointing purposes when the conditions were photometric. The images taken in non-photometric conditions were calibrated using several bright but unsaturated stars in the frames. The procedure gives internal zero-point errors of the order of $0^m.02$.

Photometry was obtained inside the same aperture as for K. The combined results are shown in Table 4.5. Note that, unlike in the 0016+16 case, the errors in V and I contribute significantly to the errors in the colours, due to the inferior quality of the optical photometry. For that reason, we have included columns with the estimated errors in the colours.

4.3.3 The Colour-Magnitude diagrams

Our sample includes 16 objects with $K \lesssim 18\overset{m}{.}1$ (inside a 6.″4-diameter aperture). We have V and I magnitudes for all of them, and therefore we can carry out a study similar to the 0016+16 one, but with fewer objects. We should keep in mind that we are sampling the luminosity function $\sim 0\overset{m}{.}5$ magnitudes less deep than in the 0016+16 case.

Membership and classification is available for all the objects in the sample from intermediate multiband photometry, and spectroscopy is available for five of them (Couch *et al.* 1991). The spectroscopic and photometric redshifts agree very well for all the objects in our sample. The two stars included in their spectroscopic sample (objects 'j' and 's') are not included in ours, because they are outside or at the edge of the IRCAM field.

This leaves us with 9 objects classified as members (4 of them with spectroscopy), and they are all E/S0's, two of them (#64 and 65) showing UV excess. The remaining 7 are: two background E/S0's at $z \sim 0.72$, three foreground E/S0 and one foreground Sab, all of them probably related with the intermediate redshift ($z \sim 0.4$) group (Couch *et al.* 1991).

Figures 4.15(a, b, c) show the C-M diagrams for all the objects in the sample. As before, we can compare the colours of the F1767.10TC cluster members with those of galaxies in Coma. We use Bower (1990) and Bower, Lucey & Ellis (1991) data for Coma galaxies to make the no-evolution prediction.

The prediction of the observed I and K magnitudes at $z = 0.66$ can be done in a similar way to the one used in previous cases. The effective wavelength of the observed K band shifts to $\sim 1.32\,\mu$m, close to rest-frame J ($\lambda_{eff} \sim 1.25\,\mu$m), so $K_{0.66}$ can be predicted from J_0 and $(J-H)_0$ as before. In the same way, the effective wavelength of the observed I band shifts to $\sim 530\,$nm, bluewards of rest-frame V ($\lambda_{eff} \sim 550\,$nm), so

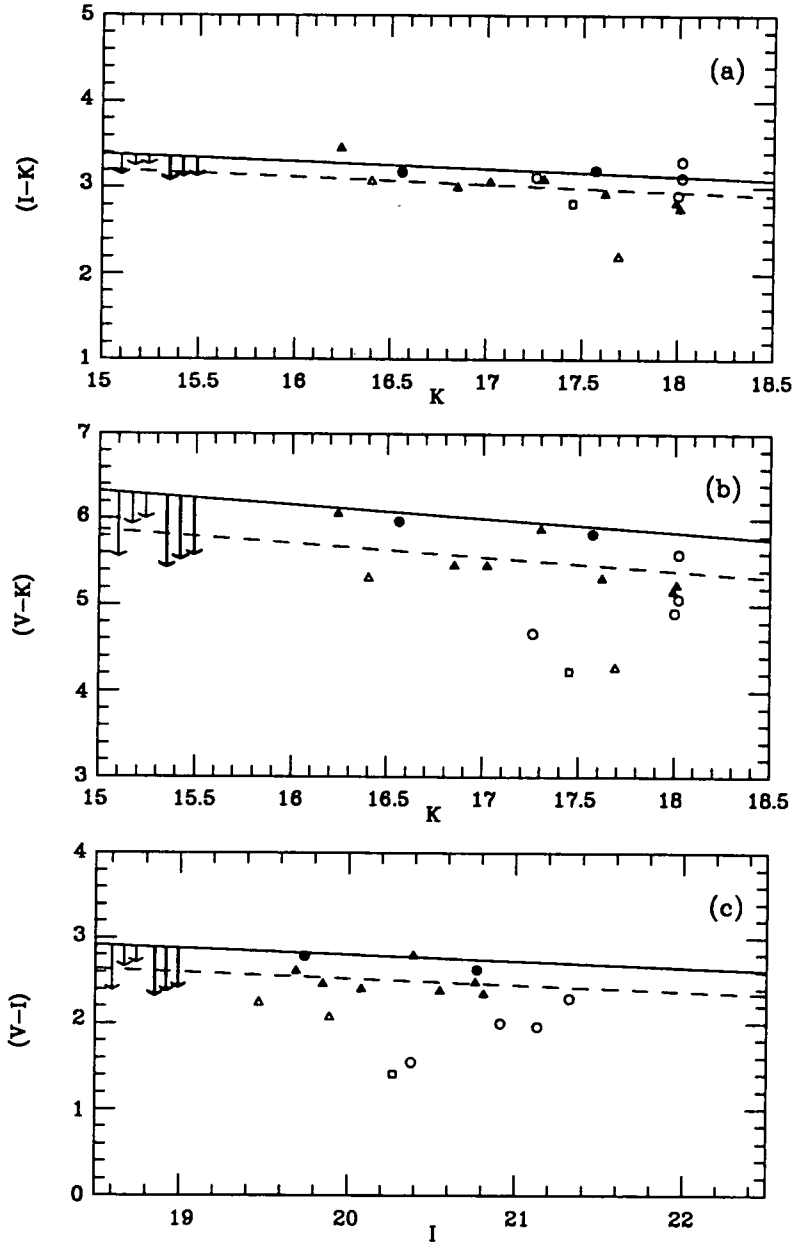

Figure 4.15. Observed colour-magnitude diagrams for all the objects in the F1767.10TC field with $K < 18^{m}.1$. Filled triangles: E/S0 members; open triangles: E/S0 members with UV-excess; filled circles: background E/S0's; open circles: foreground E/S0's; open square: foreground spiral. The solid lines show the no-evolution prediction. The dashed line shows a fit to the cluster E/S0's with the predicted slope. The arrows show the colour change at $z = 0.66$ predicted by a Bruzual (1983) c-model for $q_o = 0.0$ (thin arrows) and $q_o = 0.5$ (thick arrows) with $z_{for} = 2$, 5 and 10 (in decreasing order of arrow length). See §4.2.5.

Table 4.6 No-evolution prediction for $z = 0.66$

— Transformations for Bower (1990), and BLE photometry:

$$U_0 - V_{0.66} = -0.71 \pm 0.02 \tag{4.14}$$

$$V_0 - I_{0.66} = 0.893 - 0.153(U - V)_0 \quad (r.m.s = 0.02) \tag{4.15}$$

$$J_0 - K_{0.66} = 1.475 + 0.219(J - H)_0 \quad (r.m.s = 0.02) \tag{4.16}$$

— — —

— Adopted no-evolution C-M relations for $z = 0.66$.

($H_o = 50\,\mathrm{km\,s^{-1}Mpc^{-1}}$, $q_o = 0.5$, 6.″4-diameter aperture, no reddening included):

$$(V - I) = -0.077I + 4.34 \tag{4.17}$$

$$(V - K) = -0.160K + 8.72 \tag{4.18}$$

$$(I - K) = -0.087K + 4.69 \tag{4.19}$$

$I_{0.66}$ can be predicted from V_0 and $(U-V)_0$. Using the same set of SEDs, we obtain the transformation equations shown in table 4.6. Again, this can be done with an internal uncertainty $\lesssim 0.^m02$.

The prediction of the observed V magnitudes is more difficult. The effective wavelength of the band moves to rest-frame $\sim 330\,\mathrm{nm}$, which lies bluewards of rest-frame U ($\lambda_{eff} \sim 365\,\mathrm{nm}$). So ideally we would need colour information bluewards of rest-frame U, and this is not available for Coma galaxies. We can try to compute the transformation between $V_{0.66}$ and U_0 as a function of $(U-V)_0$ for the different SEDs and look at the differences. In all the previous cases, all the SEDs gave compatible transformations as a function of the colours independently of the galaxy-type. In this case, the results are very different for Spiral and Elliptical SEDs. This is understandable because the *shape* of the SEDs is very different for these two groups of galaxies. For the spirals we find a very strong linear dependency between $(V_{0.664}-U_0)$ and $(U-V)$. However, all the elliptical SEDs* no such dependency is observed and we get $\langle V_{0.66}-U_0\rangle = -0.71$, with an r.m.s. scatter of $0.^m02$ again. The colour range spanned by these SEDs is $0.^m71 \leq (U-V)_0 \leq 1.^m75$, much larger than that of Bower (1990) data. We believe that this set of SEDs covers reasonably well all the possibilities is spectral shape that we can expect to find among *normal* E/S0's (see Chapter 5). If this is so, this transformation can be used safely for the nearby data, keeping the internal uncertainties to the same level as before.

Using these transformation equations and taking the aperture effects into account in the same way as before ($6''.2$ corresponds to $50\,\mathrm{kpc}$ at $z = 0.664$, with $H_o = 50\,\mathrm{km\,s^{-1}\,Mpc^{-1}}$, $q_o = 0.5$) we obtain the predicted no-evolution C-M relations shown in Table 4.6.

---

* We include here the same E/S0 SEDs as in the previous cases plus the set of spectra that Couch (1981) used to mimic the UV-optical C-M relation.

We face again the reddening uncertainty. The galactic latitude of this cluster is $b^{II} \simeq 33°$. Burstein & Heiles (1982) maps give $E(B-V) < 0.03$ for this direction, and lacking of more information we will assume no reddening in the following discussion.

The solid lines in Figure 4.15 show the predicted C-M lines for Coma galaxies at $z = 0.66$. The cluster members classified as E/S0's (filled triangles) follow a tight C-M relations with slopes compatible with the predicted ones. The E/S0's with UV excess (open triangles) tend to be bluer than the normal ellipticals in all diagrams. Following the same arguments presented in §4.2.3, we have fitted straight lines to the E/S0 members with the predicted slope (dashed lines). The E/S0's are, on average, $0\overset{m}{.}28\pm0.06$, $0\overset{m}{.}45\pm0.09$ and $0\overset{m}{.}18\pm0.06$ bluer than the no-evolution lines in $(I-K)$, $(V-K)$ and $(V-I)$ respectively.

The r.m.s scatter of the E/S0 colours around the lines is $0\overset{m}{.}17$, $0\overset{m}{.}20$ and $0\overset{m}{.}15$ $(I-K)$, $(V-K)$ and $(V-I)$ respectively. The slightly worse scatter than in the case of 0016+16 is due to larger photometric optical errors. Using the observed error distribution, we find that the intrinsic scatter in $(I-K)$ and $(V-K)$ is similar to the one found in 0016+16 ($\sim 0\overset{m}{.}1$). No scatter has been detected in $(V-I)$, but given the size of the errors in $(V-I)$, we cannot rule out a scatter $\lesssim 0\overset{m}{.}07$ in this colour.

The background E/S0's ($z \sim 0.72$, filled circles) are in all cases redder than the mean C-M line for the E/S0 members, but the difference is to small to reject them as cluster members on the basis of their colours alone, because the difference in redshift is too small. The foreground E/S0's are bluer than the cluster ellipticals only in $(V-I)$. Therefore, our VIK photometry cannot be used to determine cluster membership on an object-to-object basis. In Chapter 5 we will correct statistically the colour distributions for field contamination.

4.3.4 The Colour-Colour diagram

Figure 4.16 shows the Colour-Colour diagram for all the objects in the sample. The solid line shows the predicted C-M effect, and the dashed line the observed one. All the objects lie in a relatively narrow $(I-K)$ colour range, with the exception of one of the E/S0+uvx objects, which is significantly bluer in this colour. In $(V-I)$ the E/S0 cluster members show very similar colours, with the UV-excess objects being bluer. The foreground objects are relatively well separated in $(V-I)$, but in 0016+16 we found several cluster members with similar colours relative to the cluster ellipticals, and therefore it is not safe to use this diagram to obtain membership information for individual objects.

4.3.5 Summary and discussion

In this section we have presented VIK photometry for a K-selected sample of galaxies in the cluster F1767.10TC ($z = 0.664$). This cluster provides a pilot test for the high redshift cluster study that we will present in Chapter 5, with a similar number of objects per cluster and comparable depths. In this case, membership information is available for all objects, providing a realistic test of the kind of information that we will be able to obtain when the membership information is much more scarce.

As in the case of 0016+16, we have detected significant blueing in the optical and optical-IR colours of the red galaxy population in the cluster F1767.10TC. In Figure 4.15, the arrows show the colour changes predicted by the same galaxy evolution models presented in §4.2.5 for $z = 0.66$. The comparison with the model predictions gives practically the same conclusions found for 0016+16, showing a very consistent picture for the amount of colour evolution as a function of redshift. In Chapter 5 we will extend this kind of studies to a wider redshift range.

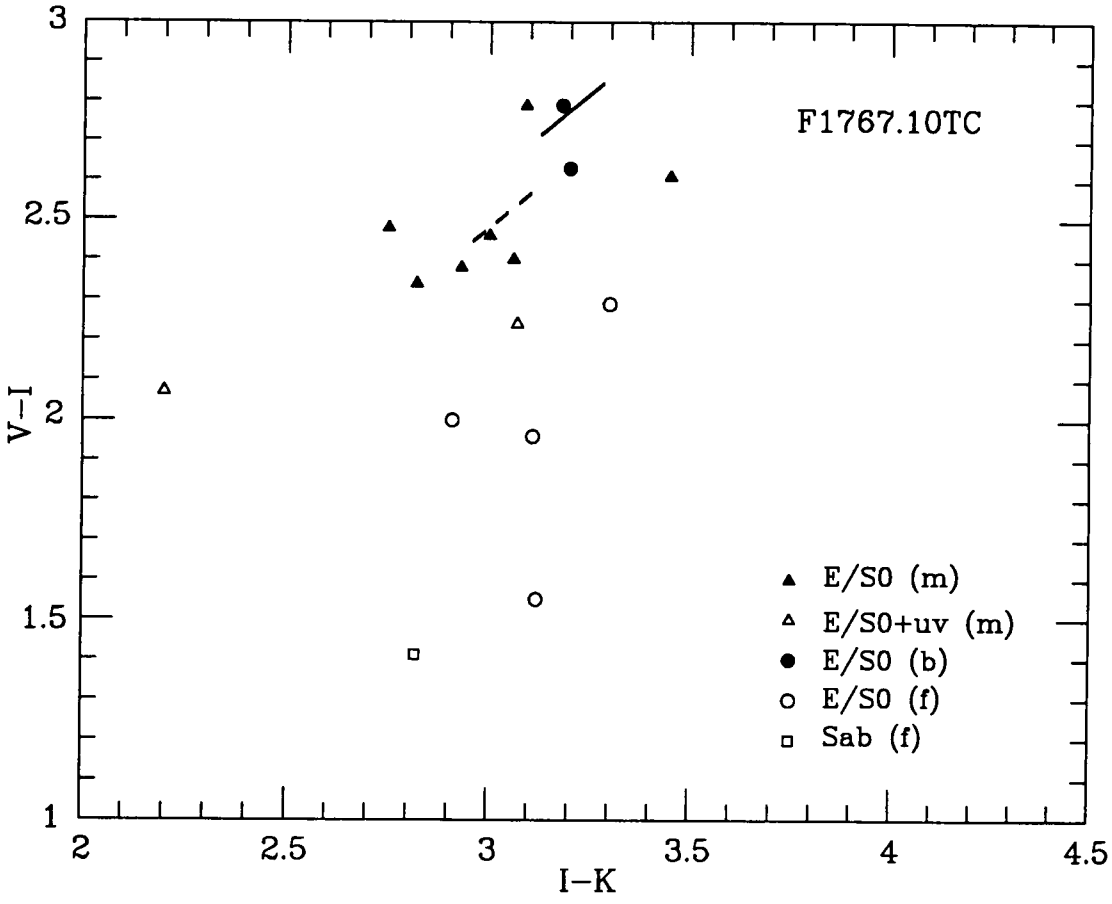

Figure 4.16. Observed colour-colour diagram for all the objects in the F1767.10TC field with $K < 18^{m}.1$. The symbols denote different types of objects (see legend), and are the same as in Figure 4.15. The solid line shows the predicted C-M effect, and the dashed line the observed one. Note: (m) members; (b) background; (f) foreground.

5 GALAXY EVOLUTION IN HIGH REDSHIFT CLUSTERS

5.1 Introduction

In previous chapters we have set the basis for the study of high redshift cluster galaxies selected in the near-IR K-band. In Chapter 2 we presented the expected advantages of selecting in the IR at high z in order to get representative fair samples of *normal* galaxies. In this chapter we will demonstrate practically that the advantages are real by comparing our samples with optically-selected ones.

The basic idea is to use the near-IR to select the sample of cluster galaxies, and the optical-IR colours to study the changes in SEDs, and therefore on the star formation history of cluster members. Photometry in the optical (that will sample light in the UV at high redshift) should be very sensitive to the effects of even small amounts of star formation. We will present precision VIK photometry for a sizeable sample of cluster galaxies with $0.5 < z < 0.9$. By comparing the measured colours with observations for nearby clusters, we will be able to detect and quantify the colour evolution as a function of z. Since redshifts will not be available for most of the objects, we will have to do this comparison in a statistical way, using the available field number counts in the relevant bands (Cowie *et al.* 1990, Lilly, Cowie & Gardner 1991, Cowie *et al.* 1991) to correct for field contamination. The results of Chapters 3 and 4 for Abell 370, 0016+16 and

F1767.10TC, for which membership information is available, provide a realistic test of these conclusions.

The amount of evolution detected will be interpreted using current models of galaxy evolution to constrain the age and history of star formation in *normal* cluster galaxies.

5.2 The cluster sample

The present list of galaxy clusters with $z \gtrsim 0.5$ is very small. Virtually all have been found in optical pass-bands, mainly in the red photographic F ($\lambda_{eff} \sim 6100$ Å) and N ($\lambda_{eff} \sim 8000$ Å) bands.

Two catalogues of distant galaxy clusters are available at the time of writing. The first is published by Gunn, Hoessel and Oke (1986, GHO hereafter). Those of interest from this sample for the present study were found in Mayall 4 m F and N prime focus plates and Hale 5 m prime focus image intensifier exposures recorded on photographic plates (approximately N band). The authors do not define precisely how their clusters were selected from this material. GHO only published redshifts for 25 clusters in their catalog. Of those, 8 have $z \geq 0.55$. Given the amount of observing time available, only 6 of them have been included in the present study (see Table 5.1). A visual inspection of the optical images published by GHO reveals that Cl1322+3115 ($z = 0.755$) does not seem to be as rich as the other clusters of similar redshift (compare, for instance, with Cl1322+3029 or Cl1322+3027). Since we intended to maximize the number of objects per image and there are several other clusters in the same redshift range, that one was not observed. At the high z end, we excluded Cl1603+4329 ($z = 0.920$) because the spectroscopic data suggests

Table 5.1. High z Cluster Sample.

Cluster	Redshift	References
0016+16	0.546	(1,2)
J1888.16CL*	0.563	(3,4)
Cl0317+1521	0.583	(5)
F1767.10TC	0.664	(4)
Cl1322+3029	0.697	(5)
Cl0020+0407	0.698	(5)
Cl1322+3027	0.751	(5)
Cl2155+0334	0.820	(5)
Cl1603+4313	0.895	(5)

* Also known as F2262.16CL and 0055−279.

References:

(1) Spinrad (1980)

(2) Koo (1981)

(3) Couch, Shanks & Pence (1985)

(4) Couch *et al.* (1991)

(5) Gunn, Hoessel & Oke (1986)

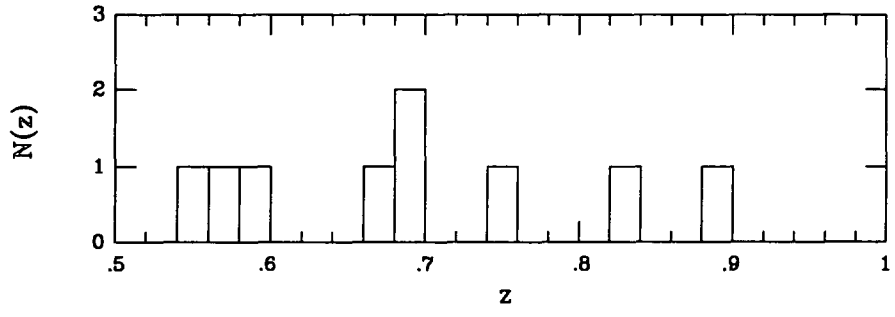

Figure 5.1. Redshift distribution of the high-z cluster sample.

it may be the superposition of two clusters at redshifts $z = 0.90$ and $z = 0.94$ (Dressler & Gunn 1990).

The second catalogue has been published by Couch *et al.* (1991, CEMM hereafter). They identify clusters from examination of high contrast film derivatives of AAT 3.9 m prime focus plates taken in the J and F passbands. CEMM selected their cluster candidates according to their contrast, σ_{cl}, above the fluctuations in the field counts as determined locally on the same film. They claim that their cluster list should be complete above a limit $\sigma_{cl} = 3.25$. Sadly, at the time of writing a large fraction of the clusters have no redshifts. Only three clusters with $z \geq 0.55$ are present, but the confirmation of one of them (J1836.23TR) as a cluster at $z = 0.68$ is regarded as tentative by these authors (they needed to obtain spectra for 9 objects to secure 2 with the same redshift). For that reason, we did not include it in our sample.

In total, therefore, 8 clusters with $z \geq 0.55$ were chosen from these catalogues for the present work, and together with 0016+16 (introduced in Chapter 4), they constitute the sample of Table 5.1. Figure 5.1 shows the redshift distribution of the galaxy clusters.

It is well known (see, *e.g.,* GHO, CEMM) that several selection effects play an important role in optically-selected catalogs of faint galaxy clusters. Distance- (redshift-) dependent selection effects can be reduced by choosing the observational wavebands in a sensible way (*i.e.* using progressively redder bands for more distant samples). Projection effects (superposition of groups of galaxies in the same line of sight) can only be safely accounted for with a large number of redshifts, which is clearly very expensive in telescope time. The *galaxy-dependent* selection effects, associated with variations in stellar populations a given epoch, are the most important in the present study. In that respect, and for

the reasons described in Chapter 2, ideally we would like to use clusters found in the IR, but this is not yet possible.*

We must, therefore, bear in mind that some problems could distort our cluster sample. However, the main aim of this work is to study the properties of galaxies as a function of redshift, not the clusters themselves. The clusters are used to provide samples of galaxies with a common z in the small areas of the sky that we can cover in reasonable amounts of observing time, given the size of the available IR detectors. Since the galaxies are selected in K, our sample should be representative of the galaxy population at a given look-back time, not biased by short term episodes of star formation, and we should be able to compare them with present-day galaxies in approximately similar environments (*e.g.* Coma). Even though the selection of the clusters does not guarantee that the ones included in our sample are the exact high z counterparts of *normal* nearby clusters, we can be fairly sure that we are comparing galaxies at very different look-back times, and in broadly similar dense environments. The differences between the high z and present-day *red* populations should reflect evolutionary changes due to look-back time differences to a much greater extent than differences due to environment effects, which would be much more subtle than the kind of effects that we will be able to measure (see, *e.g.* Bower *et al.* 1990, Bower 1990, Bower, Lucey & Ellis 1991).

---

* We will see in Chapter 6 that high redshift clusters could also be found in a systematic way in the X-ray domain, with the obvious advantage that they would be selected in a wavelength range largely unrelated to the stellar population of the galaxies present in them, and avoid the problem of mistaking chance line-of-sight alignments of unrelated groups for real clusters.

5.3 Observations and Data Reduction

The observational techniques and data reduction procedures that we used have been extensively described in previous chapters. We will summarize here only the relevant information that is specific of the high z cluster sample.

5.3.1 Infrared photometry

All the K band photometry for the high redshift clusters was gathered at the 3.8 m UKIRT, using IRCAM I and II during a period of 2 years. We followed the observational techniques and data reduction procedures described in Chapter 2. Table 5.2 presents a log of the IR observations.

Absolute photometric calibration was obtained, as before, from the frequent observation of standard stars from Elias *et al.* (1982) list. Typical uncertainties on the zero-points are $\sim 0\overset{m}{.}02 - 0\overset{m}{.}03$. A fraction of the observations were carried out in non-photometric conditions, but in every case enough photometric data was obtained for each cluster to ensure absolute zero-pointing with the required precision.

Aperture photometry was performed on the final reduced images in the same way described in previous chapters, and a similar error analysis was carried out. A $4\overset{''}{.}8$ diameter aperture was used in most cases as a compromise between getting the maximum fraction of the total light inside the aperture and the crowding problem. The exception were Cl1322+3029 and Cl2155+0334. For the first one, the K images were obtained before the image quality of the telescope an camera were substantially improved. In the second case, the seeing in the optical was $\sim 2\overset{''}{.}5$. Therefore, the inferior image quality forced us to use a $6\overset{''}{.}4$ diameter aperture.The estimated 1σ internal photometric errors are displayed in Figure 5.2 for the combined object sample.

Table 5.2: Log of the K-band observations for the high z clusters.

Cluster	R.A. (1950)	Dec. (1950)	Date	Camera	Exp. t (s)
J1888.16CL	$00^h54^m31^s.6$	$-27°56'43''$	1989 Oct 4/5	IRCAM II	2600
			1989 Oct 5/6	IRCAM II	2000
Cl0317+1521	$03^h17^m14^s.5$	$+15°21'00''$	1989 Oct 3/4	IRCAM II	6250
			1989 Oct 4/5	IRCAM II	600
Cl1322+3029	$13^h22^m00^s.7$	$+30°28'39''$	1989 Apr 9/10	IRCAM I	9000*
			1989 Apr 10/11	IRCAM I	6000
Cl0020+0407	$00^h20^m18^s.0$	$+04°07'49''$	1989 Oct 3/4	IRCAM II	4000
			1989 Oct 4/5	IRCAM II	2400
			1989 Oct 5/6	IRCAM II	1800
Cl1322+3027	$13^h22^m28^s.4$	$+30°27'10''$	1990 Jul 18/19	IRCAM II	2000*
			1990 Jul 20/21	IRCAM II	1200
Cl2155+0334	$21^h55^m23^s.8$	$+03°33'31''$	1990 Jul 17/18	IRCAM II	5200
			1990 Jul 18/19	IRCAM II	4400*
			1990 Jul 19/20	IRCAM II	5600*
			1990 Jul 22/23	IRCAM II	2400
Cl1603+4313	$16^h02^m46^s.1$	$+43°13'00''$	1990 Jul 18/19	IRCAM II	2000*
			1990 Jul 19/20	IRCAM II	800*
			1990 Jul 20/21	IRCAM II	4800
			1990 Jul 21/22	IRCAM II	8160
			1990 Jul 22/23	IRCAM II	4800

* non-photometric.

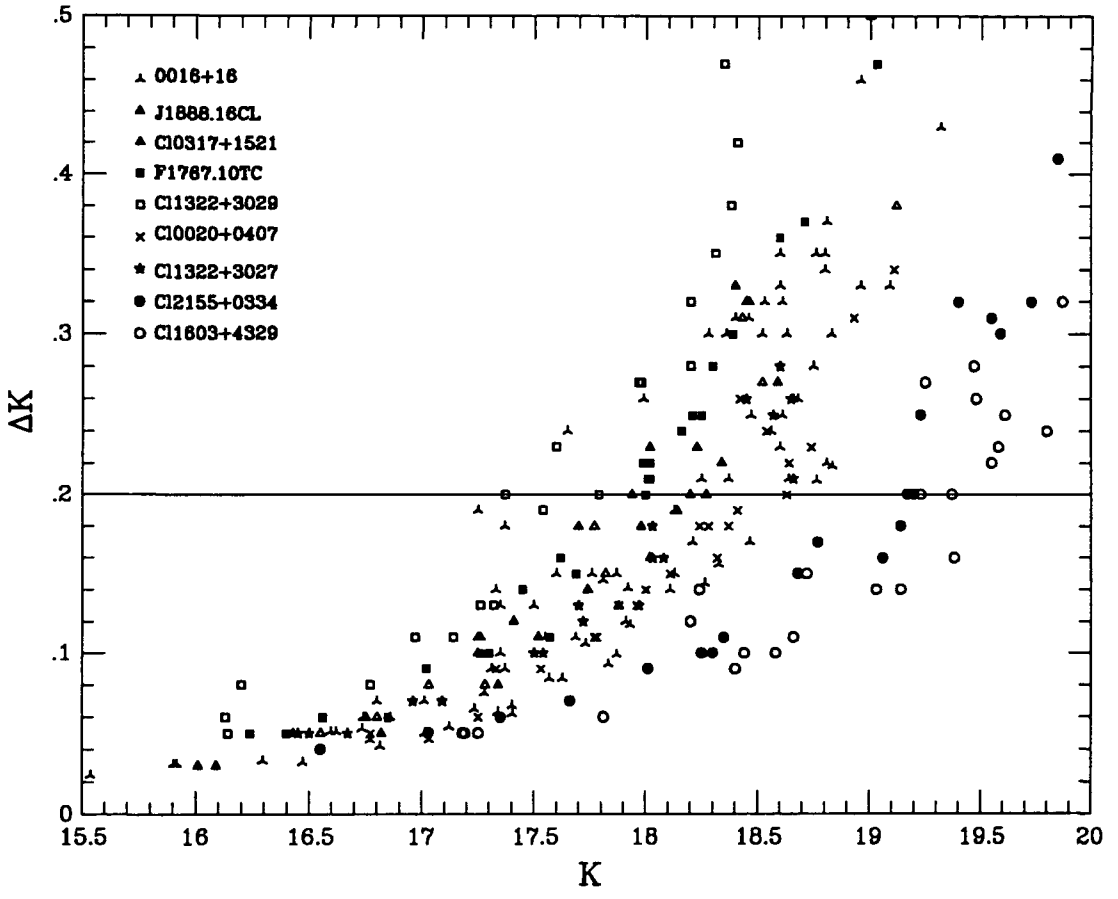

Figure 5.2. Internal photometric errors as a function of the K magnitudes for the high-z cluster sample. The field-to-field variations come from differences in exposure time, observing conditions and performance of the telescope and camera. For each field, the K limit is chosen so that $\Delta K \lesssim 0\overset{m}{.}2$ (horizontal line).

Objects were selected on the final coadded images to the limit in which the photometric errors in K were $\simeq 0\overset{m}{.}2$ (5σ). By selecting only detections above 5σ inside the aperture we can have confidence on the completeness of the catalogue to the quoted limits. That will also ensure that the optical-infrared colours will have enough precision for our study.

Contour maps of the final K images are shown in Figures 5.3 to 5.6. They give also the numbering scheme for the identification of the objects.

5.3.2 Optical photometry

Optical CCD images in the V and Kron-Cousins I bands were obtained for us, mainly in service time, at the 4.2 m WHT and 3.9 m AAT during the same 2-year period. The only exception to this are the images of J1888.16CL (also known as F2262.16CL or 0055−279), which was the subject of a CCD-based photometric study by Couch, Shanks & Pence (1985). These authors have kindly provided the original images, so that we have been able to perform a similar photometric study to the rest of the clusters. Table 5.3 contains the log of the optical observations.

The optical images were reduced in a standard way, which consisted of bias-subtraction and flatfielding. In several cases, some large-scale flat-fielding second-order residuals remained after the division by the flat-field frame due to the imperfect matching of the colours of the sky and the light used to obtain the flat-field. This problem was removed by obtaining a large-scale flatfield in the following way: all the images taken in the same filter during the same night were flat-fielded and normalized to a mean of 1. The median of all these images was then computed. This removed almost all the objects from the frames, since the images were of different fields and objects fell on uncorrelated positions. Any residual object was then removed by smoothing with a median filter of a size that

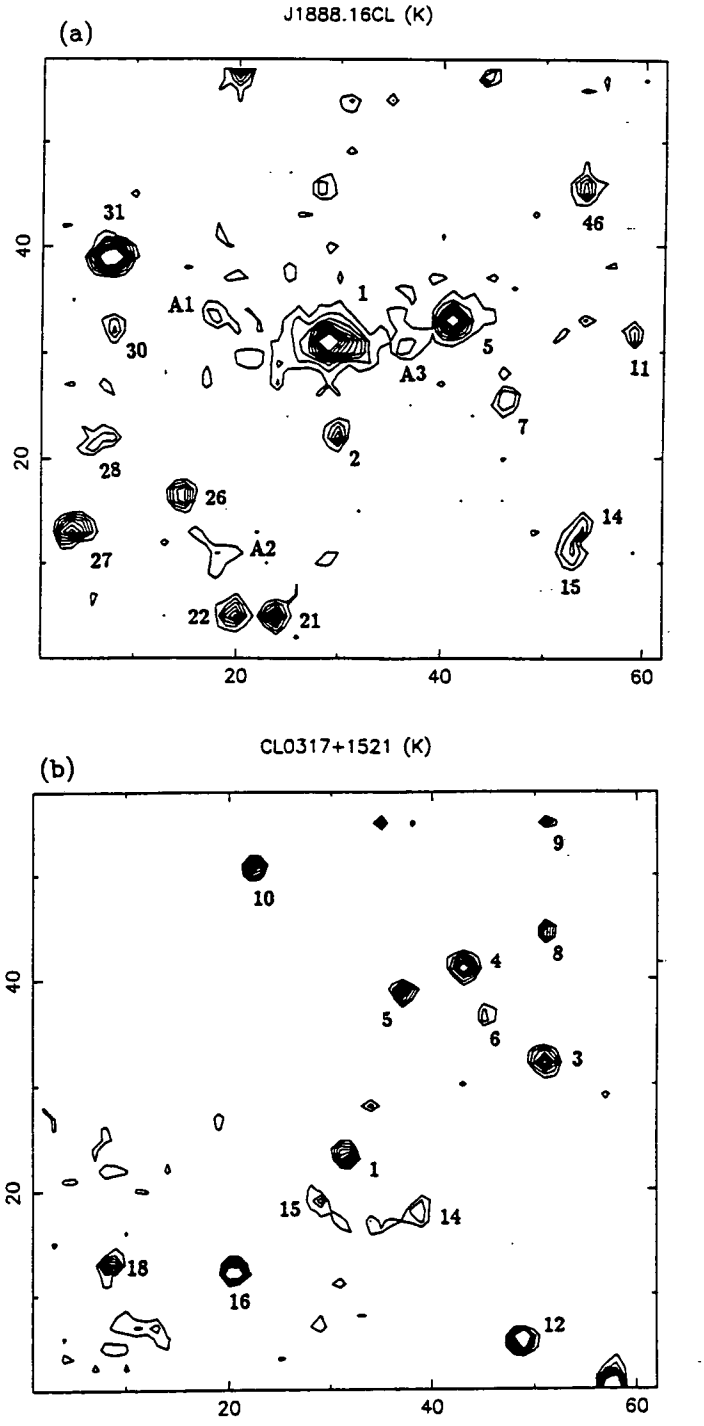

Figure 5.3. **(a)** Contour plot of the J1888.16CL (also known as F2262.16CL and 0055−279) K-band image. The scale is $1\farcs24$ pixel^{-1}. The numbers on the axes are pixels. North is up and East is left. The total exposure time is 4600 s. The contours follow a linear intensity scale, the lowest corresponding to $\mu_K = 21\fm33$ arcsec^{-2} (2σ above average sky level) and the highest to $\mu_K = 18\fm83$ arcsec^{-2} (20σ). **(b)** Same as (a) for Cl0317+1521. The total exposure time is 6850 s. The lowest contour corresponds to $\mu_K = 21\fm42$ arcsec^{-2} and the highest to $\mu_K = 18\fm92$ arcsec^{-2}.

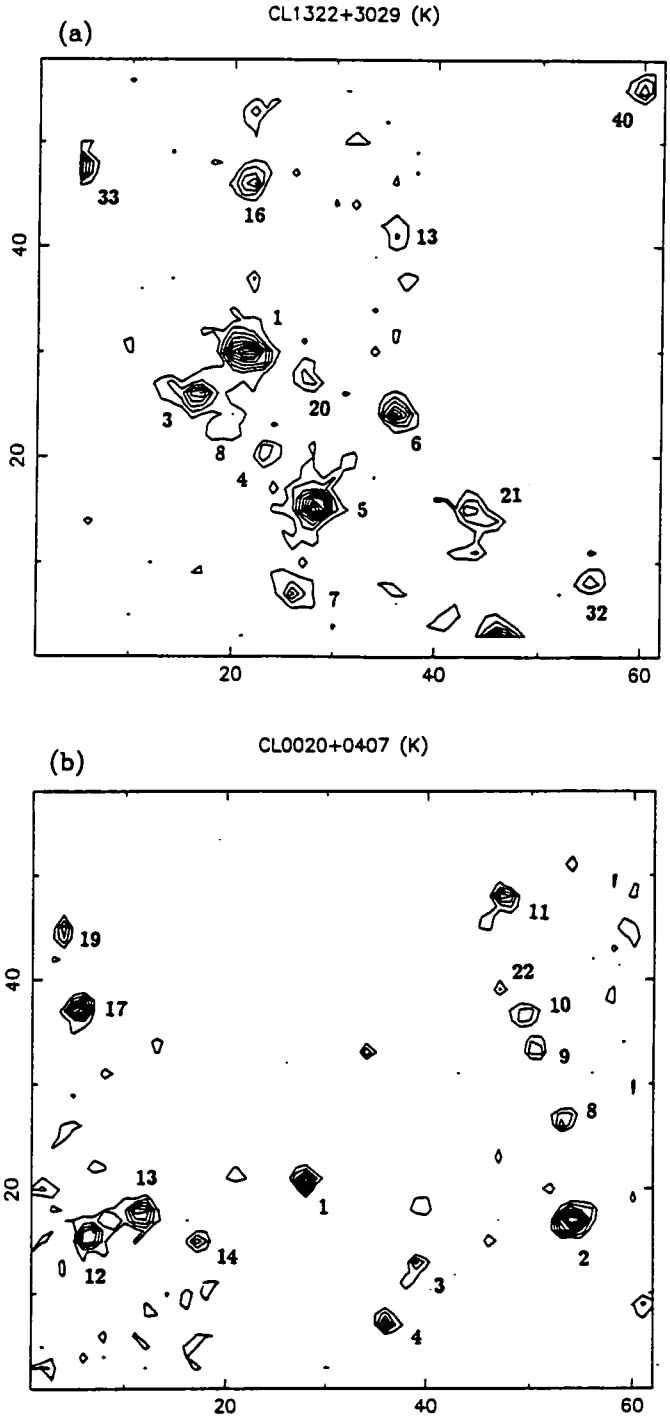

Figure 5.4. **(a)** Contour plot of the Cl1322+3029 K-band image. Scale and orientation as in Figure 5.3. The total exposure time is 15000 s. The contours follow a linear intensity scale, the lowest corresponding to $\mu_K = 21\overset{m}{.}36$ arcsec^{-2} (2σ above average sky level) and the highest to $\mu_K = 18\overset{m}{.}86$ arcsec^{-2} (20σ). **(b)** Same as (a) for Cl0020+0407. The total exposure time is 8200 s. The lowest contour corresponds to $\mu_K = 21\overset{m}{.}24$ arcsec^{-2} and the highest to $\mu_K = 18\overset{m}{.}74$ arcsec^{-2}.

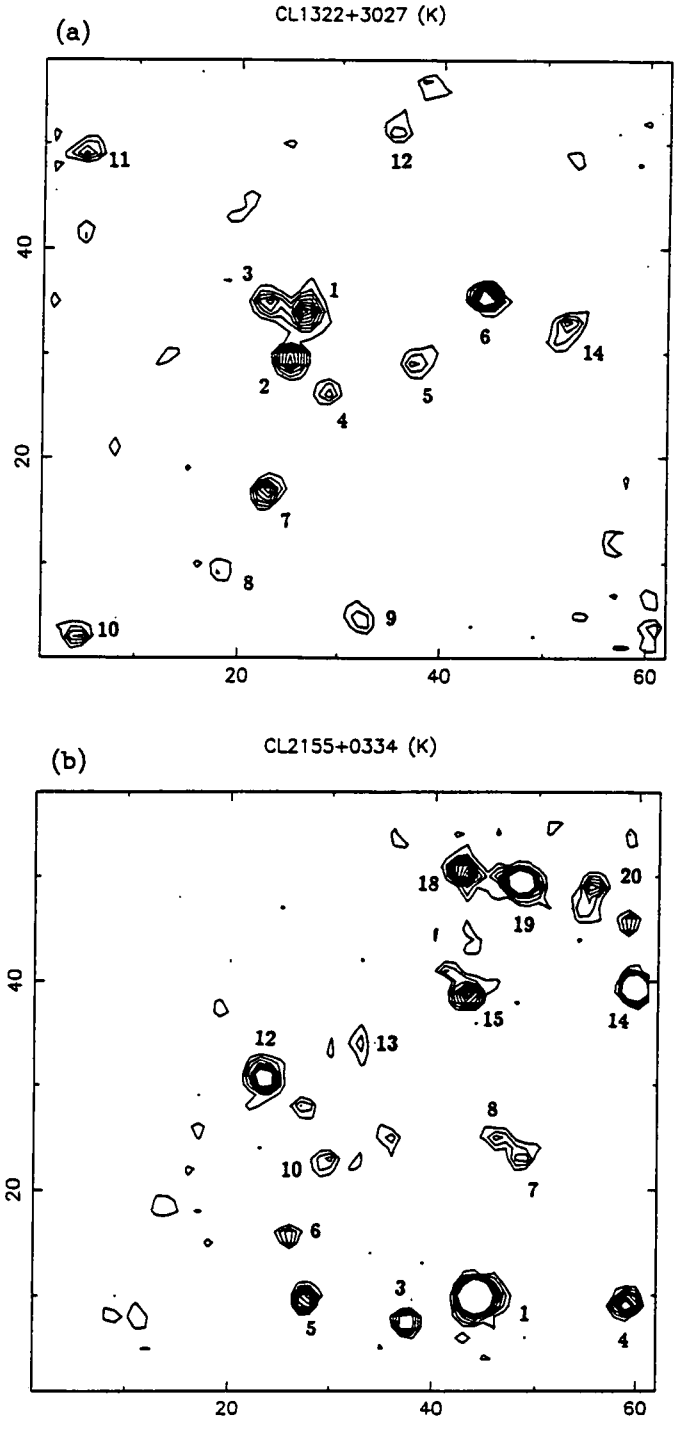

Figure 5.5. **(a)** Contour plot of the Cl1322+3027 K-band image. Scale and orientation as in Figure 5.3. The total exposure time is 3200 s. The contours follow a linear intensity scale, the lowest corresponding to $\mu_K = 21\overset{m}{.}41$ arcsec^{-2} (2σ above average sky level) and the highest to $\mu_K = 18\overset{m}{.}91$ arcsec^{-2} (20σ). **(b)** Same as (a) for Cl2155+0334. The total exposure time is 17600 s. The lowest contour corresponds to $\mu_K = 22\overset{m}{.}99$ arcsec^{-2} and the highest to $\mu_K = 20\overset{m}{.}49$ arcsec^{-2}.

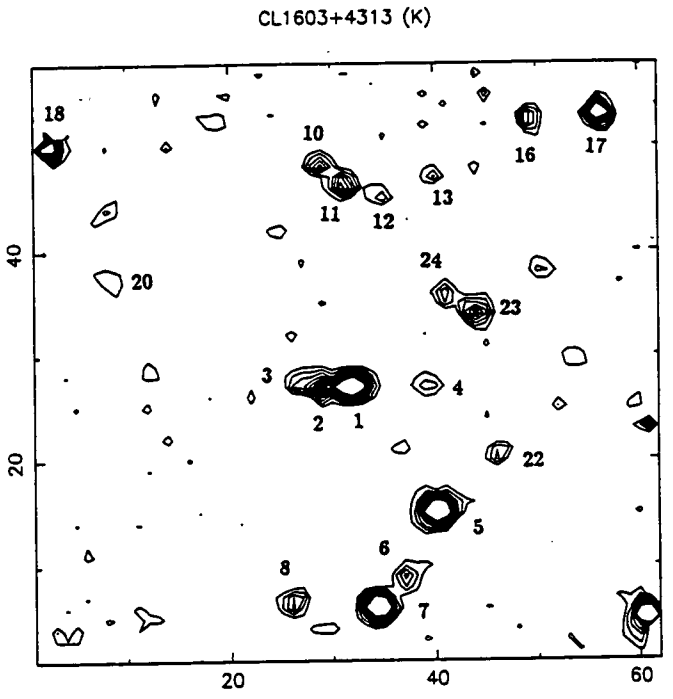

Figure 5.6. Contour plot of the Cl1603+4313 K-band image. Scale and orientation as in Figure 5.3. The total exposure time is 20560 s. The contours follow a linear intensity scale, the lowest corresponding to $\mu_K = 22\overset{m}{.}75$ arcsec^{-2} (2σ above average sky level) and the highest to $\mu_K = 20\overset{m}{.}25$ arcsec^{-2} (20σ).

Table 5.3: Log of the optical observations for the high z clusters.

Cluster	Telescope	Instrument	Detector	Scale ($''/pixel$)	Date	Seeing	Band	Exposure (s)
J1888.16CL	3.9 m AAT	Prime Focus (f/3.3)	RCA (320 × 512)	0.49	1982 Aug 27/28	1.″2	V	800
	"	"	"	"	"	1.″2	I	800
Cl0317+1521	4.2 m WHT	Taurus II (f/4)	GEC–EEV (800 × 1180)	0.27	1990 Sep 11/12	1.″1	V	2000
	"	"	"	"	"	1.″1	I	1200
Cl1322+3029	4.2 m WHT	Taurus II (f/4)	GEC (385 × 578)	0.27	1989 Jun 26/27	0.″8	V	2400
	"	"	"	"	1989 Mar 28/29	0.″9	I	1200
Cl0020+0407	3.9 m AAT	Prime Focus (f/3.3)	RCA (320 × 512)	0.49	1990 Jun 22/23	1.″2	V	2000
	"	Prime Focus (f/2)	Thompson (1024 × 1024)	0.50	1989 July 7/8	1.″0	I	1000
Cl1322+3027	4.2 m WHT	Taurus II (f/4)	GEC (385 × 578)	0.27	1989 Jun 26/27	0.″8	V	2400
	"	"	"	"	1989 Mar 28/29	0.″9	I	1200
Cl2155+0334	3.9 m AAT	Prime Focus (f/3.3)	RCA (320 × 512)	0.49	1990 Jun 21/22	2.″5	V	2000
	"	"	"	"	"	2.″5	I	1000
Cl1603+4313	4.2 m WHT	Taurus II (f/4)	GEC–EEV (800 × 1180)	0.27	1990 July 21/22	0.″8	V	8000
	"	"	"	"	1989 July 23/24	0.″9	I	12000

was chosen to be much smaller than the scale of the flat-field variations but larger than any residual object. The cluster frames were divided by this large-scale flat-field. This reduced the large-scale variations to a level comparable to the pixel-to-pixel variations on the sky. The images taken using an RCA-CCD presented some fringes, especially in the I band. These were removed by subtracting suitably-scaled fringe frames. The exception to the above procedures are the images of the cluster Cl1603+4313. These were obtained in the same observing run as the ones of 0016+16, using the *in-field chopping* technique. See §4.2.2 for a description.

Absolute photometric calibration was provided by the analysis of images of standard stars of the Landolt (1983) and Graham (1982) lists, and the zero-point errors were $\lesssim 0\overset{m}{.}02$. Photometry was performed using apertures that match those used in the IR. Similar error analysis to the ones described in previous chapters yielded the internal photometric errors shown in Figure 5.7.

The use of different telescopes, instruments and CCD detectors means that the photometry for the clusters is in slightly different systems. The differences are negligible in V, but in I some colour terms exist. Using SEDs for galaxies of different types, we have estimated the size of this effect. The differences in I response increase for redder objects, and therefore the colour changes between systems are maximum for E/S0s in the high redshift range. In $(I-K)$, the variations can reach $\sim 0\overset{m}{.}1$ for an elliptical at $z = 0.9$; in $(V-I)$ the maximum change is $\sim 0\overset{m}{.}07$. We have not corrected for those colour terms because the standard stars used do not span a wide enough colour range. Instead, we have used the appropriate filter + detector response curve in every case when computing the non-evolutionary predictions, which effectively removes this problem from our analysis.

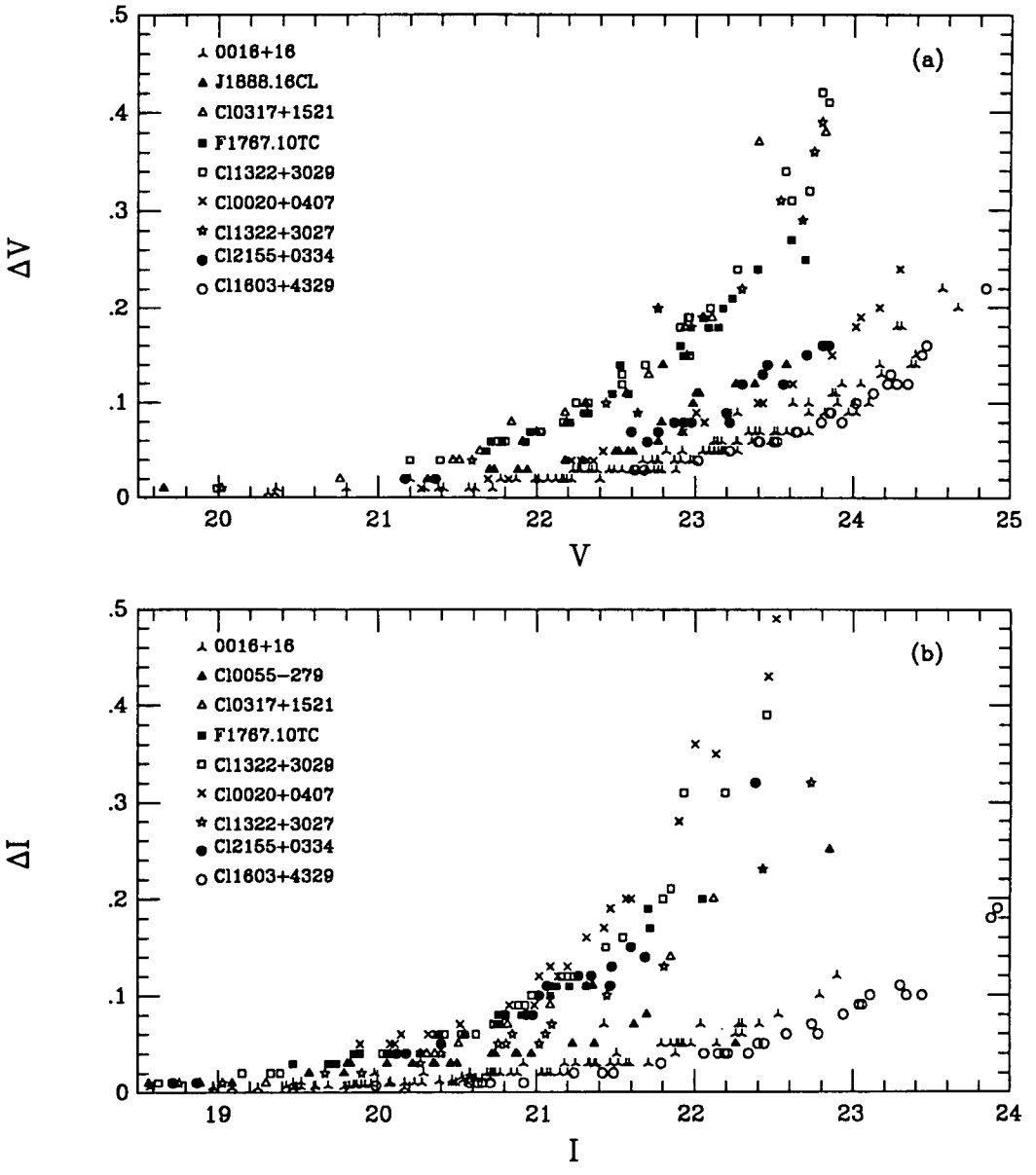

Figure 5.7. Internal photometric errors in the optical photometry as a function of the V and I magnitudes for the high-z cluster sample. The field-to-field variations come from differences in exposure time, observing conditions, telescopes and instruments.

5.4 Photometric catalogue

The final K magnitudes, colours and adopted internal 1σ errors are shown in Tables 5.4 (a) to (g). The numbering scheme is our own one in all cases except for J1888.16CL, where we adopt that of Couch, Shanks and Pence (1985). In this cluster, four objects not present in their original optical catalogue were detected in K. They have been numbered A1–A4. Similar tables for 0016+16 and F1767.10TC can be found in Chapter 4.

Depending on the galactic latitudes of the fields, some contamination from galactic stars can be expected. Figure 5.8 shows the locus of the stars on the $(V-I)$ vs. $(I-K)$ plane (Johnson 1966, Koornneef 1983, Cowie *et al.* 1991), together with the expected position of the galaxies of different spectral types at different redshifts (derived from the SEDs used to made the non-evolutionary prediction). Clearly, the stars are well separated from the galaxy positions, so we can use these colours to identify the stars. Most of the optical images have good seeing (see Table 5.3), and therefore we can use also image criteria to identify the stars. Colour and image criteria give very good agreement. The objects classified as stars have been marked '*' on the tables, and excluded from the analysis.

This catalogue presents essentially complete K-selected samples for each field. In total 160 galaxies are detected in the high z cluster sample, an average of ~ 18 per cluster. The way in which they have been selected guarantees that the photometric errors in K are always $\lesssim 0^m.2$. The errors in the optical photometry, however, depend on the colours of the objects and the total exposure times of the images, which cover a wide range. In most cases, the errors in the optical are comparable or better than the ones in the IR, but for a few very red objects they are slightly worse (see Table 5.4). In three cases, a K-detected object was not seen in the V band. For those, $\sim 3\sigma$ lower limits on the colours are given in the tables. Since they are very few, they will not significantly affect our conclusions, but we will take them into account when necessary.

Table 5.4 (a). J1888.16CL Photometric Catalogue.

Aperture = 4.″8; $K \lesssim 18^m.4$

#	K	σ_K	$(V-I)$	σ_{V-I}	$(V-K)$	σ_{V-K}	$(I-K)$	σ_{I-K}
1	16.01	0.03	2.22	0.02	5.30	0.04	3.08	0.03
31	16.09	0.03	1.09	0.01	3.57	0.03	2.48	0.03
5	16.43	0.05	2.13	0.04	5.27	0.06	3.14	0.05
27	16.82	0.05	2.15	0.04	5.12	0.06	2.97	0.05
21	17.25	0.10	2.31	0.07	5.52	0.12	3.21	0.10
26	17.34	0.08	1.83	0.05	4.84	0.09	3.01	0.09
22	17.41	0.12	2.02	0.06	5.11	0.13	3.09	0.12
46	17.41	0.12	1.66	0.04	4.47	0.12	2.81	0.12
15	17.52	0.11	2.18	0.08	5.40	0.13	3.22	0.12
28	17.70	0.18	2.14	0.06	4.80	0.19	2.66	0.18
2	17.88	0.13	1.86	0.06	4.70	0.14	2.84	0.14
A3	17.94	0.20	1.00	0.13	5.32	0.23	4.32	0.21
A1	17.98	0.18	1.44	0.18	4.82	0.23	3.38	0.21
30	18.02	0.23	1.73	0.06	4.59	0.24	2.86	0.23
7	18.02	0.16	1.82	0.04	3.86	0.16	2.04	0.16
14	18.20	0.20	1.42	0.06	4.09	0.20	2.67	0.20
A2	18.23	0.23	0.73	0.29	5.35	0.27	4.62	0.34
11	18.34	0.22	1.76	0.14	5.04	0.25	3.28	0.23

Table 5.4 (b). Cl0317+1521 Photometric Catalogue.

Aperture = 4.″8; $K \lesssim 18^m.3$

#	K	σ_K	$(V-I)$	σ_{V-I}	$(V-K)$	σ_{V-K}	$(I-K)$	σ_{I-K}
*12	16.55	0.05	3.11	0.07	5.45	0.08	2.34	0.05
*16	16.75	0.06	1.60	0.01	3.27	0.06	1.67	0.06
4	16.80	0.06	1.83	0.06	4.84	0.08	3.01	0.07
3	17.03	0.08	2.08	0.07	4.88	0.10	2.80	0.08
*10	17.25	0.11	2.17	0.04	4.22	0.12	2.05	0.11
1	17.26	0.11	1.88	0.09	4.93	0.14	3.05	0.12
5	17.28	0.08	1.67	0.10	4.90	0.12	3.23	0.10
14	17.74	0.14	1.95	0.10	4.58	0.17	2.63	0.14
*8	17.77	0.18	2.64	0.14	4.94	0.22	2.31	0.18
*18	17.82	0.15	3.00	0.37	5.58	0.40	2.58	0.15
6	18.14	0.19	1.29	0.09	3.70	0.20	2.41	0.20
9	18.27	0.20	1.24	0.06	3.24	0.20	2.00	0.20
15	18.27	0.20	1.22	0.14	4.04	0.23	2.82	0.22

Table 5.4 (c). Cl1322+3029 Photometric Catalogue.

Aperture = 6.″4; $K \lesssim 18^m.0$

#	K	σ_K	$(V-I)$	σ_{V-I}	$(V-K)$	σ_{V-K}	$(I-K)$	σ_{I-K}
5	16.13	0.06	2.70	0.07	5.89	0.09	3.20	0.06
1	16.14	0.05	2.65	0.07	5.66	0.08	3.01	0.05
33	16.20	0.08	1.36	0.02	3.79	0.08	2.43	0.08
3	16.77	0.08	2.93	0.20	6.19	0.21	3.26	0.09
*6	16.97	0.11	2.64	0.08	5.06	0.13	2.42	0.11
16	17.14	0.11	1.50	0.05	4.25	0.12	2.75	0.12
21	17.26	0.13	1.70	0.07	4.49	0.14	2.80	0.14
7	17.32	0.13	1.78	0.15	5.22	0.18	3.44	0.15
40	17.37	0.20	1.79	0.45	6.35	0.38	4.56	0.37
8	17.54	0.19	2.31	0.26	5.73	0.31	3.43	0.21
20	17.60	0.23	1.81	0.22	5.37	0.30	3.56	0.26
32	17.79	0.20	2.35	0.16	5.18	0.25	2.83	0.21
4	17.97	0.27	1.83	0.11	4.28	0.29	2.45	0.28
13	17.98	0.27	1.34	0.17	4.56	0.30	3.22	0.30

Table 5.4 (d). Cl0020+0407 Photometric Catalogue.

Aperture = 4.″8; $K \lesssim 18^m.4$

#	K	σ_K	$(V-I)$	σ_{V-I}	$(V-K)$	σ_{V-K}	$(I-K)$	σ_{I-K}
2	16.77	0.05	2.47	0.06	5.59	0.07	3.12	0.07
17	17.25	0.06	2.21	0.07	5.07	0.07	2.86	0.08
13	17.33	0.09	2.69	0.10	5.73	0.11	3.04	0.11
1	17.53	0.09	2.50	0.12	5.49	0.13	2.99	0.12
12	17.77	0.11	1.55	0.06	3.92	0.11	2.37	0.12
11	17.78	0.11	1.90	0.07	4.44	0.12	2.54	0.13
4	17.88	0.13	2.10	0.12	5.05	0.15	2.95	0.16
19	17.96	0.13	2.84	0.14	5.63	0.17	2.78	0.15
9	18.00	0.14	1.83	0.23	5.40	0.17	3.57	0.24
10	18.11	0.15	1.19	0.05	3.16	0.15	1.97	0.16
3	18.24	0.18	2.98	0.29	6.07	0.31	3.08	0.24
6	18.28	0.18	> 2.50	—	> 6.70	—	4.18	0.46
14	18.32	0.16	2.42	0.27	5.70	0.24	3.27	0.25
8	18.37	0.18	2.34	0.16	5.06	0.20	2.72	0.22
22	18.41	0.19	1.29	0.13	4.02	0.20	2.73	0.23

Table 5.4 (e). Cl1322+3027 Photometric Catalogue.

Aperture = 4.″8; $K \lesssim 18^{m}.2$

#	K	σ_K	$(V-I)$	σ_{V-I}	$(V-K)$	σ_{V-K}	$(I-K)$	σ_{I-K}
*6	16.45	0.05	2.83	0.04	5.14	0.06	2.31	0.05
1	16.50	0.05	2.77	0.11	5.94	0.12	3.17	0.05
2	16.67	0.05	2.74	0.09	5.97	0.10	3.23	0.05
3	16.96	0.07	2.78	0.19	6.09	0.20	3.31	0.08
7	17.09	0.07	2.59	0.19	5.89	0.20	3.31	0.08
5	17.50	0.10	2.99	0.39	6.30	0.40	3.31	0.11
14	17.54	0.10	2.10	0.16	5.41	0.18	3.31	0.12
*11	17.70	0.13	0.99	0.01	2.32	0.13	1.33	0.13
4	17.72	0.12	2.78	0.31	5.82	0.33	3.04	0.13
9	17.97	0.13	1.72	0.21	4.80	0.24	3.09	0.14
12	18.03	0.18	2.58	0.30	5.65	0.35	3.07	0.19
10	18.03	0.16	2.28	0.23	5.27	0.27	2.99	0.17
8	18.08	0.16	1.25	0.23	4.98	0.25	3.73	0.21

Table 5.4 (f). Cl2155+0334 Photometric Catalogue.

Aperture = 6.″4; $K \lesssim 19^{m}.3$

#	K	σ_K	$(V-I)$	σ_{V-I}	$(V-K)$	σ_{V-K}	$(I-K)$	σ_{I-K}
1	16.55	0.04	2.49	0.02	4.81	0.04	2.32	0.04
*14	17.03	0.05	2.45	0.02	4.14	0.05	1.69	0.05
19	17.35	0.06	2.52	0.07	5.35	0.08	2.83	0.07
12	17.66	0.07	2.20	0.09	4.94	0.10	2.74	0.09
18	18.01	0.09	1.85	0.15	5.19	0.13	3.34	0.15
*4	18.25	0.10	3.10	0.09	4.97	0.13	1.87	0.11
15	18.30	0.10	1.99	0.18	5.16	0.17	3.17	0.15
5	18.35	0.11	3.05	0.18	5.50	0.19	2.45	0.14
3	18.68	0.15	2.54	0.16	4.88	0.19	2.34	0.18
20	18.77	0.17	1.43	0.36	5.04	0.23	3.61	0.36
7	19.06	0.16	2.04	0.11	3.92	0.18	1.88	0.18
8	19.14	0.18	1.95	0.11	3.79	0.20	1.84	0.20
10	19.17	0.20	1.61	0.18	4.13	0.23	2.52	0.24
6	19.20	0.20	2.23	0.20	4.51	0.25	2.28	0.24
13	19.23	0.25	1.50	0.14	3.54	0.26	2.04	0.28

Table 5.4 (g). Cl1603+4313 Photometric Catalogue.

Aperture = 4.″8; $K \lesssim 19^{m}.5$

#	K	σ_K	$(V-I)$	σ_{V-I}	$(V-K)$	σ_{V-K}	$(I-K)$	σ_{I-K}
7	17.18	0.05	2.74	0.06	6.22	0.08	3.48	0.05
5	17.19	0.05	2.87	0.06	6.31	0.08	3.44	0.05
1	17.25	0.05	2.44	0.04	5.77	0.06	3.33	0.05
2	17.81	0.06	2.56	0.08	5.99	0.10	3.43	0.06
17	18.20	0.12	2.88	0.08	5.60	0.14	2.72	0.12
*18	18.24	0.14	2.63	0.03	4.38	0.14	1.75	0.14
11	18.25	0.10	2.07	0.09	5.61	0.13	3.54	0.10
23	18.40	0.09	2.03	0.06	5.12	0.11	3.09	0.09
6	18.44	0.10	1.44	0.08	5.21	0.12	3.77	0.11
3	18.58	0.10	1.84	0.14	5.66	0.16	3.82	0.11
10	18.66	0.11	2.41	0.16	5.81	0.19	3.40	0.12
8	18.72	0.15	> 1.40	—	> 6.70	—	5.32	0.27
24	19.03	0.14	1.73	0.12	5.10	0.18	3.37	0.15
4	19.14	0.14	0.53	0.05	3.54	0.14	3.01	0.15
20	19.23	0.20	> 1.50	—	> 6.20	—	4.65	0.27
16	19.25	0.27	1.66	0.10	4.60	0.28	2.94	0.27
22	19.37	0.20	2.51	0.22	5.48	0.30	2.97	0.20
12	19.38	0.16	2.84	0.44	6.20	0.46	3.36	0.17
*13	19.47	0.28	2.22	0.07	4.17	0.29	1.95	0.28

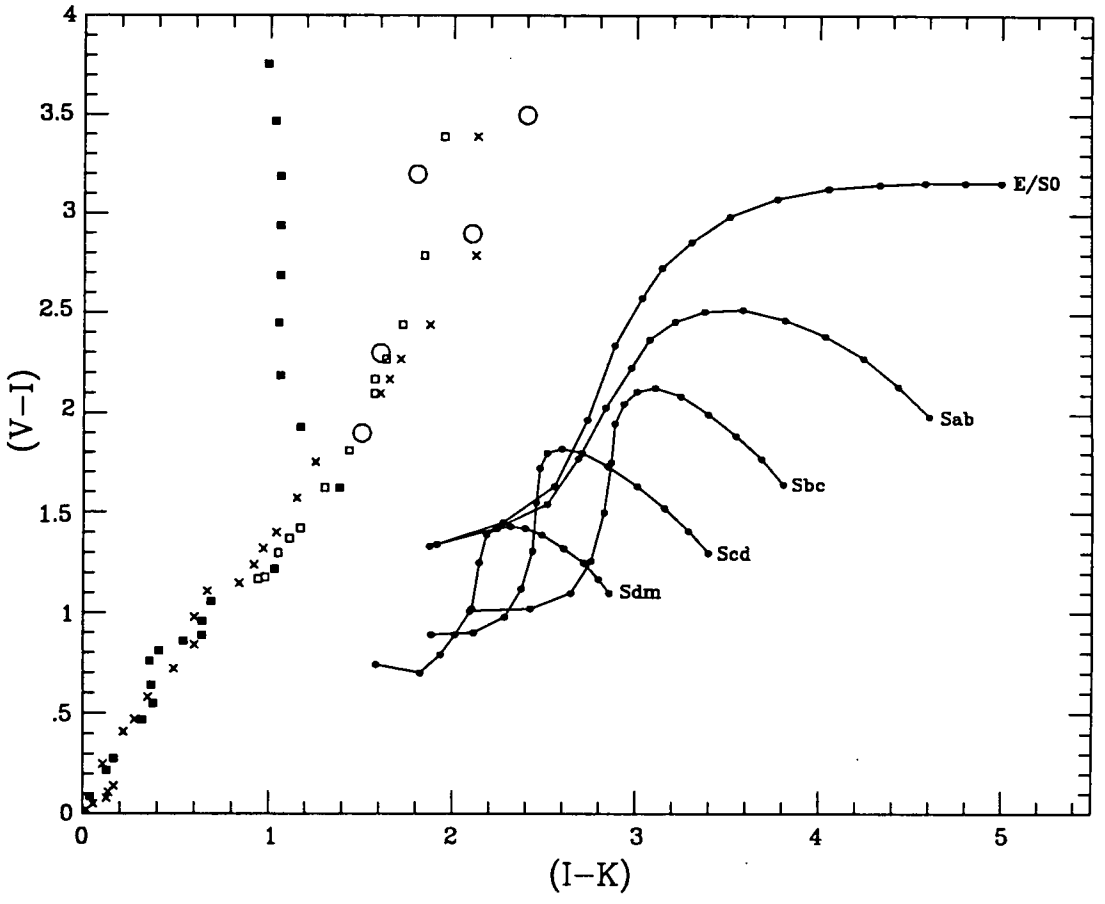

Figure 5.8. Expected position of the galactic stars on the $(V-I)$ vs. $(I-K)$ plane. Filled squares are Main Sequence stars; open squares are Giants and crosses are Supergiants (Johnson 1966, Koornneef 1983). Large open circles represent the stars that Cowie *et al.* (1991) found in their deep field images. For comparison, filled circles connected with solid lines show the locus of different types of galaxies as a function of redshift (with no evolution). The bluest point of each track in $(I-K)$ corresponds to $z = 0$ and the reddest to $z = 1.4$ in steps of 0.1.

5.5 The Colour-Magnitude diagrams

In previous chapters we have seen that the Colour-Magnitude (C-M) diagram of the cluster members contains important information regarding the evolutionary state of the galaxy population of the cluster. In particular, we have shown that the locus of the *red* members, that we can expect to be the high redshift counterparts of nearby cluster ellipticals, can be compared with the position that present day ellipticals would have in such diagram when redshift- and distance-related corrections are taken into account. The observed differences can, then, be interpreted in terms of galaxy evolution.

Note that we will always keep to the policy of displaying the raw data. This will avoid deteriorating them with uncertain corrections. We will use the local data for Coma galaxies, for which precise photometric and morphological information exists, to predict the observed magnitudes and colours of unevolved early-type galaxies at the different redshifts.

5.5.1 Non-evolutionary predictions

Since we are trying to detect small changes in the colours of the red galaxies when compared with their present-day equivalents, it is important to be sure that we know, as accurately as possible, how nearby galaxies would look like if we could place them at such redshifts. Any inaccuracy in this *non-evolutionary prediction* would affect the interpretation of our data.

It is not trivial to predict the colours and magnitudes that present-day ellipticals would have in the redshift range spanned by our cluster sample. The photometric bands sample wavelengths that bear very little relation to the ones sampled at $z \sim 0$. Using a standard *K-correction* approach would be very uncertain, because of the lack of detailed

knowledge of the spectral energy distributions (SEDs) of different spectral-type galaxies in the relevant wavelength ranges (particularly the near-IR and UV) and the lack of morphological or spectral information for most of the objects in our sample. For that reason, in previous chapters we have developed an alternative method that we will now extend to the high z range. Essentially, we will link the observed bands with the rest-frame ones that lie closest to them and then use the observed magnitudes and colours of E and S0 galaxies in the Coma cluster (Bower 1990, Bower, Lucey & Ellis 1991) to build a *no-evolution* C-M diagram at high z.

The details of the procedure and the uncertainties involved were described in Chapters 3 and 4, and will not be repeated here. The main difference is that when the redshift increases, the observed V-band moves significantly shortwards of rest-frame U, in a range in which the shape of the SEDs varies substantially from object to object and is not very well known. However, as in the case of F1767.10TC, we find that for ellipticals the observed V_z magnitudes can be predicted from rest-frame U_o magnitudes and $(U-V)_o$ colours with reasonable accuracy. Sometimes, a linear relation between $V_z - U_o$ and $(U-V)_o$ proves to be a poor fit, and a quadratic expression is required.

Table 5.5 summarizes the transformation equations between the observed VIK magnitudes and the rest-frame $UVJH$ ones for each cluster, together with an estimate of the internal uncertainty (see Chapter 4 for a discussion of the systematic errors). We emphasize again that in every case we have used the response curves of the photometric bands that correspond to the observational filter+detector setting, which takes into account the small differences in the photometric systems.

Using these equations and taking into account the relevant aperture effects as before, we can transform Coma photometry (Bower 1990, Bower, Lucey & Ellis 1991) to the redshift of each cluster, and predict the *non-evolution* C-M line. The least-squares

Table 5.5: Non-evolutionary predictions for the high z clusters.

Cluster	z	Photometric transformations	$r.m.s.$	C-M relations
J1888.16CL	0.563	$U_o - V_z = -0.45$	0.020	$(V-I) = 4.460 - 0.090 \times I$
		$V_o - I_z = 0.898 - 0.063 \times (U-V)_o$	0.012	$(V-K) = 8.639 - 0.172 \times K$
		$J_o - K_z = 1.301 + 0.445 \times (J-H)_o$	0.020	$(I-K) = 4.678 - 0.094 \times K$
Cl0317+1521	0.583	$U_o - V_z = -0.51$	0.015	$(V-I) = 4.392 - 0.086 \times I$
		$V_o - I_z = 0.892 - 0.102 \times (U-V)_o$	0.020	$(V-K) = 8.679 - 0.169 \times K$
		$J_o - K_z = 1.383 + 0.332 \times (J-H)_o$	0.015	$(I-K) = 4.631 - 0.088 \times K$
Cl1322+3029	0.697	$U_o - V_z = -0.985 + 0.384 \times (U-V)_o - 0.170 \times (U-V)_o^2$	0.014	$(V-I) = 4.365 - 0.078 \times I$
		$V_o - I_z = 0.883 - 0.213 \times (U-V)_o$	0.023	$(V-K) = 8.976 - 0.166 \times K$
		$J_o - K_z = 1.555 + 0.110 \times (J-H)_o$	0.012	$(I-K) = 4.945 - 0.092 \times K$
Cl0020+0407	0.698	$U_o - V_z = -1.012 + 0.407 \times (U-V)_o - 0.175 \times (U-V)_o^2$	0.017	$(V-I) = 4.484 - 0.082 \times I$
		$V_o - I_z = 0.896 - 0.213 \times (U-V)_o$	0.020	$(V-K) = 9.122 - 0.174 \times K$
		$J_o - K_z = 1.555 + 0.110 \times (J-H)_o$	0.013	$(I-K) = 4.991 - 0.097 \times K$

Table 5.5: (Continued)

Cluster	z	Photometric transformations	*r.m.s.*	C-M relations
Cl1322+3027	0.751	$U_o - V_z = -0.92$	0.017	$(V-I) = 4.284 - 0.070 \times I$
		$V_o - I_z = 0.868 - 0.266 \times (U-V)_o$	0.025	$(V-K) = 9.191 - 0.168 \times K$
		$J_o - K_z = 1.620 + 0.027 \times (J-H)_o$	0.007	$(I-K) = 5.216 - 0.102 \times K$
Cl2155+0334	0.820	$U_o - V_z = -1.285 + 0.363 \times (U-V)_o - 0.227 \times (U-V)_o^2$	0.017	$(V-I) = 4.867 - 0.087 \times I$
		$V_o - I_z = 0.865 - 0.340 \times (U-V)_o$	0.019	$(V-K) = 10.040 - 0.197 \times K$
		$J_o - K_z = 1.696 - 0.073 \times (J-H)_o$	0.003	$(I-K) = 5.507 - 0.111 \times K$
Cl1603+4313	0.895	$U_o - V_z = -1.233 - 0.015 \times (U-V)_o - 0.125 \times (U-V)_o^2$	0.041	$(V-I) = 4.826 - 0.083 \times I$
		$V_o - I_z = 0.821 - 0.492 \times (U-V)_o$	0.022	$(V-K) = 10.496 - 0.204 \times K$
		$J_o - K_z = 1.756 - 0.148 \times (J-H)_o$	0.014	$(I-K) = 6.079 - 0.127 \times K$

linear fits to these lines are also shown in Table 5.5 for each colour. We have used H_o = 50 km s^{-1} Mpc^{-1} and $q_o = 0.5$. The predictions depend very weakly on q_o.

5.5.2 Galactic reddening

The effect of Galactic reddening, especially in the optical wavelengths, could significantly alter the observed colours of the galaxies and should therefore be taken into account. Fortunately, the Galactic latitudes are high enough in most cases to make this effect small. Since detailed studies of the reddening in the relevant directions are not available, we have used the Burstein & Heiles (1982) maps to estimate $E(B-V)$. These authors claim that, even though the absolute reddening scale (*i.e.* the reddening at the Galactic Poles) could be controversial, their *relative* reddening scale should be accurate to within 0.01 in $E(B-V)$ or 10% in A_λ (whichever is largest). Since we are comparing relative changes in colours for the different clusters, this should not introduce significant uncertainties. Moreover, the reddening correction for the Coma data comes from the same source.

Using these $E(B-V)$ values and the Galactic extinction law (Savage & Mathis 1979, Mathis 1990), we have computed the extinction in each band. The estimated relative uncertainty in $E(B-V)$ translates into relative (cluster-to-cluster) uncertainties in the absorption corrections of the order of $\delta A_V \sim 0\overset{m}{.}03$, $\delta A_I \sim 0\overset{m}{.}02$ and $\delta A_K \sim 0\overset{m}{.}004$. The Galactic coordinates, colour-excesses and absorption for each band in the direction of the clusters are presented in Table 5.6.

5.5.3 Individual Colour-Magnitude diagrams

Figures 5.9 to 5.15 show the C-M diagrams for the objects presented in Table 5.4, excluding those objects deemed to be stars on the basis of their colours and images (§5.4). With the available information it is not possible to deal with the field contamination for individual

Table 5.6. Galactic extinction for the high z Cluster Sample.

Cluster	$l^{II}(^\circ)$	$b^{II}(^\circ)$	$E(B-V)^m$	$E(B-V)^a$	A_V	A_I	A_K
0016+16	111.6	−45.7	$\lesssim 0.03$	0.03	0.09	0.05	0.01
J1888.16CL	237.4	−88.7	$\lesssim 0.007$	0.00	0.00	0.00	0.00
Cl0317+1521	167.6	−34.2	~ 0.12	0.12	0.37	0.18	0.05
F1767.10TC	208.6	+33.5	< 0.03	0.00	0.00	0.00	0.00
Cl1322+3029	58.0	+82.2	$\lesssim 0.007$	0.00	0.00	0.00	0.00
Cl0020+0407	109.5	−57.7	$\lesssim 0.03$	0.03	0.09	0.05	0.01
Cl1322+3027	57.6	+82.1	$\lesssim 0.007$	0.00	0.00	0.00	0.00
Cl2155+0334	62.6	−38.0	$\lesssim 0.06$	0.06	0.19	0.09	0.02
Cl1603+4313	68.3	+48.1	< 0.03	0.00	0.00	0.00	0.00

Notes:

$E(B-V)^m$: as read in Burstein & Heiles (1982) maps.

$E(B-V)^a$: adopted taking into account the distance between contour levels in the maps.

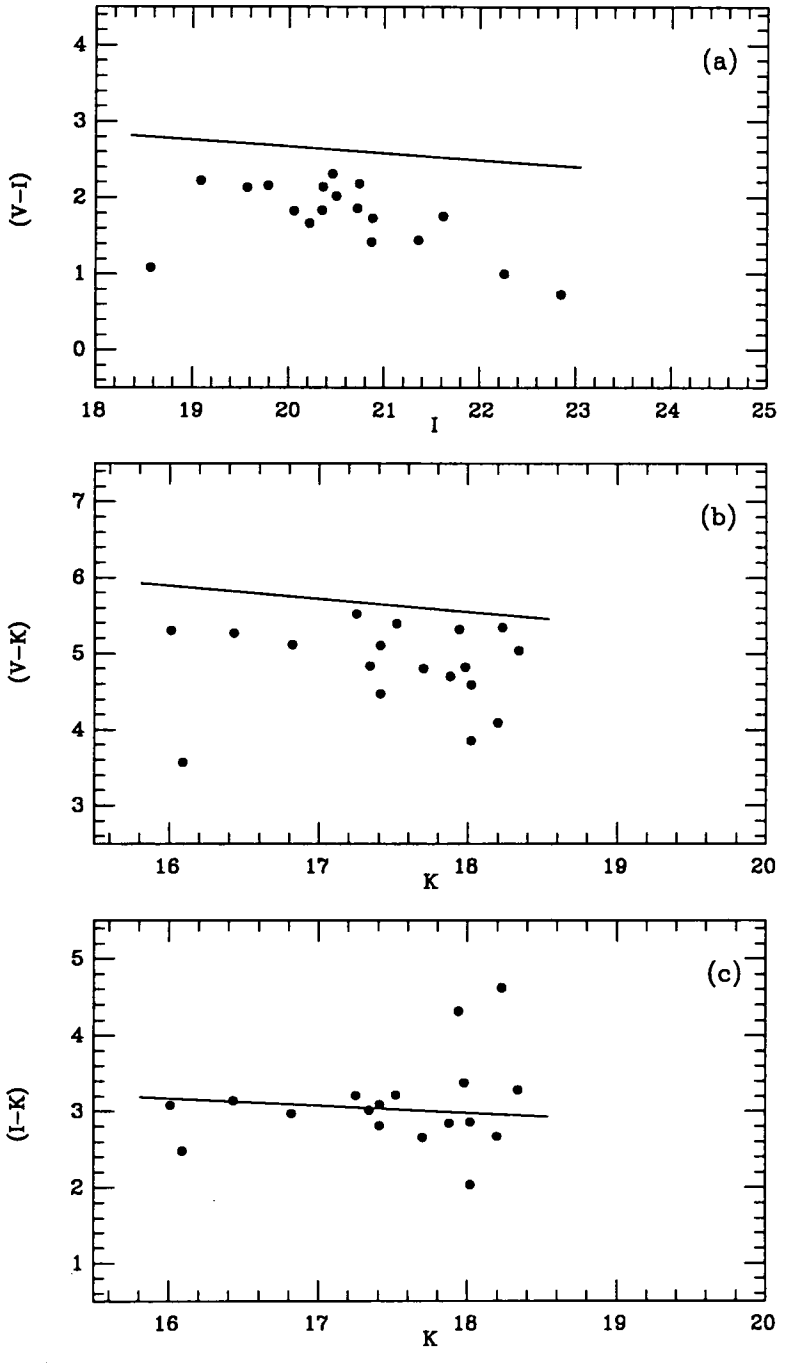

Figure 5.9. Colour-Magnitude diagrams for J1888.16CL (z = 0.563). The solid lines show the reddening-corrected non-evolutionary predictions for early-type galaxies obtained as described in text.

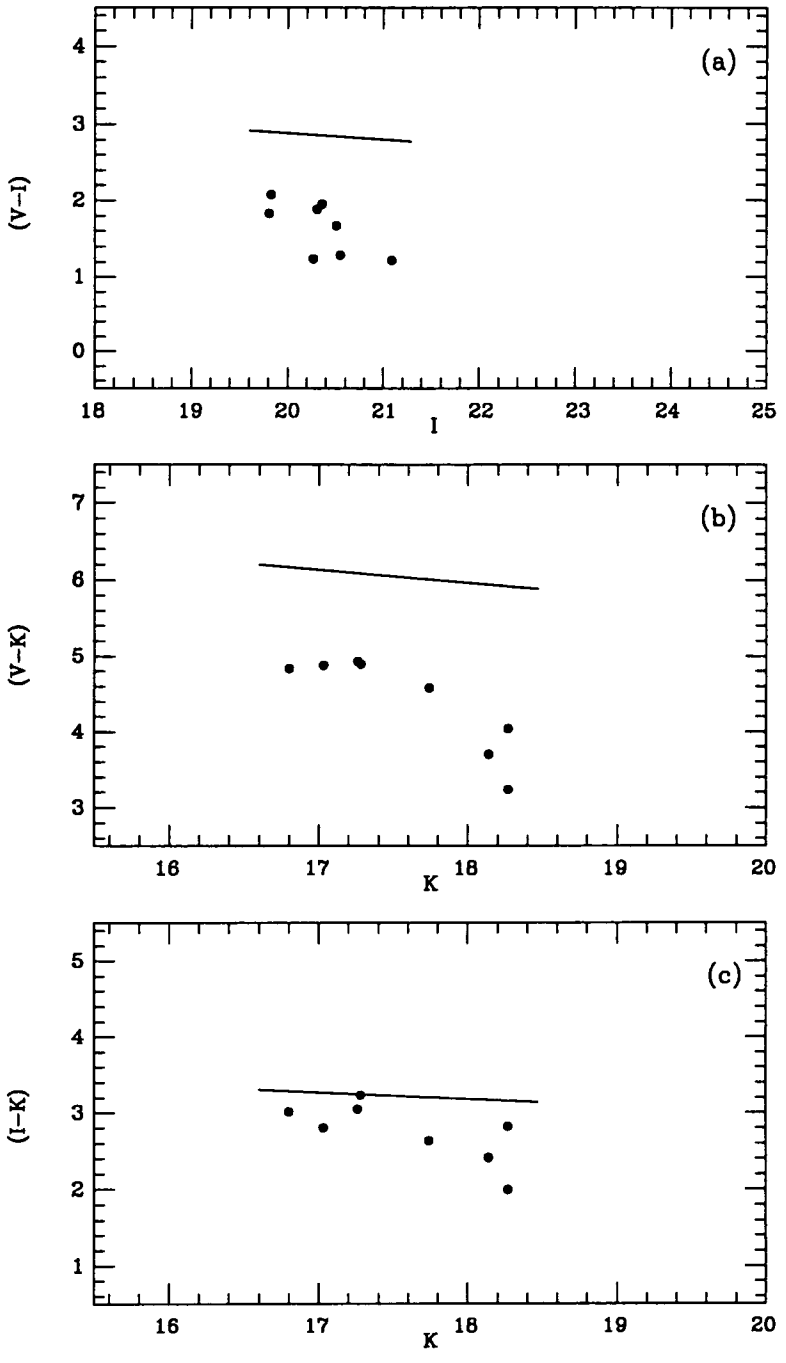

Figure 5.10. Same as Figure 5.9 for Cl0317+1521 ($z = 0.583$).

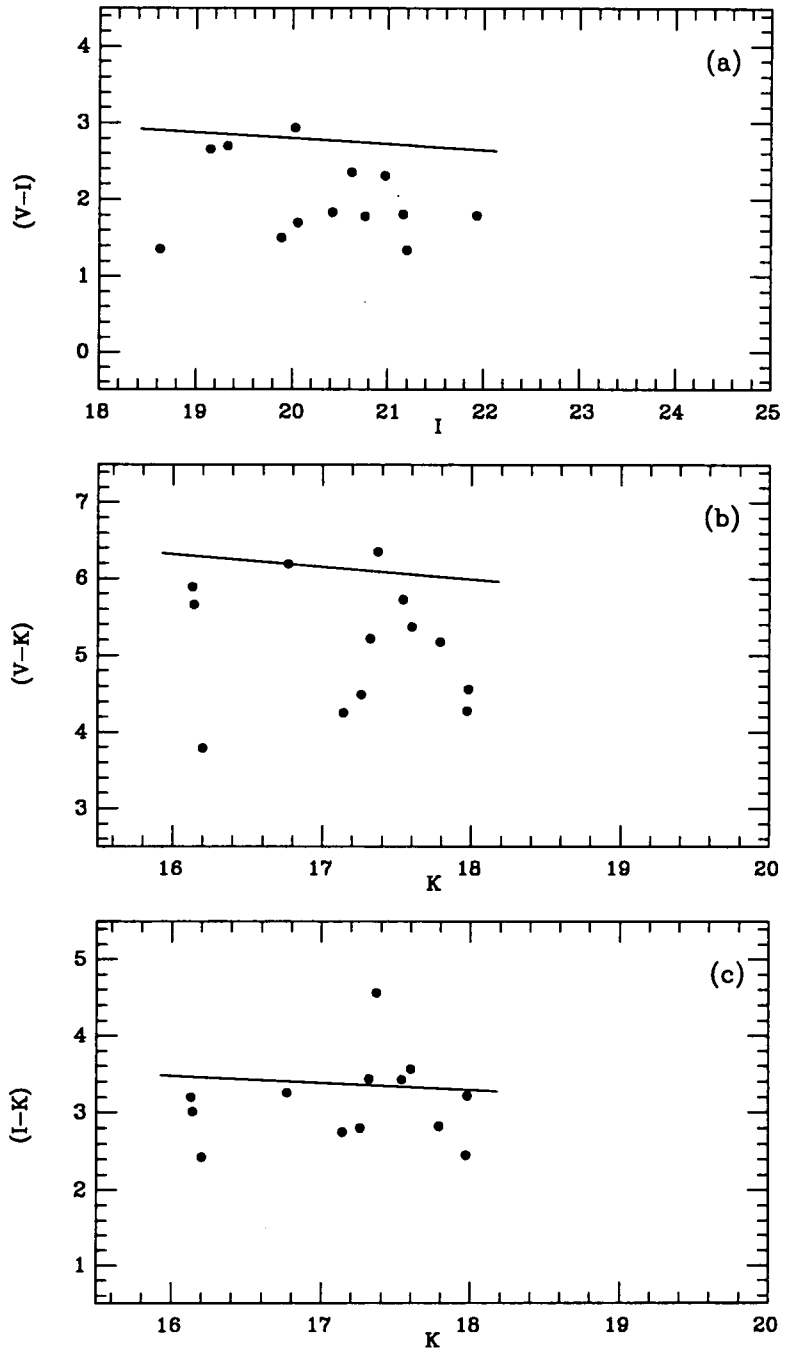

Figure 5.11. Same as Figure 5.9 for Cl1322+3029 ($z = 0.697$).

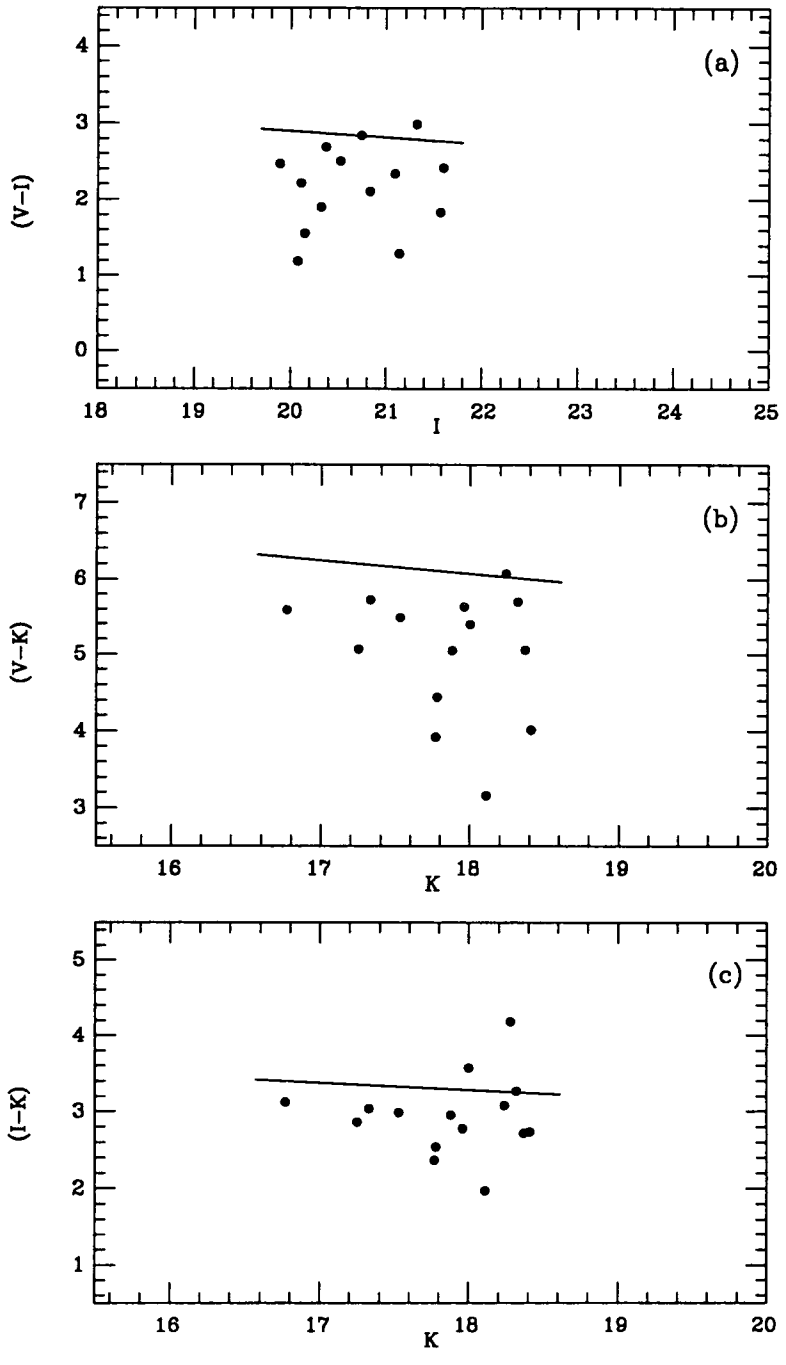

Figure 5.12. Same as Figure 5.9 for Cl0020+0407 ($z = 0.698$).

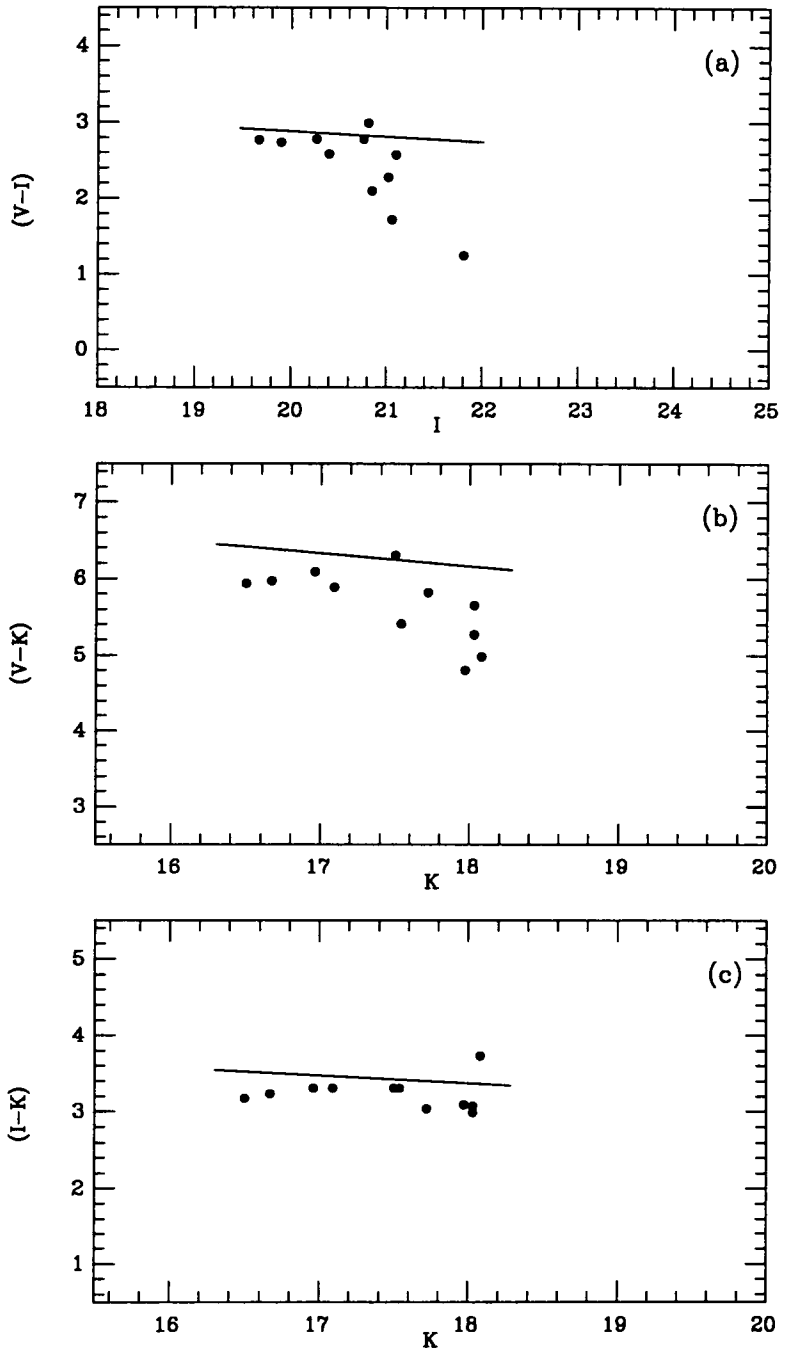

Figure 5.13. Same as Figure 5.9 for Cl1322+3027 ($z = 0.751$).

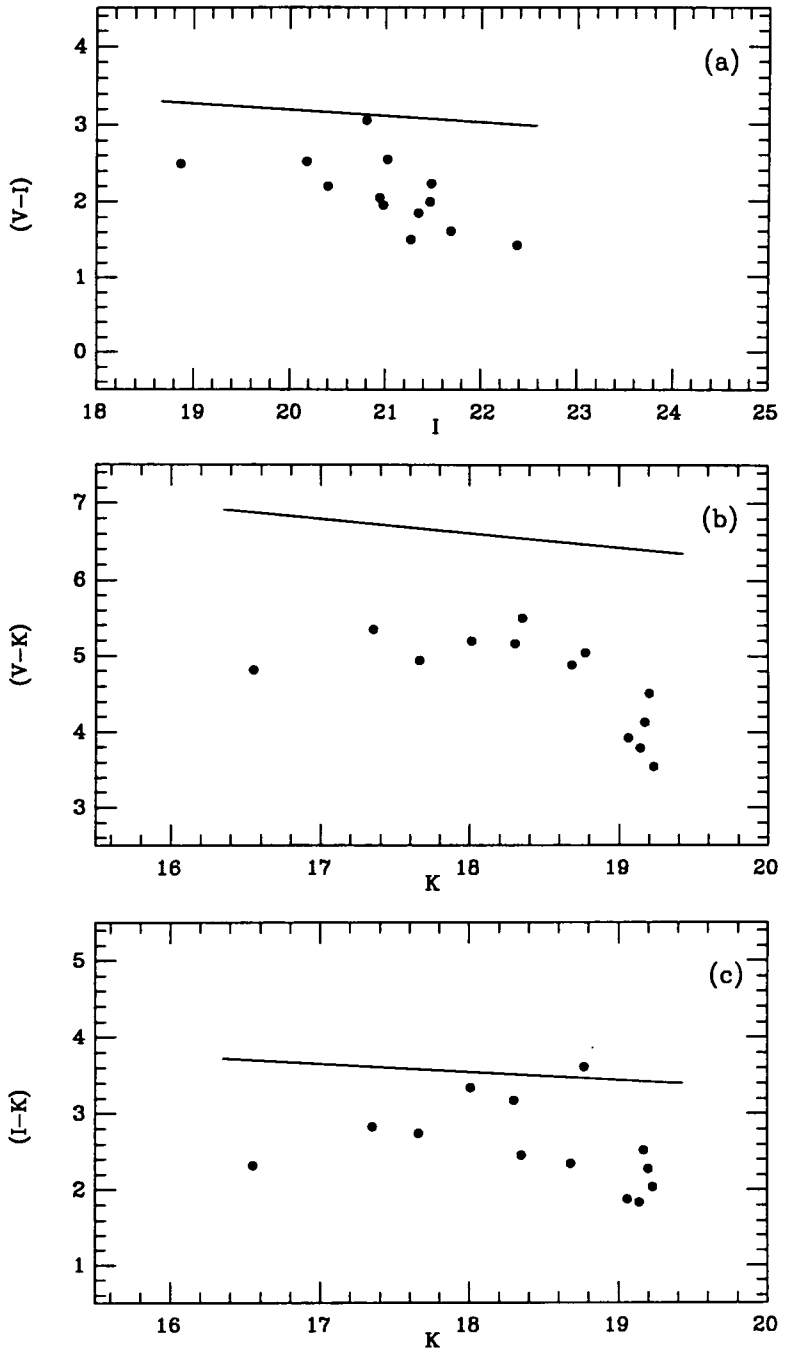

Figure 5.14. Same as Figure 5.9 for Cl2155+0334 ($z = 0.820$).

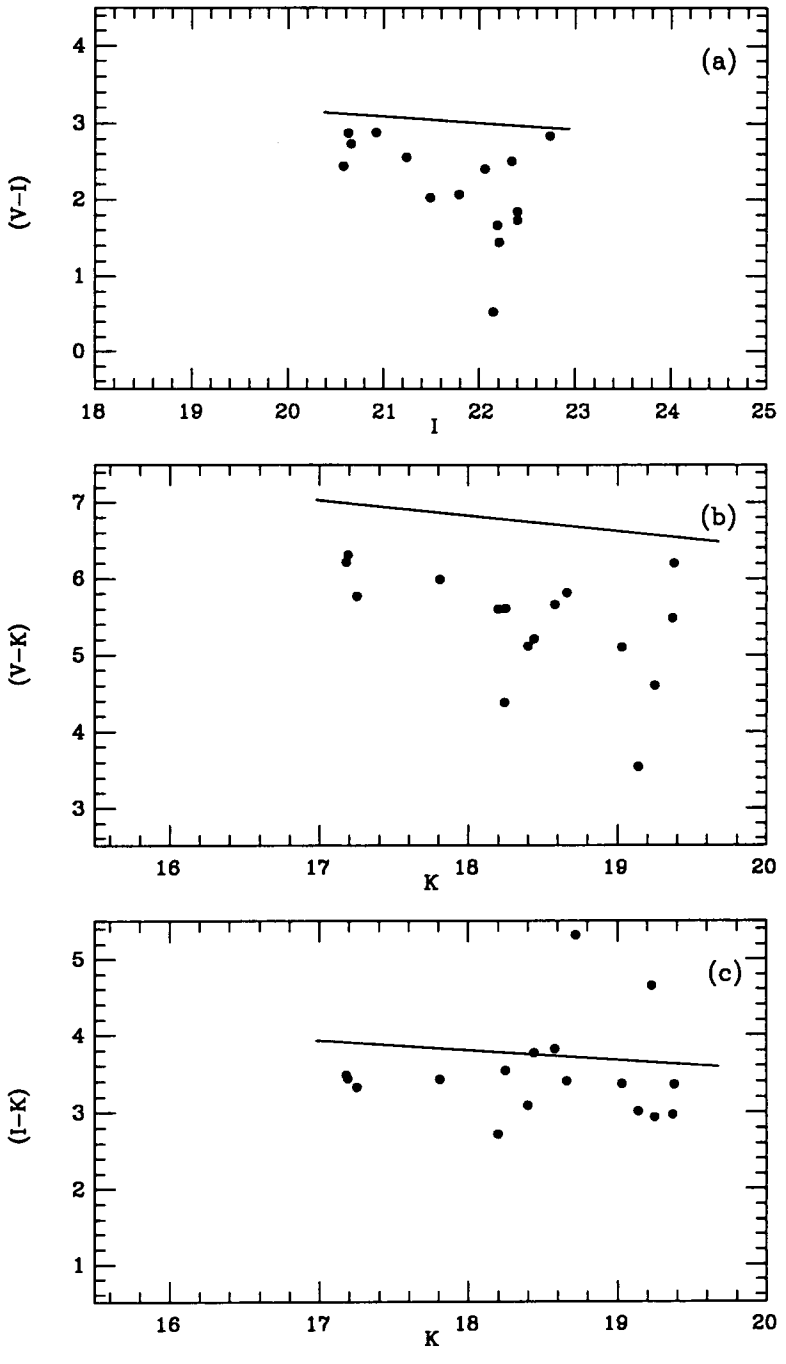

Figure 5.15. Same as Figure 5.9 for Cl1603+4313 ($z = 0.895$).

objects. In section 5.7 we will do that statistically. The solid lines show the predicted C-M lines (with no evolution, table 5.5) once the reddening has been taken into account. Similar diagrams for 0016+16 and F1767.10TC were presented in Chapter 4. The diagrams for all the clusters have been plotted on the same scale to make a direct comparison easier.

The small number of objects per cluster, and the lack of membership information prevents us to draw any strong conclusion from these diagrams before a detailed statistical study is carried out. However, two facts became immediately apparent. First, that the $(I-K)$ vs. K diagrams tend to show smaller scatter than the other two, although a few objects with very red $(I-K)$ colours (*i.e.* $\gtrsim 1^m.0$ redder than the predicted line) and *normal* $(V-I)$ and $(V-K)$ are present in some of the fields. Some examples were also found in 0016+16. We will come back to them in future sections. We also see that a vast majority of objects lie *bluewards* of the non-evolution prediction. This is not surprising since the lines should represent the locus of the reddest galaxies in a cluster in the absence of evolution. However, if the cluster members had not experienced any colour evolution, we would expect a substantial fraction of the galaxies to scatter above and below the lines. This gives us a preliminary indication that we are witnessing some colour evolution, that we will try to quantify and interpret in the following sections.

It is also apparent that there are significant cluster-to-cluster differences. They are more apparent in $(V-I)$ and $(V-K)$ than in $(I-K)$. This is not surprising, since any differences in evolutionary state of the galaxies (*i.e.*, different amounts of present or recent star formation) should affect more strongly the rest-frame ultraviolet wavelength. Differences in the field contamination also play a role. For instance, the diagrams for Cl0317+1521 and Cl2155+0334 show a remarkable lack of red objects in $(V-I)$ and $(I-K)$. These clusters are rather poor, since the number of objects detected (after taking into account the field contamination, see §5.7) is very small. The Cl0317+1521 field contains a relatively high number of stars, and therefore it could have been selected as a

cluster due to an enhancement on apparent object density produced by Galactic stars and not galaxies. In the Cl2155+0334 field only 5 cluster members were found after obtaining 20 spectra (Dressler 1991, *private communication*).

5.5.4 Combined Colour-Magnitude diagrams

To improve the statistics, we have combined the different clusters in redshift bins. Given the distribution in z, the obvious choice is to group the clusters in three bins: 0016+16, J1888.16CL and Cl0317+1521 ($\langle z \rangle = 0.56$); F1767.10TC, Cl1322+3029, Cl0020+0407 and Cl1322+3027 ($\langle z \rangle = 0.70$); Cl2155+0334 and Cl1603+4313 ($\langle z \rangle = 0.86$).

The combination of the clusters in redshift bins (*i.e., putting* them at a common z) involves correcting for differential redshift effects and for small differences in the photometric systems. To do this rigorously, we need redshift and spectral shape information for all the objects, but, since the redshift bins are relatively narrow, it can be done with enough accuracy for our purposes in the following way: the colours are zero-pointed to the reddening-corrected non-evolutionary line, *i.e.*, to a present-day elliptical of the same magnitude. This is done by subtracting the predicted colour (at the observed magnitude) from the observed colour. The relative colours will be called $\Delta(V-I)$, $\Delta(V-K)$ and $\Delta(I-K)$. This is equivalent to applying a relative K-correction to the colours of the cluster ellipticals, and putting them in the same photometric system. For the field objects and the non-elliptical members, this is only correct to first order, but, since the *jump* in redshift is small ($\Delta z < 0.05$), this will not introduce any significant uncertainty: the difference in relative corrections for an E/S0 and a Sdm is < 0.02 in $(V-I)$ and < 0.03 in $(I-K)$. The magnitudes are corrected from the differences in distance modulus (we assume $q_o = 0.5$; if we use $q_o = 0.0$ the magnitudes change by less than 0.02). The differential K-corrections on the magnitudes are $\lesssim 0.15$ regardless of the SED and can be ignored

there since the C-M relations are very flat.* The corrections due to the relative change in projected linear size of the photometric aperture can be neglected in both magnitudes ($\lesssim 0^m.007$) and colours ($\lesssim 0^m.001$).

Figures 5.16 to 5.18 show the combined C-M diagrams for the three redshift bins. A present day elliptical galaxy would lie on the $\Delta(colour) = 0.0$ line. The preliminary conclusions outlined in §5.5.3 are reinforced with the improved statistics.

The $(I-K)$ C-M is much tighter than the other two for all the redshifts. A blueing trend with redshift is clear. Even for $\langle z \rangle = 0.56$, there are more objects lying below the $\Delta(I-K) = 0$ line than above, and the fraction of blue objects increases with z. A few very red objects are present in Figures 5.16 (c) and 5.16 (c). In Section 5.12 we will consider them.

The $(V-K)$ diagrams show a similar picture, but with substantially larger scatter. The blueing trend is less clear between $\langle z \rangle = 0.56$ and $\langle z \rangle = 0.70$, although it is evident at $\langle z \rangle = 0.86$.

In $(V-I)$ the same trend continues. For $\langle z \rangle = 0.56$ and $\langle z \rangle = 0.70$ there are very few objects above the line, and none for $\langle z \rangle = 0.86$. The scatter in this colour is remarkably similar for all redshifts.

Since the presence of field objects can distort the colour distributions, we will leave the discussion here until it has been accounted for.

---

* But we have taken them into account in the colours, at least to first order, by the procedure outlined above.

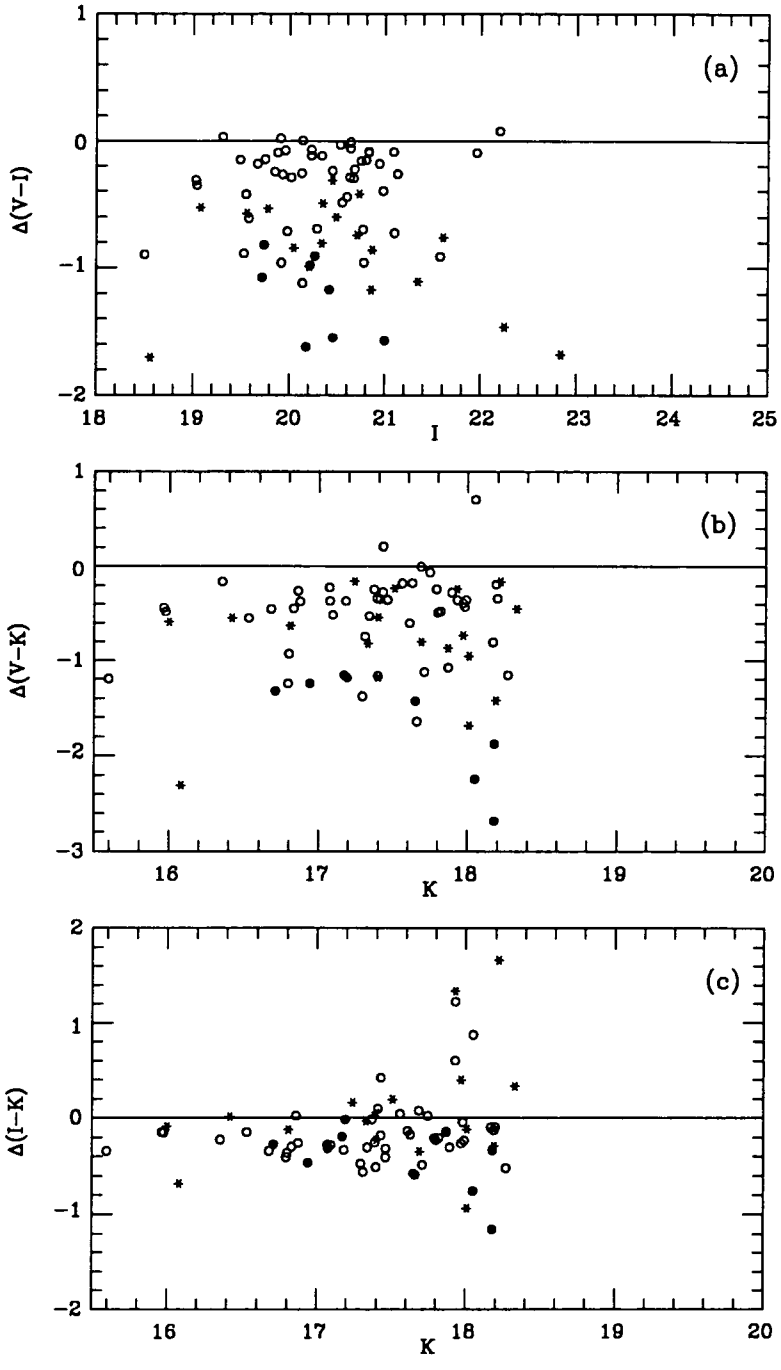

Figure 5.16. Combined Colour-Magnitude diagrams for the clusters 0016+16 (open circles), J1888.16CL (stars) and Cl0317+1521 (filed circles). The average redshift is $\langle z \rangle = 0.56$. See text for details.

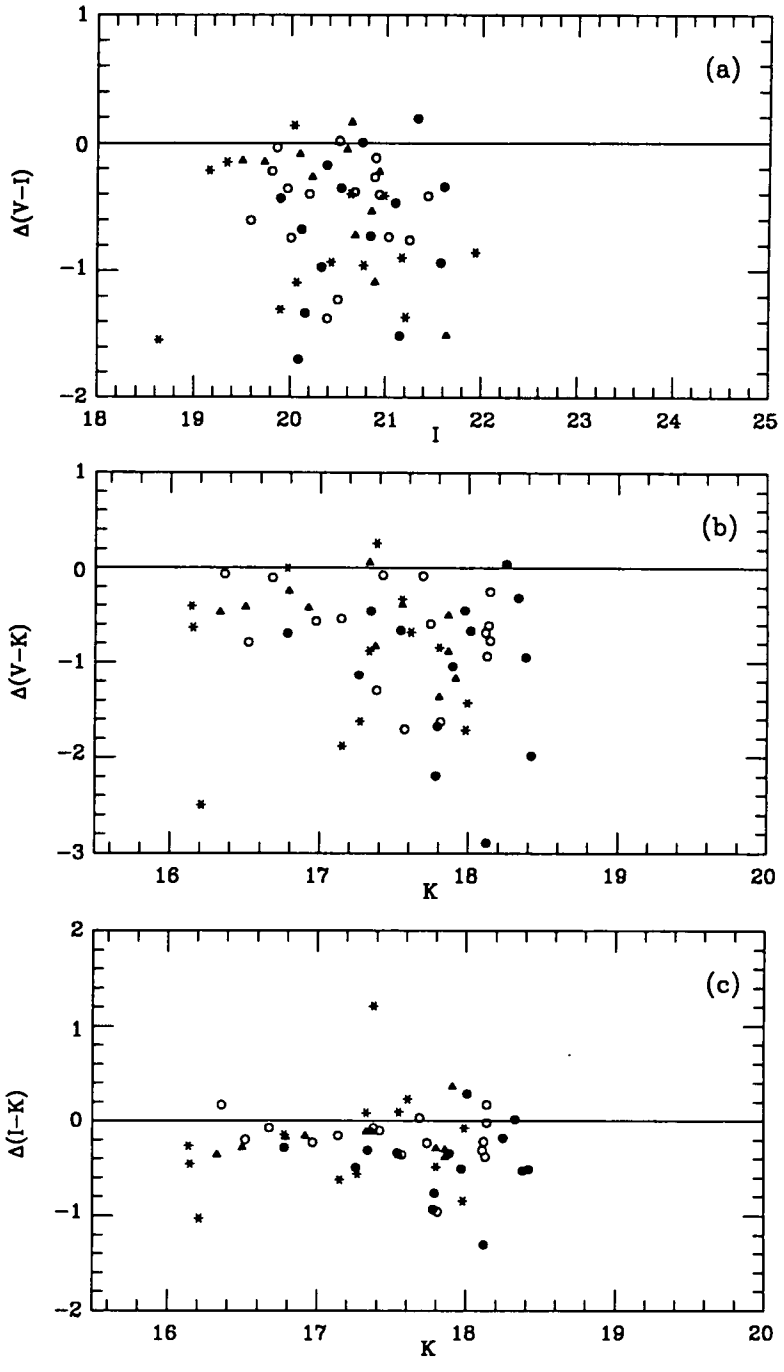

Figure 5.17. Combined Colour-Magnitude diagrams for the clusters F1767.10TC (open circles), Cl1322+3029 (stars), Cl0020+0407 (filled circles) and Cl1322+3027 (filled triangles). The average redshift is $\langle z \rangle = 0.70$. See text for details.

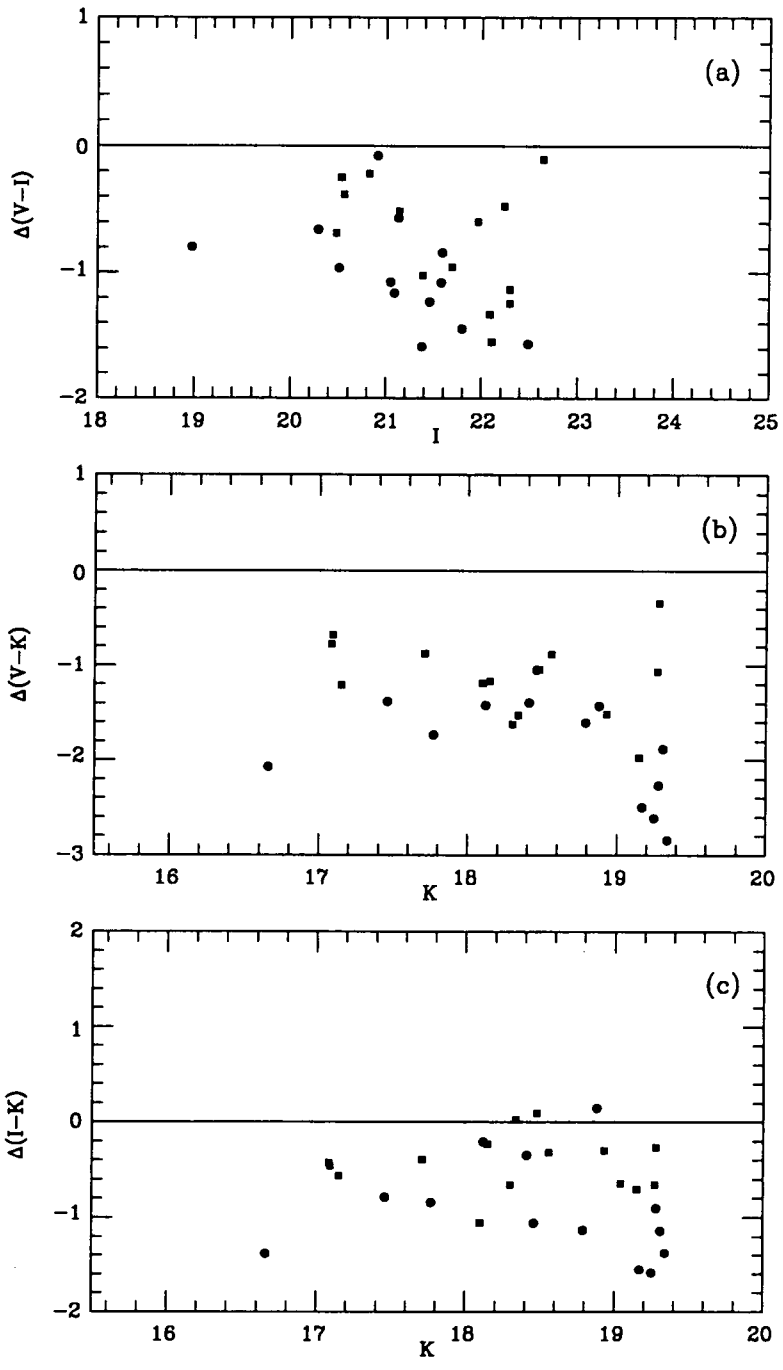

Figure 5.18. Combined Colour-Magnitude diagrams for the clusters Cl2155+0334 (filled circles) and Cl1603+4313 (filled squares). The average redshift is $\langle z \rangle = 0.86$. See text for details.

5.6 The Colour-Colour diagrams

Another way of presenting the same data is the Colour-Colour (C-C) diagram. In this section we present C-C diagrams for each redshift bin, combined in the way described in previous section. (Figures 5.19 to 5.21). For reference, we also show the expected locus of non-evolving present-day galaxies of different spectral types as a function of redshift in the same 'system' (*i.e.*, the colours are relative to those of an elliptical galaxy at the appropriate redshift).

As expected from the C-M diagrams, most of the objects sit on the bottom left quadrant, that is, they are bluer than present day ellipticals at these redshifts. For $\langle z \rangle = 0.56$ and $\langle z \rangle = 0.70$, a 'clump' of red objects appear near (0,0), being redder in $(I-K)$ for the lower z sample. Both $\langle z \rangle = 0.56$ and $\langle z \rangle = 0.70$ samples contain a few objects redder than the $\Delta(V-I) = 0.0$ line, but they are absent in the $\langle z \rangle = 0.86$ diagram.

What are the objects that are much redder in $(I-K)$ than the no-evolution prediction at each redshift? Looking at the no-evolution locus of the present day galaxies at different redshifts, the objects with $\Delta(I-K) \geq 0.5$ could, in principle, be background galaxies at very high z, although their luminosity would have to be unusually high. In that case we would also expect them to share the colour evolution seen in the clusters, but for larger look-back times. These puzzling objects do not seem to fit in our preconceived ideas about galaxy evolution (see §5.12).

5.7 Colour distributions

We present in this section the colour distributions of the objects in the high z cluster sample, grouped in the three redshift bins introduced in previous sections. We continue to

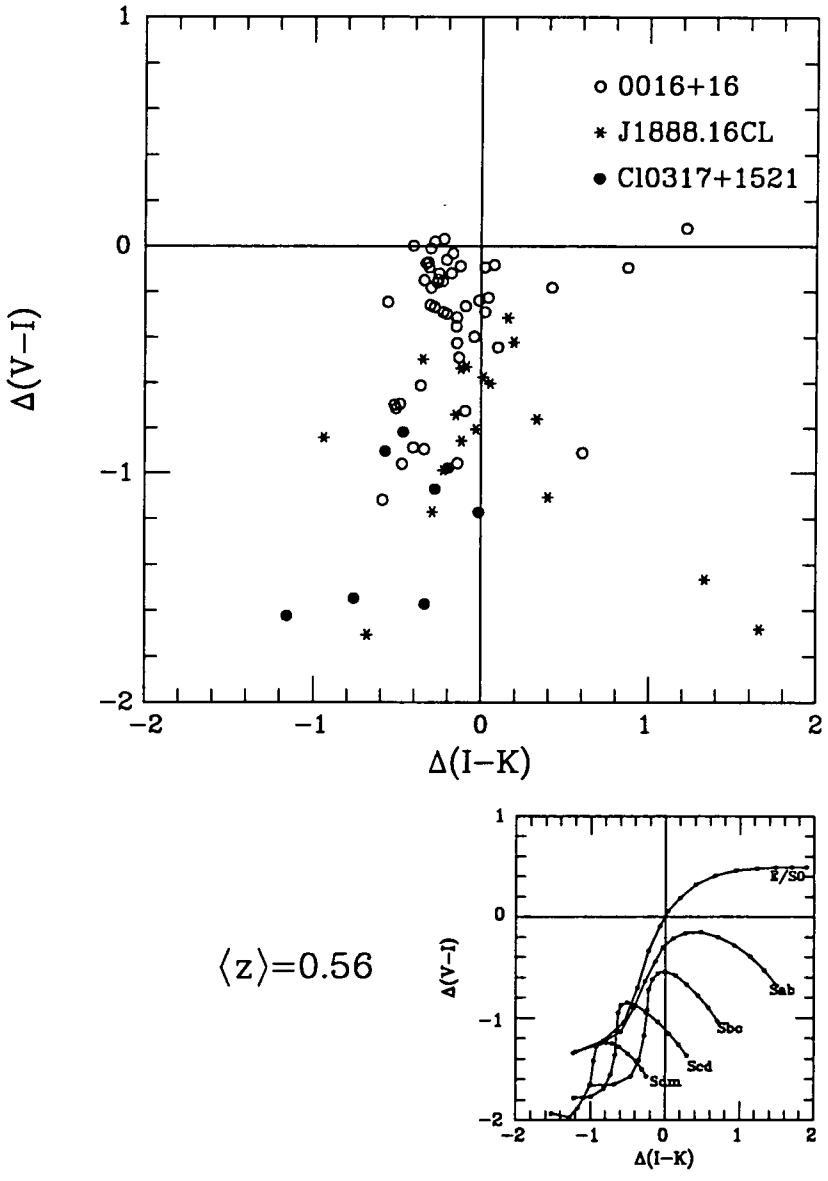

Figure 5.19. Combined Colour-Colour diagram for the clusters 0016+16 (open circles), J1888.16CL (stars) and Cl0317+1521 (filled circles). The average redshift is $\langle z \rangle = 0.56$. See text for details. For reference, the small figure at the bottom shows the locus on this diagram of different types of galaxies as a function of redshift (with no evolution). The colours have been zeroed to an E/S0 at this redshift. See figure 5.8 for details.

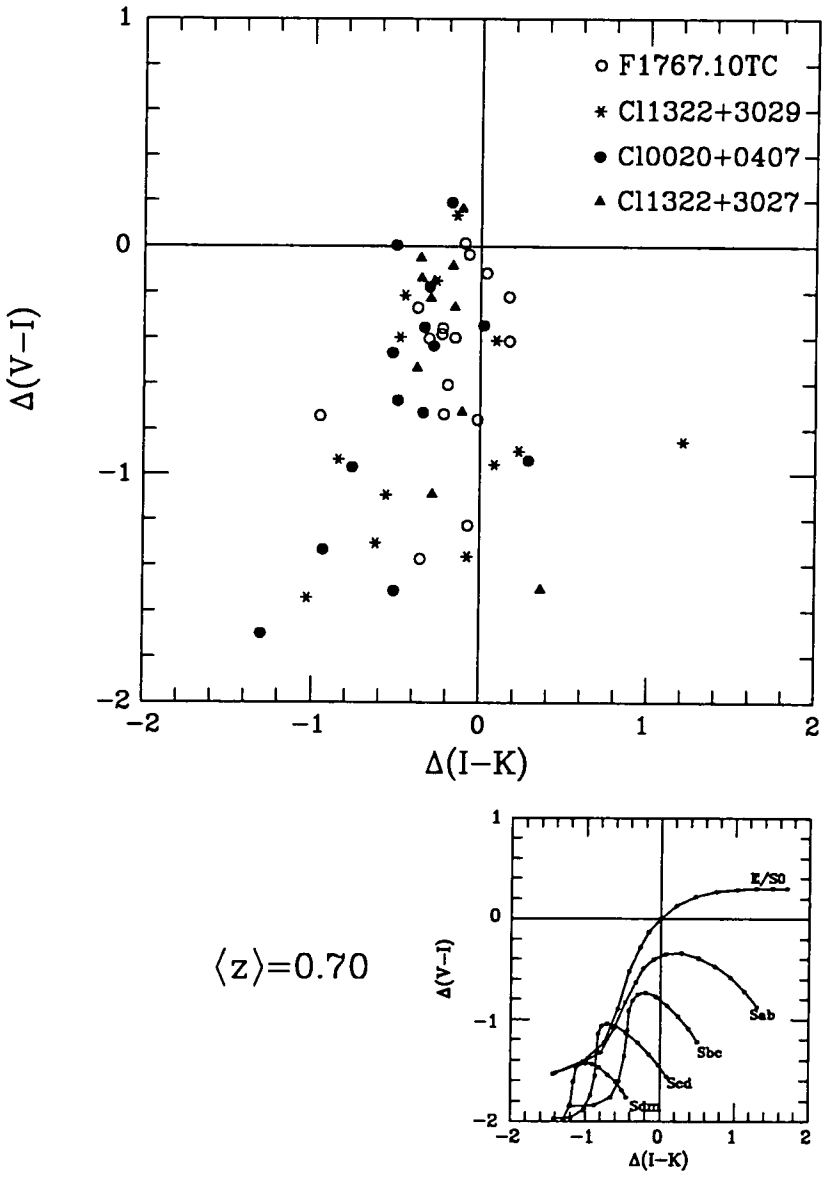

Figure 5.20. Same as figure 5.19 for the clusters F1767.10TC (open circles), Cl1322+3029 (stars), Cl0020+0407 (filled circles) and Cl1322+3027 (filled triangles). The average redshift is $\langle z \rangle = 0.70$.

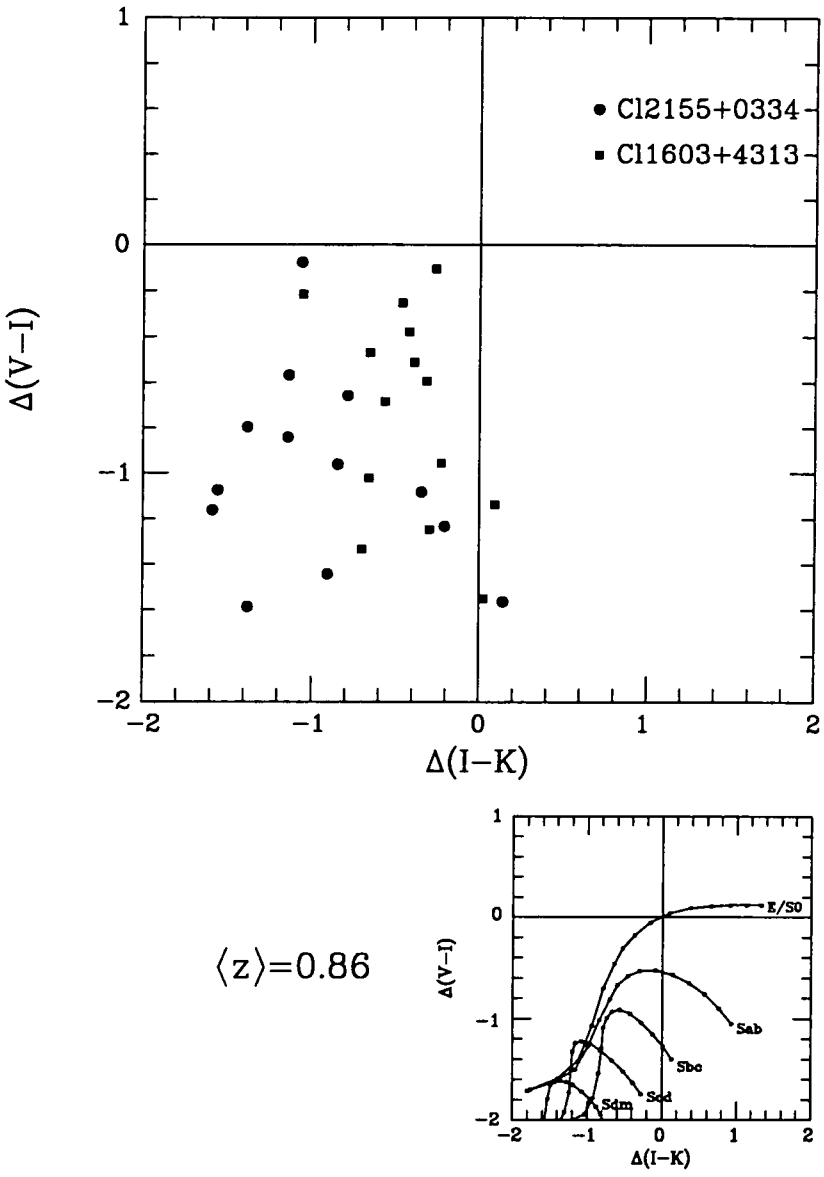

Figure 5.21. Same as figure 5.19 for clusters Cl2155+0334 (filled circles) and Cl1603+4313 (filled squares). The average redshift is $\langle z \rangle = 0.86$.

consider colours relative to a non-evolving present-day elliptical of the appropriate magnitude at the cluster redshift. The field contamination will be accounted for statistically from published field number counts.

5.7.1 Field contamination

Since no membership information is available for most of the objects in our sample, it is necessary to carry out a statistical correction of the field contamination. In every field, depending on the limiting magnitude and the properties of the cluster (redshift, richness, concentration, etc), we can expect different fractional contamination from field objects (foreground and background). First we will roughly estimate how severe this contamination will be.

Couch *et al.* (1991) describe a method to estimate the expected number of galaxies detected from a cluster and the field as a function of the cluster properties, redshift and limiting magnitude in different passbands. They use the cluster luminosity function for Abell 1942, a richness class 3 cluster at $z = 0.22$ (Couch & Newell 1984). Their method has been extended to the K band using Cowie *et al.* (1991)'s near-IR galaxy counts.

Using this method, we estimate that for an unevolving cluster like Abell 1942 at $z = 0.56$ we can expect to detect $N_{clust} \sim 16$ cluster members and $N_{field} \sim 3$ field galaxies per IRCAM frame to $K_{lim} = 18^m.0$.* For $z = 0.70$, $N_{clust} \sim 16$ and $N_{field} \sim 5$ to $K_{lim} = 18^m.5$; and for $z = 0.86$, $N_{clust} \sim 20$ and $N_{field} \sim 9$ to $K_{lim} = 19^m.5$. Even though these numbers should be taken only as roughly indicative, and changes in cluster properties

* We use aperture magnitudes in our work, while the published number counts and luminosity functions refer to total magnitudes. An average correction of $\sim 0^m.2$ from aperture magnitudes to total magnitudes has been applied. It was determined from the images of isolated galaxies on the frames. This is only correct on average and for statistical purposes.

and evolution could change them substantially, it is clear that field contamination is a potentially severe problem, particularly at the high redshift end of our sample.

Very recently Cowie *et al.* (1991) have carried out a very deep K-band galaxy survey in four relatively high galactic latitude fields using infrared arrays. Given the small size of the detectors and the depth of the survey, very small areas of the sky were sampled ($\sim$ 8 arcmin^2 in total). They present K-band number counts to $K = 23$. For three of the fields they also give detailed $U'BVIK$ photometry for samples complete to $K < 19\overset{m}{.}5$ (total magnitude). They also provide a star/galaxy separation criterion. Two problems arise when trying to use these data for our purposes. First, large scale structures could change the number of objects from field to field. However, the observed variations do not seem to be inconsistent with Poisson noise. We have used the average of three fields, which should reduce this uncertainty. Secondly, the actual colour distribution could, in principle, change from field to field due to localized variations in the galaxy population. This is difficult to test, since the total number of objects is small, but there is no evidence in that sense. The small number of objects in each field means that the shot noise will be relatively large. In Cowie *et al.*'s sample, there are only 7 objects with $K < 18\overset{m}{.}2$ and 20 with $K < 19\overset{m}{.}5$. Fortunately, we can expect the field contamination for the bright limiting magnitudes to be small compared to the number of cluster members ($N_{field} \lesssim 4$), and the accuracy of the correction is less important. For the clusters with fainter limiting magnitudes, for which the field correction becomes more critical, the statistics are much better.

A possible way out of the problem of the poor statistics on the field corrections would be to model the field colour distribution at different limiting magnitudes using data for local samples and applying redshift and evolution correction to them, but this has the obvious disadvantage that the colour and luminosity evolution corrections are far from well understood, and this would introduce very large uncertainties. Also, this would not

reduce the potential uncertainties arising from large-scale structure, so we prefer to use the purely empirical method.

Figure 5.22 shows the colour distribution for field objects with $K \leq 19\overset{m}{.}5$ from Cowie *et al.* (1991). They come from selected areas SSA13, SSA17 and SSA22. Objects classified as stars by these authors have been excluded. We will use this as the basic set of data to correct from field contamination.

5.7.2 Field-corrected colour distributions

For each cluster we have computed the expected number of field objects in the imaged area to the appropriate magnitude limit using the adopted number counts published by Cowie *et al.* (1991). To the limits that we are considering ($K < 19\overset{m}{.}5$), no significant incompleteness corrections were applied to the counts. In the magnitude range of interest, the differential counts can be adequately represented by $N(m) = 0.0126 \times 10^{0.316m}$ galaxies $\mathrm{deg}^{-2}\,\mathrm{mag}^{-1}$. The total IRCAM field in the $1\overset{''}{.}24\,\mathrm{pixel}^{-1}$ mode is $1.54\,\mathrm{arcmin}^2$, but since the frames for each cluster were taken at slightly different positions (*cf.* Chapter 2), the final effective field was $\sim 1.38\,\mathrm{arcmin}^2$.

For each cluster, a field colour distribution with the appropriate limiting magnitude was extracted from the data presented in previous section, put in the same colour system and then subtracted from the cluster colour distribution after scaling to the expected number of field objects. The results are shown in Figures 5.23 to 5.25 for each colour. The uncorrected colour distributions (hollow histogram) and field-corrected ones (filled area) are shown. Some small *negative* numbers arise from uncertainties in the field contamination. Given the small number of objects involved, the size of the errors is compatible with field-to-field variations due to shot noise. In fact, the absence of large negative numbers

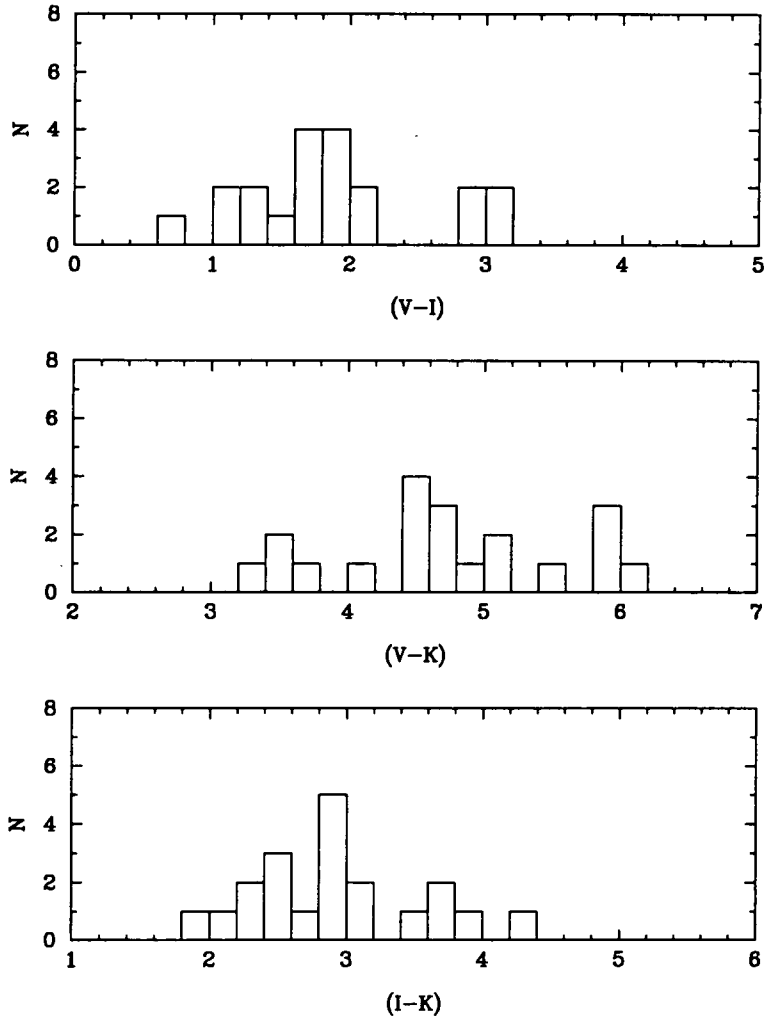

Figure 5.22. Field colour distributions for objects with $K \leq 19^m.5$ from Cowie *et al.* (1991).

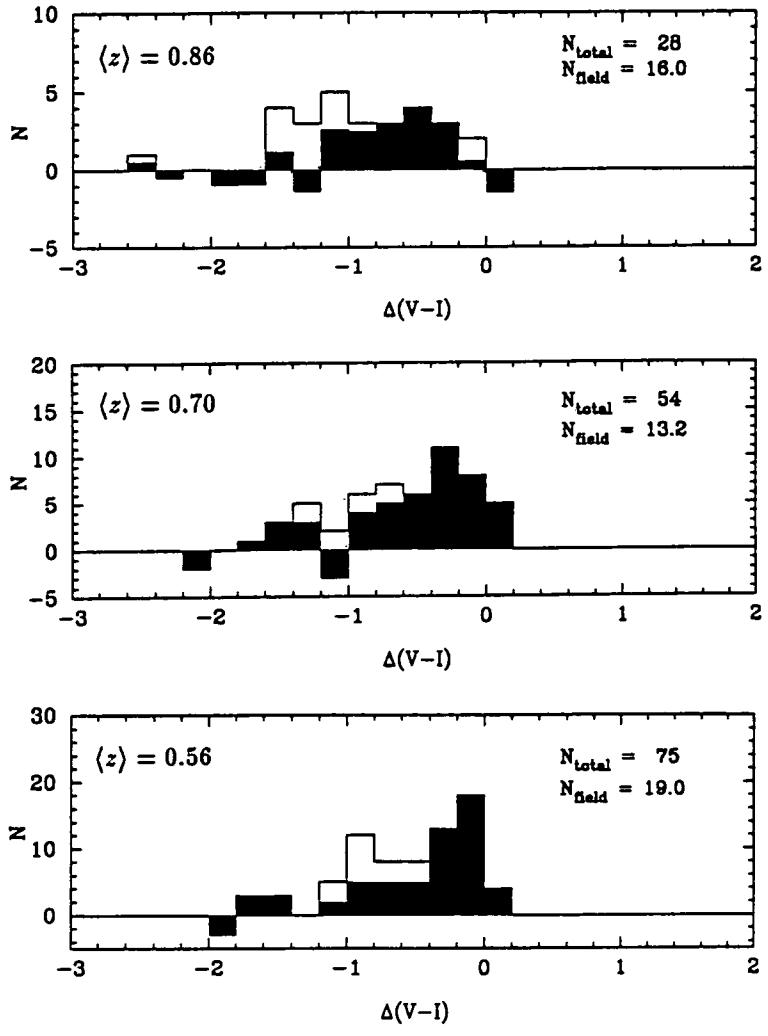

Figure 5.23. $(V-I)$ colour distributions for the combined sample of clusters in the three redshift bins before (hollow histogram) and after (black-filled area) correcting from field contamination. Each diagram shows the number of objects in the sample before the correction (N_{total}) and the expected number of field objects (N_{field}).

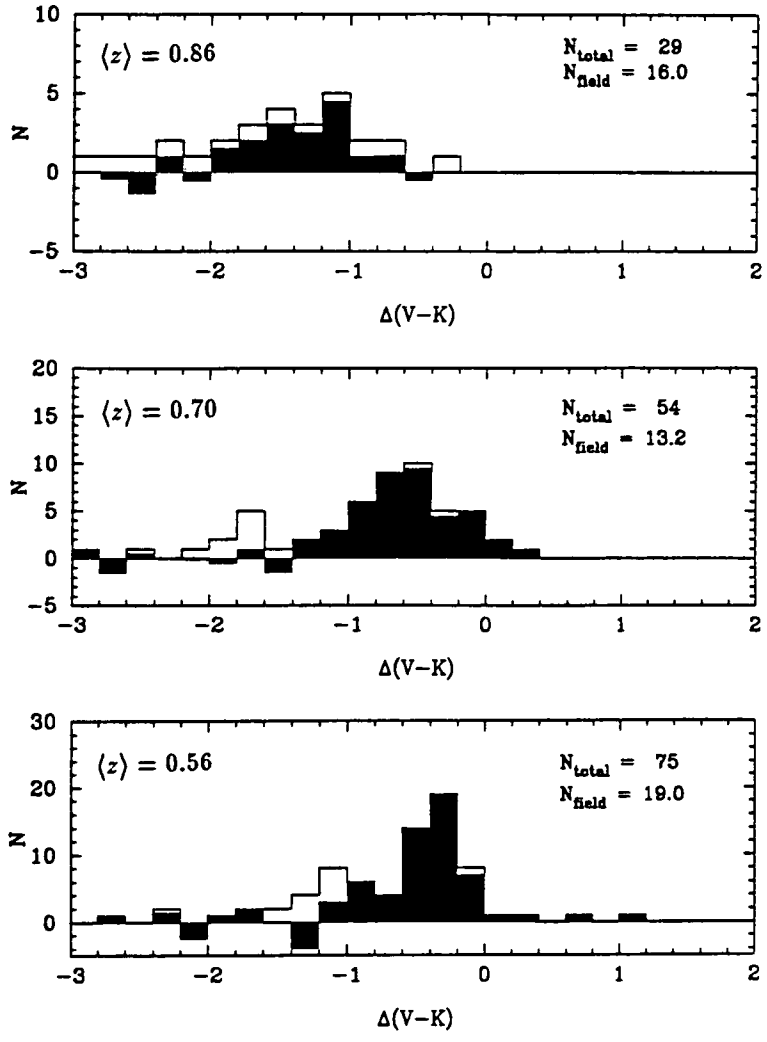

Figure 5.24. Same as Figure 5.23 for $(V - K)$.

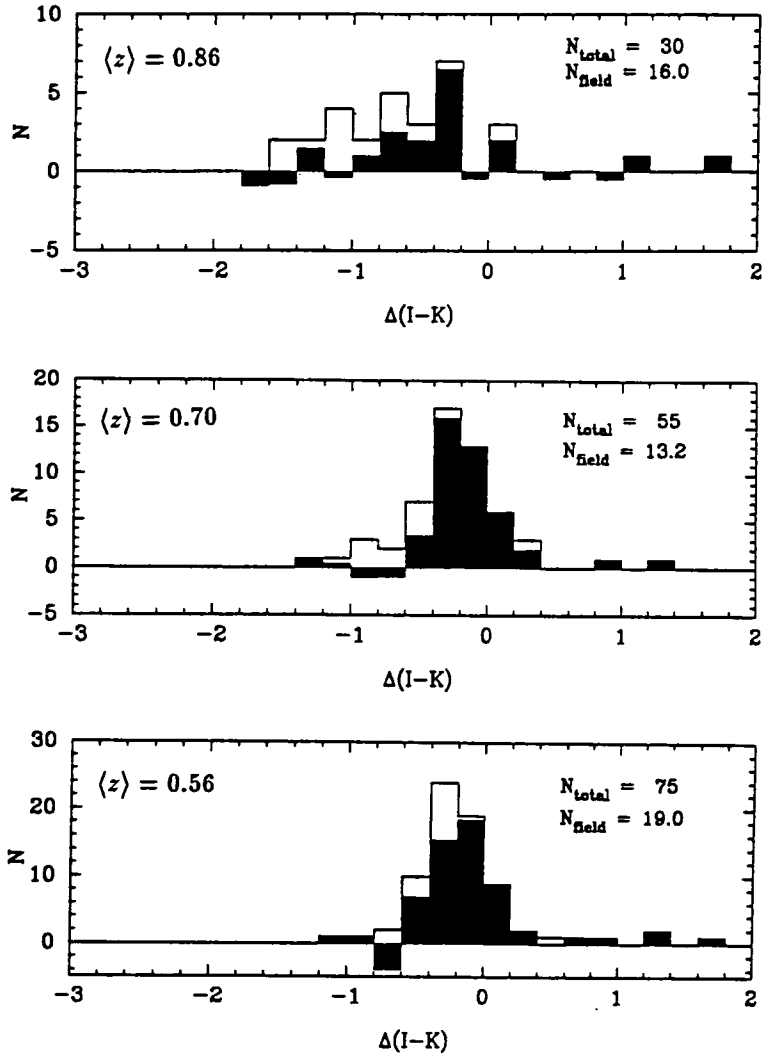

Figure 5.25. Same as Figure 5.23 for $(I - K)$.

gives some confidence to the field-correction procedure, although does not guarantee its accuracy.

We can use the data presented in Chapter 4 for 0016+16 and F1767.10TC to check how accurately we have been able to subtract the field contamination from the colour distributions. This will give confidence on the conclusions that we will be able to extract from our data without detailed membership information. We present the comparisons in Figures 5.26 and 5.27 (see captions).

For 0016+16 it is clear that both sets of histograms look very similar. Most of the field objects are subtracted from the blue tail of the distribution. Since the colour distributions deduced from the available membership information and our empirical colour subtraction are virtually the same, global photometric properties can be quite safely deduced statistically without redshift information. Another important point is that the available spectroscopy and narrow band SEDs can discriminate which objects are not E/S0s. In 0016+16 sample there are four objects (8%) classified as spirals (two Sab's, one Sbc and one Scd). The Sab's do not deviate from the E/S0 colour-magnitude lines, and given that the narrow band classification is only accurate to ± 1 spectral class, they could be ellipticals. The two later spirals appear in the blue tails of the $(V-K)$ and $(V-I)$ distributions, but their $(I-K)$ colours are similar to those of E/S0s. Since the number of spirals is small, they do not distort significantly the colour distributions, and have negligible statistical effect.

The situation with F1767.10TC (Figure 5.27) is less clear for several reasons. First, the small number of objects makes the statistical field correction more uncertain. However, this problem is less severe after binning the clusters in redshift groups. Second, CEMM found that this cluster presents significant contamination from a group at $z \sim 0.43$, and this is not taken into account by our field correction. Also, two of the reddest objects have

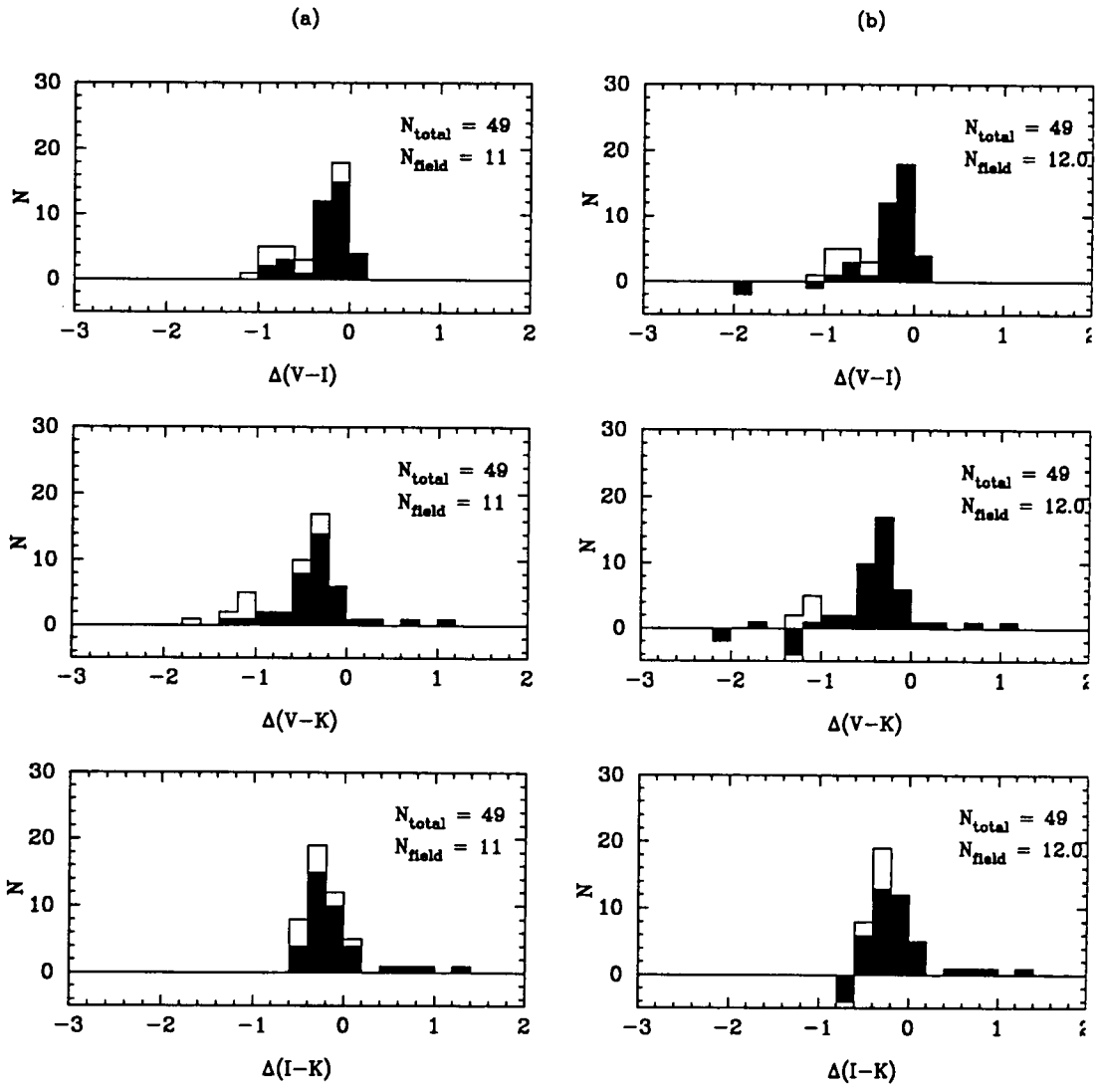

Figure 5.26. Test of the field-contamination correction for 0016+16. **(a)** Colour distributions for all the galaxies in the sample (hollow histograms) and cluster members and unclassified objects (black-shaded areas). We have used the membership information presented in Chapter 4. **(b)** The hollow histograms are the same as in (a) and the black shaded areas show the field-corrected colour distribution using the procedure presented in this section.

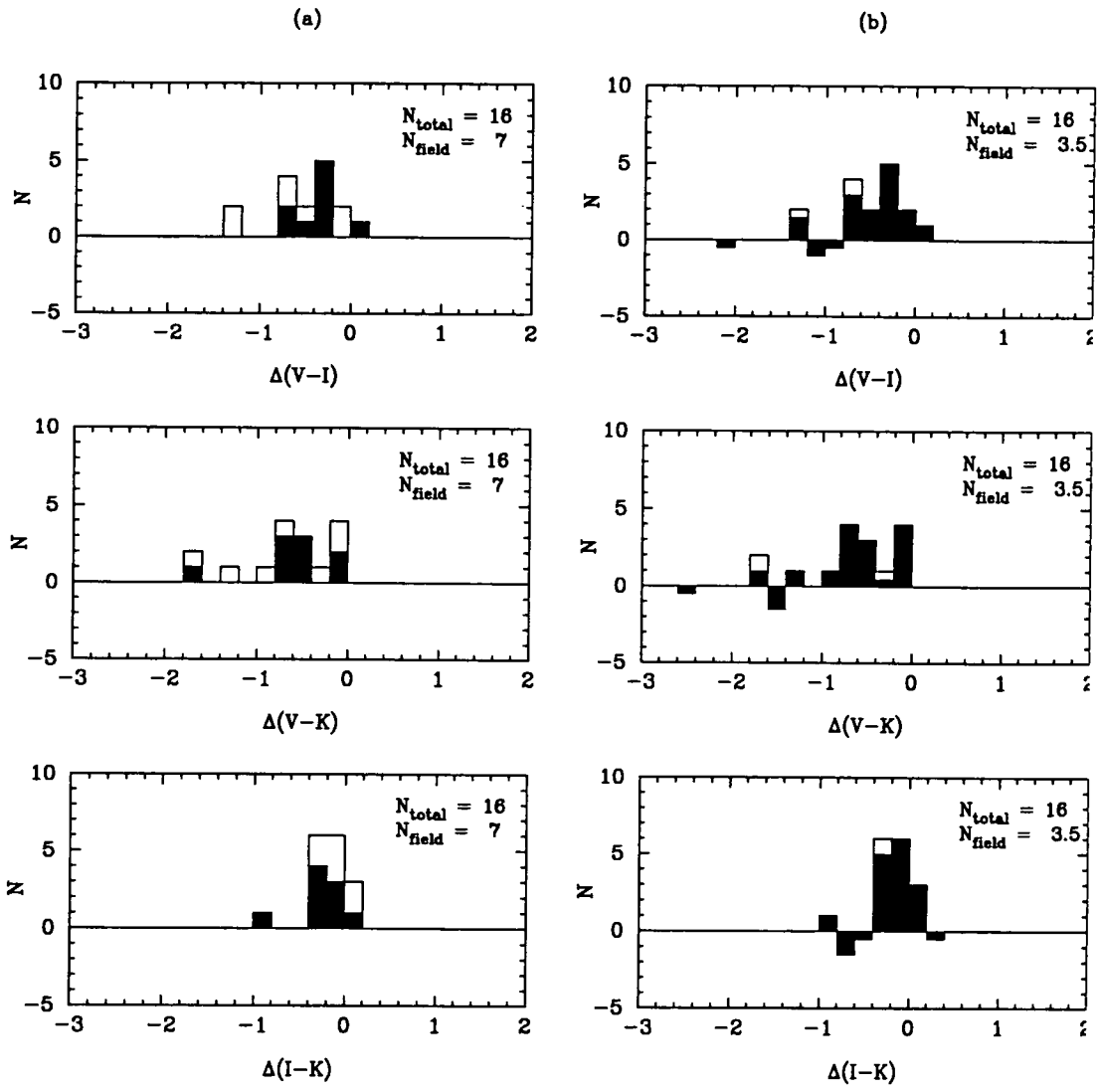

Figure 5.27. Test of the field-contamination correction for F1767.10TC. **(a)** Colour distributions for all the galaxies in the sample (hollow histograms) and cluster members (black-shaded areas). We have used the membership information presented in Chapter 4. **(b)** The hollow histograms are the same as in (a) and the black shaded areas show the field-corrected colour distribution using the procedure presented in this section.

a photometric *redshift* of 0.72, and have been considered background objects. However, since the photometric redshifts have uncertainties of 0.05, these objects could be members. Furthermore, a change in redshift of 0.05 is not very important when considering the evolutionary state of the galaxies (although it is crucial when studying the cluster as a dynamical entity), and they are well inside the $\langle z \rangle = 0.70$ bin, so we should include them in our colour distribution discussion. If we include them, both sets of histograms give pictures that are not too different given the uncertainties. The F1767.10TC sample does not contain any object classified as spiral, which is not unexpected from their small frequency and the number of detected members. Again, this means that the high z sample will be dominated by E/S0s, and the small contamination from spirals will have very little statistical effect.

It seems clear that, provided that there is no severe contamination from unrelated groups in the same line-of-sight, the statistical properties of the cluster member colours can be derived from our photometric data. And even if there is *some* contamination from *foreground* groups, the properties of the *red objects* will not appear severely distorted. The situation is less clear if the contamination from *background* groups is important. Although the evolution with z of the volume density of groups and clusters is not known, in hierarchical clustering scenarios, we should expect the abundance of clusters and groups to decrease rapidly with redshift (see, *e.g.*, Frenk *et al.* 1990), and therefore make the probability of finding *background* groups smaller.

5.8 Evidence for Evolution

After showing that the field-subtraction procedure works reasonably well, let us consider the field-corrected colour distributions presented in Figures 5.23–5.25. In this section we

will not consider the very red objects mentioned above, which scatter to the right hand side of the distribution.

There is clear evidence for colour evolution as a function of redshift, shown by the following facts:

- The *red envelope* disappears at high redshift: at $\langle z \rangle = 0.86$ there are *no* galaxies with colours as red as those of present-day ellipticals at all wavelengths.

- This effect is stronger in $(V-K)$ because the wavelength baseline is longer, which produces larger colour differences since both bands sample light that comes from stars with very different temperatures. In K the changes are small and slow, because it is dominated by long-lived cool stars, while in V —that samples light in the UV— the main contributors are young, short lived, hot stars that produce strong and rapid evolution.

- The $\Delta(I-K)$ distributions show a clear, relatively narrow peak for all the redshift bins. The peak centre moves bluewards when redshift increases. A blue tail appears at $\langle z \rangle = 0.86$, not present at lower redshifts.

- In $(V-I)$ and $(V-K)$, the peaks are somewhat weaker, but the blueward trend is stronger, particularly in $(V-K)$. Significant blue tails, that tend to grow with redshift, are present.

Using our present knowledge of galactic evolution, we can first interpret, at least qualitatively, what we think it is going on. The fact that the red envelope disappears at high redshift implies that *the witnessed evolution is not just the continuation to higher redshift of the Butcher-Oemler effect.* All the galaxies, even the reddest, presumably oldest, are evolving. Superimposed to that general ageing of the stellar populations, the growth of the blue tails with redshift indicates that a large fraction of the galaxies are

experiencing some sort of star formation, probably linked to the B-O effect observed at lower redshifts. Let us look at that in more detail.

The $(I - K)$ colours are measuring the properties of the underlying old stellar populations in the galaxies. The systematic change in this colour with redshift represents the ageing of the bulk of the old stars that were born during the major episode of star formation at the beginning of the galaxy life. The $(I - K)$ distribution is quite narrow, implying that in this colour galaxy-to-galaxy and cluster-to-cluster variations are relatively unimportant and that the underlying population is quite homogeneous. This suggests that the bulk of the initial star formation in cluster galaxies happened at a common epoch, and with similar characteristics.

When sampling shorter wavelengths —in the rest-frame UV range—, episodic star formation, even in relatively small amounts, will produce substantial changes in the colours (see, *e.g.,* Figure 5.31). This means that differences in the evolutionary state of the cluster galaxies will show in these colours, and be unimportant at longer wavelengths. We will be seeing galaxies with very little present or recent star formation, mixed with galaxies that are forming new stars or have formed them in the recent past. Only a small fraction of the galaxy mass ($< 10\%$) needs to be turned into stars to produce colour changes as large as observed in the blue tails (Figure 5.31), in agreement with the conclusions of Bower, Lucey & Ellis (1991). These episodes of star formation can be triggered by interaction of the galaxies with the intracluster medium (see, *e.g.,* Dressler & Gunn 1990) or by galaxy collisions and mergers (Lavery & Henry 1988). The recent star formation history of the galaxies might change because they lie at different distances from the cluster centre and therefore in different gas and galaxy density environments, or because they have different intrinsic properties (mass, gas fraction, etc). Therefore, even if all of them had a common underlying old stellar population, their short wavelength colours will be different, making the colour distributions broader and with significant blue tails. Whichever mechanism is

responsible, substantial differences from galaxy-to-galaxy might be expected, but some systematic evolution with redshift is clear.

We are, therefore, witnessing significant colour evolution in representative samples of cluster galaxies at different look-back times, free from the UV biases that may distort the apparent properties of a galaxy population when optical selection criteria are applied.

5.9 Statistical analysis of the colour distributions

In the previous section, we have described qualitatively the properties of the field-corrected colour distributions, but a more quantitative approach is clearly needed. We need to estimate a representative central location and scale of the distributions. Since they are highly non-Gaussian, the use of the mean and the standard deviation does not seem adequate. We need to use estimators that are insensitive to localized misbehaviour of the data, and not very sensitive to the assumed nature of the population from which data are drawn (*i.e.*, they should work well for Gaussian and non-Gaussian intrinsic distributions). It is desirable also to use efficient estimators, to be able to extract the maximum amount of information from a limited number of objects.

This is a well known problem to astronomers that try to estimate the redshift and velocity dispersion of galaxy clusters from a limited number of redshifts. In recent years, different estimators have been developed (Beers, Flynn & Gebhardt 1990, and references therein). These authors carried out a detailed comparative study of several of the most frequently used ones. They give quantitative criteria to determine the best indictor(s) depending on the number of data points and the shape of the distribution. They also describe methods to derive realistic confidence intervals for the central location and size

Table 5.7: Statistical descriptors for the colour distributions.

Colour	$\langle z \rangle$	$C_{BI}^{\dagger}$	$S_{BI}^{\ddagger}$
$(V-I)$	0.56	$-0.33^{+0.08}_{-0.08}$	$0.45^{+0.08}_{-0.09}$
	0.70	$-0.39^{+0.07}_{-0.09}$	$0.46^{+0.08}_{-0.07}$
	0.86	$-0.66^{+0.10}_{-0.11}$	$0.35^{+0.08}_{-0.07}$
$(V-K)$	0.56	$-0.43^{+0.05}_{-0.04}$	$0.37^{+0.08}_{-0.08}$
	0.70	$-0.58^{+0.07}_{-0.06}$	$0.40^{+0.05}_{-0.05}$
	0.86	$-1.31^{+0.10}_{-0.11}$	$0.35^{+0.06}_{-0.06}$
$(I-K)$	0.56	$-0.17^{+0.04}_{-0.03}$	$0.29^{+0.06}_{-0.05}$
	0.70	$-0.18^{+0.03}_{-0.03}$	$0.22^{+0.04}_{-0.04}$
	0.86	$-0.39^{+0.14}_{-0.14}$	$0.58^{+0.25}_{-0.25}$

Notes:

† Biweight central location estimator. The errors show 68% ($\sim 1\sigma$) confidence limits.

‡ Biweight scale estimator. The errors show 68% ($\sim 1\sigma$) confidence limits.

estimators. Following these criteria, we decided to use the *biweight* location and scale estimators (C_{BI} and S_{BI} respectively) as the most suitable for our distributions, and their *bootstrap* method to determine the confidence intervals for these estimators. We have used the code kindly provided by T.C. Beers and K. Gebhardt to perform the calculations. One small difficulty arose from the small *negative* numbers in our colour distributions. Since it is not straightforward to deal with 'negative frequencies', we proceeded as follows. As a first approximation, we ignored them (*i.e.*, we set the negative frequencies to zero), and computed the biweight estimators. Then, we calculated how much the negative frequencies would change these estimators by adding the same amount of *positive* frequencies symmetrically with respect to the centre, and re-doing the calculations. The changes were only $\lesssim 0\overset{m}{.}02$, which we consider to be a good estimate of the reliability of the estimators. Table 5.7 contains the results, which will be used in the following sections.

As a further test of our field subtraction procedure and the reliability of the *biweight* estimators we perturbed the expected field contamination by $\pm 1\sigma$ and re-computed the statistical estimators. In all cases, C_{BI} and S_{BI} changed by less than 1σ. The changes are typically $\lesssim \frac{1}{2}\sigma$. This, again, demonstrates the adequacy of our procedure.

Some contamination from spirals can be expected, but we have seen that for 0016+16 and F1767.10TC its effect on the global colour distributions is negligible. We have imaged only the cluster cores, where the expected proportion of spirals should be very small if the Morphology-Density relation holds for this redshift range. In any case, since we use statistical descriptors that are not sensitive to the presence of a few objects with different properties from the bulk of the sample, the effect of a few spirals will not be important. For example, in the case of 0016+16, C_{BI} and S_{BI} change by less than $0\overset{m}{.}015$ and $0\overset{m}{.}030$ respectively when we exclude the spirals. Therefore, we expect the C_{BI} and S_{BI} to adequately describe the colour distributions of early-type galaxies in our clusters.

5.10 Comparison with evolutionary models

We have quantified the amount of colour evolution detected in cluster galaxies as a function of redshift. In this section we will compare these results with galaxy evolution models. We are trying to see, first, if the changes in the galaxy colours are compatible with our present ideas about galaxy evolution and, second, to determine the acceptable range of model parameters, which will give us information on the star formation history of the galaxies: the epoch and duration of the main episode of star formation and the presence of significant bursts happening afterwards. We must keep in mind that substantial uncertainties still exist in these models, especially concerning the contribution of late stages of stellar evolution to the model SEDs. For that reason, we will consider *relative* changes in colours with redshift, instead of absolute colours. The uncertainties will affect the changes in colours only as a second order effect, while they would produce a first order effect in the absolute colours. Each colour will be put in a scale relative to the colour that a non-evolving model galaxy would have at each redshift, which can be directly compared with the $\Delta(colour)$ defined in previous sections for the cluster galaxies in our sample.

We have to expect at least *passive evolution*, since the stellar population of a galaxy must change as a function of time (stars evolve and die) even if no star formation happened after the initial burst. Superimposed on that, there might be some star formation activity. For that reason, we will consider two sets of models. First, purely passive evolution, represented by Bruzual (1983) c-models, in which the star formation rate (SFR) is constant for a period τ at the beginning of the galaxy life, and goes to zero afterwards. Second, a model in which the SFR declines exponentially (Bruzual μ-models) so that a fraction μ of the galaxy mass is transformed into stars after the first Gyr of the lifetime of the galaxy.* A solar neighbourhood Initial Mass Function (IMF, Scalo 1986) was used.

---

* The parameter μ is related to the e-folding time τ of the SFR by $\mu \equiv 1 - \exp(-\frac{1\,\mathrm{Gyr}}{\tau})$.

Since the look-back time at a given z depends on cosmological parameters, we will consider cosmologies with $q_o = 0.0$ and 0.5. We will take $H_o = 50\,\mathrm{km\,s^{-1}\,Mpc^{-1}}$ throughout this section because the current theory of stellar evolution (and therefore galaxy evolution models) predict timescales that are two long for large H_o values (*e.g.*, ages of globular clusters). For a given cosmology, the present age of the galaxies is determined by the redshift of their formation (z_{for}). In this context, the 'epoch of galaxy formation' means the beginning of the major episode of star formation.

In Figure 5.28 we present the results for a c-model with $\tau = 1$ Gyr, compared with the properties of our cluster colour distributions for different cosmologies and z_{for}. In Figure 5.29 we do the same for a $\mu = 0.5$ model (SFR e-folding time = 1.44 Gyr). In the $(I - K)$ figures we have included a data point at $z = 0.37$. It comes from our $(685 - K)$ colour distribution Abell 370 cluster members (Chapter 3).*

We must comment first that regardless of how well any particular model fits the observational points, it is clear that the observed colours show significant trends with redshift and therefore colour evolution is evident. The range of models that we have considered bracket the measured amount of evolution. The c-models in particular (*i.e.*, passive evolution of an old stellar population) explain reasonably well the redshift trend of the colour distributions. For $z \lesssim 0.4$–0.5, they predict very little colour evolution, compatible with what we measured for Abell 370. This was already suggested by the early models of Tinsley & Gunn (1976). Due to the uncertainties in the models, any conclusions about the redshift of galaxy formation and q_o should be regarded with caution. However, all models predict $z_{for} > 2$, regardless of the cosmology. This conclusion is very model-independent, and holds even if we consider models with a very short timescale for the

* Strictly speaking, the $(685 - K)$ colour distribution does not correspond exactly to $(I - K)$. However, MacLaren, Ellis & Carter (1988) did not detect any evolution in the $(685 - 862)$ colours of Abell 370 E/S0's, and therefore the $(685 - K)$ and $(I - K)$ colours should contain equivalent evolutionary information.

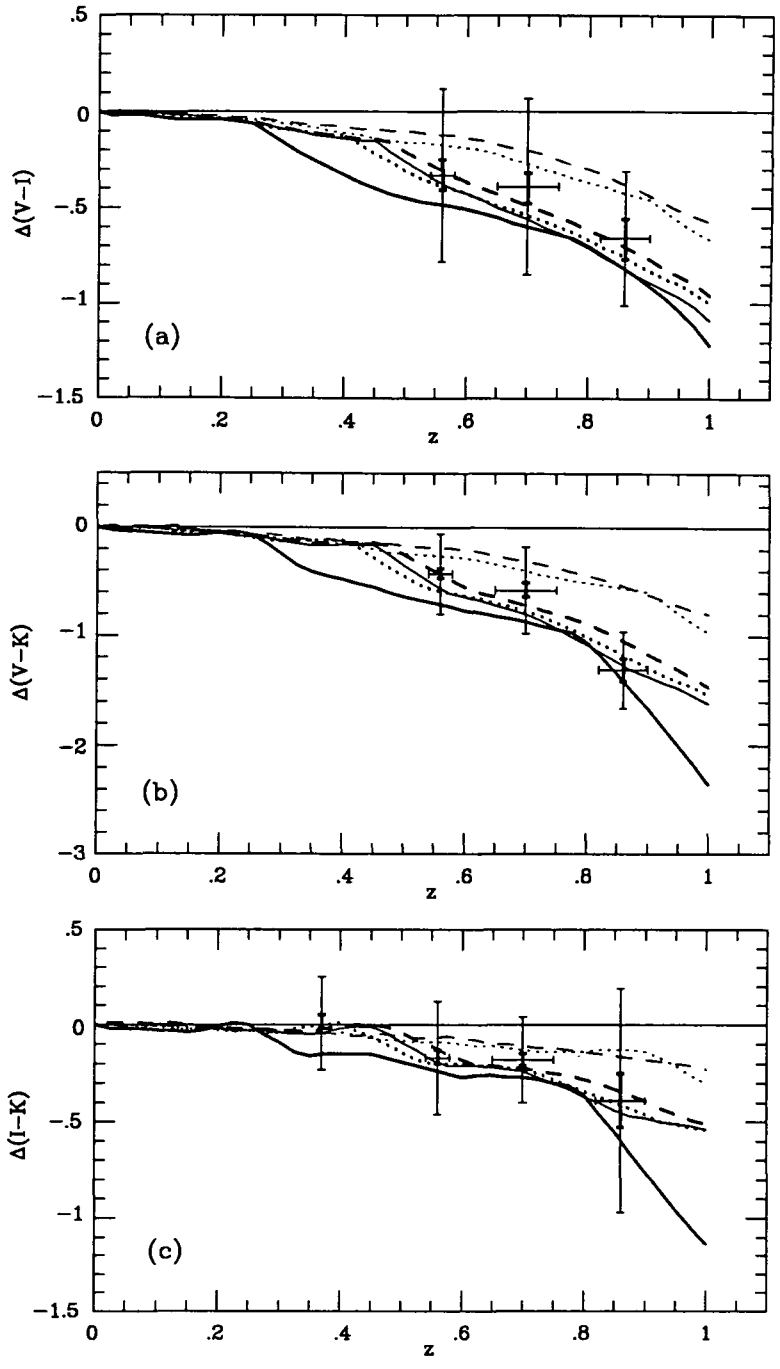

Figure 5.28. Comparison of the colour distribution properties with Bruzual (1983) c-models ($\tau = 1\,\mathrm{Gyr}$) with $z_{for} = 2$ (solid lines), $z_{for} = 5$ (dotted lines) and $z_{for} = 10$ (dashed lines) for $q_o = 0.5$ (thick lines) and $q_o = 0.0$ (thin lines). See text for details. Horizontal error bars show the redshift range of the bins. Thick vertical error bars show the 1σ confidence limits for the centre of the field-corrected colour distributions (C_{BI}). Thin vertical error bars show the width of the distributions (S_{BI}).

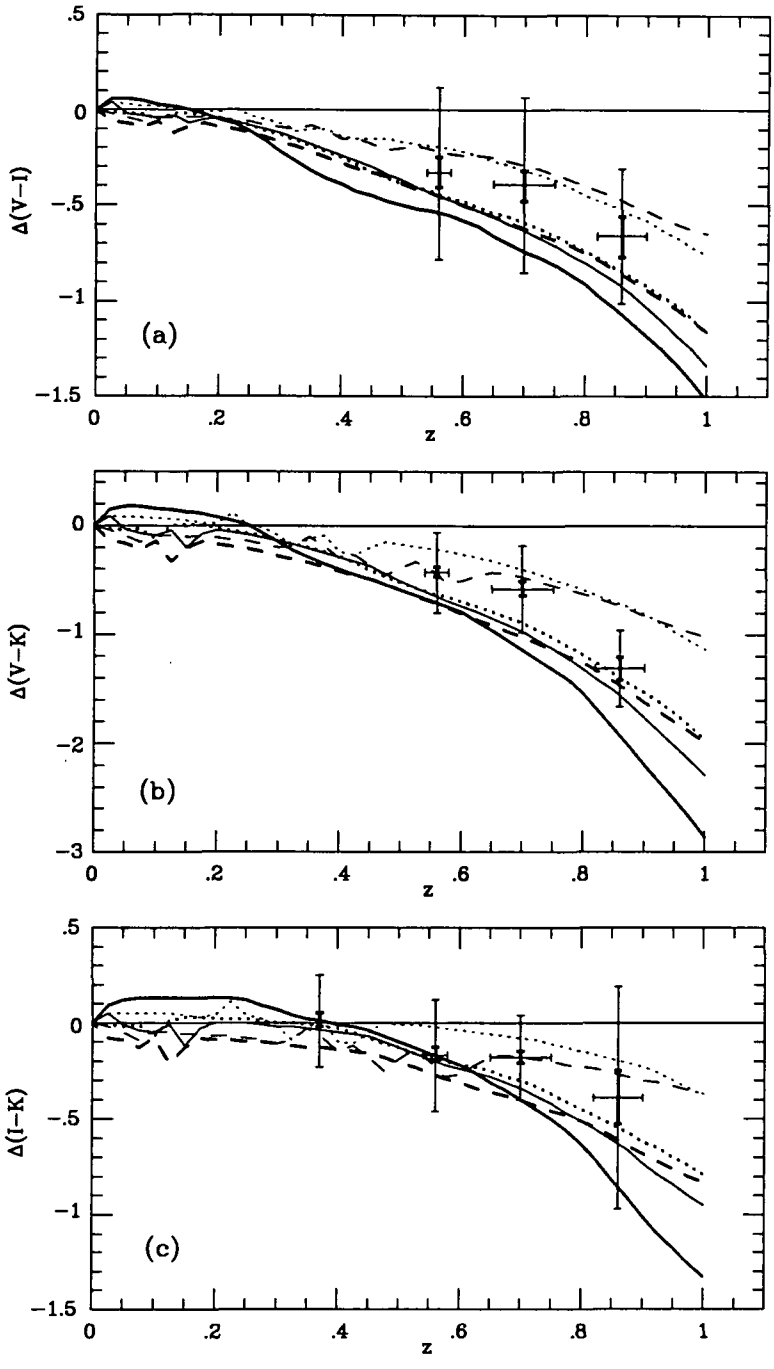

Figure 5.29. Same as Figure 5.28 for μ-models ($\mu = 0.5$).

SFR (an instantaneous burst). The higher limit for z_{for} is very model- and cosmology-dependent. If $q_o = 0.5$, the models are not very sensitive to z_{for} because of the short time interval for $z > 2$, but in this cosmology a passively-evolving c-model is favoured because the μ-models predict too much evolution. For $q_o = 0.0$, the higher limit of z_{for} is model dependent, but a $z_{for} \leq 5$ is favoured with reasonable confidence.

The μ-models with $q_o = 0.5$ predict too much evolution in all cases. Since older ages are favoured, low q_o values are preferred with these models. The larger amount of evolution predicted by the μ models is produced because the star formation last longer (although at a reducing rate), and therefore the models take longer to reach the red colours of present-galaxies.

Taking these limits at face value, the age T of present-day early-type galaxies should be $T \gtrsim 10.6$ Gyr if $q_o = 0.5$, and $13.1 \lesssim T \lesssim 16.3$ Gyr if $q_o = 0.0$. With the available information it is not possible to disentangle the galaxy evolution effects from the cosmology effects. However, we have seen that the observed colour evolution of cluster galaxies with redshift can be naturally explained using current galaxy evolution models.

We have seen in previous chapters that other galaxy evolution models are available. Here we have restricted ourselves to Bruzual (1983) models to keep the size of the parameter space manageable. It is worth mentioning here that, as we showed in Chapter 4, the very successful Arimoto & Yoshii (1987) model for giant ellipticals predicts colour changes compatible with those of Bruzual's c-models with $\tau \simeq 1$ Gyr. The reason is that the SFR timescale in both models is very similar, and in Arimoto & Yoshii's models it also goes abruptly to zero when the superwind phase occurs. However, both sets of models treat in a very different way the chemical evolution of the galaxies. In any case, the conclusions of this section regarding Bruzual's c-model would also hold if we had used Arimoto & Yoshii (1987) model.

5.11 Comparison with previous work

In the last few years, extensive photometric and spectroscopic work on the evolutionary state of the galaxies in intermediate ($0.35 < z < 0.55$) and high redshift clusters has been carried out by Dressler, Gunn and their collaborators (Dressler & Gunn 1982, 1983; Dressler, Gunn & Schneider 1985; Schneider, Dressler & Gunn 1986; Dressler 1986b, 1987; Gunn 1989; Gunn & Dressler 1988; Dressler & Gunn 1988, 1990; and Dressler & Gunn 1991).*

For the intermediate redshift clusters, they confirm on a broader statistical basis the results of the work by other authors regarding the over-abundance of *blue* ('active') cluster galaxies when compared with nearby clusters (see Chapter 1). In this section we will concentrate on their results for higher redshift ($z \gtrsim 0.5$) clusters. In Dressler & Gunn (1990), they use the 4000 Å break (D_{4000}, Bruzual 1983) to show that there is strong evidence for evolution in this spectral feature when compared with samples at lower redshift. It has been shown by Hamilton (1985), Dressler & Shectman (1988) and Kimble, Sandage & Davison (1988) that the D_{4000} dependence with absolute luminosity, presumably correlated with metal abundance, is weak for luminous galaxies like those in their sample and ours. Thus, we can expect the 4000 Å discontinuity to be reduced by either hotter turn off for an old population or contamination by younger, hotter stars, but not by variations in metal abundance from galaxy to galaxy or as a function of lookback time.**

---

* Other groups have also produced significant contributions to the field (see Chapter 1), but in this section we will concentrate on the work of that group since it is directly related with ours.

** In our photometric study, the colour dependence with metallicity for early-type galaxies has been accounted for, at least to first order, by subtracting off the Colour Magnitude effect.

Dressler & Gunn study suggests that the distributions of D_{4000} for cluster members in the highest redshift range show a shift in centroid and upper boundary towards smaller values. The shift in centroid, already present in the $z = 0.35$–0.40, was interpreted as another manifestation of the *Butcher-Oemler effect*, seen as a decrease in D_{4000} by ongoing or recent star formation. By $z = 0.546$ (0016+16), the lowering of the centroid is enhanced, and a slight decrease of the upper boundary begins to show, although the effect does not seem as convincing as for higher redshifts. This indicates that at $z \geq 0.7$, even the reddest (and presumably oldest) cluster galaxies show significant spectral evolution. If we assume that these are the counterparts of present-day cluster ellipticals, this can be used to impose significant constrains on the galaxy formation and evolution theories. Dressler & Gunn conclude that, taking their results at face value, and using Tinsley & Gunn (1976) or Bruzual (1983) models, they can place limits to the epoch of the bulk of star formation as $2 < z < 5$ for a Universe with $\Omega = 1$. The lower bound is quite model independent, and thus places a strong limit on the amount of late star formation that could have occurred in these galaxies. Since the time interval is small at higher z, the upper bound is much less well determined.

When considering these results, Dressler & Gunn (1990) acknowledge some concern about two problems. First they consider the possibility that aperture effects might play some role, but they conclude that since D_{4000} is quite insensitive to metal abundance and the metric size changes very little in the high redshift interval, this should not be a major problem. Their second concern is that, since they select their objects is the optical, namely the Thuan & Gunn (1976) r band, they might have missed the oldest, reddest cluster members by selecting in the rest-frame ultraviolet. They argue that, since they sample at least 2 magnitudes into the luminosity function, it seems certain that their sample of the brightest galaxies in the ultraviolet contains at least some of the reddest objects. For example, they include the two cD galaxies in the cluster Cl1322+3027. Another problem

that might work in the opposite sense is that D_{4000} weakens for bluer systems and therefore the spectrum may be featureless, making the redshift more difficult to obtain, and some of such objects could be missed.

However, we have shown in Chapter 2 that in order to obtain a fair sample of the galaxy population at high z, *i.e.,* a sample that contains the same relative proportion of galaxy types at all redshift, it is necessary to select the galaxies in the near-IR, and we consider that, even if Dressler & Gunn have included *some* of the reddest objects in their sample, the colour and D_{4000} distributions that they obtain could be distorted by this *ultraviolet bias.* In fact, they also acknowledge the need of extending this kind of study to the near-IR domain.

In order to quantify the distortion introduced by optically selecting galaxies at high redshift, we have used our Abell 370 sample (Aragón-Salamanca, Ellis & Sharples 1991, Chapter 3) to model the differences between optical (r) and near-IR (K) selected samples. Our $(685-K)$ can be transformed into $(r-K)$ using the calibration between 685 and R that we presented in Chapter 3 and the transformation between r and R given by Schneider, Gunn and Hoessel (1983). Taken redshift corrections into account (without evolution), our Abell 370 K-selected sample can be put at any redshift, and we can therefore model the differences between optical- and IR-selected samples. Figure 5.30 shows $(r-K)$ vs. K C-M diagrams for model clusters at different redshifts, indicating the areas of the diagram that we would miss when applying different selection criteria. Dressler & Gunn (1990) spectroscopy reaches a limit of $r \sim 23$, which has been drawn on the diagrams. The limit of our K photometry varies from cluster to cluster, and representative values of the limits have been drawn at each redshift.

The differences in the sample selection are obvious. The colour distribution for K selected samples are uniformly de-populated when the redshift increases, but the ones

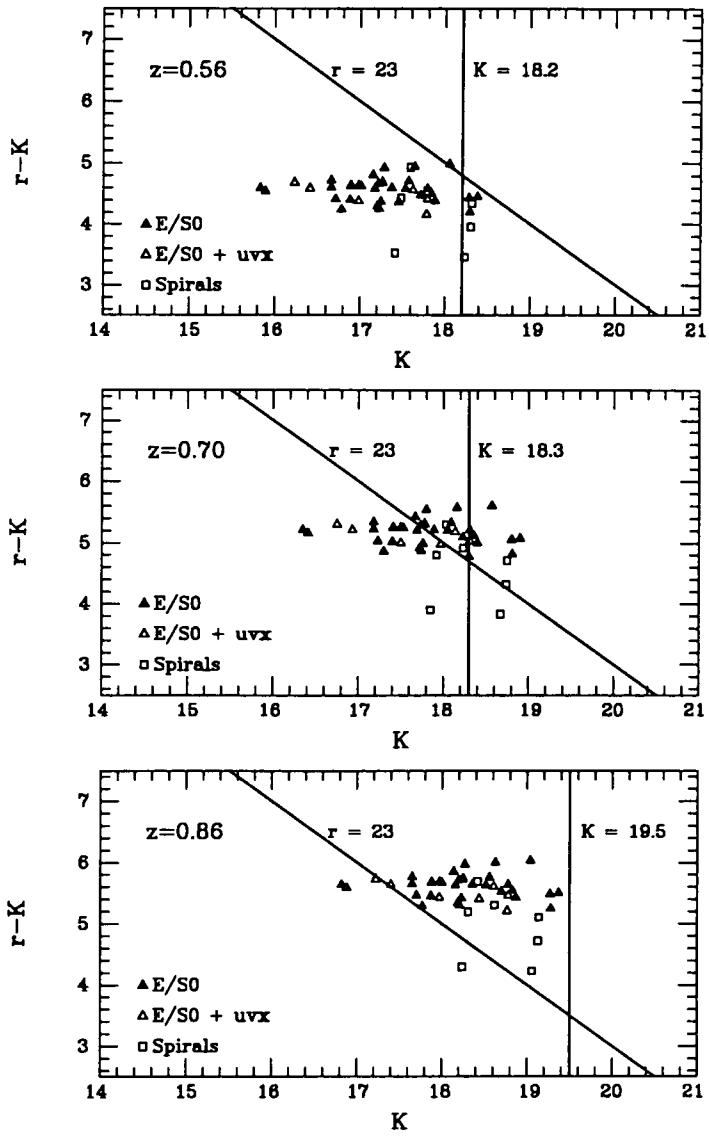

Figure 5.30. $(r - K)$ vs. K C-M diagrams for model clusters at different redshifts, based on the data for Abell 370 (see text). The vertical lines show the limits of a K-selected sample at different limiting magnitudes (representative of our data). The inclined lines show the limits of an r selected sample with $r < 23$.

for the r-selected samples loose progressively more red objects. So, even though some *red* galaxies would be present in a high-z sample (for a non-evolving cluster like Abell 370), selecting in the optical we view a distorted picture of the galaxy population of the cluster. If colour evolution is present, the biases in an optically-selected sample would be even more important, since the selection would strongly favour objects with recent star formation against the passively evolving red galaxies.

Having proven the advantages of selecting in the near-IR, we can question ourselves about the advantages or disadvantages of using spectroscopic information (like D_{4000}) instead of photometric data when studying the evolutionary state of the galaxies at high redshift. Obviously, the main advantage of the spectroscopy is that it provides redshifts, and therefore, membership information, and photometry alone cannot supply that on an object-by-object basis. However, we can always obtain statistical information, as shown in previous sections. The advantage of photometry is that is is much less expensive in telescope time (particularly since the advent of high quantum efficiency imaging detectors in the optical and the near-IR), and much larger *complete* samples can be built for a given amount of observing time.

But, can we obtain equivalent information regarding the evolutionary state of a galaxy following both approaches? The 4000 Å break is a good example of spectroscopic feature that can be reliably measured in medium to low dispersion spectra, and which is sensitive to the stellar population present in a galaxy. Figure 5.31 (a) shows that the rest-frame $(U-V)^*$ colours and D_{4000} are tightly correlated for observed SEDs of different galaxy spectral types and model spectra, and a quadratic fit

$$D_{4000} = 1.218 + 0.207(U-V)_o + 0.358(U-V)_o^2, \qquad r.m.s. = 0.05 \qquad (5.1)$$

* Roughly corresponding to observed $(V-I)$ for this redshift range.

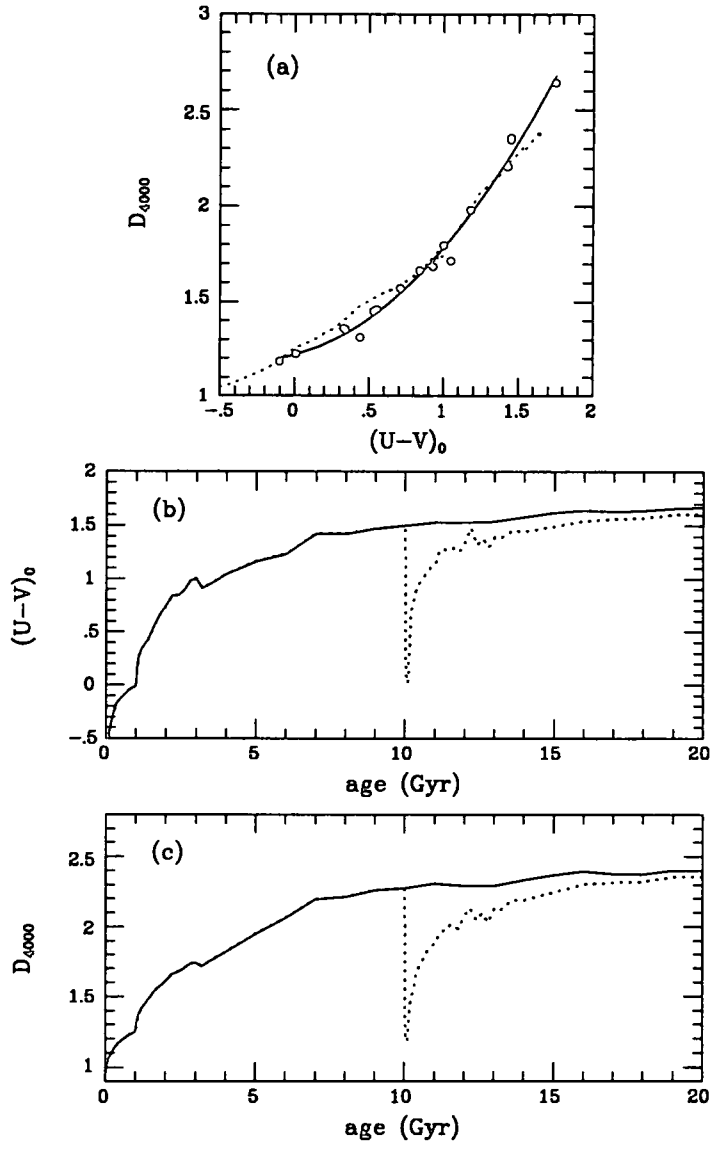

Figure 5.31. (a) Correlation of D_{4000} vs. rest-frame $(U-V)$ for galaxies of different spectral types (filled circles). The solid line is a least squares second order polynomial fit to the points. The dotted line shows the same correlation for a passively evolving old stellar population (Bruzual 1983, c-model with $\tau = 1\,\mathrm{Gyr}$). (b) Time evolution of the rest-frame $(U-V)$ colours of a Bruzual (1983) c-model with $\tau = 1\,\mathrm{Gyr}$ (solid line), and the same model with a 10%-mass burst of star formation happening at an age of 10 Gyr (dotted line). (c) Time evolution of D_{4000} for the same models presented in (c). Note that when drawing (c) we did not use the correlation plotted in (a) but we measured D_{4000} on the model spectra.

can be used to transform one into the other with high accuracy.

Figure 5.31 (b) and (c) present the effect of a burst of star formation on the rest-frame $(U - V)$ colour and 4000 Å break of a passively-evolving old stellar population. We have used a Bruzual (1983) c-model ($\tau = 1$ Gyr) which suffers a short burst of star formation (10% of its mass is transformed into stars with a standard IMF) at an age of 10 Gyr. Both indicators show a very similar behaviour. The fractional changes and timescales are similar, since the stars that contribute to the changes in both of them are virtually the same. Therefore, the differences in sensitivity of these indicators to star formation will depend only on the accuracy of our measurements, and, for a given amount of telescope time, the photometry will be more advantageous. We do not know the value of typical D_{4000} errors in Dressler & Gunn (1990), but assuming that the size of the bins in their histograms (0.1) is a representative value, they would be able to detect such a burst ~ 6 Gyr after it took place. To do this with our $(V - I)$ colours we need errors of $\sim 0^m.1$, which is well within the capabilities of our photometry.

Therefore, we can detect changes of comparable size on the stellar populations with our photometry, at a smaller cost in telescope time, and with the advantage of having a more representative sample of the cluster galaxy population because of our selecting in the near-IR. However, the comparison of the observed colours with those of nearby galaxies is more complicated, and the redshift corrections might introduce uncertainties than could, in principle, distort our conclusions, while the redshift corrections to spectral indices like D_{4000} are much more straightforward. We have discussed the origin and size of these uncertainties in previous chapters, and they should be kept in mind. It is worth mentioning that this problem results more from our lack of detailed knowledge of the spectroscopic and photometric properties of nearby galaxies in the UV and near IR than from our lack

of ability of observing high redshift objects. Observational programs intending to alleviate this problem would be extremely useful.

A direct comparison between our results and those of Dressler & Gunn is possible because these authors have kindly provided their D_{4000} measurements for 0016+16 and Cl1322+3027. Figures 5.32 (a) and (b) show the comparison between D_{4000} and $(V-I)$ colours for these clusters.* The solid line represents the calibration presented in Figure 5.31 (a) at the adequate redshift, and the dotted line a least-squares second order polynomial fit to the points. The agreement is very good, confirming our previous conclusions. Figures 5.32 (c) and (d) compare the D_{4000} distribution for 0016+16 cluster members measured by Dressler & Gunn (1990) and the one that we get transforming our measured $(V-I)$ colours into D_{4000}. Both distributions are very similar, although the second is somewhat narrower, due to the high accuracy of the optical colours. This shows that $(V-I)$ and D_{4000} measure basically the same thing at this redshift.

Despite all we have said, it would be absurd to think that spectroscopy is not necessary when studying galaxies in high redshift clusters. In fact, we would not have been able to develop a work like this if a great deal of spectroscopic work had not been carried out before to determine the redshift of the clusters and their reality as such. We only suggest that, once a cluster has been identified and confirmed, photometric work can substantially enlarge the samples in a reasonable amount of observing time, and important information can be derived from the photometry without the need of spectroscopy for all the objects. Moreover, it can help to build cleaner and more representative samples if near-IR bands are included, and this information can be used to statistically correct the spectroscopic samples from selection biases. Evidently, both methods are complementary.

* Some of the objects measured by Dressler & Gunn are not in our K-selected sample due to the small IRCAM field of view, but optical photometry is available for them, and they have been included.

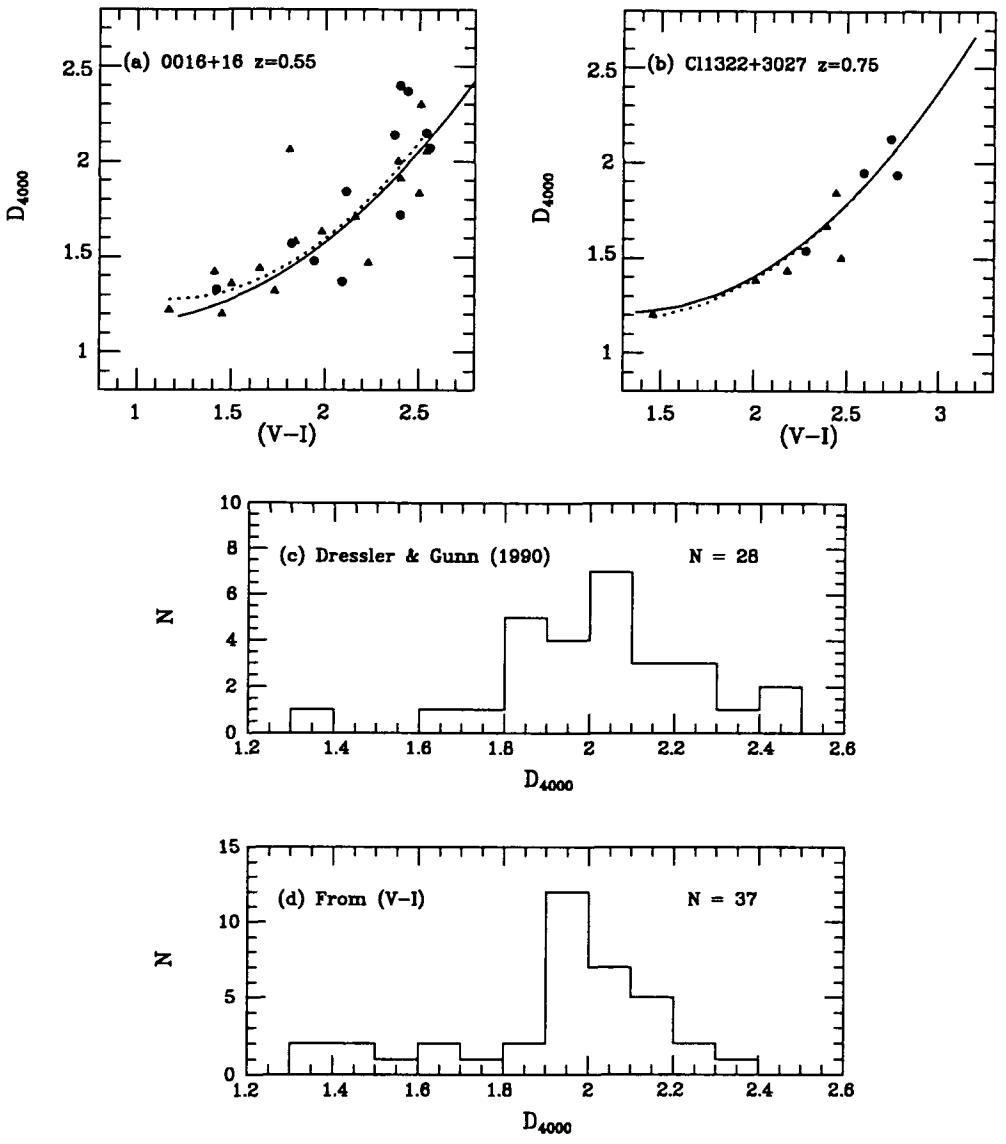

Figure 5.32. **(a)** Comparison between D_{4000} from Dressler & Gunn and $(V-I)$ for 0016+16. Filled circles: objects in our K-selected sample; filled triangles: other cluster members. The solid line represents the calibration presented in Figure 5.31(a) at the adequate redshift, and the dotted line a least-squares fit to the points (excluding the discrepant one). **(b)** As (a) but for Cl1322+3027. **(c)** D_{4000} distribution for 0016+16 cluster members from Dressler & Gunn (1990). **(d)** D_{4000} distribution for 0016+16 cluster members derived from the $(V-I)$ colours and the calibration presented in Figure 5.31(a) at $z = 0.55$.

5.12 Very red objects in $(I-K)$: what are they?

In Chapter 4 and in previous sections of this chapter we have found several objects which show remarkably red $(I-K)$ colours ($\gtrsim 4.0$), and a broad range of optical colours. Cowie *et al.* (1991) sample contains only one of such objects to $K_{lim} = 19\overset{m}{.}5$.

Elston (1991) found an overabundance of red galaxies with $(R-K) > 4.5$ for samples with $K > 17^{m}$. He showed that these objects are very peculiar and cannot be understood in the framework of current galaxy evolution models (*e.g.* Bruzual 1983), since they are redder than the brightest cluster galaxies and radiogalaxies at these apparent magnitudes. Elston, Rieke & Rieke (1989) used optical spectroscopy and $BVRIJHK$ photometry to study two of such galaxies in detail. They claimed each to have $z = 0.8$, and visual-IR colours similar to those of a current-day elliptical, but their rest-frame UV-optical colours show a significant ultraviolet excess. They have observed $(V-I)$ colours of 2.98 and 2.28. A non-evolving giant elliptical at $z = 0.8$ would have $(V-I) \approx 3.1$. They have, therefore, UV-excesses that differ by as much as $0\overset{m}{.}7$ (V samples light at ~ 3000 Å at this redshift). They are as luminous as the brightest cluster galaxies at their redshift. But, if all the very red objects detected in Elston (1991) survey are similar to these two, they must have in total a volume density similar to that of L^{*} galaxies. If, using Bruzual (1983) models, one tries to make a galaxy several magnitudes more luminous than its companions, it generally must be accompanied by very blue colours at all wavelengths. Since they are not present in local surveys, they must have faded by about 2 magnitudes more than the *normal* galaxies to vanish by $z = 0$. This obviously presents a challenge to standard models of galaxy evolution.

Are our very red galaxies in $(I-K)$ the same as Elston's (1991) red objects? Their position on the C-C diagram is not compatible with the colours of a present day giant elliptical at any redshift. Their $(V-I)$ colours are too blue, with a large variation from

object to object, but their observed $(I - K)$'s are compatible with being high redshift ellipticals, in accordance with the results of Elston, Rieke & Rieke (1989). If the two galaxies studied by these authors are typical of the rest of the red galaxies found by Elston (1991), it is clear that our red objects would fit in his sample, and they could be background, unusually luminous galaxies, that our knowledge of galactic evolution is not able to explain.

However, Glazebrook (1991) finds in his K-selected spectroscopic sample a significant number of galaxies that are up to 1 magnitude redder in $(R - K)$ than present day ellipticals in the redshift range $0.1 < z < 0.2$. His spectroscopic sample is not complete beyond this redshift and therefore we do not know if they are present at higher redshifts. If they do, our red objects do not need to be at high z and their luminosity does not have to be unusually high, although their extremely red colours remain unexplained.

We have speculated in previous chapters about the possibility that current models of galaxy evolution are not adequate in the near IR because of their lack of AGB stars. Chokshi & Wright (1987) made an attempt to include these late stages of stellar evolution in Bruzual (1983) models, and we have used their results in Chapter 3. Depending on the actual contribution of the AGB to the luminosity of the galaxies and its time evolution, their models show that it is possible that a burst of star formation could make the optical-IR colours of galaxies *redder*. Whether the inclusion of AGB stars in galaxy evolution models could explain the nature of the red objects remains unclear because of the large uncertainties that still exist. But we presented some evidence in Chapter 4 that suggests a lack of light in the near IR SEDs of current galaxy evolution models.

5.13 Luminosity evolution at 2μm

Let us consider now the amount of luminosity evolution undergone by galaxies in high redshift clusters. The tests applied so far —mainly studying the colour distributions in the C-M and C-C diagrams— are not very sensitive to luminosity evolution because the C-M relations are very flat. In this section we will present the magnitude-redshift relation for the Brightest Cluster Galaxies (Hubble diagram) and the K luminosity functions for the galaxies in the high redshift sample.

5.13.1 The K Hubble diagram

The Hubble diagram for Brightest Cluster Galaxies (BCG's) in optical wavelengths has been a classic cosmological test aiming to determine q_o, the the deceleration parameter of the Universe (Peach 1970, 1972; Gunn & Oke 1975; Sandage, Kristian & Westphal 1976; Kristian, Sandage & Westphal 1978; Hoessel 1980; Schneider, Gunn & Hoessel 1983a,b). It soon became apparent that, even though BCG's are very good standard candles (see ahead), the uncertainties in the evolutionary corrections are much larger than the effects of cosmology, and the Hubble diagram for BCG proved to be more useful to study galaxy evolution than cosmology.

The V Hubble diagram for BCG's, using 'fully corrected' magnitudes (taking into account the aperture correction to a standard metric size, galactic absorption, K-correction, Bautz-Morgan class correction and richness correction, see recent review by Sandage 1988) has an intrinsic scatter of only $0^m\!.28$ up $z \sim 0.5$, proving that BCG's are very good standard candles.* Since the evolutionary correction in observed V is large and

* Very recently, Djorgovski *et al.* (1991) gave an explanation for the BCG's being such good standard candles. As a consequence of the scaling relation between the luminosity and surface brightness, the aperture magnitudes of these objects have a relatively small scatter. See original paper for details.

not very well known, the formal values of q_o obtained from this diagram are meaningless (Sandage 1988).

At very high redshifts, the V Hubble diagram has been extended to $z = 1.8$ using radio galaxies (Djorgovski, Spinrad & Maar 1985, Spinrad 1986, Spinrad & Djorgovski 1987). They conclude that for $z > 0.8$ the data cannot be fit by any q_o value in the case of no evolution, whereas a good fit is obtained using a Bruzual (1983) evolving model with $q_o = 0.0$ and $H_o = 50$.

In the near-IR, the K corrections are appreciably smaller than in B and V, and the evolution term is relatively insensitive to starburst evolution (termed *active evolution* by Lilly & Longair 1984). Furthermore, the amplitude of the evolutionary correction for passive evolution (*i.e.*, the gradual evolution of the HR diagram of an old coeval evolution with time) is also much smaller in the K band that in the $UBVR$ bands. For that reason, several attempts have been made to extend the Hubble diagram to the K band (Grasdalen 1980, Lebofsky 1980, Lebofsky & Eisenhardt 1986, Lilly & Longair 1982, 1984, Lilly 1989). By using radio galaxies, the Hubble diagram can be extended to $z > 3$. Radio galaxies prove to be also good standard candles, with an intrinsic dispersion of about $0^m.4$ for the full redshift range studied (Lilly 1989). Lilly & Longair (1984) concluded that if $q_o \sim 0.5$ radio galaxies are ~ 1 mag brighter at $z = 1$ than they are today.

From the observed optical and IR magnitude-redshift relations, Sandage (1988) concluded that evolution must be invoked if the prediction of the standard cosmological model is accepted (see also Yoshii & Takahara 1988).

Most of the high redshift data ($z > 0.5$) comes from radio galaxies, and some concern exists about how representative this class of objects is of the galaxy population in general. They are a rare population ($\sim \frac{1}{1000}$), and it is not well known to which extend

the fact that they present strong radio emission could affect their stellar populations and evolution (*e.g.* Chambers & Charlot 1990).

With all that in mind we have used our sample of high redshift clusters to study the Hubble diagram for BCG's in the near-IR. To extend the diagram to lower redshifts, we have used the data for intermediate redshift clusters presented in Smail *et al.* (1991, *in preparation*, see also Chapter 6) and the data for Coma from Bower, Lucey & Ellis (1991, BLE). The K photometry has been obtained inside a fixed metric aperture of 50 kpc diameter ($H_o = 50$). The size was chosen so that the minimum aperture diameter was $\sim 5\farcs0$ at high redshift. Since the angular diameter for a fixed linear size depends on q_o, two values for this parameter (0.0 and 0.5) have been considered. The K magnitude for NGC4889 (the brightest cluster member in Coma) has been obtained from the CCD V photometry of BLE, which extends to $\sim 100\farcs0$ and their $(V-K)$ colour inside an $11\farcs0$ diameter aperture, using an $(V-K)$ colour gradient of $\Delta(V-K)/\delta\log(A/D(0)) = -0.1$.*

The Galactic reddening was determined from Burstein & Heiles (1982) maps, and the K-corrections were obtained for the empirical E/S0 SED presented in previous chapters. The uncertainty in the K-correction at 2μm might be as large as $\sim 0\overset{m}{.}15$ (estimated from the different SEDs available), which is very important when considering colour evolution, but not so much for the luminosity evolution.

Table 5.8 contains the K magnitudes inside a projected 50 kpc-diameter aperture for $q_o = 0.0$ and 0.5, and the adopted galactic absorption and K-corrections for the different clusters. Figure 5.33 shows the K magnitude-redshift diagram for the BCG's (after taking the Galactic extinction and K-correction into account) for the two values of q_o that we are considering. The dashed line is a least squares fit to the data. The formal

* Changing the gradient by as much as factor 2 introduces changes in the K magnitude of $\sim 0\overset{m}{.}09$, which are negligible for our purposes.

Table 5.8: Photometric data for the K Hubble diagram.

Cluster	z	$K^{50kpc}_{q_o=0.0}$	$K^{50kpc}_{q_o=0.5}$	K_K	A_K
Coma (NGC4889)	0.023	8.96	8.96	−0.07	0.00
Abell 963	0.206	13.21	13.15	−0.40	0.00
Abell 1942	0.224	13.50	13.46	−0.42	0.00
2244-02	0.329	14.85	14.81	−0.50	0.01
Abell 370	0.374	14.53	14.43	−0.52	0.00
0024+16	0.391	14.84	14.71	−0.53	0.01
0016+16	0.546	15.71	15.56	−0.56	0.01
J1888.16CL	0.563	15.75	15.61	−0.56	0.00
Cl0317+1521	0.583	16.57	16.50	−0.56	0.05
F1767.10TC	0.664	16.37	16.24	−0.56	0.00
Cl1322+3029	0.697	16.34	16.16	−0.56	0.00
Cl0020+0407	0.698	16.51	16.46	−0.56	0.01
Cl1322+3027	0.751	16.40	16.22	−0.57	0.00
Cl2155+0334	0.820	16.67	16.57	−0.57	0.02
Cl1603+4313	0.895	17.20	17.06	−0.58	0.00

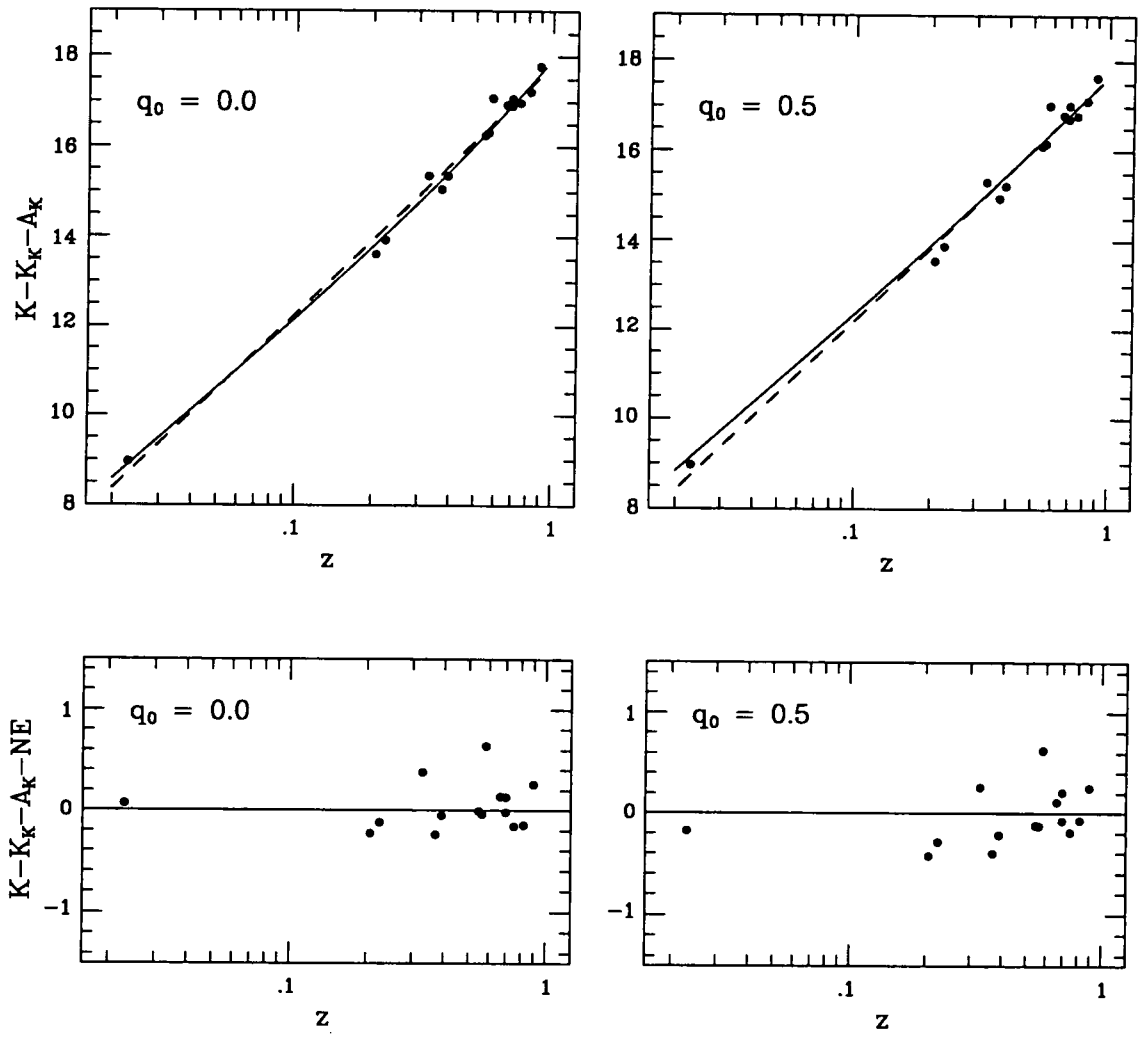

Figure 5.33. Top diagrams: magnitude-redshift relation (Hubble diagram) for the Brightest Cluster Galaxy in K. The dashed line is a least squares fit to the data. The solid line shows the no-evolution prediction, normalized to the data at $z = 0.7$. The K magnitudes have been measured inside a projected 50 kpc-diameter aperture (for two different values of q_0) and have been corrected from Galactic extinction and K-correction. Bottom diagrams: same data after subtracting the no-evolution prediction (shown as the solid line on the top diagrams).

photometric errors are smaller than the size of the points. The *r.m.s.* scatter around this line is $\sim 0^m\!.28$, which is similar to the one found in the optical V diagram after applying the Bautz-Morgan class correction and the richness correction (Sandage 1988). Without these corrections, the V Hubble diagram shows an scatter of $0^m\!.35$ (Sandage & Hardy 1973). We do not have enough information to apply such corrections in our sample, but the small scatter that we obtain without introducing them shows that the BCGs are better standard candles in K than in the optical, as expected.

The solid lines on the top diagrams show the no-evolution predictions. They have been normalized to the data at $z = 0.7$, were the density of points is higher. The points agree very well with the no-evolution prediction. The *r.m.s.* around the no-evolution line is $0^m\!.23$ for $q_o = 0.0$ and $0^m\!.28$ for $q_o = 0.5$. Therefore, the data are consistent with no evolution in the K luminosity of BCG's. This argues against the kind of strong luminosity evolution implied by the radio galaxies, suggesting that radio galaxies and BCG's have very different evolutionary histories.

5.13.2 The K Luminosity functions

Although BCG's do not show evidence for luminosity evolution, it could be argued that they might be a special class of objects that do not share the same evolution as the rest of the cluster galaxies, even though their colour evolution does not seem to deviate from the trend shown by other red members. Let us consider now the properties of the luminosity functions (LFs) of the whole galaxy population in the high redshift cluster sample.

Since the number of objects per cluster is relatively small, we have combined them in the three redshift bins considered in previous sections. As before, we will consider K

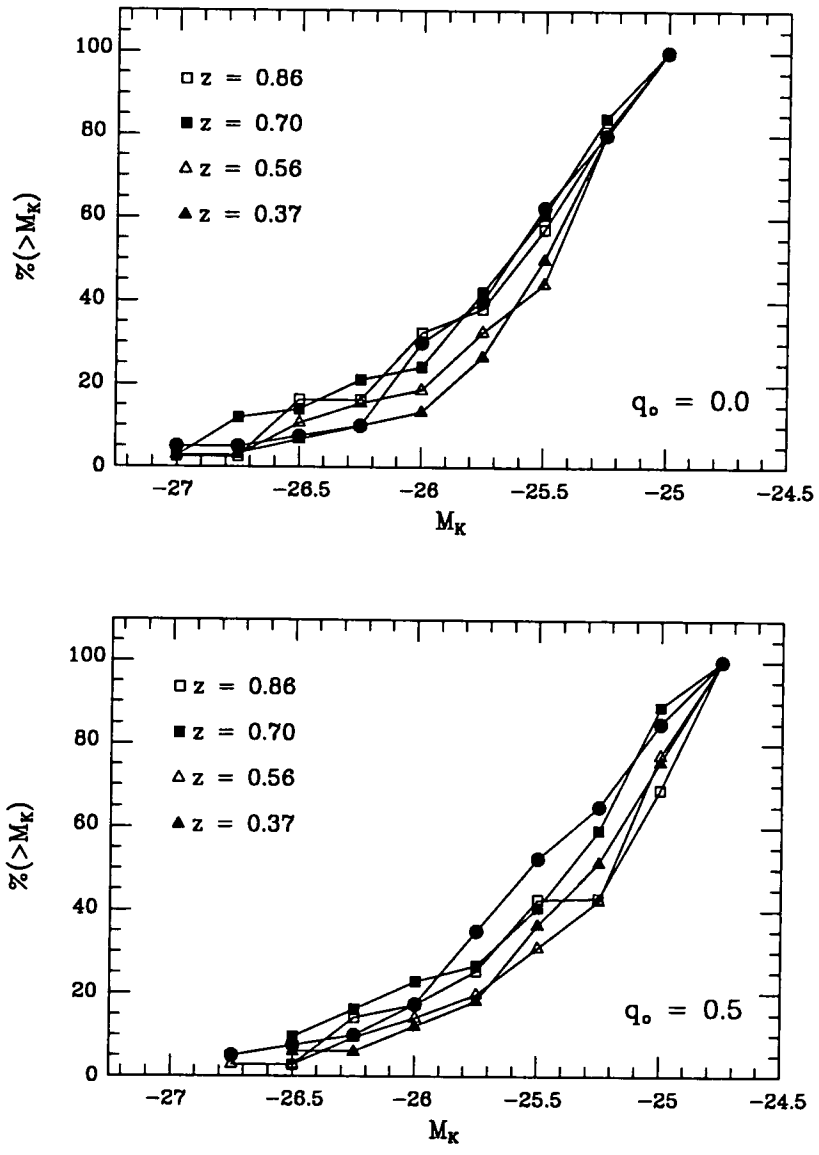

Figure 5.34. Cumulative K luminosity functions for the galaxies in the high z cluster sample after field correction. The data is presented in the three redshift bins introduced in previous sections. Two values of q_o have been considered. The LF of Abell 370 has been plotted for comparison.

magnitudes inside a fixed 50 kpc-diameter projected aperture.* The field contamination has been taken into account following similar procedures to the ones described in §5.7. Figure 5.34 shows the cumulative luminosity functions for the three redshift bins and two q_o values, after the Galactic extinction and K-correction has been taken into account. All the luminosity functions have been cutoff at $M_K = -25\overset{m}{.}0$ for $q_o = 0.0$ $M_K = -24\overset{m}{.}75$ for $q_o = 0.5$ to ensure similar depths for all clusters. For comparison we plot on the same graph Abell 370 luminosity function.

A Kolmogorov-Smirnov test indicates that all the high redshift LFs are compatible with each other, and with the one of Abell 370. The probability for the null hypothesis (*i.e.*, each LF is compatible with any other) is always $\gtrsim 65\%$. This indicates that our data are compatible with no luminosity evolution between $z = 0.37$ and $z = 0.9$, in line with what we found for the BCG's. The data rule out a global luminosity evolution $> 0\overset{m}{.}5$ in K (between those redshifts) at a $\sim 95\%$ confidence level.

To test if this result is in contradiction with the detected colour evolution, we have plotted in Figure 5.35 the expected luminosity evolution in K for the same galaxy evolution models presented in §5.10. Since the detected colour evolution was well bracketed by these model results, we can expect them to represent a realistic range of the amount of luminosity evolution that we can expect. The actual value is model dependent, but the range of models considered predict a luminosity change between $0\overset{m}{.}2$ and $0\overset{m}{.}5$ from $z = 0.37$ to $z = 0.9$. Therefore, the colour evolution detected implies a luminosity evolution that is not inconsistent with what we measure.

Lilly & Longair (1984) detect a luminosity evolution in K of $\sim 0\overset{m}{.}5$ for radio galaxies in the same redshift range ($q_o = 0.5$), which is only marginally consistent with the results from our LFs. Regrettably, a LF for a K-selected sample of galaxies in a low

---

* $H_o = 50$ km s^{-1} Mpc^{-1} has been considered throughout this section.

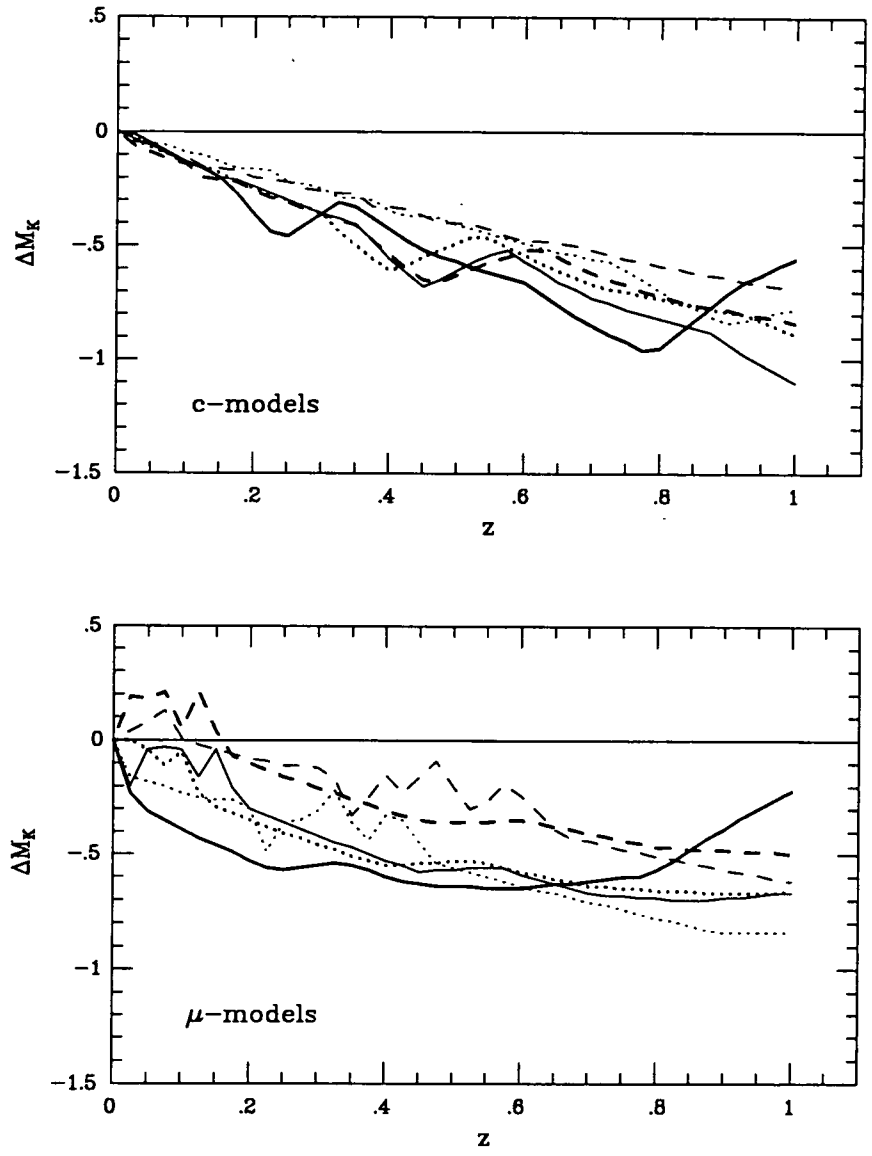

Figure 5.35. K Luminosity evolution for the same Bruzual (1983) models presented in Figures 5.28 and 5.29. The c-models have $\tau = 1\,\mathrm{Gyr}$ and a standard IMF, with $z_{for} = 2$ (solid lines), $z_{for} = 5$ (dotted lines) and $z_{for} = 10$ (dashed lines) for $q_o = 0.5$ (thick lines) and $q_o = 0.0$ (thin lines). The μ-models have $\mu = 0.5$. The rest of the parameters are as for the c-models.

redshift cluster is not available, and the comparison cannot be extended to $z = 0$, but the Hubble diagram suggests that the amount of luminosity evolution in K between $z \sim 0$ and $z \sim 0.9$ is rather small, and inconsistent with a brightening of 1 magnitude by $z = 1$ as measured for radio galaxies.

5.14 Conclusions

In this Chapter we have carried out an optical-IR study of nine clusters in the redshift range $0.5 < z < 0.9$. The main conclusions are:

1. To study galaxy evolution as a function of redshift it is necessary to build samples in a way that is independent of the evolutionary effects that we are trying to measure.

2. The selection of high redshift galaxies in the near-IR produces a much more representative sample of the cluster galaxy population than optical selection criteria. Samples selected at 2μm contain basically the same proportion of all galaxy types at all redshifts, while optically selected samples are strongly biased towards blue, star forming objects.

3. Field contamination can be removed with sufficient accuracy using published field data to derive the colour distribution of the cluster members.

4. The field-corrected colour distributions show *systematic* evolution as a function of redshift: (i) The *red envelope* disappears at high redshift. At $z \sim 0.9$ there are *no* galaxies as red as present-day ellipticals at all wavelengths, implying that even the reddest, presumably oldest galaxies, had significantly evolved when the Universe

was 40–50% its present age. (*ii*) The colour distributions at long wavelengths show strong, relatively narrow peaks, indicating that the bulk of the old stellar population in cluster galaxies is quite homogeneous, suggesting a common origin and epoch of formation. The peaks move towards the blue when redshift increases. (*iii*) A tail of blue objects grows with redshift, and is stronger in shorter wavelength colours.

5. The bulk of the detected colour evolution can be interpreted in the framework of current galaxy evolution models as the ageing of an old stellar population. The amount of evolution detected implies that most of the star formation in cluster galaxies happened at $z > 2$.

6. Superimposed on the *passive* evolution, a substantial fraction of the cluster galaxies shows evidence for episodic star formation, but only a small fraction ($< 10\%$) of their total mass needs to be turned into stars to explain the observed colour changes. The fraction of objects involved increases with redshift. We suggest this may be linked to the *Butcher-Oemler effect* observed at lower redshifts.

7. The K magnitude-redshift relation (Hubble diagram) for the Brightest Cluster Galaxies is very tight. Without applying the richness and Bautz-Morgan corrections, the scatter in K up to $z \simeq 0.9$ is $\sigma = 0\overset{m}{.}28$, while in the optical it is $\sigma = 0\overset{m}{.}35$ up to $z \simeq 0.5$. The scatter is also significantly smaller than for radio galaxies, which have $\sigma \simeq 0\overset{m}{.}4$.

8. We have not detected significant amounts of luminosity evolution at 2μm, in contrast with the results obtained for radio galaxies. The measured limits on the K luminosity evolution are however compatible with the implications of the detected colour evolution, according to simple evolutionary models.

6 THE FUTURE: TOWARDS HIGHER REDSHIFTS

6.1 Introduction

In this thesis we have carried out an optical-IR study of normal galaxies in clusters with $0.37 < z < 0.9$, obtaining substantial information on the evolutionary state of the stellar populations in these galaxies as a function of redshift, covering a significant range of look-back times. However, only by gathering data for galaxies at redshifts as high as possible, and therefore by extending the available look-back time baseline, we will be able to understand the physical processes which led to the formation of galaxies of different morphological types and to directly test the alternative theories of galaxy formation and evolution. We have shown that passive evolution is a perfectly adequate description of the measured colour evolution in *red* cluster galaxies to $z = 0.9$, but models with some residual star formation lasting longer (*e.g.*, μ-models) could also work if z_{for} is high. Optical-IR photometry for galaxies at $z \sim 1.5$–2 would give a definite answer to that problem, because it would be able to detect the presence of relatively few very young stars, that would be absent if there is no residual star formation. It also would provide tighter limits for z_{for}, because, for example, the expected difference in colour evolution between models with $z_{for} = 2$ and $z_{for} = 5$ is only a few tenths of a magnitude at $z = 1$, but it is > 1 mag at $z = 1.5$.

To test the influence of the environment, it is necessary to study galaxies with $z > 1$ in the field and in clusters (if they exist). A redshift $z \approx 1.5$ corresponds to a look-back time of 80% of the cosmic age. *Any* objective constrains on the *normal* population of galaxies at that epoch will represent an important development in observational cosmology.

Important questions to answer are:

1. Is the mean stellar population at $\langle z \rangle = 1.5$ consistent with passive evolution of the present mixture of galaxy types, or is more radical evolution witnessed? A measure of the rate of change of star formation would allow us to place more stringent limits on the epoch of major star formation.

2. What limits can be placed on on evolution in the galaxy luminosity function (LF)? Is the high z LF consistent, for example, with a picture where the most massive systems formed by merging subunits?

3. Is there evidence for evolution in the clustering of galaxies? Dense bound systems are not expected at high redshift in the standard Cold Dark Matter cosmologies (Frenk *et al.* 1990): it is now possible to verify the situation observationally.

Provided the selection criteria are rigorously understood, even a few (10–20) $z > 1$ galaxies would make major inroads on these problems. The major hurdle has been to define practical and reliable search strategies. We have demonstrated that it is essential to select fair samples of galaxies at all redshifts that are representative of the normal galaxy population, avoiding the ultraviolet bias and keeping the selection effects under control. The near-IR observations play a pivotal role in that respect.

With all that in mind, we have developed three different strategies to extend this kind of studies beyond $z = 1$: study of gravitationally lensed galaxies, search for clustered galaxies producing C IV absorption lines in QSOs and follow-up of ROSAT high redshift

clusters. We will present them in this chapter, demonstrating their feasibility, showing how much progress it has been made in each direction and what the future plans are.

6.2 Optical-Infrared studies of Gravitationally Lensed Galaxies

Giant luminous arcs were first discovered in the galaxy clusters 2244−02 ($z = 0.328$, Lynds & Petrosian 1986) and Abell 370 at $z = 0.374$ (Soucail *et al.* 1987a). Several possible explanations were considered for the origin of such structures, *e.g.* regions of star formation generated by explosive events, light echoes of a previously bright object at the centre of the cluster, etc. (Miller & Goodrich 1988), but the spectroscopical measurement of the redshift of the giant arc in Abell 370 ($z_{arc} = 0.724$, Soucail *et al.* 1988b) confirmed the hypothesis that the giant arcs are gravitationally-lensed background galaxies (Paczyński 1987).

The list of candidate giant arcs extends now to more than ten (Fort 1990, and references therein), and extensive photometric and spectroscopic work has been carried out on the brighter examples to determine the redshift and nature of the lensed object (see, *e.g.,* Soucail *et al.* 1987a,b, 1988b; Miller & Goodrich 1988; Giraud 1988; Fort *et al.* 1988; Pello-Descayre *et al.* 1988; Lynds & Petrosian 1989; Aragón-Salamanca & Ellis 1990; Pello *et al.* 1990; Soucail *et al.* 1990; Wlérick *et al.* 1990; Ellis, Allington-Smith & Smail 1991; Pello *et al.* 1991) There has been a steady rise in the number of spectroscopically confirmed arcs. At the time of writing, the total number stands at 7. These are serendipitous finds, *i.e.,* discovered in a heterogeneous set of optical images of clusters obtained for other purposes by different groups, without a well-defined search strategy, and so do not constitute a complete sample. However, concerted efforts are now underway to construct such a sample from existing homogeneous data sets (Smail *et al.* 1991) or from surveys

(see ahead). Most giant arcs have very blue optical colours, but due to their high redshift, the optical bands are sampling the UV part of the spectrum where small amounts of star formation might produce a substantial enhancement of the flux. Observations in the near-IR can be used to determine if the lensed galaxies are dominated by young stellar populations or are just normal galaxies undergoing short term starburst (see ahead).

There has been also intensive theoretical work to build realistic models of gravitational lenses produced by clusters of galaxies, predicting the shape, frequency and distribution of lensed images (Grossman & Narayan 1988, 1989; Nemirnoff & Dekel 1989; Bergmann, Petrosian & Lynds 1990; Hammer & Rigaut 1989; Mellier *et al.* 1990; Hammer 1990). Using these models and the observed properties of arcs it is possible to constrain the shape and amplitude of the cluster gravitational potential, and therefore infer the amount and distribution of dark matter in clusters.

Grossman & Narayan (1988) and Nemirnoff & Dekel (1989) demonstrated that for each giant arc there should be many small distorted images of background galaxies (*arclets*), and that the occurrence rate for arcs of different sizes would test the lensed hypothesis further, and might add a new probe of the mass distribution in the cluster lenses and the nature of the background population. Fort *et al.* (1988) and Tyson, Valdes & Wenk (1990) found a large number of such arclets, which are often apparent only after subtraction of deep frames taken in different passbands. They present strikingly blue optical colours and show tangential elongation with respect to the cluster centre. Their distribution has been used to map the cluster potential and therefore constrain the mass distribution. Using a well-defined sample of arclets in clusters at different redshifts, the redshift distribution of the background objects as a function of colour can in principle be derived (Ismail *et al., in preparation*).

The lensing phenomenon provides another powerful tool in observational cosmology. The clusters can be used as *gravitational telescopes*. Since the process conserves surface brightness, any image magnification produces easily recognisable features and hence access to a high redshift population which is difficult to obtain. A major advantage of lensing arises because the objects lie behind a totally unrelated cluster. However, a sizeable sample is needed to determine whether selection effects are operating. This is a more efficient way of building a sample of high redshift of field galaxies than direct searches at optical/infrared wavelengths, because of the plethora of underluminous foreground objects that can only be eliminated via time-consuming spectroscopy. Even if the redshift of the lensed objects is not known, it must be higher than that of the cluster. A photometric study, including the essential near-IR, would provide with crude spectral energy distributions necessary to understand the nature and evolutionary status of these objects. Ideally, we would like to find and select the arcs in the IR. This is still not easy to do for a sizeable sample with the available arrays, but it should be feasible in the near future. In fact, we have found in K a candidate arc parallel to the giant arc in 2244−02 that had not been seen in the optical.

One of the questions that can be answered with optical and IR photometry for a sizeable sample of arcs is whether the population of lensed galaxies is intrinsically blue across a wide wavelength range, indicating that they are strong star forming objects, or some biases are at work to select only blue objects. Since most arcs are found in optical wavelengths, the UV bias discussed in Chapter 2 might be important. Another possible selection bias is caused by objects being selected above an apparent surface brightness limit, a similar problem seen in faint galaxy surveys (Phillipps, Davies & Disney 1990). Arc searches are thus biased towards including objects with high surface brightness, which might be those sharing the highest star formation rates and bluest colours. At its extreme,

these two effects could combine to produce a preponderance of highly-magnified H II regions of normal galaxies in the sample, misidentifying them as less magnified galaxies. The IR flux can help to clarify if an old underlying population, indicative of a normal galaxy, is present.

Work is in progress in this direction. Y. Mellier, B. Fort & G. Soucail, (Toulouse) are imaging a very large selection of clusters with $0.2 < z < 0.6$ to faint limits at the ESO 3.6-m and NTT telescopes to create a large new objective sample of arcs. We are imaging the candidate arcs in the IR using IRCAM at UKIRT and IRIS* at the AAT. The results of the optical-IR survey will be presented elsewhere (Ellis *et al., in preparation*). Later in this section we will present the first results of that work, concerning mainly the giant arc in Abell 370.

The gravitational magnification is in some cases large enough to obtain *spatially resolved* photometry and spectroscopy of the lensed galaxies, enabling us, for example, to detect the intrinsic rotational velocity of the source galaxy in an emission line of the spectrum of the arc. Soucail & Fort (1991) have exploited this possibility to try and constrain the value of H_o. From the measured rotational velocity, an absolute magnitude of the galaxy can be derived applying the Tully-Fisher relation. From the apparent magnitude (corrected for gravitational magnification and redshift effects), a distance modulus can be derived, and related to the cosmological parameters H_o and q_o. Several uncertain corrections have to be applied (inclination of the lensed galaxy, K-correction, evolutionary correction,...). Soucail & Fort apply this method to the giant arc in Abell 2390 ($z_{clust} = 0.231$, $z_{arc} = 0.913$), and discuss these uncertainties in detail. They conclude that with a sample of several arcs at different redshifts, both H_o and q_o could be determined. Even though one has to be cautious and not to underestimate the size of the difficulties

* IRIS is a new infrared camera that uses a 128 × 128 HgCdTe ('Mer-cad-tel') array, available as a common user instrument for imaging and spectroscopy at the AAT (Allen 1990, 1991).

and uncertainties involved, spatially resolved optical-IR photometry and spectroscopy of relatively bright large arcs could yield very useful information regarding the dynamical properties and star formation rates for different components of the high redshift galaxies and, perhaps, constrain the value of cosmological parameters. A very suitable candidate for such a study is the arc is the cluster 0500−24 ($z_{clust} = 0.321$, $z_{arc} = 0.91$, Giraud 1988, and private communication), which is well within the capabilities of IRIS and LDSS at the AAT.

6.2.1 Arcs in Abell 370

The giant arc in the rich cluster Abell 370 (z = 0.374) is one the most impressive examples of several now known. The pioneering spectroscopic techniques of Soucail *et al.* (1988b) led to a convincing discovery of an emission line throughout the arc supporting the hypothesis of a gravitationally-lensed background galaxy at z = 0.72. A fainter arc in the same cluster (A5, about 45 arcsecs south of the giant arc) is now claimed to be due to a lensed galaxy with z ∼ 1.3 (Soucail *et al.* 1990).

The optical study is based on CCD data taken at the AAT through 4 intermediate-band filters centred at 418, 502, 685 and 862 nm plus broad-band U presented by MacLaren *et al.* (1988). Deep V-band images were also obtained at the 1.5m Danish telescope at La Silla as part of a search for distant supernovae (Nørgaard-Nielsen *et al.* 1989). A summed 4 hour exposure in V shows both the giant and A5 arcs used in this analysis (Figure 6.1(a)). Infrared K (≡ 2μm) images were taken using the IRCAM on UKIRT with 1.″24 pixels in two nights (5/6 July 1989, 1600 s; and 28/29 October 1989, 3600 s —service observation). We followed the same reduction and calibration techniques discussed in Chapter 2. The final coadded K image is shown in Figure 6.1(b); the giant arc is clearly visible but A5 is not detected.

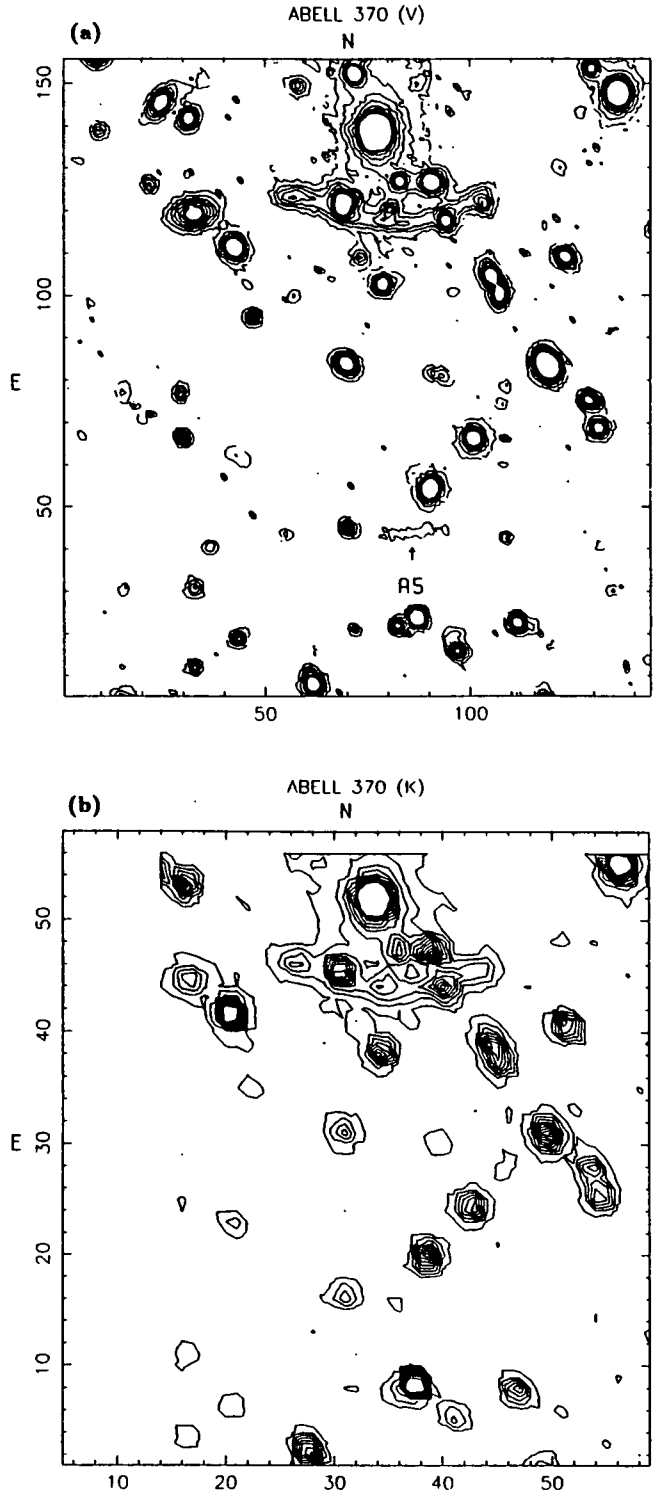

Figure 6.1. (a) 4 hour V-band image of Abell 370 obtained with the 1.5-m Danish telescope at 0.″47 pixel^{-1}. The lowest contour has μ_V=26^m.0 arcsec^{-2}. (b) 5200 s K-band image (scale 1.″24 pixel^{-1}). The lowest contour has μ_K=21^m.7 arcsec^{-2}. North is up, and East is left on both images. The numbers on the axis are pixels.

The giant arc is very prominent in U, where no contamination from galaxies can be seen (see Plate 1 in MacLaren *et al.* 1988), but this is mainly because the cluster galaxies are themselves very red in $(U - V)$. The arc does not seem to be intrinsically very blue, since it is easily visible in K.

We have used the photometry to obtain a low resolution SED for the giant arc. Since it is heavily contaminated by cluster members in most images, we measured the arc flux in four uncontaminated portions in the different photometric bands. Using the measured flux and the method described in MacLaren *et al.* (1988), together with the absolute calibration for the K band of Koornneef (1983), we built SEDs for the four portions. The four portions share the same SED within photometric uncertainties. Figure 6.2 shows the average SED of the arc compared with the spectra of present day galaxies of different spectral types for $z = 0.37$, the cluster redshift, and $z = 0.72$, the spectroscopic redshift of the arc. The arc SED can readily be understood in terms of a Sb or Sc galaxy at the spectroscopic redshift $z = 0.723$. The K measurement is somewhat too high for any normal galaxy at the cluster redshift. Thus our broad-band photometry provides reasonable independent support for the lensing of a normal background spiral, and the apparently blue optical colours are naturally explained without the need of unusually strong star formation. Indeed, they stress the dangers of inferring galaxy evolution from optical data alone.

Precise redshifts are not necessarily required to make interesting statements about the galaxy population behind the cluster. The arc A5 is a good example; it is considerably fainter than the giant arc, much bluer and now a tentative redshift $z = 1.3$ is available (Soucail *et al.* 1990). Our 5200 s integration at 2μm with IRCAM failed to detect A5, implying $(V - K) \leq 3\overset{m}{.}7$ ($V = 21\overset{m}{.}5$). Another 6300 s integration in K of the A5 area was taken the night of 16/17 November 1990 using the 'in field' chopping technique. Although the weather conditions were rather poor, photometric calibration was obtained

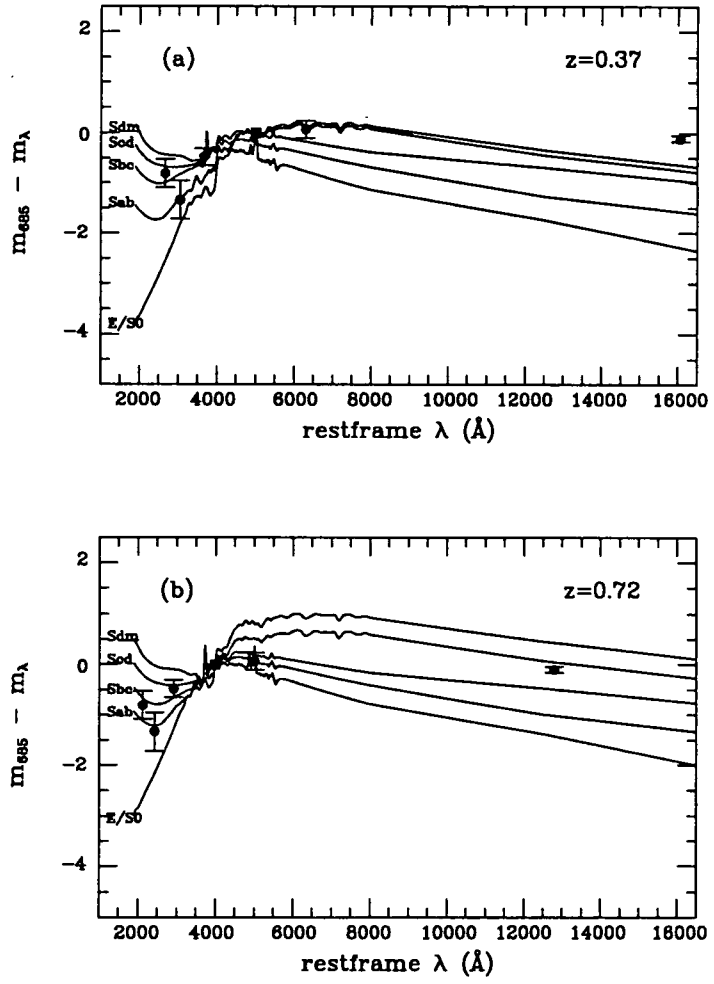

Figure 6.2. Mean rest-frame SED of the giant arc in Abell 370 compared with those of present-day galaxies of different morphological types, assuming the arc has (**a**) $z = 0.37$ —the cluster redshift, and (**b**) $z = 0.72$ —the spectroscopic redshift of Soucail *et al.* (1988b). Error bars represent the scatter in colour within 4 portions uncontaminated by cluster galaxies. The arc and galaxy SEDs have been normalized at the observed 685 band.

using previous images taken in photometric conditions. This image was coadded to our previous data, providing a 4σ detection of A5 ($K = 19\overset{m}{.}4 \pm 0\overset{m}{.}25$), giving $(V-K) = 3\overset{m}{.}51$. At the proposed redshift, the lensed galaxy is bluer than all but the most spectacular star-forming galaxies known (for example, the Sm/Irr NGC4449 placed at $z = 1.3$ would have $(V-K) = 3\overset{m}{.}3$). Even at $z = 0.37$, the colour of this arc is just compatible with being a normal Scd. We can estimate a magnification of ~ 5 from the axial ratio of the arc image. This would be a lower limit, since the arc is probably unresolved. From that, we can estimate that the lensed galaxy, if at $z = 1.3$, is fainter than $M_V \sim -20\overset{m}{.}89$ ($H_o = 50$, $q_o = 0.5$, with a K-correction appropriate for an Sdm). This is at least ~ 1 mag fainter than an L^* galaxy (Tammann, Yahil & Sandage 1979), and would not have been detected (or recognized as a high z galaxy) if it had not been lensed. The connection between such a population and that inferred in faint field galaxy surveys is discussed in some detail by Tyson (1990) and Ellis (1990b).

This section demonstrates the feasibility of our approach, and shows some interesting results. When the same kind of analysis is applied to a sizeable sample of arcs, we expect to obtain statistical information on the nature an evolutionary state of high redshift field galaxies, very difficult to obtain at the present by any other means.

6.3 C IV Absorption Lines in the Spectra of High Redshift QSOs

The discovery of metallic absorption line systems in the spectra of QSOs opened exciting new opportunities in observational cosmology. Very important information concerning the formation and evolution of galaxies and heavy elements, and the large scale structure of the Universe can be inferred from the study of such systems (see, *eg*, Weymann, Carswell

& Smith 1981, Sargent 1988, Sargent, Boksenberg & Steidel 1988, Bergeron 1988, and references therein). It is beyond the scope of this thesis to describe the results obtained in this field, but we will use the absorption lines systems as signposts to tell us where to look efficiently for high redshift galaxies.

Imaging QSOs with known metallic absorption lines in their spectra has already provided a promising approach for identifying *normal* galaxies at high redshift. Bergeron (1988) pioneered this work for $z_{abs} < 1$* using Mg II systems and, via direct spectroscopic confirmation, finds most Mg II absorbers are luminous field galaxies. To push this technique to $z > 1$, we are carrying out an $I + K$ imaging survey of $z_{em} > 1.9$ QSOs with *clustered* C IV systems such that $1.2 < z_{abs} \ll z_{em}$. QSOs are selected (mainly from the list of Sargent, Boksenberg & Steidel 1988), if there are $N \geq 3$ absorption line systems with a restframe velocity range $\Delta V \leq \pm 2000\,\mathrm{km\,s^{-1}}$. This method increases the chance of detecting luminous galaxies associated with the absorber and checks for the presence of rich clusters at early epochs.

Some concern could exit about whether absorbers with $z_{abs} \simeq z_{em}$ would distort the aims of the program, since the presence of a luminous QSO in the cluster might affect the galaxy population. There is no clear evidence at the present for an effect like that (see, *e.g.,* Foltz *et al.* 1988), but we have decided to eliminate all such QSOs from our list.

In order to identify high z galaxies from the images, we plan to proceed in two stages. Firstly, we must build up a photometric sample to check for an excess population, at relevant angular separations from the QSO, over the expectation of published field counts (Cowie *et al.* 1991). Using the models derived by Couch *et al.* (1991), and extending them to the near IR, we can predict that for a non evolving Coma-like cluster at $z = 1.5$

* In this section we will call 'z_{em}' the redshift of the emission lines coming from the QSO, and 'z_{abs}' the redshift of the absorption line systems in the QSO spectra produced by intervening foreground material.

viewed against the field counts, $K = 19\overset{m}{.}5$–$20\overset{m}{.}5$ is the optimum depth for the project. Brighter than $K = 19\overset{m}{.}0$, the cluster luminosity function is barely sampled; fainter than $20\overset{m}{.}5$, field counts dominate. At $K = 19\overset{m}{.}5$, $N_{cluster} \simeq 8$, $N_{field} \simeq 8$ per IRCAM field (in the $1\overset{''}{.}24$ pixel mode), yielding a 2.8σ excess detection. This calculation has been done neglecting any possible evolution in the cluster galaxies, while the field counts are empirical. If luminosity evolution is present and cluster galaxies get brighter at high redshift, as the colour evolution would imply if strong merging is not present, the computed number density contrast should be an underestimate, making the cluster detection easier. This indicates that 5 QSO studied in this way would provide $\gtrsim 6\sigma$ confirmation of the existence of clusters associated with the paths to the absorption line QSOs. But, after building the photometric sample, only spectroscopy would unambiguously determine whether the detected objects do belong to high redshifts clusters (see ahead).

In Figure 6.3 we show a pilot $I + K$ exposure of the kind required for the QSO Q0151+048 (≡PHL1222) at $z_{em} = 1.99$ (Sargent, Boksenberg & Steidel 1988). The K image is a 5.7 hour total integration obtained at UKIRT with IRCAM on the nights 20/21, 21/22 and 22/23 July 1990. We used the 'in field' chopping technique described in Chapter 2. The final image is flat to $\frac{\sigma_{sky}}{sky} = 3 \times 10^{-5}$, equivalent to a 1σ surface brightness detection limit of $23\overset{m}{.}8\,\mathrm{arcsec}^{-2}$. Photometry inside a $5\overset{''}{.}0$-diameter aperture reaches $K = 20\overset{m}{.}4$ (3σ). The I image is a 1250 s integration taken at the WHT on the night 24/25 July 1990. The detection limit for aperture photometry is $I = 22\overset{m}{.}8$ (3σ inside $5\overset{''}{.}0$).

Objects A and B are physically-associated QSOs (Meylan *et al.* 1990). The compactness of object C and its optical-IR colours indicate that it is probably an M star (see Chapter 5), in agreement with Meylan *et al.* (1990). The cluster of faint objects D–I with $K \simeq 19\overset{m}{.}0$–$20\overset{m}{.}0$ may be associated with a $z_{abs} = 1.66$ system, but no excess count is apparent. The $(I - K)$ colour provides additional information on the individual galaxies

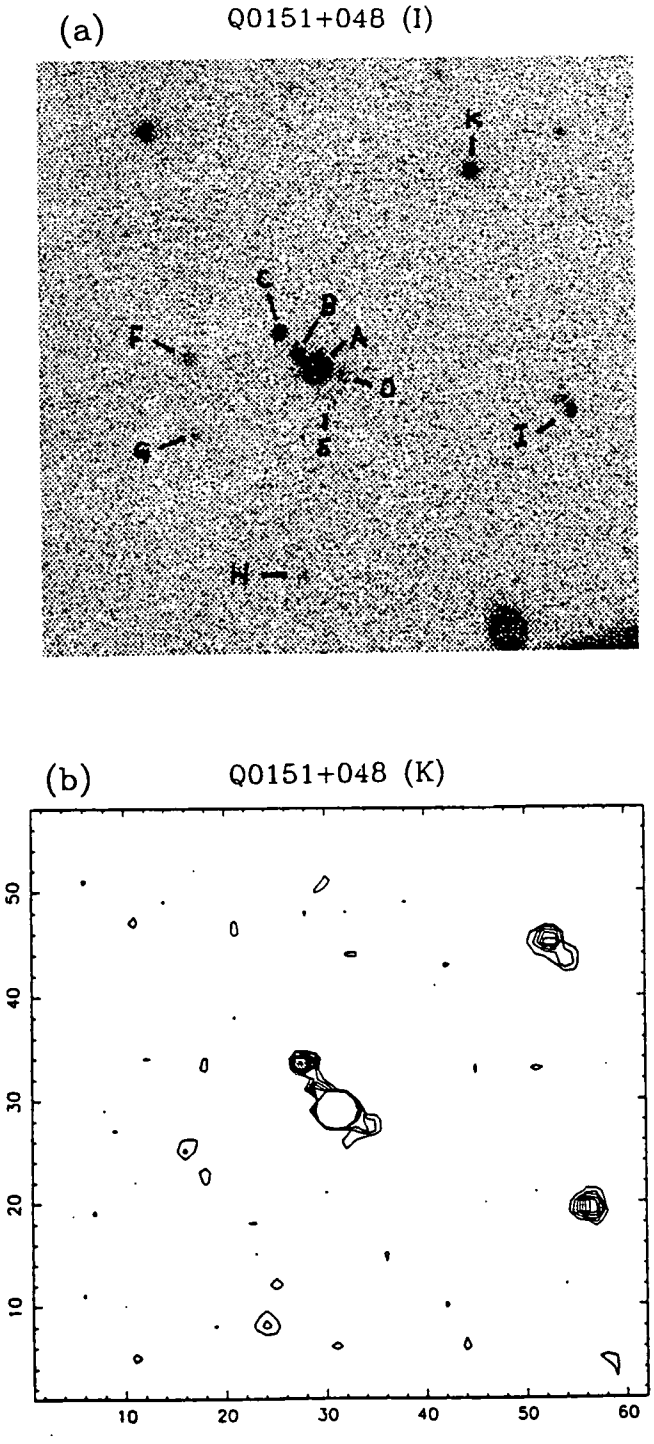

Figure 6.3. **(a)** *I* image of QSO Q0151+048≡PHL1222 taken on the WHT in 0.″8 seeing. The total integration is 1250 s. North is up and East is left. The scale is 0.″27 pixel^{-1}. **(b)** *K* image of the same field taken at UKIRT with IRCAM, in the 1.″24 pixel mode. The total integration is 5.7 hours. The lowest contour corresponds to $\mu_K = 23^m.0$ arcsec^{-2} (2σ above sky level). Objects A and B are physically-associated QSOs. C is probably an M star. D–I are candidate cluster members associated with the $z_{abs} = 1.66$ C IV absorption line system.

close to the QSO. An unevolving L_K^* at $z = 1.5$ ($q_o = 0.5$) has $K = 19\overset{m}{.}4$ with I ranging from $22\overset{m}{.}5$ (Sdm) to $25\overset{m}{.}0$ (E/S0). If the colour evolution detected at lower redshift (Chapter 5) can be extrapolated to $z = 1.5$, passively-evolving galaxies would be $\sim 0\overset{m}{.}9$ bluer and ~ 1 mag brighter in K than their present day counterparts.* Since this implies that all L^* galaxies can be seen to our K limit, this is a very powerful evolutionary test. For Q0151+048, objects D, E and F have $(I - K) = 1.68 \pm 0.07$ ($\sim 0\overset{m}{.}7$ bluer than present-day starburst galaxies), suggesting that if they are members of a high redshift system they are remarkably sub-luminous and uniformly blue. Objects G, H and I have $(I - K) = 2.08 \pm 0.11$, comparable to a present day starburst galaxy at this redshift, but too blue for a passively- evolving early-type galaxy. Evidently, more quasars need to be studied to understand the significance of this, potentially very exciting, result. Using a 'Butcher-Oemler' approach, *i.e.*, subtracting the expected field contamination from the colour distributions, we can check whether the excess population is predominantly *red* as must be the case if clusters contain non-evolved or passively evolving ellipticals, or they are consistently blue, suggesting much stronger evolution.

Although the first priority is the necessary imaging, could redshifts be measured for such samples? Even without evolution, the brightest members at $z = 1.5$ will have $K \simeq 18$, $I \simeq 20$–23. If the excess population is blue, as might be the case for Q0151+048, the sample will be within the reach of LDSS-2 on the WHT (Allington-Smith *et al.* 1990) given the likelihood of emission lines (C IV, Mg II, [O II]). However, this is speculative until the imaging aspect is complete, and even without redshifts, we can reach interesting statistical conclusions regarding the presence or absence of cluster of galaxies associated with the absorption line systems.

---

* This has been estimated from the measured colour evolution up to $z = 0.9$ using a Bruzual (1983) c-model to extrapolate to $z = 1.5$. No merging has been considered.

6.4 ROSAT high redshift clusters

Since the first X-ray survey of the sky by the UHURU satellite it is known that 'rich' nearby clusters were powerful X-ray sources (Gursky *et al.* 1971, Kellogg *et al.* 1972). Subsequent spectroscopic studies detected X-ray emission lines of highly ionized iron and demonstrated that the X-ray emission was produced by thermal radiation of a hot gas with temperatures in the range of 30 to 100 million degrees (Mitchell *et al.* 1976, Serlemitsos *et al.* 1977). The HEAO1 and *Einstein* surveys of significant samples of nearby clusters demonstrated that as a class, clusters of galaxies are bright X-ray sources with luminosities between 10^{42} and 10^{45} ergs s^{-1} (Johnson *et al.* 1983, Abramopoulos & Ku 1983, and Jones & Forman 1984). The increased sensitivity of the *Einstein* imaging detectors also provided the capability to study clusters at redshifts $\gtrsim 0.5$ (Henry *et al.* 1979). The analysis of the X-ray emission from clusters of galaxies has provided with a powerful tool to study the intra-cluster medium, and the formation and dynamical evolution of structures consisting of gravitationally bound galaxies. Several authors (*e.g.*, Kaiser 1986, Shaeffer & Silk 1988) have pointed out the the X-ray observations of such systems may offer important advantages with respect to studies in other wavelengths, particularly at early epochs of the universe. For a description of the cluster properties as determined from X-ray observations, see recent reviews by Giacconi & Burg (1990); Forman & Jones (1990); Fabian, Nulsen & Canizares (1991), and references therein.

Assuming that the hot gas present in galaxy clusters is in hydrostatic equilibrium, the temperature inferred from its X-ray emission is a measure of the confining gravitational potential. Since the X-ray luminosity depends on the square of the gas density, the emission is dominated by the densest clump along each line of sight, and the detection of clusters is almost unaffected by projection effects. Also, the X-ray temperatures should be a better estimator of the gravitational potential than velocity dispersions, which are very dependent

on such effects. These considerations make us expect a catalogue of X-ray selected clusters of galaxies to be more representative of the actual cluster population than an optically selected one (see, *e.g.*, Frenk *et al.* 1990).

The successful launch of the X-ray satellite ROSAT (Trümper 1983) in June 1990 and the completion of the all-sky survey and several deep pointed observations in selected areas with the PSPC (Position Sensitive Proportional Counter, Pfefferman & Briel 1986) will provide a very useful dataset to extend the present knowledge of X-ray emission from clusters of galaxies. At the North Ecliptic Pole (NEP), where all the stripes that build the all-sky survey overlap, the effective exposure time is 45,000 s, which exceeds most *pointed* allocations. Since the exposure falls to only 15,000 s at an ecliptic latitude $\beta = 89°$, the optimum area to reveal the potential of long ROSAT exposures is a field of $\simeq 2°$ centred at the NEP. Additionally, in collaboration with Voges (Max Planck Institut für extraterrestrial Physik, Munich), a deep 40,000 s pointed exposure is available and provides improved spatial resolution for the inner 40 arcmin NEP area. The NEP images reach a limiting flux of $f_\nu \leq 10^{-14}$ ergs cm^{-2} s^{-1} (Böringer 1991, private communication), which is ~ 3 times fainter than the *Einstein* Medium Sensitivity Survey (EMSS, Gioia *et al.* 1990). There are already ~ 75 catalogued sources in the pointed image, and when the final survey frames are added, the catalogue is likely increase to $\sim$ 200–300 sources, with ~ 60 *very* faint sources in the inner 40 arcmin (Böringer 1991, private communication). These numbers match no evolution predictions based on the EMSS counts (Gioia *et al.* 1990) and known X-rays luminosity functions (Kowalski *et al.* 1984, Edge *et al.* 1990) and suggest 15% of the detections (30–40) will be moderate to high redshift clusters (Figure 6.4), with $z > 1$ examples in the inner 40 arcmin. These predictions are based on our present knowledge of the X-ray luminosity function and the density of clusters (with no evolution). Since checking the required input physics (evolution of clustering and the X-ray luminosity function) are part of the motivation for conducting the observations, the predictions are

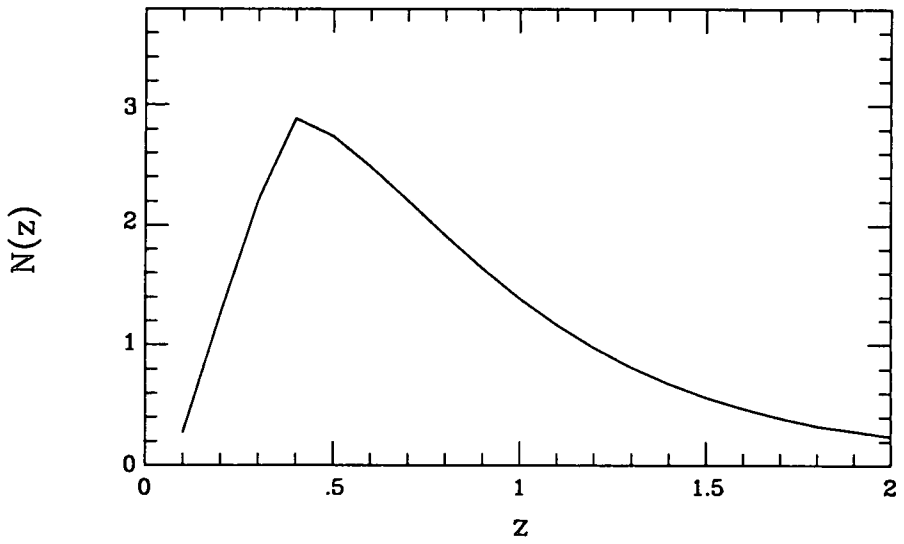

Figure 6.4. The expected distribution, assuming no evolution, for a sample of clusters selected to the ROSAT flux limit $f_\nu \simeq 2 \times 10^{-14}\,\mathrm{ergs\,cm^{-2}\,s^{-1}}$ in the inner $1\,\mathrm{deg}^2$ NEP area (Böringer 1991, private communication). The prediction assumes $H_o = 50\,\mathrm{km\,s^{-1}\,Mpc^{-1}}$ and $q_o = 0.5$.

necessarily very uncertain. But, with our present knowledge, we can expect that ROSAT will be able to detect $z > 1$ clusters if they exist.

An international collaboration including H. Böringer (Max Planck Institut für Extraterrestrial Physik, Munich), J. Huchra (CfA), P. Henri (University of Hawaii), R. Burg and R. Giacconi (STScI), and R. Ellis and the author (Durham) has been set up to follow-up the ROSAT observations from ground-based telescopes (UH 2.2-m, INT, CfA 1.2-m, Multi-Mirror Telescope, Canada-France-Hawaii 3.5-m telescope and WHT). Nearby clusters ($z < 3$) will be identified by correlating digitized sky surveys; wide field imaging is ongoing with the aim of distinguishing Active Galactic Nuclei from clusters via $(B - I)$ colours, morphology and galaxy surface density. In that respect, R. Ellis and the author are conducting an optical follow-up of the ROSAT detections. We have obtained I CCD images (to $I \sim 23$) of all the sources detected in the inner 40 arcmin NEP area at the prime focus of the INT (5–11 July 1991), revealing several distant cluster candidates. Finally, faint object spectroscopy of promising candidates will check the AGN/cluster separation and provide the redshift distribution.

ROSAT high redshift cluster sample will provide the first secure limits on the co-moving number density of high redshift clusters by avoiding many of the difficulties inherent with the deep optical surveys (Gunn, Hoessel & Oke 1986, Couch *et al.* 1991, see also Chapter 5). The abundance of clusters beyond $z \sim 0.5$ is very uncertain because the contrast of the cores of even the richest clusters against the projected field counts falls below 3σ (Couch *et al.* 1991). Many detected clusters are likely to be heavily contaminated by foreground groups and other missed in a way that depends on the average galaxy colours and the observing waveband. A reliably determined number density of galaxy clusters should be a very powerful test of the predictions of current theories of galaxy formation. For instance, standard Cold Dark Matter models (*e.g.,* Frenk *et al.* 1990)

predict a dramatic decline in the number density of rich clusters beyond $z \simeq 0.5$, and this will be directly tested with such a sample.

When using high redshift clusters of galaxies for monitoring galaxy evolution, all the selection effects of optically-selected samples represent a major problem, because we only detect *what we are allowed to see*. Since ROSAT will select clusters at wavelengths that are not directly related with those at which the stellar population data is gathered, these problems should be largely alleviated. The number of clusters found with $z > 1$ (if any) will be necessarily small, but since the effects we are trying to measure must be substantial due to the enormous look-back time interval, even a modest number of clusters will represent much progress.

Obviously, if we do not find any $z > 1$ clusters, it does not necessarily mean that they do not exist. Evolution in the X-ray luminosity function (*cf.* Edge *et al.* 1990) and central concentration of the emission (produced by the amount of intra cluster gas available, its temperature, metallicity, distribution, ...) might make a large difference in the X-ray appearance of a high redshift cluster. But, since the sample of clusters will span a large range of redshifts (Figure 6.4), these effects will be tested directly.

If we find such X-ray selected $z > 1$ clusters, we will be able to build near-IR selected samples of *normal* cluster galaxies, to extend the study presented in Chapter 5 with a substantial increase in look-back time baseline. This will test whether we are able to understand the evolutionary changes when getting closer to the epoch of galaxy formation, keeping the stellar population related selection effects under control. With only 3–4 clusters with $1 < x < 1.5$, and ~ 10 members detected in each, we would be able to add one or two more points to Figures 5.28 and 5.29 at high z, making the discrimination between the different evolutionary parameters (epoch and duration of star formation, rate of evolution, etc) much more unambiguous.

6.5 Summary

In this Chapter we have proposed three new approaches to the study of *normal* galaxies in the field and in clusters beyond $z = 1$: study of gravitationally lensed galaxies, search for clustered galaxies producing C IV absorption lines in QSOs and optical-IR follow-up of ROSAT high redshift clusters. Each method exploits different ways of finding and selecting high redshift galaxies in a controlled way. We hope that these methods will allow us to identify the precursors of present galaxies at very early epochs. Comparing their properties with nearby samples, as we did in Chapters 3 to 5, we aim to understand the origin and evolution of galaxies via the study of their properties as a function of look back time. We emphasize the importance of well-defined selection criteria that find galaxies in wavelengths that are as independent as possible of the properties of the stellar populations that we try to determine.

Each of the projects involves substantial international collaboration. A significant amount of progress has been made in each direction, and the preliminary results are very encouraging, since they show the feasibility of our approaches and are starting to provide valuable information.

7 CONCLUSIONS

In this thesis we have carried out an optical-infrared study of galaxies in clusters at intermediate and high redshifts. Our aim was to detect, quantify and analyze the amount of evolution present in early-type galaxies as a function of look-back time, and use this information to constrain how and when *normal* early-type galaxies formed, and the evolutionary path that led to the present galaxy population in clusters.

Our main conclusions and achievements have been presented at the end of each chapter. We summarize them here:

(*i*) Recognizing the need to construct galaxy samples independent of biases arising from the evolutionary effects that we are trying to detect, we demonstrated that IR-selected samples are much more reliable than optically-selected ones. In particular, they do not suffer from the ultraviolet bias, and 2μm-selected samples would contain approximately the same proportion of all galaxy types independently of redshift. Moreover, at very high redshifts ($z > 1$), near-IR imaging can be used to detect galaxies of all types in reasonable amounts of observing time, while optical imaging would almost exclusively detect blue, star forming galaxies.

(*ii*) On the other hand, the optical bands sample light in the extreme blue and ultraviolet part of the spectrum for high redshift objects, and are sensitive to small amounts of star formation. Therefore, optical-IR colours of IR-selected samples

of galaxies at different z's can be used to study the effects of star formation and evolution on *normal* galaxies as a function of look-back time.

(*iii*) We have developed data processing techniques with infrared arrays to provide the necessary high precision photometry at very faint limits. We demonstrated our success in obtaining very flat images, reaching 1σ surface brightness detection limits fainter than $\mu_K = 23\overset{m}{.}6\,\mathrm{arcsec}^{-2}$.

(*iv*) As a first step towards the high redshift domain, we carried out a detailed optical-infrared study of the rich cluster of galaxies Abell 370 at $z = 0.37$. We constructed a new catalogue of infrared photometry for 53 galaxies in this cluster with $K < 17\overset{m}{.}5$. Using published optical CCD photometry and spectroscopy, we studied the optical-infrared colour-luminosity (c-L) and colour-colour relations for cluster members. The observed c-L diagram is closely similar in slope and zero point to that of present-day ellipticals, suggesting that the bulk of the early-type galaxies do not show significant *overall* colour evolution at $z = 0.37$. However, the E/S0's show a scatter around the main c-L line that is larger than the observational errors and appears to be distinctly non-Gaussian. Interestingly, the spectra of those galaxies with colours redder than the mean line (60% of the early-type members) generally show post-starburst type features, whereas those bluer are largely normal early-type galaxies. This suggests some portion of the scatter in the c-L relation may represent the effects of recent star formation in which an early-type galaxy undergoes a short-term burst of star formation whose post-burst phase may drive it to the red section of the c-L relation via the contribution of asymptotic giant branch (AGB) stars. The size and duration of the AGB effect is broadly compatible with earlier explanations for the blue bursting population and the ultraviolet-excess ellipticals. However, the predominance of this effect does suggest the bulk of the galaxy population in Abell 370 must have suffered this activity at some time

and that it is not restricted to recently-arrived galaxies destined to form the less-substantial S0 population. Only a small fraction ($\sim$ 10%) of the total galaxy mass needs to be involved in such star formation activity.

(v) The next step was a detailed study of two of the clusters of a higher redshift sample, 0016+16 ($z = 0.55$) and F1767.10TC ($z = 0.66$), to test the feasibility and reliability of the extension of our previous work to larger distances. We obtained accurate optical and IR photometry for sizeable K-selected galaxy samples in both clusters. The red members show a very tight c-L diagram, indicating that they form a very homogeneous population. However, a small but significant scatter in the colours around the main c-L line was detected. Since the observed slope of the c-L relation is similar to that of nearby samples (Coma), any colour evolution must have very little luminosity dependence. We detected a small but significant blueing in the optical-IR colours of the red population in both clusters when compared with present-day cluster galaxies. The colour changes are consistent with the ageing of an old stellar population.

(vi) The main analysis is an optical-IR study of nine clusters in the redshift range $0.5 < z < 0.9$. Membership information was not available for most of the objects, but we demonstrated that field contamination can be removed with sufficient accuracy using published field data to derive the colour distribution of the cluster members. The field-corrected colour distributions show *systematic* evolution as a function of redshift: (a) The *red envelope* disappears at high redshift. At $z \sim 0.9$ there are *no* galaxies as red as present-day ellipticals at all wavelengths, implying that even the reddest, presumably oldest galaxies, had significantly evolved when the Universe was 40–50% its present age. (b) The colour distributions at long wavelengths show strong, relatively narrow peaks, indicating that the bulk of the old stellar population in cluster galaxies is quite homogeneous, suggesting a common origin

and epoch of formation. The peaks move towards the blue when redshift increases. (*c*) A tail of blue objects grows with redshift, and is stronger in shorter wavelength colours.

(*vii*) The bulk of the detected colour evolution presented in (*vii*) can be interpreted as the ageing of an old stellar population. The amount of evolution detected implies that most of the star formation in cluster galaxies occurred before $z \approx 2$. Superimposed on this *passive* evolution, a substantial fraction of the cluster galaxies shows evidence for episodic star formation, but only a small fraction ($<$ 10%) of their total mass needs to be turned into stars to explain the observed colour changes. The fraction of objects involved increases with redshift. We suggest this may be linked to the *Butcher-Oemler effect* observed at lower redshifts.

(*viii*) The K magnitude-redshift relation (Hubble diagram) for the brightest cluster galaxies is very tight. The scatter in K up to $z \simeq 0.9$ is $\sigma = 0^m.28$. We did not detect significant amounts of luminosity evolution at 2μm, in contrast with the results obtained for radio galaxies. The measured limits on the K luminosity evolution are however compatible with the implications of the detected colour evolution, according to simple evolutionary models.

(*ix*) Finally, we propose three new approaches to the study of *normal* galaxies in the field and in clusters beyond $z = 1$: study of gravitationally lensed galaxies, search for galaxies producing clustered metallic absorption lines in QSOs and optical-IR follow-up of ROSAT high redshift clusters. Each method exploits different ways of finding and selecting high redshift galaxies in a controlled way. We emphasize the importance of well-defined selection criteria that find galaxies in wavelengths that are as independent as possible of the properties of the stellar populations that we try to determine. We demonstrated that the projects are feasible, and

are already yielding interesting results. We hope that these methods will allow us to identify the precursors of present galaxies in very early epochs, and obtain equivalent information to that presented in this thesis regarding their evolutionary status.

ACKNOWLEDGMENTS

First of all, I would like to thank my supervisor Richard Ellis, for the support, guidance and patience that made this work possible, and for teaching me to have a general view of Astronomy. Thanks also for believing in my potential as an astronomer a few years ago, and giving me the opportunity of coming to Durham to do a Ph.D. when I was about to give up Astronomy and become a yuppie. I have never regretted it. I hope he counts me among his friends, because I count him among mine.

Also I would like to thank all the people who have collaborated in the work presented in this thesis, Ray Sharples, Warrick Couch and Dave Carter. I owe them many careful observations and ideas.

Many thanks to all the people in the Physics Department —scientists or not— for such a wonderful working atmosphere, many stimulating conversations (not necessarily about science) and for putting up with my horrible accent. Special mention (in alphabetical order) to Nobuo Arimoto (the best office mate I could have ever dreamt for), Richard Bower, Mike Fitchett, Carlos Frenk and John Lucey. They taught me most of what I know about observations, interpretation of data (statistics!) and galaxy evolution. Any misinterpretation of their ideas is my own fault.

I would also like to thank Alan Lotts (yes, there are friendly STARLINK managers!) for his endless patience and help with unfriendly computers. I am indebted to all the people in the STARLINK project, for providing the necessary hardware and software tools. Richard Bower deserves another mention here for his TEXpertise.

Thanks to all the staff of UKIRT and La Palma, for making the observations possible —and carrying out many of them in service time— and to PATT for their generous allocation of observing time.

All my fellow students and friends in the Physics Department deserve much more than this mention for many shared hours. Thanks Rafael, Esperanza, Alberto, Ian (for suffering me during many tropical hours), Steve, Stella (for much more than the lifts in all those cold mornings), Nial, Gordon, Dom,... I owe them many pints.

Many friends have made my life worth living during the last few years, sharing many happy and unhappy moments. I would have never made it without them. Mike F., Rafael (yes, you are both here again), Mike M., Andoni, Inma, Wendy, Catherine(s), José María, Luisa, Cristina, Pepe, Benja, Susana, Javier, Chenchon, several generations of Shincliffers..., many thanks. You all know how important you are.

My first steps as an astronomer were guided by the people in the Departamento de Astrofísica of the Universidad Complutense de Madrid, and George Efstathiou (Oxford). Thanks for all the things I have learned from you.

I am very grateful to the Physics Department and SERC for the financial support that allowed me to survive during the last three years.

And finally, I will take this opportunity to thank all my family, particularly my parents, for all their unconditional love and support over the years. They have always been there, no matter how I was or what I did. I will never be able to pay them back, but they know that I will always love them. *Me gustaría aprovechar esta ocasión para agradecer a toda mi familia, en particular a mis padres, todo su amor y apoyo incondicional durante todos estos años. Siempre han estado ahí, sin importarles como soy o lo que hago. Nunca podre pagarles lo que han hecho por mi, pero ellos saben que les querré siempre.*

BIBLIOGRAPHY

Aaronson, M., 1977. *Ph.D. Thesis*, Harvard University.

Aaronson, M., 1978. *Astrophys. J. Lett.*, **221**, L103.

Abramopoulos, F. & Ku, W., 1983. *Astrophys. J.*, **271**, 446.

Allen, D., 1990. *AAO Newsletter*, No. 55.

Allen, D., 1991. *AAO Newsletter*, No. 57.

Allington-Smith, J.R., Breare, J.M., Ellis, R.S., Parry, I.R., Shaw, G.D. & Webster, J., 1990. *Proc. S.P.I.E.*, **1235**, 691.

Aragón, A., Gorgas, J. & Rego, M., 1987. *Astr. Astrophys.*, **185**, 97.

Aragón-Salamanca, A. & Ellis, R.S., 1990. in *Gravitational Lensing*, p. 288, Eds. Mellier, Y., Soucail, G. & Fort, B., Springer-Verlag, Berlin.

Aragón-Salamanca, A., Ellis, R.S. & Sharples, R.M., 1991. *Mon. Not. R. astr. Soc.*, **248**, 128.

Arimoto, N. & Yoshii, Y., 1986. *Astr. Astrophys.*, **164**, 260.

Arimoto, N. & Yoshii, Y., 1987. *Astr. Astrophys.*, **173**, 23.

Beers, T.C., Flynn, K. & Gebhard, K., 1990. *Astron. J.*, **100**, 32.

Benn, C. & Nicholson, D., 1988. *RGO/La Palma Technical Note No. 45*, Isaac Newton Group. La Palma.

Bergeron, J., 1988. in *QSO Absorption Lines: Probing the Universe*, p. 127, Eds. Blades, J.C., Turnsheck, D. & Norman, C.A., Cambridge University Press, Cambridge.

Bergmann, A.G., Petrosian, V. & Lynds, R., 1990. *Astrophys. J.*, **350**, 23.

Bessell, M.S. & Brett, J.M., 1988. *Publs. astr. Soc. Pacif.*, **100**, 1134.

Bevington, P.R., 1969. *Data Reduction and Error Analysis for the Physical Sciences*, McGraw-Hill, New York.

Bica, E., 1988. *Astr. Astrophys.*, **195**, 76.

Bica, E. & Alloin, D., 1986. *Astr. Astrophys.*, **162**, 21.

Bica, E. & Alloin, D., 1987. *Astr. Astrophys.*, **186**, 49.

Bica, E., Alloin, D. & Santos Jr., J.F.C., 1990. *Astr. Astrophys.*, **235**, 103.

Birkinshaw, M. & Gull, S.F., 1984. *Mon. Not. R. astr. Soc.*, **206**, 359.

Birkinshaw, M., Gull, S.F. & Hardbeck, H., 1984. *Nature*, **309**, 34.

Birkinshaw, M., Gull, S.F. & Moffet, A.T., 1981. *Astrophys. J. Lett.*, **251**, L69.

Blumenthal, G.R., Faber, S.M., Primack, J.R. & Rees, M.J., 1984. *Nature*, **311**, 517.

Bothum, G.D. & Dressler, A., 1986. *Astrophys. J.*, **301**, 57.

Bower, R.G., 1990. *Ph.D. Thesis*, University of Durham.

Bower, R.G., Ellis, R.S., Rose, J.A. & Sharples, R.M., 1990. *Astron. J.*, **99**, 530.

Bower, R.G., Lucey, J.R. & Ellis, R.S., 1991. Mon. Not. R. astr. Soc. in press.

Broadhurst, T.J., Ellis, R.S. & Shanks, T., 1988. *Mon. Not. R. astr. Soc.*, **235**, 827.

Bruzual, G., 1981. *Ph.D. Thesis*, University of California, Berkeley.

Bruzual, G., 1983. *Astrophys. J.*, **273**, 105.

Burstein, D., Bertola, F., Buson, L.M., Faber, S.M. & Lauer, T.R., 1988. *Astrophys. J.*, **328**, 440.

Burstein, D. & Heiles, C., 1982. *Astron. J.*, **87**, 1165.

Butcher, H. & Oemler, A., 1978. *Astrophys. J.*, **219**, 18.

Butcher, H. & Oemler, A., 1984. *Astrophys. J.*, **285**, 426.

Butcher, H., Oemler, A. & Wells, D.C., 1983. *Astrophys. J. Suppl.*, **52**, 183.

Buzzoni, A., 1989. *Astrophys. J. Suppl.*, **71**, 817.

Chambers, K.C., Miley, G.K. & van Breugel, W., 1987. *Nature*, **329**, 604.

Chambers, K.C. & Charlot, S., 1990. *Astrophys. J. Lett.*, **384**, L1.

Charlot, S. & Bruzual A., G., 1991. *Astrophys. J.*, **367**, 126.

Chokshi, A. & Wright, E.L., 1987. *Astrophys. J.*, **319**, 44.

Colles, M., Ellis, R.S., Taylor, K. & Hook, R.N., 1990. *Mon. Not. R. astr. Soc.*, **224**, 408.

Collins, C.A., Nichol, R.C. & Lumsden, S.L., 1991. Mon. Not. R. astr. Soc. in press.

Couch, W.J., 1981. *Ph.D. Thesis*, Australian National University.

Couch, W.J., Ellis, R.S., Godwin, J. & Carter, D., 1983. *Mon. Not. R. astr. Soc.*, **205**, 1287.

Couch, W.J., Ellis, R.S., Malin, D.F. & MacLaren, I., 1991. *Mon. Not. R. astr. Soc.*, **249**, 606.

Couch, W.J. & Newell, E.B. , 1984. *Astrophys. J. Suppl.*, **56**, 143.

Couch, W.J., Shanks, T. & Pence, W.D., 1985. *Mon. Not. R. astr. Soc.*, **213**, 215.

Couch, W.J. & Sharples, R.M., 1987. *Mon. Not. R. astr. Soc.*, **229**, 423.

Couchman, H.M.P. & Carlberg, R.G., 1991. Astrophys. J. in press.

Cousins, A.W.J., 1976. *Mem. R. Astron. Soc.*, **81**, 25.

Cowie, L.L., Gardner, J.P., Lilly, S.J. & McLean, I., 1990. *Astrophys. J. Lett.*, **360**, L1.

Cowie, L.L., Gardner, J.P., Wainstcoat, R.J. & Hodapp, K.W., 1991. *preprint.*

D'Agostino, R.B., 1982. in *Encyclopedia of Statistical Sciences*, Vol. 2, p. 315, Eds. Kotz, S. & Johnson, N. Wiley & Sons, New York.

Davies, R.D., Lasenby, A.N., Watson, R.A., Daintree, E.J., Hopkins, J., Beckman, J., Sanchez-Almeida, J. & Rebolo, R., 1987. *Nature*, **326**, 462.

Davis, M., Efstathiou, G., Frenk, C.S. & White, S.D.M., 1985. *Astrophys. J.*, **292**, 371.

Djorgovski, S., de Carvalho, R., Shlosman, I. & Schombert, J., 1991. in *Morphological and Physical Classification of Galaxies*, Eds. Bursrello, G., Longo, G. & Capaccioli, M., Springer-Verlag, Berlin (in press).

Djorgovski, S., Spinrad, H. & Mear, J., 1985. in *New Aspects of Galaxy Photometry*, Lect. Notes in Phys., Ed. Nieto, J.L. Vol. 232, p. 193, Springer-Verlag, Berlin.

Dressler, A., 1980. *Astrophys. J.*, **236**, 351.

Dressler, A., 1986a. *Astrophys. J.*, **301**, 57.

Dressler, A., 1986b. in *Spectral Evolution of Galaxies*, p. 375, Eds. Chiosi, C. & Renzini, A., Reidel, Dordrecht.

Dressler, A., 1987. in *Nearly Normal Galaxies: from the Planck Time to the Present*, p. 265, Ed. Faber, S.M., Springer-Verlag, New York.

Dressler, A. & Gunn, J.E., 1982. *Astrophys. J.*, **263**, 533.

Dressler, A. & Gunn, J.E., 1983. *Astrophys. J.*, **270**, 7.

Dressler, A. & Gunn, J.E., 1983. *Astrophys. J.*, **270**, 7.

Dressler, A. & Gunn, J.E., 1988. in *Large Scale Structure of the Universe*, p. 311, Eds. Audouze, J. *et al.*, Kluwer, Dordrecht.

Dressler, A. & Gunn, J.E., 1990. in *Evolution of the Universe of Galaxies: Edwin Hubble Centennial Symposium*, A.S.P. Conference Series, Vol. 10, p. 200, Ed. Kron, R.G..

Dressler, A. & Gunn, J.E., 1991. *preprint.*

Dressler, A., Gunn, J.E. & Schneider, D.P., 1985. *Astrophys. J.*, **294**, 70.

Dressler, A. & Shectman, S.A., 1988. *Astron. J.*, **95**, 284.

Edge, A.C., Stewart, G.C., Fabian, A.C. & Arnaud, K.A., 1990. *Mon. Not. R. astr. Soc.*, **245**, 559.

Efstathiou, G. & Silk, J., 1983. *Fundam. Cosmic Physics*, **9**, 1.

Eisenhardt, P. & Chokshi, A., 1990. *Astrophys. J. Lett.*, **351**, L9.

Elias, J.H., Frogel, J.A., Mathews, K., & Neugebauer, G., 1982. *Astron. J.*, **87**, 1029.

Ellis, R.S., 1990a. in *Evolution of the Universe of Galaxies: Edwin Hubble Centennial Symposium*, A.S.P. Conference Series, Vol. 10, p. 248, Ed. Kron, R.G..

Ellis, R.S., 1990b. in *Gravitational Lensing*, p. 236, Eds. Mellier, Y., Soucail, G. & Fort, B., Springer-Verlag, Berlin.

Ellis, R.S. & Allen, D.A., 1983. *Mon. Not. R. astr. Soc.*, **203**, 685.

Ellis, R.S., Allington-Smith, J.R. & Smail, I., 1991. *Mon. Not. R. astr. Soc.*, **249**, 184.

Ellis, R.S., Couch, W.J., MacLaren, I. & Koo, D.C., 1985. *Mon. Not. R. astr. Soc.*, **217**, 239.

Elston, R., 1991. in *Astrophysics with Infrared Arrays*, A.S.P. Conference Series, Vol. 14, p. 3, Ed. Elston, R.

Elston, R., Rieke, M.J. & Rieke, G.H., 1989. *Astrophys. J.*, **341**, 80.

Evrard, A.E., 1990. *Astrophys. J.*, **363**, 349.

Fabian, A.C., Nulsen, P.E.J. & Canizares, C.R., 1991. *Astr. Astrophys. Rev.*, **2**, 191.

Faber, S.M., 1972. *Astr. Astrophys.*, **20**, 361.

Fitchett, M., 1988. *Mon. Not. R. astr. Soc.*, **230**, 161.

Foltz, C.B., Chaffee, F.H., Weymann, R.J. & Anderson, S.F., 1988. in *QSO Absorption Lines: Probing the Universe*, p. 53, Eds. Blades, J.C., Turnsheck, D. & Norman, C.A., Cambridge University Press, Cambridge.

Forman, W. & Jones, C., 1990. in *Clusters of Galaxies*, p. 257, Eds. Oegerle, W.R., Fitchett, M.J. & Dainly, L., Cambridge University Press, Cambridge.

Fort, B., 1990. in *Gravitational Lensing*, p. 221, Eds. Mellier, Y., Soucail, G. & Fort, B., Springer-Verlag, Berlin.

Fort, B., Prieur, J.L., Mathez, G., Mellier, Y. & Soucail, G., 1988. *Astr. Astrophys.*, **200**, L17.

Frenk, C.S., White, S.D.M., Efstathiou, G. & Davis, M., 1990. *Astrophys. J.*, **351**, 10.

Frogel, J.A., Mould, J. & Blanco, V.M., 1990. *Astrophys. J.*, **352**, 96.

Gavazzi, G.& Trincheri, G., 1989. *Astrophys. J.*, **342**, 718.

Giacconi, R. & Burg, R., 1990. in *Clusters of Galaxies*, p. 377, Eds. Oegerle, W.R., Fitchett, M.J. & Dainly, L., Cambridge University Press, Cambridge.

Gioia, I.M., Maccacaro, T., Schild, R.E., Wolter, A., Stocke, J.T., Morris, S.L. & Henry, J.P., 1990. *Astrophys. J. Suppl.*, **72**, 567.

Giraud, E., 1988. *Astrophys. J. Lett.*, **334**, L69.

Glazebrook, K., 1991. *Ph.D. Thesis*, University of Edinburgh.

Graham, J.A., 1982. *Publs. astr. Soc. Pacif.*, **94**, 244.

Grasdalen, G.L., 1980. in *Objects of High Redshift*, IAU Symp. No. 92, p. 269, Eds. Abell, G.O. & Peebles, P.J.E., Reidel, Dordrecht.

Grossmann, S.A. & Narayan, R., 1988. *Astrophys. J. Lett.*, **324**, L37.

Grossmann, S.A. & Narayan, R., 1989. *Astrophys. J.*, **344**, 637.

Guiderdoni, B. & Rocca-Volmerange, B., 1987. *Astr. Astrophys.*, **186**, 1.

Guiderdoni, B. & Rocca-Volmerange, B., 1990. *Astr. Astrophys.*, **227**, 362.

Gunn, J.E., 1989. in *The Epoch of Galaxy Formation*, p. 167, Eds. Frenk, C.S. *et al.*, Kluwer, Dordrecht.

Gunn, J.E., 1990. in *Clusters of Galaxies*, p. 341, Eds. Oegerle, W.R., Fitchett, M.J. & Dainly, L., Cambridge University Press, Cambridge.

Gunn, J.E. & Dressler, A., 1988. in *Towards Understanding Galaxies at High Redshift*, p. 227, Eds. Renzini, A. & Kron, R.G., Kluwer, Dordrecht.

Gunn, J.E. & Gott, J.R., 1972. *Astrophys. J.*, **176**, 1.

Gunn, J.E., Hoessel, J.G. & Oke, J.B., 1986. *Astrophys. J.*, **306**, 30.

Gunn, J.E., Longair, M.S. & Rees, M.J., 1978. in *Observational Cosmology*, Eight advanced course of the Swiss Society of Astronomy and Astrophysics, Eds. Maeder, A., Marinet, L. & Tamman, G.

Gunn, J.E. & Oke, J.B., 1975. *Astrophys. J.*, **195**, 255.

Gursky, H., Kellog, E.M., Murray, S., Leoug, C., Tananbaum, H. & Giacconi, R., 1971. *Astrophys. J. Lett.*, **169**, L81.

Guth, A.H., 1981. *Phys. Rev.*, **D23**, 347.

Hamilton, D., 1985. *Astrophys. J.*, **297**, 371.

Hammer, F., 1990. in *Gravitational Lensing*, p. 271, Eds. Mellier, Y., Soucail, G. & Fort, B., Springer-Verlag, Berlin.

Hammer, F. & Rigaut, F, 1989. *Astr. Astrophys.*, **226**, 45.

Henry, J.P., Brandvardy, G., Briel, V., Fabricant, D., Feigelson, E., Murray, S., Soltan, A. & Tananbaum, H., 1979. *Astrophys. J. Lett.*, **385**, L15.

Henry J.P. & Lavery, R.J., 1987. *Astrophys. J.*, **323**, 473.

Henry, J.P., Soltan, A., Briel, U. & Gunn, J.E., 1982. *Astrophys. J.*, **262**, 1.

Hoessel, J.G., 1980. *Astrophys. J.*, **241**, 493.

Hubble, E.P., 1925a. *Astrophys. J.*, **62**, 409.

Hubble, E.P., 1925b. *Astrophys. J.*, **64**, 321.

Hubble, E.P., 1936. *The Realm of the Nebulae*, Yale University Press, New Haven.

Hubble, E.P. & Humason, M.L., 1931. *Astrophys. J.*, **74**, 43.

Jablonka, P., Alloin, D. & Bica, E., 1990. *Astr. Astrophys.*, **235**, 22.

Jarvis, J.F. & Tyson, J.A., 1980. *Astron. J.*, **86**, 476.

Johnson, H.L., 1966. *Ann. Rev. Astr. Astrophys.*, **4**, 193.

Johnson, M.W., Cruddace, R.G., Ulmer, M.P., Kowalski, M.P. & Wood, K.S., 1983. *Astrophys. J.*, **266**, 425.

Jones, C. & Forman, W., 1984. *Astrophys. J.*, **276**, 38.

Kaiser, N., 1986. *Mon. Not. R. astr. Soc.*, **222**, 323.

Keeping, E.S., 1962. *Introduction to Statistical Inference*, Van Nostrand, Princeton.

Kellog, E.M., Gursky, H., Tananbaum, H., Giacconi, R. & Pounds, K., 1972. *Astrophys. J. Lett.*, **174**, L65.

Kimble, R.A., Sandage, A. & Davison, A.F., 1988. *preprint.*

Kolb, E.W. & Turner, M.S., 1990. *The Early Universe*, Addison-Wesley.

Koo, D.C., 1981. *Astrophys. J. Lett.*, **251**, L75.

Koo, D.C., 1988. in *Towards Understanding Galaxies at High Redshift*, p. 209, Eds. Renzini, A. & Kron, R.G., Kluwer, Dordrecht.

Koo, D.C., 1990. in *Evolution of the Universe of Galaxies: Edwin Hubble Centennial Symposium*, A.S.P. Conference Series, Vol. 10, p. 268, Ed. Kron, R.G..

Koornneef, J., 1983. *Astr. Astrophys.*, **128**, 84.

Kowalski, M.P., Ulmer, M.P., Cruddace, R.G. & Wood, L.S., 1984. *Astrophys. J. Suppl.*, **56**, 403.

Kristian, J. Sandage, A. & Westphal, J.A., 1978. *Astrophys. J.*, **221**, 383.

Kron, R.G., 1978. *Ph.D. Thesis*, University of California, Berkeley.

Kron, R.G., 1980. *Astrophys. J. Suppl.*, **43**, 305.

Landolt, A.U., 1983. *Astron. J.*, **88**, 439.

Lavery, R.J. & Henry, J.P., 1986. *Astrophys. J. Lett.*, **304**, L5.

Lavery, R.J. & Henry, J.P., 1988. *Astrophys. J.*, **330**, 596.

Lebofsky, M.J., 1980. in *Objects of High Redshift*, IAU Symp. No. 92, p. 257, Eds. Abell, G.O. & Peebles, P.J.E., Reidel, Dordrecht.

Lebofsky, M.J. & Eisenhardt, P.R.M., 1986. *Astrophys. J.*, **300**, 151.

Lee, K.L., 1979. *J. Am. Stat. Ass.*, **74**, 708.

Lee, T.J., MacLean, I.S. & Wade, R., 1989. *Infrared Phys.*, **29**, 175.

Lilly, S.J., 1987. *Mon. Not. R. astr. Soc.*, **229**, 573.

Lilly, S.J., 1988. *Astrophys. J.*, **333**, 161.

Lilly, S.J., 1989. in *The Epoch of Galaxy Formation*, p. 63, Eds. Frenk, C.S. *et al.*, Kluwer, Dordrecht.

Lilly, S.J., Cowie, L.L. & Gardner, J.P., 1991. *Astrophys. J.*, **369**, 79.

Lilly, S.J. & Gunn, J.E., 1985. *Mon. Not. R. astr. Soc.*, **217**, 551.

Lilly, S.J. & Longair, M.S., 1982. *Mon. Not. R. astr. Soc.*, **199**, 1053.

Lilly, S.J. & Longair, M.S., 1984. *Mon. Not. R. astr. Soc.*, **211**, 833.

Lucey, J.R, Currie, M.J. & Dickens, R.J., 1986. *Mon. Not. R. astr. Soc.*, **221**, 453.

Lynds, R. & Petrosian, V., 1986. *Bull. Am. astr. Soc.*, **18**, 1014.

Lynds, R. & Petrosian, V., 1989. *Astrophys. J.*, **336**, 1.

MacLaren, I., 1987. *Ph.D. Thesis*, University of Durham.

MacLaren, I., Ellis, R.S. & Couch, W.J., 1988. *Mon. Not. R. astr. Soc.*, **230**, 249.

Maddox, S.J., Efstathiou, G., Sutherland, W.J. & Loveday, J., 1990. *Mon. Not. R. astr. Soc.*, **242**, 43p.

Margon, B., Downes, R.A. & Chanan, G.A., 1985. *Astrophys. J. Suppl.*, **59**, 23.

Margon, B., Downes, R.A. & Spinrad, H., 1983. *Nature*, **301**, 221.

Mathis, J.S., 1990. *Ann. Rev. Astr. Astrophys.*, **28**, 37.

McCarthy, P.J., van Breugel, W., Spinrad, H. & Djorgovski, S., 1987. *Astrophys. J. Lett.*, **321**, L29.

McClure, R.D. & van den Berg, S., 1968. *Astrophys. J.*, **73**, 313.

McLean, I.S., Chuter, T.C., MacCaughrean, M.J. & Rayner, J.T., 1986. *Proc. S.P.I.E.*, **627**, 430.

Mellier, Y., Soucail, G., Fort, B & Mathez, G., 1988. *Astr. Astrophys.*, **199**, 13.

Mellier, Y., Soucail, G., Fort, B., Le Borgne, J.F. & Pello, R., 1990. in *Gravitational Lensing*, p. 261, Eds. Mellier, Y., Soucail, G. & Fort, B., Springer-Verlag, Berlin.

Meylan, G., Djorgovski, S., Weir, N. & Shaver, P., 1990. in *Gravitational Lensing*, p. 111, Eds. Mellier, Y., Soucail, G. & Fort, B., Springer-Verlag, Berlin.

Mihalas, D., & Binney, J., 1981. *Galactic Astronomy: Structure and Kinematics*, (2nd edition) W.W. Freeman & Co., San Francisco.

Miller, J.S. & Goodrich, R.W., 1988. *Nature*, **331**, 685.

Miller, G.E., & Scalo, J.M., 1979. *Astrophys. J. Suppl.*, **41**, 513.

Mitchell, R.J., Culhane, J.L., Davison, P.J. & Ives, J.C., 1976. *Mon. Not. R. astr. Soc.*, **176**, 29p.

Mobasher, B., 1987. *Ph.D. Thesis*, University of Durham.

Moffet, A.T. & Birkinshaw, M., 1989. *Astron. J.*, **98**, 1148.

Morgan, W.W., 1958. *Publs. astr. Soc. Pacif.*, **70**, 364.

Morgan, W.W., 1959. *Publs. astr. Soc. Pacif.*, **71**, 92.

Morgan, W.W., 1972. in *External Galaxies and Quasi-Stellar Objects*, IAU Symp. No. 44, Ed. Evans, D.S., Reidel, Dordrecht.

Nemirnoff, R.J. & Dekel, A., 1989. *Astrophys. J.*, **344**, 51.

Newberry, M.V., Kirshner, R.P. & Boroson, T.A., 1988. *Astrophys. J.*, **335**, 629.

Nørgaard-Nielsen, H.U., Hansen, L., Jørgensen, H.E., Aragón-Salamanca, A., Ellis, R.S. & Couch, W.J., 1989. *Nature*, **339**, 523.

O'Connell, R.W., 1976. *Astrophys. J.*, **206**, 370.

O'Connell, R.W., 1980. *Astrophys. J.*, **236**, 430.

Paczyński, B., 1987. *Nature*, **325**, 572.

Peach, J.V., 1970. *Astrophys. J.*, **159**, 753.

Peach, J.V., 1972. in *External Galaxies and Quasi-Stellar Objects*, IAU Symp. No. 44, p. 314, Ed. Evans, D.S., Reidel, Dordrecht.

Peletier, R.F., Davies, R.L., Illingworth, G.D., Davis, L.E. & Cawson, M., 1990. *Astr. Astrophys.*, **100**, 1091.

Pello, R., Le Borgne, J.F., Mathez, G., Mellier, Y., Sanahuja, B. & Soucail, 1990. in *Gravitational Lensing*, p. 293, Eds. Mellier, Y., Soucail, G. & Fort, B., Springer-Verlag, Berlin.

Pello, R., Le Borgne, J.F., Soucail, G., Mellier, Y. & Sanahuja, B., 1991. *Astrophys. J.*, **366**, 405.

Pello-Descayre, R., Soucail, G., Sanahuja, B., Mathez, G. & Ojero, E., 1988. *Astr. Astrophys.*, **190**, L11.

Pence, W.D., 1976. *Astrophys. J.*, **203**, 39.

Persson, S.E., Frogel, J.A. & Aaronson, M., 1979. *Astrophys. J. Suppl.*, **39**, 61.

Peterson, B.A., Ellis, R.R., Kibblewhite, E.J., Bridgeland, M.T., Hooley, T. & Horne, D., 1979. *Astrophys. J. Lett.*, **233**, L109.

Pfefferman, E. & Briel, U.G., 1986. *Proc. S.P.I.E.*, **597**, 208.

Phillipps, S., Davies, J.I. & Disney, M.J., 1990. *Mon. Not. R. astr. Soc.*, **242**, 235.

Pickles, A.J., 1985. *Astrophys. J.*, **296**, 340.

Pickles, A.J. & van der Kruit, P.C. , 1991. Astr. Astrophys. Suppl. in press.

Pritchet, C., 1977. *Astrophys. J.*, **203**, 39.

Readhead, A.C.S., Lawrence, C.R., Myers, S.T., Sargent, W.L.W., Hardebeck, H.E. & Moffet, A.T., 1989. *Astrophys. J.*, **346**, 566.

Renzini, A., 1981. *Ann. Physique*, **6**, 87.

Renzini, A., 1989. in *Evolutionary phenomena in galaxies*, p. 422, Eds. Beckman, J.E. & Pagel, B.E.J., Cambridge University Press, Cambridge.

Renzini, A, & Buzzoni, A., 1983. *Mem. Astr. Soc. Italy*, **54**, 739.

Renzini, A. & Buzzoni, A, 1986. in *Spectral Evolution of Galaxies*, p. 195, Eds. Chiosi, C. & Renzini, A., Reidel, Dordrecht.

Renzini, A., & Fusi Pecci, F., 1988. *Ann. Rev. Astr. Astrophys.*, **26**, 199.

Rich, R.M., 1988. *Astr. Astrophys.*, **95**, 828.

Rich, R.M., 1990. *Astrophys. J.*, **362**, 604.

Rose, J.A., 1985. *Astron. J.*, **90**, 1927.

Rose, J.A., Sharples, R.M., Ellis, R.S. & Bower, R.G., 1989. in *The Epoch of Galaxy Formation*, p. 371, Eds. Frenk, C.S. *et al.*, Kluwer, Dordrecht.

Salpeter, E.E., 1955. *Astrophys. J.*, **121**, 161.

Sandage, A., 1961. *The Hubble Atlas of Galaxies*, Carnegie Institution, Washington.

Salvador-Solé, E., Sanromà, M. & Rdz. Jordana, J.J., 1989. *Astrophys. J.*, **337**, 636.

Sandage, A., 1988. *Ann. Rev. Astr. Astrophys.*, **26**, 561.

Sandage, A. & Hardy, E. , 1973. *Astrophys. J.*, **183**, 743.

Sandage, A., Kristian, J. & Westphal, J.A., 1976. *Astrophys. J.*, **205**, 688.

Sandage, A. & Visvanathan, N., 1978. *Astrophys. J.*, **223**, 707.

Sargent, W.L.W., 1988. in *QSO Absorption Lines: Probing the Universe*, p. 1, Eds. Blades, J.C., Turnsheck, D. & Norman, C.A., Cambridge University Press, Cambridge.

Sargent, W.L.W. Boksenberg, A. & Steidel, C.C., 1988. *Astrophys. J. Suppl.*, **68**, 539.

Saunders, W., Frenk, C.S., Rowan-Robinson, M., Efstathiou, G., Lawrence, A., Kaiser, N., Ellis, R.S., Crawford, J., Xiao-Yang, X. & Parry, I., 1991. *Nature*, **349**, 32.

Savage, B.D. & Mathis, J.S., 1979. *Ann. Rev. Astr. Astrophys.*, **17**, 73.

Scalo, J.M., 1986. *Fundam. Cosmic Physics*, **11**, 1.

Schneider, D.P., Dressler, A. & Gunn, J.E., 1986. *Astron. J.*, **92**, 523.

Schneider, D.P., Gunn, J.E. & Hoessel, J.G., 1983a. *Astrophys. J.*, **268**, 476.

Schneider, D.P., Gunn, J.E. & Hoessel, J.G., 1983b. *Astrophys. J.*, **264**, 337.

Serlemitsos, P.J., Smith, B.W., Boldt, E.A., Holt, S.S. & Swank, J.A., 1977. *Astrophys. J. Lett.*, **211**, L63.

Shaeffer, R. & Silk, J., 1988. *Astrophys. J.*, **333**, 509.

Smail, I., Ellis, R.S., Fitchett, M.J., Nørgaard-Nielsen, H.U., Hansen, L. & Jørgensen, H.E., 1991. Mon. Not. R. astr. Soc. in press.

Smoot, G.F., Bennett, C.L., Kogut, A., Aymon, J., Backus, C., De Amici, G., Galuk, K., Jackson, P.D., Keegstra, P., Rokke, L., Tenorio, L., Torres, S., Gulkis, S., Hauser, M.G., Janssen, M., Mather, J.C., Weiss, R., Wilkinson, D.T., Wright, E.L., Boggess, N.W., Cheng, E.S., Kelsall, T., Lubin, P., Meyer, S., Moseley, S.H., Murdock, T.L., Shafer, R.A. and Silverberg, R.F., 1991. *Astrophys. J. Lett.*, **371**, L1.

Soucail, G. & Fort, B., 1991. *Astr. Astrophys.*, **243**, 23.

Soucail, G., Fort, B., Mellier, Y. & Picat, J.P., 1987a. *Astr. Astrophys.*, **172**, L14.

Soucail, G., Mellier, Y., Fort, B., Hammer, F. & Mathez, G., 1987b. *Astr. Astrophys.*, **200**, L17.

Soucail, G., Mellier, Y., Fort, B. & Cailloux, M., 1988a. *Astr. Astrophys. Suppl.*, **73**, 471.

Soucail, G., Mellier, Y., Fort, B., Mathez, G. & Cailloux, M., 1988b. *Astr. Astrophys.*, **191**, L19.

Soucail, G., Mellier, Y., Fort, B., Mathez, G., Cailloux, M., 1990. in *Gravitational Lensing*, p. 291, Eds. Mellier, Y., Soucail, G. & Fort, B., Springer-Verlag, Berlin.

Spinrad, H., 1980. in *Objects of High Redshift*, IAU Symp. No. 92, p. 39, Eds. Abell, G.O. & Peebles, P.J.E., Reidel, Dordrecht.

Spinrad, H., 1986. *Publs. astr. Soc. Pacif.*, **98**, 269.

Spinrad, H. & Djorgovski, S., 1987. in *Observational Cosmology*, IAU Symp. No. 124, p. 129, Eds. Hewitt, A., Burbidge, G. & Fang, L.-Z., Reidel, Dordrecht.

Strecker, D.W., Erickson, E.F. & Witteborn, F.C., 1979. *Astrophys. J. Suppl.*, **41**, 501.

Sunyaev, R.A. & Zel'dovich, Ya.B., 1972. *Astrophys. Sp. Phys.*, **4**, 173.

Tamman, G.A., Yahil, A. & Sandage, A., 1979. *Astrophys. J.*, **234**, 775.

Thompson, L.A., 1986. *Astrophys. J.*, **306**, 384.

Thompson, L.A., 1988. *Astrophys. J.*, **324**, 112.

Thuan, T.X. & Gunn, J.E., 1976. *Publs. astr. Soc. Pacif.*, **88**, 543.

Tinsley, B.M., 1972. *Astrophys. J.*, **20**, 283.

Tinsley, B.M., 1980. *Fundam. Cosmic Physics*, **5**, 287.

Tinsley, B.M. & Gunn, J.E., 1976. *Astrophys. J.*, **203**, 52.

Trümper, J., 1983. *Adv. Space. Res.*, **2**, No. 4, 241.

Turnrose, B.E., 1976. *Astrophys. J.*, **210**, 33.

Tyson, J.A., 1988. *Astron. J.*, **96**, 1.

Tyson, J.A., 1990. in *Gravitational Lensing*, p. 230, Eds. Mellier, Y., Soucail, G. & Fort, B., Springer-Verlag, Berlin.

Tyson, J.A. & Jarvis, J.F., 1979. *Astrophys. J. Lett.*, **230**, L153.

Tyson, J.A. & Seitzer, P., 1988. *Astrophys. J.*, **335**, 552.

Tyson, J.A., Valdes, F. & Wenk, R.A., 1990. *Astrophys. J. Lett.*, **349**, L1.

Unger, S.W., Brinks, E., Laing, R.A., Tritton, K.P. & Gray, P.M., 1988. *Observer's Guide*, Isaac Newton Group, La Palma.

van den Berg, S., 1960a. *Astrophys. J.*, **131**, 215.

van den Berg, S., 1960b. *Astrophys. J.*, **131**, 558.

van den Berg, S., 1976. *Astrophys. J.*, **206**, 883.

de Vaucouleurs, G., 1959. in *Handbuk der Physics, vol. 53, Astrophysics IV: Stellar Systems*, p. 275, Ed. Flügge, S., Springer-Verlag, Berlin.

Vauglin, I., 1988. *Ph.D. Thesis*, L'Université Claude Bernard, Lyon.

Weinberg, S., 1972. *Gravitation & Cosmology*, Wiley, New York.

Weymann, R.J., Carswell, R.F. & Smith, M.G., 1981. *Ann. Rev. Astr. Astrophys.*, **19**, 41.

White, S.D.M., 1986. in *Inner Space/Outer Space*, p. 228, Eds. Kolb, E.W. *et al.*,, University of Chicago Press.

White, S.D.M., 1989. in *Physics of the Early Universe*, Proc. of the 36th Scottish Universities Summer School in Physics, Eds. Peacock, J.A., Heavens, A.F. & Davis, A.T.

White, S.D.M., Frenk, C.S., Davis, M., 1983. *Astrophys. J. Lett.*, **271**, L1.

White, S.D.M, Silk, J. & Henry, J.P., 1981. *Astrophys. J. Lett.*, **251**, L65.

Whitmore, B.C. & Gilmore, D.M., 1991. *Astrophys. J.*, **367**, 64.

Wlérick, G., Vanderriest, C., Hammer, F., Lelièvre, G., Horville, D., Renard, L., Arnaud, J., & Gouiffes, C., 1990. in *Gravitational Lensing*, p. 295, Eds. Mellier, Y., Soucail, G. & Fort, B., Springer-Verlag, Berlin.

Wood, D.B., 1966. *Astrophys. J.*, **145**, 36.

Wyse, R.F.G., 1985. *Astrophys. J.*, **299**, 593.

Yoshii, Y. & Takahara, F., 1988. *Astrophys. J.*, **326**, 1.